# Four qubits in two ions: demonstrating a universal gate set with polyqubits

Andres Vazquez-Brennan

Linacre College
University of Oxford

*A thesis submitted for the degree of*
*Doctor of Philosophy*

Hilary 2026

## Abstract

Current quantum computing devices typically only use two of the many long-lived energy eigenstates present in each information carrier (trapped atomic ions, superconducting circuits, etc.). Each carrier then stores a single qubit. However, the information per carrier can be increased by using more states. Exploiting such multi-level systems reduces the proportion of expensive gates between carriers in favour of cheaper gates on a single carrier; increases the connectivity within the register's Hilbert space; and leads to more expressive native operations.

Information in multi-level systems has typically been manipulated as qudits, which require computation to be carried out in base-$d$ rather than binary. While this is advantageous for problems that naturally deal with $d$-level variables, most algorithms are agnostic to the numeric base used. In such cases, computation using qubits enables access to more developed compilation tools and avoids the need for a qubit-to-qudit circuit translation.

Exploiting multi-level systems while retaining qubit logic can be achieved by encoding $n$ qubits in a $2^n$-level system, referred to as an $n$-polyqubit. Here, we demonstrate all the building blocks for universal computation with 2-polyqubits using trapped ions. Four states across the hyperfine structure of the $S_{1/2}$ and $D_{5/2}$ levels in $^{137}Ba^+$ with low magnetic field sensitivity are used to store the 2-polyqubit. Single- and two-qubit gates within a single ion, implemented using a 1762 nm laser that drives quadrupole transitions, are characterised using randomised benchmarking and quantum process tomography. Errors in these gates are analysed and found to likely arise from small detuning miscalibrations that, because population can be driven in a loop, lead to interference effects. This results in large, non-Markovian, coherent errors. Additionally, a novel protocol is proposed for native two-ion gates. A two-ion light shift interaction is used, which results in a complex interaction with little computational value if the 2-polyqubit is encoded using arbitrary states in the ion. However, by choosing atomic states which split into two groups with equal light shifts, the resulting Hamiltonian naturally decomposes into a two- three- or four-qubit interaction, depending on how the logical states are arranged over the atomic states. This is used to generate two- and four-qubit GHZ states across two ions. To the author's knowledge, this is the first demonstration of a native two-carrier polyqubit gate in any platform.

# Four qubits in two ions: demonstrating a universal gate set with polyqubits




Andres Vazquez-Brennan
Linacre College
University of Oxford

A thesis submitted for the degree of
*Doctor of Philosophy*

Hilary 2026

To Mum and Dad,
without whose love and unerring belief
this thesis would not exist.

# Acknowledgements

While for you, dear reader, this section is likely what starts off this entire thesis, it is what closes it off for me, alongside what has been a fantastic period of my life. I am thus very glad to have the opportunity to thank many of the people that have made it so special, rich, interesting and, primarily, fun and joyous.

I must commence with the person who, not dissuaded by seeing "string theory" (violin strings, mind you) in my CV, decided to take me on for a DPhil in ion trapping. My supervisor Chris Ballance has been a fantastic source of knowledge, inspiration, and drive to *do* things in the lab. Particularly at the start of my DPhil, I came out of meetings in awe of the natural world, and of what we can do with those twinkling dots that I saw on the screen every day. It's very easy to forget the fact that we work so closely with things as far removed from everyday life as single atoms, and the passion and understanding that you've shared with me in those discussions have helped me keep the wonder of what we do alive.

Just as important as the captain of HMS ABaQuS have been my fellow crew members, with whom I've had the great pleasure of keeping the ship alive – even when it has taken on water! While our little submarine and its gremlins have fought back with all their might, arriving at the final port surrounded by you all has been a true privilege for me. I shall start with my older twin Jamie, who came aboard just a few months before me. You have been so keen to teach me all the tricks you have, and taken immense care of me when the seas have been rough inside and out of the lab. Amongst so many other things, you have made the terminal and the universe of not-quantum bits a far less scary place for me. It also dawned on me that you are the person that I have spent the most hours in the same room with over the last four years, for which I consider myself very fortunate. Sophie joined the crew a few years after me and has filled the lab with a tremendous vitality and positivity since day one. You have battled the gremlins with ferocious words, and in doing so have greatly expanded my French vocabulary. Thank you so much for entertaining my long rambles about physics, states, phases, lasers, code, and for always rebutting with fantastic ideas, which have often been key for getting through the abyss of a theory derivation. I am especially grateful for the immense support that you have given me in the final stretch of writing. But no ship has sailed without its grizzled veterans. Ana, I have tremendous admiration for your tenacity and your drive, and for your ability to work so hard yet still do so with laughter. The experiment exists and works because of you. Thank you for not just that minor task, but also for your keenness and desire

to teach and help me through the process. I am equally indebted to Fabian, the boat's lieutenant and surrogate Mama, for making sure that there was a lab there for me to join, and for carrying me through. Our little foray into what felt more like chemistry (or possibly alchemy) than physics in my first few months was gruelling, but tremendous fun, and I am immensely grateful to you for taking me under your wing. Thank you also for being the person that placed polyqubits on my lap – without you doing so, this thesis would have been very different. William, like me, has brought many sea shanties onboard. Of the many great, unknown melodies that you have graced my ears with, your introduction to bardcore has truly revolutionised my musical experience. Thank you for having brought such a spark to the lab and for being the master of keeping ions cold – though I am sure that the best of the quantum thermodynamics is yet to be seen. Finally, thank you to Ollie for having brought such enthusiasm and tenacity during your time in the experiment. It has been amazing to work with you all, and I hand the baton knowing that, in the strong hands of Sophie and William, the ship will sail steady on its course.

Fortunately, ours is not the only vessel that sails under the OITG flag, and frequent contact with their crew while refuelling has been the source of much amusement and ideas that have contributed to this thesis. There are far too many people to thank and, though I am unable to thank everyone, I am immensely thankful to all of you and the culture of camaraderie and eager willingness to collaborate you all have contributed towards. I joined without having first visited, and I have often said that, in doing so, I blindly struck gold. One person who has helped me develop a lot of the ideas I find most interesting in this thesis through many long and fantastic discussions has been David Nadlinger. Thank you for taking such a keen interest and having so willingly shared your deep physical intuition with me. Another person who I have repeatedly enjoyed bouncing many ideas off of has been the fellow NPL trapper Donovan; thank you for this, and for making conversations about often quite deep physics extremely funny. Gabriel has, from the start, made a great effort to welcome me into the group, and has been someone that I have always been able to turn to for support and advice of any kind. Thank you deeply for this, and for sharing your encyclopedic knowledge of all things ion trapping. So much time in this thesis has also been saved by the members of Lab3 allowing me to plunder their coffers of MiniCircuits treasures on so many occasions – though I am far more grateful for having spent time with the fantastically good nature of everyone in that lab. Thank you also to the admiral of the fleet, David Lucas, for being so attentive in the final few months of the DPhil, when I have been in need of funding, support or navigating through the bureaucracy of the physics department. In fact, one of the best things that has happened to me throughout the writing process has been the waves of support, encouragement and good wishes that I have felt from everyone in the group at large, which have helped me get through a lot of long nights. Thank you all from the bottom of my heart for this, but particularly my fellows in the Old Library bay, Lorenzo, Arjun and Shuying.

Thank you also to Saumya Shivam, and Fabian once more, with whom I collaborated on a theory project. This was my first foray into polyqubits and was the foundation of much of the theory that was further developed in this thesis.

I have been immensely fortunate in that many people have contrived to fish me out of HMS ABaQuS and in doing so have given me the energy and happiness that is as essential to completing a DPhil as any laser. Chief amongst these conspirators have been Oscar and Yunuen, who have kept my mouth full of laughter and my belly full of food, and with whom I have evoked Chavela and Joaqín on so many memorable nights. Thank you for doing everything in your power to keep me well clear of the straight and narrow. Euge has often helped them out in this task, but her I thank for having taught me the most out of anyone over these four years. You have taught me to search, to question, and the joys of freedom, and have also always been unfalteringly present whenever I have had need of someone. Thank you so much. Thank you also to Misha, who helped me disconnect from the lab and connect to many more important things, like capitalist German card games. I never thought that I'd find the free agricultural market such a warm and safe space. Thank you for bringing so much urvertrauen to my life. This word I was introduced to by Rahel, who I must also thank as a gatekeeper of my sanity over the last few months. I doubt that there is a single cobble in Oxford that we have not trodden upon. Thank you also to Simon, for your wisdom and your kindness and for so many great late-night jams. Jenifer, our rituals have been like a clock over this last year and a bit, bringing comfort in their regularity and a safe, welcoming space – thank you so much for your friendship. Thank you also to Hada, and Paola and Diana, for, without thinking, integrating me into all the activity that has surrounded Victoria House and the wider Mexican community in Oxford. It has brought such warmth to me over the years. Furthermore, almost all the people I have mentioned I have met through, or are in some way related to, the incredible salsa community that there is in this town. I am immensely grateful to it and to people like Gwyneth who pour so much energy into it, for opening the gates to so many things in Oxford.

One major source of wellbeing in my life has always been music, and without the vast amount of it that Oxford has afforded to me, I would certainly not have been able to enjoy the process of the DPhil in the way that I did, and it would likely have resulted in a much diminished outcome. There have been far too many people to mention all of them, but I am thankful for everyone in all the groups or collectives that I have been a part of during my time here. These have been, in chronological order: Monkeys on Typewriters, Los del Barco, Salsazón, RanKanKan, Paul Lodge and the Disappearing Men, The Space Pebbles (for one night only), Los Grillos, Quaraoke™ and Los Bueyes. I would particularly like to thank the (past and present) members of Los Grillos, Yunuen, Oscar, Simon, Pip, Tyler, Miguel, Hernando and the special guests Sam and Tobias, for having made such a fantastic adventure possible. My skills in Inkscape, which were invaluable when making figures for this thesis, were honed making posters for this band.

In keeping with the nautical analogy, I would like to thank another boat, the Rocket, for keeping me afloat, mostly healthy, and certainly happy for what was a truly unique year on the Thames. If nothing else, its contributions to this thesis were that my time in the Physics department increased drastically – which may not be entirely unrelated to the fact that it has fantastic showers. This also brings me to acknowledging the contribution that the Beecroft building has brought to my DPhil, not just in the fantastic scientific facilities that it affords, but also by providing an office and a place of work to build a routine out of. Being the creature of habit that I am, this has been invaluable to me – and which I have observed many people in other faculties miss dearly.

More than anybody else, my family have been the main people without whom I would have been entirely unable to complete this thesis. Mum, you have for so many years taught me to do well purely for the sake of it and for the joy of it. Your care, love, encouragement and belief has never faltered for a second, and you have always been a pillar to lean upon. Thank you so much for being such a part of who I am. Dad, my love of physics, of maths, of building and designing things, is so inextricably tied to your desire to teach it and imbue it in me. I still keep the many pages that you filled with any interesting maths thing that you wanted to tell me about – pages covered with parabolas, ellipses, inertia, tension, gravity... Thank you so much for sparking a passion that has kept me going so far down this journey. Ana and Liam, thank you for being such fantastic siblings, for believing in me, for tolerating the neverending maths talk with Dad at the dinner table, and for being overall wonderful people. And to Grandad, thank you so much for being the best orientative example in how to live life and write a thesis I could ever ask for.

Finally, I would particularly like to thank Sophie, David and Chris for their detailed reading of early versions of this manuscript. Their huge help, often requested with entirely unreasonable time constraints, has contributed enormously to the legibility of this manuscript.

# Abstract

Current quantum computing devices typically only use two of the many long-lived energy eigenstates present in each information carrier (trapped atomic ions, superconducting circuits, etc.). Each carrier then stores a single qubit. However, the information per carrier can be increased by using more states. Exploiting such multi-level systems reduces the proportion of expensive gates between carriers in favour of cheaper gates on a single carrier; increases the connectivity within the register's Hilbert space; and leads to more expressive native operations.

Information in multi-level systems has typically been manipulated as qudits, which require computation to be carried out in base-$d$ rather than binary. While this is advantageous for problems that naturally deal with $d$-level variables, most algorithms are agnostic to the numeric base used. In such cases, computation using qubits enables access to more developed compilation tools and avoids the need for a qubit-to-qudit circuit translation.

Exploiting multi-level systems while retaining qubit logic can be achieved by encoding $n$ qubits in a $2^n$-level system, referred to as an $n$-polyqubit. Here, we demonstrate all the building blocks for universal computation with 2-polyqubits using trapped ions. Four states across the hyperfine structure of the $S_{1/2}$ and $D_{5/2}$ levels in $^{137}Ba^+$ with low magnetic field sensitivity are used to store the 2-polyqubit. Single- and two-qubit gates within a single ion, implemented using a 1762 nm laser that drives quadrupole transitions, are characterised using randomised benchmarking and quantum process tomography. Errors in these gates are analysed and found to likely arise from small detuning miscalibrations that, because population can be driven in a loop, lead to interference effects. This results in large, non-Markovian, coherent errors. Additionally, a novel protocol is proposed for native two-ion gates. A two-ion light shift interaction is used, which results in a complex interaction with little computational value if the 2-polyqubit is encoded using arbitrary states in the ion. However, by choosing atomic states which split into two groups with equal light shifts, the resulting Hamiltonian naturally decomposes into a two- three- or four-qubit interaction, depending on how the logical states are arranged over the atomic states. This is used to generate two- and four-qubit GHZ states across two ions. To the author's knowledge, this is the first demonstration of a native two-carrier polyqubit gate in any platform.

# Contents

**List of Figures** **xii**

**List of Tables** **xv**

**List of Abbreviations** **xvi**

**1 Introduction** **1**
1.1 Why just 1s and 0s? . . . 3
1.2 Why *not* just 1s and 0s? . . . 4
1.3 Thesis outline . . . 6

**2 Qubits, qudits and Polyqubits** **7**
2.1 Notation . . . 9
2.2 Qubits . . . 12
2.3 Qudits . . . 16
2.4 Polyqubits . . . 19
2.5 Discussion . . . 21
2.5.1 Hardware comparison . . . 21
2.5.2 Protocol comparison . . . 25
2.5.3 Entanglement in polyqubits . . . 27
2.6 Summary . . . 28

**3 Ion trapping theory** **29**
3.1 State evolution . . . 29
3.2 Trapping mechanism . . . 31
3.2.1 Quantised motion . . . 33
3.2.2 Two-ion chains . . . 34
3.3 Ion-laser interactions . . . 35
3.3.1 Resonant driving . . . 35
3.3.2 Light shifts . . . 38
3.4 TSR sequences . . . 40
3.4.1 Linear connectivity . . . 41
3.4.2 Closed-loop interferometers . . . 43

3.4.3 Cyclic connectivity . . . 45
3.4.4 Discussion . . . 46
3.5 Calculating the Rabi frequency . . . 49
3.5.1 Electronic multipole moments . . . 50
3.5.2 Beam geometry . . . 52
3.5.3 Beam tensor components . . . 53
3.6 Two-ion light shift gates . . . 54
3.6.1 The geometric phase . . . 55
3.6.2 Generating the state-dependent force . . . 58
3.7 Summary . . . 63

**4 Primitive Polyqubit operations 64**
4.1 Intra-ion gates . . . 65
4.1.1 The impact of connectivity . . . 68
4.1.2 Diagonal gates . . . 69
4.2 Inter-ion gates . . . 71
4.2.1 Review of Mølmer-Sørensen decompositions . . . 74
4.2.2 Inter-ion two-qubit light shift gates . . . 76
4.2.3 General inter-ion LS gates . . . 81
4.3 State preparation . . . 85
4.4 Readout . . . 85
4.4.1 Heralded SPAM protocol for leakage detection . . . 88
4.5 Summary . . . 89

**5 Sources of Error 91**
5.1 Background theory . . . 92
5.1.1 Quantum processes . . . 92
5.1.2 Fidelity and error metrics . . . 93
5.1.3 Evolution under stochastic Hamiltonians . . . 96
5.2 Intra-ion gates . . . 99
5.2.1 Detuning and LS miscalibration . . . 100
5.2.2 Sources of dephasing . . . 103
5.2.3 Rotation angle miscalibration . . . 108
5.2.4 Off-resonant excitation . . . 109
5.2.5 Spontaneous decay . . . 109
5.2.6 Raman and Rayleigh scattering . . . 110
5.3 Inter-ion gates . . . 112
5.3.1 Control errors . . . 113
5.3.2 Motional heating . . . 118
5.3.3 Motional dephasing . . . 119

5.3.4 Polarisation . . . 120
5.4 Summary . . . 122

**6 Experimental apparatus and choice of states 124**
6.1 The $^{137}Ba^{+}$ ion . . . 124
6.1.1 Choice of species . . . 124
6.1.2 Choice of isotope . . . 126
6.1.3 Level structure . . . 127
6.2 Choosing the computational manifold . . . 128
6.2.1 Key design desiderata . . . 128
6.2.2 The intermediate-field regime . . . 130
6.2.3 Ground, metastable or both? . . . 132
6.2.4 Properties of the chosen manifold . . . 134
6.3 More than two qubits per ion . . . 137
6.3.1 Intra-ion gates . . . 138
6.3.2 Inter-ion gates . . . 140
6.4 Laser systems . . . 141
6.4.1 Control system . . . 141
6.4.2 Quadrupole laser system . . . 142
6.4.3 532 nm laser system . . . 146
6.5 Summary . . . 146

**7 Experimentally implementing intra-ion gates 148**
7.1 Characterisation protocols . . . 148
7.1.1 Randomised Benchmarking . . . 148
7.1.2 Quantum Process Tomography . . . 150
7.2 Calibration routines . . . 152
7.2.1 Calibrating light shifts . . . 153
7.2.2 Transition frequency and Rabi frequency calibration . . . 156
7.2.3 Driving tone phases . . . 159
7.3 RBM results . . . 160
7.3.1 Sources of error . . . 162
7.4 Quantum Process Tomography . . . 171
7.4.1 Experimental procedure and data processing . . . 171
7.4.2 Results . . . 172
7.5 Summary . . . 174

**8 Experimentally implementing inter-ion gates 182**
8.1 Gate circuits . . . 183
8.1.1 Partial tomography . . . 183

8.1.2 Generating and measuring GHZ states . . . 184
8.1.3 Echo sequences . . . 185
8.2 Choosing the mode . . . 190
8.3 Setting the beam polarisation . . . 193
8.4 State-Dependent Forces on a Single Polyqubit . . . 195
8.5 Gate implementation . . . 196
8.5.1 Beam alignment . . . 197
8.5.2 Calibrating gate parameters . . . 198
8.5.3 Calibrating gate phases . . . 200
8.6 Results . . . 202
8.6.1 Sources of error . . . 204
8.7 Conclusion . . . 212

**9 Conclusion** **214**
9.1 Outlook . . . 214
9.1.1 Breaking the multi-photon resonance condition . . . 215
9.1.2 Improving error characterisation . . . 215
9.1.3 Expressive inter-ion gates . . . 216
9.1.4 Increasing the system size . . . 216
9.1.5 Partitioned intra-ion gates . . . 217

**Appendices**

**A Fidelity Expressions and Proofs** **220**
A.1 Exponentials of null operators . . . 220
A.2 Small rotations of involutory operators . . . 220
A.3 State fidelity of small diagonal unitaries . . . 221

**B Sequence of TSRs in the atomic frame** **223**
B.1 Derivation of a sequence of TSR pulses . . . 223
B.2 Deriving the LS correction through the TSR phase . . . 225

**C Bit-string identities** **227**
C.1 Sum over all bit-strings . . . 227
C.2 Sum over bit-strings of definite parity . . . 228

**D Sleepy gate identities** **229**
D.1 Sleepy Gate with imbalanced SDF phase and amplitude . . . 229
D.2 General expression for the Sleepy Gates unitary . . . 231

**E LS Gate decompositions** **233**

**References** **235**

# List of Figures


2.1 Sketch showing a qubit, qudit and polyqubit architecture. . . . . 8
2.2 Example polyqubit state containing a Bell pair. . . . . 11
2.3 Qubit placement in a polyqubit circuit diagram. . . . . 12
2.4 A qubit on a Bloch sphere. . . . . 13
2.5 Conversion between CNOT and CZ gates. . . . . 15
2.6 Example connectivity graph, showing four transitions that form a cycle. . 19

3.1 Confining potentials in an ion trap, and string of ions. . . . . 31
3.2 Sketch of the motional modes of a two-ion chain. . . . . 34
3.3 Sketch of the effect of light-shifts on multi-level systems. . . . . 38
3.4 Cyclic and linear computational manifolds, and sketch of transitions with different energy directions. . . . . 41
3.5 Loop interferometer experiments. . . . . 43
3.6 Definitions of the laser beam geometry. . . . . 52
3.7 Behaviour of an off-resonantly driven classical oscillator. . . . . 57
3.8 Diagram of how state-dependent forces are generated in LS gates. . . . . 58

4.1 Full connectivity graph for a 2-polyqubit, with the gate implemented when driving a TSR on each transition. . . . . 66
4.2 Single-qubit gate in terms of controlled rotations. . . . . 67
4.3 Protocol to synthesise TSRs on forbidden transitions, and possible connectivity graphs with a 4-cycle. . . . . 68
4.4 Sketch of RF tones used to implement a circuit containing a diagonal gate. 70
4.5 Sketch of arbitrary two-beam LS on a 2-polyqubit, and the LS used to implement the Sleepy Gates. . . . . 78
4.6 Circuit diagrams for implementing gates on more than two qubits using intra-ion CNOT gates. . . . . 79
4.7 Decomposition of some useful gates using few inter-ion gates. . . . . 80
4.8 LS structure for implementing a CCCZ gate. . . . . 83
4.9 Readout scheme for multi-level systems in ion traps. . . . . 86
4.10 Schemes for reading out a subset of qubits in a register of polyqubits using auxiliary ions. . . . . 88

5.1 Example of a typical experimental noise power spectral density. . . . . 96
5.2 Breaking the multi-photon resonance condition when driving transitions on-resonance in the presence of light-shifts. . . . . 102
5.3 Simulated errors due to spontaneous decay and off-resonant scatter. . . . . 111
5.4 Mean and median fidelity of small random diagonal gates . . . . . 115
5.5 Simulated errors from motional heating and motional decoherence in two-ion gates. . . . . 119
5.6 Simulated error due to mis-set LS in Sleepy Gates. . . . . 121

6.1 $^{137}Ba^{+}$ level structure. . . . . 125
6.2 Breit-Rabi diagram for the $D_{5/2}$ level. . . . . 130
6.3 Possible manifold choices in the $S_{1/2}$ level. . . . . 132
6.4 Sketch of the chosen polyqubit manifold. . . . . 134
6.5 Calculated properties of the chosen manifold as a function of magnetic field. 135
6.6 Two-beam LS on the chosen encoding. . . . . 136
6.7 Sketch of the modulation for the quadrupole laser system. . . . . 142
6.8 Geometric $\beta$ factors for quadrupole transitions. . . . . 143
6.9 Setting the EOM modulation index. . . . . 145

7.1 Dipole and quadrupole light shifts on the chosen polyqubit states. . . . . 154
7.2 Measurements to extract the magnetic field and quadrupole beam polarisation. . . . . 155
7.3 Polyqubit RBM experiments. . . . . 160
7.4 RBM survival probability in polyqubit RBM experiments initialised to $|00\rangle$ and an even superposition . . . . . 164
7.5 Ramsey contrast measurements used to extract the magnetic field noise and laser frequency noise PSD. . . . . 165
7.6 Comparison between experimental errors and simulated errors from magnetic field and laser frequency noise. . . . . 167
7.7 Simulated RBM traces when breaking the multi-photon resonance condition. 168
7.8 Comparison between experimental errors and simulated errors from breaking the multi-photon resonance condition. . . . . 170
7.9 Average error of gates in an intra-ion universal gate set extracted with Quantum Process Tomography. . . . . 172
7.10 Breakdown of the error generators extracted from Quantum Process Tomography for different kinds of errors. . . . . 173
7.11 QPT data for the CZ gate. . . . . 176
7.12 QPT data for the identity gate. . . . . 177
7.13 QPT data for a Hadamard gate on the LSB qubit. . . . . 178
7.14 QPT data for a Hadamard gate on the MSB qubit. . . . . 179

7.15 QPT data for a T gate on the LSB qubit. . . . . 180
7.16 QPT data for a T gate on the MSB qubit. . . . . 181

8.1 Circuits used for evaluating two-ion LS gates. . . . . 183
8.2 Time scan of a $ZZZZ$ gate. . . . . 186
8.3 Motional trajectories when using a motional echo sequence. . . . . 187
8.4 Effects of SDF phase mismatches on each ion in a monoqubit LS gate. . . . 189
8.5 Simulated single-beam LS as a function of beam geometry. . . . . 193
8.6 Measured single-beam light shifts. . . . . 194
8.7 State-dependent forces on pairs of states in the encoding. . . . . 195
8.8 Single-ion SDF experiment on a full polyqubit. . . . . 197
8.9 Effects of phase errors on the closing gates. . . . . 201
8.10 GHZ contrast and population measurements. . . . . 203
8.11 Loss in Ramsey contrast due to noisy light shifts from the 532 nm beams. 206
8.12 Simulated errors due to polarisation miss-sets in the chosen beam geometry. 209
8.13 Variation in the parity contrast over multiple days. . . . . 212

# List of Tables

6.1 Properties of different $Ba^+$ ions. . . . . 126
6.2 Properties of the chosen manifold . . . . . 134

7.1 Errors in polyqubit RBM. . . . . 161
7.2 Errors in monoqubit RBM. . . . . 162

8.1 Properties of the four radial modes. . . . . 191
8.2 Measured GHZ fidelities. . . . . 203
8.3 Common parameters in inter-ion gates. . . . . 204
8.4 Summary of expected errors. . . . . 210

E.1 Analytical rotation rates in the presence of incorrect two-beam LS. . . . . 234

# List of Abbreviations

**QEC** . . . . . Quantum Error Correction.

**QIP** . . . . . Quantum Information Processing.

**CoM** . . . . . Centre of Mass.

**SPAM** . . . . . State-Preparation And Measurement.

**LS** . . . . . Light Shift.

**MS** . . . . . Mølmer-Sørensen.

**MSB** . . . . . Most Significant Bit (i.e. the leftmost bit $i_1$ in $|i_1 i_0\rangle$).

**LSB** . . . . . Least Significant Bit (i.e. the rightmost bit $i_0$ in $|i_1 i_0\rangle$).

**TSR** . . . . . Two-State Rotation.

**FD** . . . . . Fluorescence Detection.

**RPE** . . . . . Robust Phase Estimation.

**PSD** . . . . . Power Spectral Density.

**LF** . . . . . Low Frequency (referring to the set of radial modes along the direction of weakest confinement).

**HF** . . . . . High Frequency (referring to the set of radial modes along the direction of strongest confinement).

**PBS** . . . . . Polarising Beam Splitter.

**QWP** . . . . . Quarter-Wave Plate

**HWP** . . . . . Half-Wave Plate

**AOM** . . . . . Acousto-Optic-Modulator

**SDF** . . . . . State-Dependent Force (also referred to as a Spin-Dependent Force in the literature).

**PSD** . . . . . Power Spectral Density

**DDS** . . . . . Direct Digital Synthesis

**EM** . . . . . Electromagnetic

**IP** . . . . . In-Plane

**OOP** . . . . . Out-Of-Plane

**RWA** . . . . . Rotating-Wave Approximation

*That's really interesting – in a bad way.*

— Chris Ballance, on a day when the lab gremlins were particularly enjoying themselves.

# 1 Introduction

It is impossible to overstate the impact and ubiquity of computers in the modern world[1]. Within the span of a single human lifespan, they have revolutionised the way we communicate with each other, democratised access to almost all human knowledge, and enabled previously unimaginable understanding and predictive power of the natural world, amongst an uncountable list of other achievements. Nonetheless, computers are fundamentally machines built for a purpose, and, like any other machine, their ability to carry out said purpose is simultaneously enabled and constrained by the physics that describes its constituent parts. For example, the great feats of ingenuity that were the early electro-mechanical devices, such as those used to crack the Enigma code [1], encoded information in electric voltages and currents as modern computers do. However, these electrical signals were controlled by the movement of large magnetic relays. The inertia and friction in these mechanical moving parts would make building a device with the Gigahertz clock speeds of current processors completely out of the question.

Modern-day computers are able to overcome such limitations by replacing these relays with transistors, devices governed by *quantum* instead of classical physics. Nonetheless, information is still encoded in macroscopic currents and voltages, which are well-described by Maxwell's equations. Their state is thus a *classical* variable, so the information they encode is incapable of displaying any effects outside the realm of classical physics. Certain

[1] Even the author's kettle has a computer.

problems, such as simulating the behaviour of large quantum systems, are believed to have no efficient solution using such classical computers. This is far from a purely academic question: pharmaceutical drugs and novel exotic materials such as superconductors are examples of quantum systems that we are currently incapable of efficiently simulating. Such simulations could deepen our understanding of these systems and streamline the discovery of new drugs and materials, whose impact in society could be vast.

This difficulty may stem from the fact that, as Feynman famously declared, "*Nature isn't classical, dammit*" [2], yet we are trying to simulate it using classical variables. If information were not just manipulated by quantum systems as it is currently, but *encoded* in their quantum state, effects such as superposition and entanglement could be harnessed by the processor. A device like this would be a *quantum computer*. Since the information they store and manipulate would obey the same physics as the quantum systems we wish to study, it stands to reason that they could simulate their behaviour more efficiently than classical computers [2][2].

Nonetheless, to quote Feynman again, building such a quantum computer is a "*wonderful problem, because it doesn't look so easy*". Efforts to build them over the last twenty to thirty years certainly agree with him. The difficulty arises from the fragility of quantum coherence. A particle storing some information in a superposition state may couple to an external source of noise, becoming entangled with it. The state of the particle will thus be mixed [3], destroying the information it carried. Unfortunately, *some* coupling to an environment is necessary for readout. On top of this, the no-cloning theorem [4] makes checking for such errors a perniciously difficult task, sparking the field of quantum error correction (QEC) [5–7].

In spite of this, progress over the last few years has been staggering. Error rates in single-qubit (quantum bit) and two-qubit operations below $10^{-6}$ [8] and $10^{-4}$ [9] respectively have been demonstrated. Devices capable of manipulating hundreds of qubits exist [10–12], displaying many of the building blocks for fault-tolerant quantum computation [12, 13]. Furthermore, their use in tackling meaningful simulation problems,

[2] If nothing else, a quantum simulator could *emulate* a target system.

intractable on other devices, is emerging [14] and recent theoretical proposals suggest that other applications in cryptography may be within closer reach than anticipated [15].

However, modern quantum devices are still not large enough to definitively exploit the advantages over classical computers in useful problems. There are still immense challenges ahead, both in the development and engineering of hardware, and the design of architectures and protocols. It is towards problems of the latter kind that the work in this thesis aims to contribute.

## 1.1 Why just 1s and 0s?

Most[3] classical computers store information in *bits*, variables that can only take the values 0 and 1. The quantum equivalent is a *qubit*, which can exist in any superposition of states $|0\rangle$ and $|1\rangle$, and outputs 0 or 1 when measured. Mathematically, qubits exist in a *Hilbert space*, whose dimensionality is often regarded as the fundamental resource used by a quantum computer [17]; the Hilbert space of a qubit is 2-dimensional. A register of $n$ qubits is described by a quantum state that exists in a $2^n$-dimensional Hilbert space. This exponential scaling of the Hilbert space dimension from a linear increase in the number of qubits is central to the computational advantages of a quantum computer [17].

Qubits are encoded in hardware using two long-lived states of a quantum object. We refer to such objects as *information carriers*. In this thesis, trapped atomic ions that are levitated in vacuum, and thus are well-isolated from their environment, are used as the information carriers. Ions were used in the demonstration of the highest-fidelity operations mentioned previously, as well as the highest-fidelity state-preparation and measurement (SPAM) operations [18]. Nonetheless, a whole zoo of quantum computing platforms exist, which use other physical systems as the information carriers. Some examples are resonant superconducting circuits [19]; trapped neutral atoms [20]; photonic circuits [21]; defects in silicon crystals [22, 23]; nitrogen vacancies in diamonds [24]; and many others.

These platforms have encoded information using qubits almost universally, despite all of them possessing more than two long-lived states suitable for storing quantum information. Restricting these systems to just two levels is often reasonable, since they

[3] Many of the earliest computers, such as ENIAC [16], used decimal rather than binary arithmetic.

are the simplest to manipulate with high fidelity. However, as discussed in Chapter 2, many of the challenges in increasing the size of quantum computers are not intrinsic to operations on a large Hilbert space, but instead stem from the need to control many physical information carriers. A more efficient use of physical resources could be reached by using *more* than two states within each carrier for computation. While this does increase the complexity of many operations, only slight modifications to the techniques for qubit manipulation are required, which can be done with very low error. The subsequent increase in Hilbert space dimensionality may compensate for a small drop in fidelity.

Instead of qubits, $d$-level systems are often used to store a *qudit*, the quantum version of a base-$d$ digit; the computation is then carried out in base-$d$. They have been implemented in trapped ions [25–29], superconducting circuits [30–32], photonic circuits [33, 34], silicon defects [35] and many more. Qudits of high dimensionality have been demonstrated, with $^{137}Ba^{+}$ ions [26] – the same species used in this thesis – having been used to control a 25-level qudit, and photons used to manipulate 32-level ones [36].

Multi-level computation affords a plethora of advantages, as will be discussed in detail in Chapter 2. Amongst these is a reduced reliance on two-carrier gates (the equivalent of two-qubit gates in qubit systems) which typically carry orders of magnitude higher error than single-carrier ones. Additionally, the effective connectivity of the system is also increased, since information is packed more densely. This reduces the need for physical transport operations [11, 37] or SWAP gates [38].

## 1.2 Why *not* just 1s and 0s?

The advantages of multi-level systems described above relate to the hardware, and are independent of the fact that information is stored in base-$d$. Indeed, most algorithms are agnostic to the base used[4].

In the general case, the use of qubits is likely advantageous. Circuit compilation [38, 41–43] and optimisation is far more mature for qubits than for qudits [44, 45]. This allows circuits to be made shallower, reducing errors. Furthermore, most algorithms are developed for qubits and thus require a transpilation step – the circuit must be rewritten

[4] A notable exception arises when tackling problems that depend on $d$-level variables, in which case qudits enable strikingly efficient compilation [39, 40].

using qudit gates. Such transpilation can be sidestepped by using polyqubits. Another noteworthy benefit of regular qubits is precisely that they *are* regular – they are ubiquitous in quantum information processing (QIP). Almost every researcher in the field is more familiar with qubits than qudits. As an example, the matrix

$$\begin{pmatrix} 1 & 0 & 0 & 0 \\ 0 & 1 & 0 & 0 \\ 0 & 0 & 0 & 1 \\ 0 & 0 & 1 & 0 \end{pmatrix} \tag{1.1}$$

will likely be recognised by everyone in QIP as the matrix for a two-qubit `CNOT` gate, but by very few people as the single-ququart gate that flips states $|2\rangle \leftrightarrow |3\rangle$. Similarly, Nielsen and Chuang's textbook [46], likely the most widely used in QIP, mentions the word "qudit" exactly once[5]. Information and intuition are much more prevalent for qubits than qudits, which can streamline the research process.

It seems that much could be gained from combining multi-level hardware with qubit logic. This can be done by recognising that the $2^n$-dimensional Hilbert space spanned by $n$ qubits is indistinguishable from the Hilbert space spanned by a single qudit of dimension $d = 2^n$. Indeed, such a qudit can be reinterpreted as $n$ qubits that all exist in the same information carrier: we refer to this as an *$n$-polyqubit* [47], although the term *virtual qubits* is also common in the literature [27, 48–51]. This thesis will deal almost exclusively with 2-polyqubits, which can be hosted in a 4-level system.

Logical operations on a single carrier (intra-carrier gates) can then act on one, or many of the qubits it hosts. With this realisation, the advantages of multi-level systems become easier to interpret. Fewer inter-carrier gates (which act on more than one carrier) are needed, because some are now intra-carrier gates (which act on just one carrier). Such operations are closer to regular single-qubit operations than two-qubit ones. Furthermore, the connectivity increases because gates between qubits in the same carrier are always accessible, even if gates between some carriers are not.

While polyqubits are certainly not new, they have not been studied to the same depth as generic qudit operations, and targeted hardware implementations are rare [31, 52]. Additionally, native hardware operations do not generally have a simple structure when

[5] This is in page 343 in the author's edition. In fairness, "qutrit" is mentioned four times, including once in the same sentence as "qudit" and in the glossary.

viewed through a polyqubit lens. Thus, constructing operations that act on some qubits, but not others, is non-trivial, particularly for inter-carrier gates. Indeed, to the author's knowledge, no demonstration of inter-carrier polyqubit gates has been reported.

This is the gap that this thesis aims to fill. It presents theoretical work that builds upon previous constructions of polyqubit gates from native multi-level hardware operations in ion trapping systems, and proposes a native inter-ion polyqubit gate. These are then implemented experimentally, first characterising operations on a single ion, and then demonstrating two- and four-qubit gates across two ions using the proposed scheme. In addition, a survey of errors in multi-level systems is undertaken, identifying sources of error that are unique to such systems.

## 1.3 Thesis outline

We begin with a broad, hardware-agnostic overview and comparison of qubits, qudits and polyqubits in Chapter 2, after which the physics of multi-level operations in ion traps is introduced in Chapter 3. Chapter 4 then applies these operations to polyqubit gates, including the novel proposal for native inter-ion gates. This is followed by an analysis of the sources of error in single-ion and two-ion operations in Chapter 5. Chapter 6 provides an overview of the experimental apparatus and discusses the atomic states used to encode two qubits per ion. Intra-ion operations are experimentally implemented and characterised with randomised benchmarking and quantum process tomography in Chapter 7, and the proposed inter-ion gate mechanism is demonstrated in Chapter 8. Finally, Chapter 9 summarises the thesis and provides future research directions.

*Hello, this is Sophie Decoppet.*

— Sophie Decoppet, on the phone to Toptica, delivered in the style of Audrey Hepburn.

# 2 Qubits, qudits and Polyqubits

At an abstract level, the total Hilbert space dimension accessible to a quantum computer can be thought of as its fundamental computational resource. Indeed, in theory, all computers with the same Hilbert space dimension can be considered equivalent, since any unitary on that Hilbert space can be synthesised on each of them, using their universal gate sets. However, for universal, fault-tolerant computation, this synthesis needs to be made efficient in the number of operations required. This depends, amongst other things, on the structure underlying the Hilbert space, its partition into subspaces, and the ensuing native gate set [17]. The tensor product of these subspaces is then what forms the full Hilbert space. This partition is often physically motivated, as the full quantum register is almost always made up of a collection of physically distinct objects (individual trapped ions, neutral atoms, superconducting resonators, etc.) which will be referred to as individual *information carriers*. Nonetheless, mathematically, one could construct other valid tensor product structures for the full Hilbert space, which *do not* have to correspond to a physical partition into subsystems. As long as one has the tools to fully control and measure each *logical*[1] subsystem, such logical partitions make sense [53, 54].

Qubits, qudits and polyqubits can be thought of as different ways of partitioning a full Hilbert space. They are represented in Figure 2.1. Logically, a qubit is simply a

[1] Note that this does *not* refer to a logical qubit/qudit in the context of error correction and fault tolerance. While the two concepts can be related, we will not discuss error correction in this thesis.

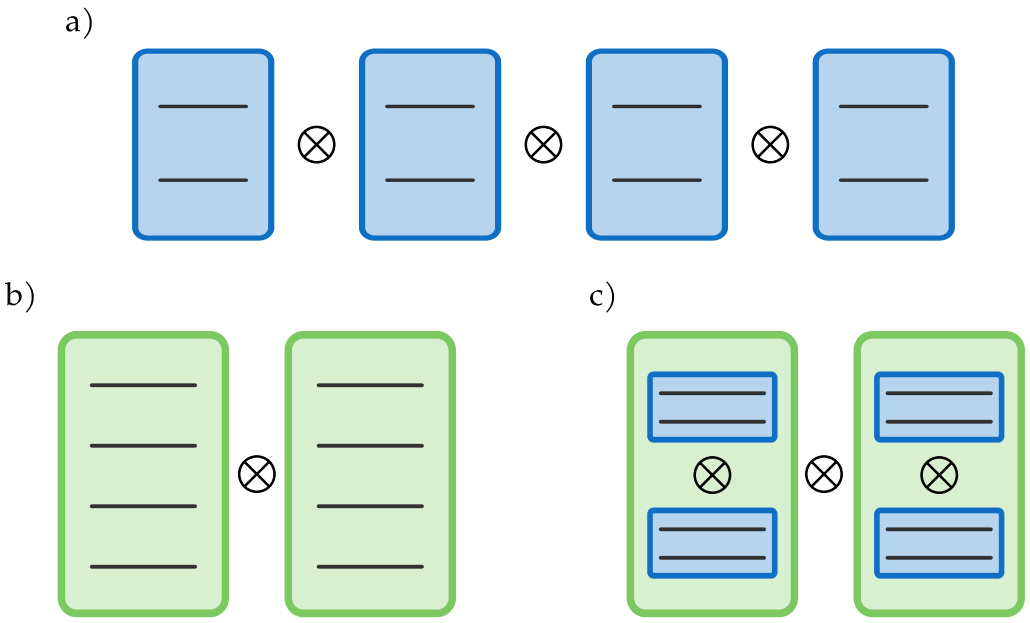



**Figure 2.1:** Three possible partitions of a 16-dimensional Hilbert space into a) four qubits, b) two ququarts and c) four qubits spread across two 2-polyqubits. Notice that, while each information carrier contains two qubits, these are not "separate", in the sense that the four states in the carrier are the four *tensor product* states of the qubits: $|00\rangle$, $|01\rangle$, $|10\rangle$, $|11\rangle$.

two-level quantum system, so that the full Hilbert space is mathematically constructed as a tensor product of two-level subspaces. Qubits are also the quantum equivalent of classical bits, and thus calculations using qubits are expressed in binary, or base 2. Their generalisation to a $d$-level subsystem ($d > 2$) is a qu*d*it, which enables computation in base $d$. Usually, the physical Hilbert space partition matches the logical one. Then, each information carrier, which is either a two-level or a multi-level system[2], stores one qubit or qudit, respectively. The case of hosting one qubit per information carrier is by far and away the most common architecture in quantum information science, so we will use the term *monoqubit* to refer to it. This term specifies both a computational architecture (the Hilbert space is split into qubits) and a hardware one (one qubit is hosted in each carrier). The term *qubit* will be reserved to refer to the computational architecture only[3].

It can be easily seen that a multi-level information carrier could host something other than just a single qudit. As a specific case, if its dimension is $d = 2^n$, $n \in \mathbb{Z}$, then its Hilbert

[2]For these definitions, we consider the information carriers to only contain the computational states and ignore any other states which may be physically present.

[3]On the other hand, the word *qudit* will be used to refer to both a computational and hardware architecture interchangeably, although when confusion may arise, the hardware architecture will be referred to as *multi-level*. The author hopes that the concept referred to will be clear from context.

space could be interpreted as the tensor product of $n$ qubits, which is discussed in detail in Section 2.4. This makes the physical and logical partitions of the Hilbert space different: indeed, now each information carrier is thought of as hosting $n$ qubits, instead of a single qudit. This is what we refer to as a *polyqubit* [47], although the term *virtual qubits* is also common in the literature [27, 48–51]. When needed, the number of qubits will be specified by referring to an $n$-polyqubit. Because the vast majority of this thesis will deal with the case of 2-polyqubits, when no $n$ is specified, $n = 2$ is implied.

The aim of this chapter is to provide a broad, platform-independent discussion on qubit, qudit and polyqubit computation, as well as to introduce necessary notation. We discuss how the three architectures are related to each other; how universal computation can be carried out using all three of them; outline their advantages and disadvantages; and briefly outline specific use cases that are well suited to each. Because the remainder of the thesis contains an experimental demonstration of polyqubits, emphasis will be placed on these over the others: the entirety of Chapter 4 will be dedicated to polyqubit operations in ion trap systems.

## 2.1 Notation

Most works that deal with multi-level computation carry considerable notational baggage compared to regular qubit-based computation. This, in part, is inherent to the increased number of states and operations that need to be described (e.g. a single-qudit operation may need to specify *which* states within the qudit it acts upon, which is unnecessary in qubits). This work introduces a further complication, in that we will wish to interpret a single state in a multi-level system as the joint state of many qubits. The ability to easily and clearly switch between labelling a particular state by its physical state (e.g. the atomic state in an ion), or the qudit/qubit state it encodes will be invaluable. We use the following convention, mostly inspired by [48]:

- Physical (i.e. atomic) states will mostly be labelled by Greek letters, $|\nu\rangle, |\mu\rangle$. At times, it will be convenient to label a state according to a transition that drives it. Because only linear or (singly) cyclical connectivity graphs will ever be considered

(see Section 2.3) we can always make this mapping one-to-one. A transition $T$ drives $|T\rangle \leftrightarrow |T+1\rangle$.

- Qudit states will be labelled by Latin letters in Serif font, $|i\rangle$. The label "$i$" should be interpreted as a base-10 number. Often, the qudit and atomic states are indexed by the same number, in which case they can be used interchangeably.

- The state of individual qubits within an information carrier will be labelled by Latin letters in sans-Serif font, $|\mathsf{q}\rangle$. Often this will be used within a larger bit-string, so that $|\mathsf{q}_{(n-1)}...\mathsf{q}_1\mathsf{q}_0\rangle \triangleq |\text{bin}(i)\rangle$ where bin($i$) is the binary representation of the decimal number $i$. We will often use a vector notation to denote an n-bit string $\mathbf{b} = (b_{n-1},...,b_1,b_0)$ and $\mathbf{i}$ will sometimes be used to refer to the bit-string corresponding to decimal number $i$. We will always index the qubits in an information carrier by increasing significance, which increases from right to left in a ket or bit-string. The most discussed case will be that of two qubits per ion; the qubits $|\mathsf{q}_1\rangle$ and $|\mathsf{q}_0\rangle$ in the state $|\mathsf{q}_1\mathsf{q}_0\rangle$ will be referred to as the Most-Significant Bit (MSB) and Least-Significant Bit (LSB) qubits, respectively. See Section 2.4.

Further complication arises when considering tensor product states of two information carriers, which each contain potentially many qubits. It will be convenient to be able to distinguish which qubits are in each carrier, while also being able to read the full state as one bit-string. We will separate the states of the carriers by a ":" as in

$$|\mathsf{q}_{(n-1)}...\mathsf{q}_1\mathsf{q}_0:\mathsf{r}_{(n-1)}...\mathsf{r}_1\mathsf{r}_0\rangle \triangleq |\mathsf{q}_{(n-1)}...\mathsf{q}_1\mathsf{q}_0\rangle \otimes |\mathsf{r}_{(n-1)}...\mathsf{r}_1\mathsf{r}_0\rangle \tag{2.1}$$

We could also write a two-qudit state $|i:j\rangle$, in which case we will also refer to $|i\rangle$ and $|j\rangle$ as the most- and least-significant qudits.

As an example, consider the following state of two ququarts (where a ququart is a four-level qudit with states $\{|0\rangle,|1\rangle,|2\rangle,|3\rangle\}$):

$$|\psi\rangle = \frac{1}{\sqrt{2}}(|1:1\rangle + |3:3\rangle), \tag{2.2}$$

The polyqubit state encoded by it (under the mapping in Equation (2.29)) is

$$|\psi\rangle = \frac{1}{\sqrt{2}}(|01:01\rangle + |11:11\rangle), \tag{2.3}$$

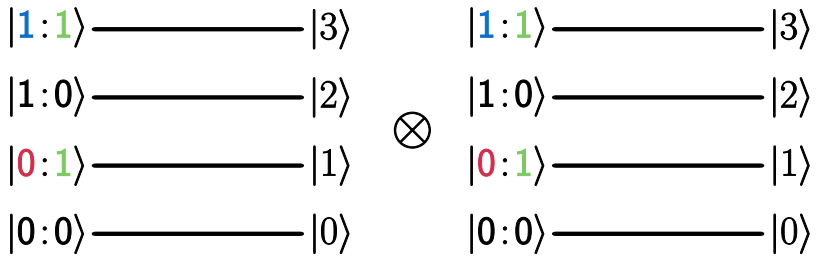



**Figure 2.2:** The state in Equation (2.4) with colours showing how the qubits in the state are spread in each polyqubit. The corresponding qudit states under the mapping (2.29) are shown as an aid.

which we could rewrite to show its structure more clearly (see Figure 2.2 for the colour of the qubit label):

$$|\psi\rangle = \frac{1}{\sqrt{2}}(|0{:}0\rangle_{\mathsf{MSB}} + |1{:}1\rangle_{\mathsf{MSB}}) \otimes |1{:}1\rangle_{\mathsf{LSB}}\,. \tag{2.4}$$

The LSB qubit in each carrier is in state $|1\rangle$, while the MSB qubits in the two carriers are in a Bell state. When splitting up individual qubit states in this way, we will always write the state such that the significance of both the qubits and the information carriers decreases left to right. We point out that nothing has been said about which physical states in the carrier are used, since it is not necessary when discussing the purely computational properties of the states. In fact, it may be convenient to change the physical states used mid-calculation.

Furthermore, we will often come across unitaries whose only non-zero entries are along the main diagonal. We will write them

$$\operatorname{diag}\{\alpha,\beta,\gamma,\delta\} \triangleq \begin{pmatrix} \alpha & & & \\ & \beta & & \\ & & \gamma & \\ & & & \delta \end{pmatrix} \tag{2.5}$$

Here, and going forward, we use the convention that all empty entries in a matrix are 0.

Finally, when drawing circuit diagrams, qubits or qudits will be ordered with significance increasing downwards (Figure 2.3). This refers to the significance of qubits within a carrier as well as the significance of the carriers themselves. In a polyqubit circuit, the top wire will always be the LSB qubit of the least significant carrier. In addition, dashed lines will be used to separate information carriers.

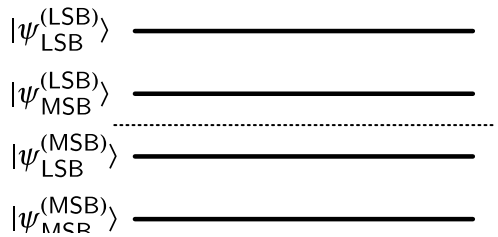



**Figure 2.3:** Circuit diagram showing the ordering of two qubits for a circuit containing two 2-polyqubits. The subscript index in each state vector specifies the significance of the qubit within the carrier, while the superscript index (in brackets) specifies the significance of the carrier. Since only two carriers are used, the labels LSB and MSB are used for them as well as the qubits.

## 2.2 Qubits

We begin by discussing the basic behaviour of single qubits, before generalising to higher-dimensional states. We only discuss their logical behaviour and thus drop the distinction between monoqubits and polyqubits, since these differ only at the hardware level.

A qubit is a computational object whose state is a normalised vector $|\psi\rangle = \sum_{i=0}^{1} c_i |i\rangle$ in a two-dimensional Hilbert space $\mathscr{H}_2$. The two basis states $\{|0\rangle, |1\rangle\}$ form the *computational basis*. Imposing the normalisation condition allows us to rewrite the complex amplitudes $c_i$ in a more intuitive form:

$$|\psi\rangle = e^{i\gamma}\left(\cos\left(\frac{\theta}{2}\right)|0\rangle + e^{i\phi}\sin\left(\frac{\theta}{2}\right)|1\rangle\right). \tag{2.6}$$

As shown in Figure 2.4, we can map the angles $\theta \in (0, \pi)$ and $\phi \in (0, 2\pi)$ to the azimuthal and polar angles of a unit sphere to visualise the state $|\psi\rangle$ as a unit vector on the surface of a sphere, known as the Bloch sphere. The angle $\gamma \in (0, 2\pi)$ is a global phase, which does not affect the dynamics or measurement statistics of the state and thus is usually ignored. We will later see that, while multi-level systems also possess an irrelevant global phase, when considering operations on just two states, the analogue of the global phase cannot be ignored, since it induces a relative phase with respect to the remaining states.

Quantum logic gates on a single qubit transform the state by two-dimensional unitary matrices, which, up to a global phase, form the group $SU(2)$[4]. These unitaries can be

[4] $SU(n)$ is the group of $n$-dimensional unitary matrices whose determinant is 1, as opposed to the general unitary group $U(n)$. While quantum dynamics are described by matrices in $U(n)$, these only differ from a matrix in $SU(n)$ by a global phase, so the distinction is often ignored.

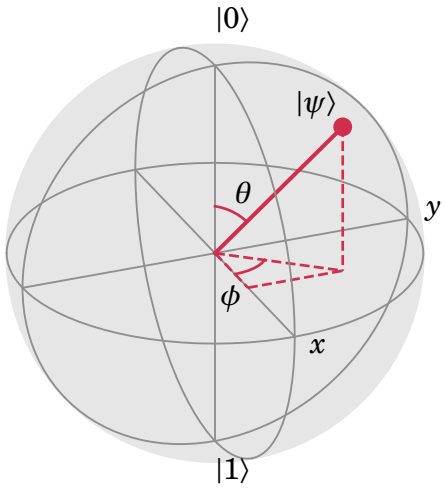



**Figure 2.4:** The state $|\psi\rangle$ of a single qubit represented on the Bloch sphere, with the angles $\phi$ and $\theta$ marked. The computational states $|0\rangle$ and $|1\rangle$ are placed at the North and South poles, respectively.

generated using the Pauli matrices [46]:

$$\mathbb{1} = \begin{pmatrix} 1 & \\ & 1 \end{pmatrix} = |0\rangle\langle 0| + |1\rangle\langle 1|, \tag{2.7}$$

$$\sigma_z = \begin{pmatrix} 1 & \\ & -1 \end{pmatrix} = |0\rangle\langle 0| - |1\rangle\langle 1|, \tag{2.8}$$

$$\sigma_x = \begin{pmatrix} & 1 \\ 1 & \end{pmatrix} = |1\rangle\langle 0| + |0\rangle\langle 1|, \tag{2.9}$$

$$\sigma_y = \begin{pmatrix} & -i \\ i & \end{pmatrix} = i(|1\rangle\langle 0| - |0\rangle\langle 1|). \tag{2.10}$$

An arbitrary $SU(2)$ matrix $U$ can be written as[5]

$$R(\theta,\phi,\nu) = \exp\left(-i\frac{\theta}{2}\mathbf{n}\cdot\boldsymbol{\sigma}\right) = \cos\left(\frac{\theta}{2}\right)\mathbb{1} - i\sin\left(\frac{\theta}{2}\right)\mathbf{n}\cdot\boldsymbol{\sigma} \tag{2.11}$$

where $\mathbf{n}\cdot\boldsymbol{\sigma} = n_x\sigma_x + n_y\sigma_y + n_z\sigma_z$ for some normalised vector[6]

$$\mathbf{n} = (n_x, n_y, n_z)^T = (\cos\nu\cos\phi, \cos\nu\sin\phi, \sin\nu)^T. \tag{2.12}$$

On the Bloch sphere, the effect of this unitary is to rotate the qubit state clockwise by an angle $\theta$ about the unit vector $\mathbf{n}$. Because of this, unitary operations are often referred to as just "rotations" (even when more than two states are involved).

[5]The expansion $\exp(-i\theta\hat{O}) = \cos(\theta)\mathbb{1} - i\sin(\theta)\hat{O}$ holds for all involutory operators $\hat{O}$ such that $\hat{O}^2 = \mathbb{1}$. This will be useful for analysing two-qubit gates later.

[6]The convention chosen makes rotations with $\nu = 0$ equatorial.

In most platforms, it is not possible to directly implement single-qubit rotations about arbitrary axes. For example, in trapped ions, the only rotations typically available[7] are *equatorial* ($\mathbf{n} = (\cos(\phi), \sin(\phi), 0)^T$) and *polar* rotations ($\mathbf{n} = (0,0,1)^T$)[8] which have $\mathbf{n}\cdot\boldsymbol{\sigma} = \cos(\phi)\sigma_x + \sin(\phi)\sigma_y \triangleq \sigma_\phi$ and $\mathbf{n}\cdot\boldsymbol{\sigma} = \sigma_z$ respectively. We write $R_i(\theta)$, $i \in \{x, y, z\}$ for rotations about the $i^{\text{th}}$ axis, where $R_z(\theta)$ rotations are polar rotations, and $R_\phi(\theta)$ for equatorial rotations. Despite only being able to implement a restricted set of single-qubit unitaries directly, an arbitrary unitary can be constructed from a suitable sequence of the available rotations, for example using an Euler decomposition [46]

$$R(\theta, \phi, \nu) = R_z(\gamma) R_x(\beta) R_z(\alpha) \tag{2.13}$$

where the Euler angles $(\alpha, \beta, \gamma)$ are functions of the rotation parameters $(\theta, \phi, \nu)$.

Euler decompositions require the ability to implement a continuously parametrised set of gates, which may be challenging to calibrate and cannot be implemented fault-tolerantly. Instead, arbitrary unitaries can also be synthesised to an arbitrary precision by repeated application of gates from a small set, which form a *single-qubit universal gate set* [55]. These may not be possible to implement natively, but can easily be constructed from an Euler decomposition. A common gate set to choose contains the Hadamard `H` and phase `S` gates, which generate the Clifford group [56], and a non-Clifford gate, typically chosen to be the `T` gate. These are given by

$$\mathtt{H} = \frac{1}{\sqrt{2}}\begin{pmatrix} 1 & 1 \\ 1 & -1 \end{pmatrix} \quad , \quad \mathtt{S} = e^{i\pi/4} R_z\left(\frac{\pi}{2}\right) = \begin{pmatrix} 1 & \\ & i \end{pmatrix} \quad , \quad \mathtt{T} = e^{i\pi/8} R_z\left(\frac{\pi}{4}\right) = \begin{pmatrix} 1 & \\ & e^{i\pi/4} \end{pmatrix}. \tag{2.14}$$

While this is sufficient for single-qubit computation, any useful computation requires more than one qubit. The state of $n$ qubits exists in the tensor product space of the Hilbert space of each qubit, $\mathscr{H}_2^{\otimes n} = \mathscr{H}_2 \otimes \mathscr{H}_2 \otimes ... \mathscr{H}_2$. Multi-qubit (as well as multi-qudit) states can be either *separable* or *non-separable*. Separable states are those that can be written as the tensor product of states of individual qubits, $|\psi\rangle = \bigotimes_i |\psi_i\rangle$, while non-separable states are those that cannot. Non-separable states are often called *entangled*[9],

[7] While driving a transition off-resonantly does rotate the qubit about an axis off the equator, the author is not aware of this being used for computation.

[8] These are usually implemented virtually, as explained in 4.1.2.

[9] The reader is referred to the end of this chapter for a discussion of entanglement and non-separability in polyqubits.

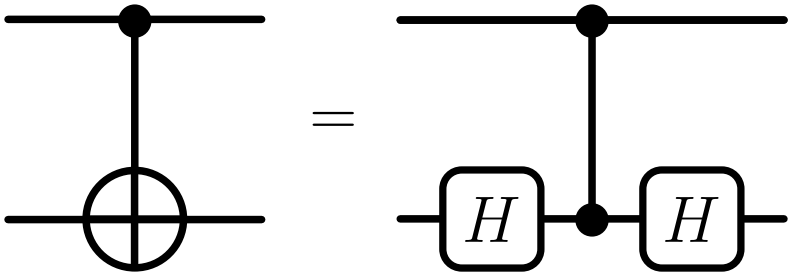



**Figure 2.5:** Circuit diagram showing the conversion between the CNOT and CZ gates up to single-qubit Hadamard gates.

since measurements of the two qubits exhibit correlations that cannot be explained with classical physics. These correlations exist even if the two qubits exist in different information carriers[10] and can be experimentally probed using Bell tests [57–61], resulting in the astonishing predictions of non-locality and non-realism of quantum mechanics [62]. Entangled states are also a fundamental resource for many protocols in quantum information, including quantum communication [63], quantum key distribution [64, 65] and distributed quantum computation [66, 67] amongst many others.

The canonical non-separable states are the two-qubit Bell states[11]:

$$|\Phi^{\pm}\rangle = \frac{1}{\sqrt{2}}(|00\rangle \pm |11\rangle) \tag{2.15}$$

$$|\Psi^{\pm}\rangle = \frac{1}{\sqrt{2}}(|01\rangle \pm |10\rangle) \tag{2.16}$$

A multi-qubit generalisation of $\Phi^+$ is the $n$-qubit GHZ state:

$$|\mathrm{GHZ}_n\rangle = \frac{1}{\sqrt{2}}\left(|0\rangle^{\otimes n} + |1\rangle^{\otimes n}\right) \tag{2.17}$$

It can be shown [46, 55] that the concept of a universal gate set can be extended to a register of multiple qubits. The full gate set contains all the gates in a single-qubit universal gate set (applied to any qubit) as well as a single two-qubit gate (with the ability to apply it between any pair of qubits). The most common choice for the two-qubit gate is the CNOT gate, which flips the state of a target qubit if the control qubit is in the $|1\rangle$ state:

$$\mathtt{CNOT} = \begin{pmatrix} 1 & & & \\ & 1 & & \\ & & & 1 \\ & & 1 & \end{pmatrix} \tag{2.18}$$

[10] The state is then said to be *non-local* as well as non-separable.

[11] These states are usually constructed across two information carriers; however, since we're defining them abstractly in terms of qubits, the ":" in the kets are not included.

While in many platforms CNOT gates cannot be directly applied, they can be implemented from small numbers of native single- and two-qubit gates [68]. Thus, many algorithms, as well as decompositions of multi-qubit gates, are proposed [55] and implemented [37] assuming CNOT gates. Later on in this thesis, it will be more convenient to use the CZ gate, which is equivalent to the CNOT up to single-qubit Hadamard gates (see Figure 2.5) and flips the sign of the $|11\rangle$ state. Its action is symmetric in the two qubits, and its representation in the computational basis is diagonal: $\mathtt{CZ} = \mathrm{diag}\{1,1,1,-1\}$.

It is worth noting that being able to implement more than just a bare universal gate set is a desirable trait, since it allows for more efficient gate decompositions and algorithm implementations [39, 68, 69]. This will be a point that we return to repeatedly in this chapter. However, because the universal gate set does not usually correspond to the native gates in a platform, experimentalists almost always have access to these more expressive gate sets. Demonstrating a universal gate set is then more of a benchmark of experimental capability, rather than just forming the fundamental building blocks of computation.

## 2.3 Qudits

As mentioned previously, a qudit can be thought of as a generalisation of a qubit, which encodes a number in base $d > 2$. While the field of QIP has almost exclusively considered qubit-based computation and monoqubit devices, interest in high-dimensional computation has been rapidly increasing in recent years. This has undoubtedly been aided by improvements in experimental techniques that have placed the extra control schemes required for manipulating qudits well within reach of current hardware. Indeed, programmable universal qudit processors have been constructed across many platforms, including trapped ions [25], superconductors [32] and integrated photonic circuits [33]. Single-qudit control has been repeatedly demonstrated in many other platforms, including solid-state spins [35], magnetic molecules [70] and neutral atoms [71, 72].

A general qudit state is a ket $|\psi\rangle = \sum_{i=0}^{d-1} c_i |i\rangle$ in the $d$-dimensional Hilbert space $\mathscr{H}_d$, where the states $|i\rangle \in \{|0\rangle, |1\rangle, ..., |d-1\rangle\}$ form the computational basis. We will also at times refer to the set of computational basis states as the *computational manifold*, particularly in the context of the set of physical states used to embed a qudit or polyqubit. As opposed

to qubits, geometric parametrisations of the $c_\alpha$ amplitudes cannot be represented in a single three-dimensional representation, like the Bloch sphere [73].

In a natural extension of single-qubit gates, single-qudit gates are elements of $SU(d)$ up to a global phase. These exhibit richer behaviour than single-qubit gates: for example, they can couple all states in the qudit or just a subset of them. This is exemplified by the two qutrit (3-dimensional qudit) gates:

$$G_1 = \begin{pmatrix} 1 & & \\ & & 1 \\ & 1 & \end{pmatrix}, \tag{2.19}$$

$$G_2 = \begin{pmatrix} & & 1 \\ 1 & & \\ & 1 & \end{pmatrix}. \tag{2.20}$$

The first matrix flips the states $|1\rangle \leftrightarrow |2\rangle$ only, while the second matrix permutes the states $|x\rangle \rightarrow |(x+1) \bmod 3\rangle$.

We will see in Section 4.1 that the native gates implemented in atomic systems are *two-state rotations* (TSRs). These are $SU(2)$ rotations applied to just two states in a qudit. We construct them by embedding the two-dimensional Pauli matrices (2.7) in a larger matrix:

$$\mathbb{1}^{i,j} = |i\rangle\langle i| + |j\rangle\langle j|, \tag{2.21}$$

$$\sigma_z^{i,j} = |i\rangle\langle i| - |j\rangle\langle j|, \tag{2.22}$$

$$\sigma_x^{i,j} = |j\rangle\langle i| + |i\rangle\langle j|, \tag{2.23}$$

$$\sigma_y^{i,j} = i\left(|j\rangle\langle i| - |i\rangle\langle j|\right). \tag{2.24}$$

All other entries are zero. Note that these matrices are not symmetric under exchange of indices (except $\sigma_x^{i,j}$): $\sigma_\alpha^{j,i} = \sigma_x^{i,j}\sigma_\alpha^{i,j}\sigma_x^{i,j}$ for $\alpha \in \{x, y, z\}$. This implies

$$\sigma_\phi^{j,i} = \sigma_{-\phi}^{i,j} \tag{2.25}$$

where $\sigma_\phi^{i,j}$ is defined analogously as for qubits. Then, in analogy to (2.11), we define an arbitrary TSR as

$$R^{i,j}(\theta,\phi,\nu) = \exp\left(-i\frac{\theta}{2}\mathbf{n}\cdot\boldsymbol{\sigma}^{i,j}\right) = \cos\left(\frac{\theta}{2}\right)\mathbb{1}^{i,j} - i\sin\left(\frac{\theta}{2}\right)\mathbf{n}\cdot\sigma^{i,j} + \tilde{\mathbb{1}}^{i,j} \tag{2.26}$$

where, for convenience, we introduce the identity over all states not involved in the TSR as $\tilde{\mathbb{1}}^{i,j} = \mathbb{1} - \mathbb{1}^{i,j}$.

One subtlety of TSRs is that they impart a global phase on the subspace. While this is irrelevant for qubits, this is not the case for qudits. Indeed, as can be directly calculated from (2.26), a $\pi$-rotation about the $x$-axis of the $\{|1\rangle, |2\rangle\}$ subspace of a qutrit is

$$R_x^{12}(\pi) = \begin{pmatrix} 1 & & \\ & & -i \\ & -i & \end{pmatrix}. \tag{2.27}$$

Note that this differs from gate $G_1$ in (2.19) by a diagonal gate $\mathrm{diag}\{1, -i, -i\}$. This will not commute with subsequent gates, in particular with TSRs on the $\{|0\rangle, |1\rangle\}$ or $\{|0\rangle, |2\rangle\}$ subspaces, and thus cannot be ignored.

It can be shown that any single-qudit unitary can be decomposed into a string of up to $d(d-1)/2$ equatorial TSRs $R_\phi^{i,j}(\theta)$ and up to $d$ polar TSRs $R_z^{i,j}(\theta)$ by the method of Givens rotations [74, 75]. Thus, the set of all equatorial and polar TSRs forms a universal single-qudit gate set[12]. It is useful to introduce the *connectivity graph* as a tool for visualising these rotations within the rest of the qudit[13]. This is displayed in Figure 2.6: the nodes of the graph are the states in the computational basis and the edges represent allowed TSRs. It is usually not possible to drive all TSRs in hardware: for example, the transition that would have to be driven could be forbidden. It can be shown that a minimum requirement for implementing universal single-qudit unitaries is that the connectivity graph is connected, that is, for every pair of states, there exists a path that connects them [74, 75]. In particular, *full* connectivity (that is, all possible edges are allowed) is not required.

However, the set of equatorial TSRs is by no means the only gate set that could be used. An alternative that mirrors the qubit gate set (2.14) includes qudit generalisations of the qubit `H` and `T` gates [76]. Another physically inspired alternative involves considering the qudit as a single spin of size $J = (d-1)/2$, so that the computational basis is reinterpreted as the eigenbasis of an effective $J_z$ operator. Then, the operators $U = \exp\left[-i\theta(J_x \cos\phi + J_y \sin\phi)\right]$, which rigidly rotate the whole spin, alongside arbitrary diagonal gates $\mathrm{diag}\{e^{i\phi_0}, \ldots, e^{i\phi_{(d-1)}}\}$, are also universal [35]. Note that the rigid rotations are analogous to the equatorial $SU(2)$ rotations of single-qubit operations, while the diagonal gates are a generalised polar rotation. Having many distinct gate sets at one's

[12] While this set is infinite and continuously parametrised, as we avoided in the qubit case, we point out that two-state analogues of the `H`, `S` and `T` gates can be used to synthesise continuous TSRs in the same way as for single qubits, so a finite gate set can be constructed.

[13] This tool can equally be used with polyqubits, since it generally applies to multi-level systems.

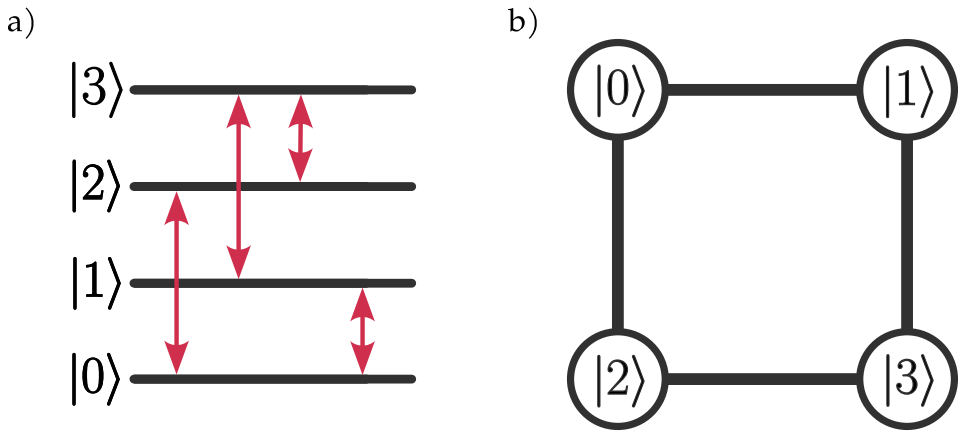



**Figure 2.6:** a) The four states of a ququart, on which four possible TSRs can be driven. b) The corresponding connectivity graph. Edges of the graph correspond to allowed TSRs between the states. Note that the transitions $|0\rangle \leftrightarrow |3\rangle$ and $|1\rangle \leftrightarrow |2\rangle$ cannot be driven, so they are not connected in the graph. Thus, the graph is not fully connected, but it is connected.

disposal allows experimentalists and algorithm designers to choose the most appropriate gates for their problem, which is one of the advantages of qudit computation.

Just like in qubits, a single two-qudit gate is sufficient to complete a universal qudit gate set [77, 78]. This is typically chosen to be a generalisation of the qubit `CNOT` gate (the `CEX` [25, 79], the `CINC` [25, 78] or `CSUM` [33, 77]), or a generalisation of the qubit `CZ` gate [80]. However, it has also been beneficial to express algorithms directly in terms of the native hardware gates, resulting in drastic reductions in gate counts for certain algorithms [39, 81]. The choice of two-qudit gate is not as standardised as it is for single qubits.

## 2.4 Polyqubits

As mentioned previously, an $n$-polyqubit is a set of $n$ qubits which are all in the same multi-level information carrier. This carrier must contain $2^n$ states, since this is the dimensionality the Hilbert space of $n$ qubits $\mathscr{H}_2^{\otimes n}$. As will be discussed later, this allows us to carry out computation using qubit algorithms and gates, while leveraging the advantages of multi-level systems. Nonetheless, we could also view a polyqubit through a different lens: instead of considering it as $n$ qubits in a single carrier, it could be seen as a choice of universal gate set for a single qudit which uses a different "language" from what qudits are usually framed in. Which view is more useful will likely depend

on the context and the problem at hand, although in this thesis the first picture will often be the most useful.

An arbitrary $n$-polyqubit state is given by

$$|\psi\rangle = \sum_{q_{(n-1)}\ldots q_1 q_0 \in B} c_{q_{(n-1)}\ldots q_1 q_0} |q_{(n-1)}\ldots q_1 q_0\rangle \tag{2.28}$$

where $B$ is the set of all bit strings of length $n$. The states $\{|q_{(n-1)}\ldots q_1 q_0\rangle \,|\, (q_{(n-1)}\ldots q_1 q_0) \in B\}$ form the computational $n$-polyqubit basis and are equivalent to the computational basis for $n$ qubits.

We can change from a qudit to a polyqubit picture by introducing a mapping between states in $\mathscr{H}_{2^n}$ to states in $\mathscr{H}_2^{\otimes n}$. While there are infinitely many such mappings [48], we will only make use of the obvious mapping from the qudit computational basis $|i\rangle$ to the ket labelled by the $n$-bit binary representation of $i$, $|i\rangle \to |\text{bin}(i)\rangle$ [45, 51]. The experimental results in this thesis involve 2-polyqubits embedded in a four-level system; the mapping above corresponds to

$$|0\rangle \to |00\rangle\,, \tag{2.29}$$

$$|1\rangle \to |01\rangle\,, \tag{2.30}$$

$$|2\rangle \to |10\rangle\,, \tag{2.31}$$

$$|3\rangle \to |11\rangle\,. \tag{2.32}$$

Because computationally a polyqubit is just a set of qubits, finding a universal gate set for them is easy: we can just directly use the qubit gate set described in Section 2.2 containing universal single-qubit gates and one two-qubit gate. The key difference between applying this gate set on polyqubit systems instead of regular monoqubit ones is that, in polyqubits, not all two-qubit gates are two-body gates. Indeed, gates between two qubits in the same carrier are single-body. We thus split polyqubit gates into intra-carrier gates, which involve just one information carrier (including single-qubit gates), or inter-carrier gates, which involve two carriers. In Chapter 4 we will refer to these as *inter-ion* and *intra-ion gates*.

The challenge in constructing polyqubit gates arises from the fact that, because they are embedded in a multi-level system, the accessible native operations are more similar

to those described for qudits in Section 2.3 than the native qubit gates from Section 2.2. Thus, we must find efficient decompositions for gates that act only on certain subsets of qubits, in terms of operations that generally affect every qubit. Efficient decompositions of intra-carrier gates have been well studied previously, and various proposals for two-qubit inter-carrier gates in terms of native gates exist [47–50]. An in-depth discussion of these decompositions is delayed to Chapter 4, where they are discussed specifically in the context of ion traps.

## 2.5 Discussion

The implementation of qubits, qudits and polyqubits is compared at a hardware level and a broader computational level.

### 2.5.1 Hardware comparison

#### 2.5.1.1 Proportion of inter-carrier gates

Because both qudits and polyqubits make use of multi-level systems, their relationship to qubits at the hardware level is similar. The key trait of these systems is that the amount of information stored per information carrier is higher. This is advantageous since, in almost all QIP platforms, single-body gates are implemented with higher fidelity than two-body ones, both in monoqubit [8, 9, 11, 12] and qudit systems [25][14]. The difference between their fidelities is often at least an order of magnitude. Because each multi-level information carrier contains more information than a single qubit, the number of two-body gates required for algorithms is usually reduced [39]. This is particularly clear when considering polyqubits, as some two-qubit gates become local gates.

#### 2.5.1.2 Fewer information carriers

Many experimental difficulties and sources of error depend on the number of information carriers in the system, rather than the dimensionality of the Hilbert space directly. For example, in trapped ion systems, two-ion gates are mediated by the motional modes of the ion chain (see Section 3.6). Because the number of modes increases with the number

[14] To the author's knowledge, no polyqubit two-body gates have yet been reported. However, in this work, the trend is also observed.

of ions, complex pulse schemes are required to ensure the atomic states are disentangled from the many motional modes at the end of the gate operation [82, 83]. In addition, errors arising from spatial crosstalk [68, 84] are only due to the physical information carriers, independent of platform. Furthermore, reconfiguring operations, such as those used in trapped ion QCCD architectures [10] and neutral atom arrays [11], are often the largest contributor to the algorithmic time budget. They also introduce errors associated with the transport itself, and due to the idling time. Finally, many platforms exhibit reduced connectivity between physical information carriers, such as superconducting ones [38] or those based on distributed quantum computation across nodes [66]. All of these issues can be mitigated by using fewer, multi-level information carriers, without reducing the total Hilbert space dimension.

#### 2.5.1.3 Native gate expressivity

Multi-level systems often exhibit greater gate expressivity than monoqubit systems. This is because many physical platforms can natively implement gates that are equivalent in monoqubits, but have very different computational properties for qudits or polyqubits. For example, the ability to implement *parallel* TSRs in a single qudit is sufficient to *also* implement rigid spin rotations [35]. This extends to two-body gates too. In ion trap systems, there are three native methods of driving two-body gates, namely Mølmer-Sørensen gates [85], light-shift gates [86] and Cirac-Zoller gates [87]. In monoqubit architectures, they are equivalent up to single-qubit gates. However, as discussed in Section 4.2, they address very different subspaces within an atomic manifold and thus implement inequivalent qudit gates. By harnessing this native expressivity and tailoring algorithms specifically to the hardware, spectacular reductions in gate count can be observed in qudit-based algorithms over their qubit-based equivalent [39, 81].

This also ports to polyqubits, arguably in a more striking way. The two-ion gate mechanism proposed in Section 4.2.2 and demonstrated in Chapter 8 can act as a two-, three- or four-qubit gate by surrounding it in intra-ion operations. Clearly, there is no equivalent scheme in monoqubit systems, since a single two-body operation cannot be

equivalent to a four-body operation up to local operations. In addition, the Mølmer-Sørensen gate could be used to implement multi-qubit gates, whose two-qubit gate decompositions would otherwise be expensive.

#### 2.5.1.4 Operational complexity

Multi-level computation comes at the cost of more complex one-body gates. Indeed, state-of-the-art single-qudit fidelities [25] are significantly below their monoqubit equivalents [8, 10]. However, the ubiquity of monoqubits in QIP experiments means that they have been investigated and optimised far more deeply than multi-level systems. In addition, while the number of native operations needed for arbitrary gates increases with qudit dimension, it has been shown that the error of the native operations used to construct them does not have to [25]. Thus, the increase in error can be small.

Readout operations are also necessarily more complex in multi-level systems (see Section 4.4) since more information is encoded in each information carrier. The length, and thus error rate, of these schemes increases linearly with the number of states. An additional issue arises in polyqubits: the usual readout schemes collapse the state of all qubits simultaneously, making it challenging to read out a subset of the qubits in a carrier. To the author's knowledge, the only known method involves mapping information to an auxiliary polyqubit or monoqubit [48], which may incur errors. This may impact the feasibility of algorithms that rely heavily on mid-circuit measurements, such as error-correction or Repeat-Until-Success schemes [88, 89]. Nevertheless, these issues may be mitigated by proper qubit placement, so that all auxiliary qubits are in the same polyqubit. Then, all auxiliary qubits can be read out at once. In addition, this does not affect algorithms where only one measurement is carried out at the end.

#### 2.5.1.5 Decoherence

Superposition states in multi-level systems are naturally more sensitive to environmental noise and perturbations [17, 79]. Indeed, recent experiments on trapped ion qudits of dimension up to 25 showed an increase in dephasing rate with dimension [26]. This is particularly problematic in polyqubits, since errors will be natively multi-qubit even if they involve just one information carrier. Useful error correction may thus require

larger-distance codes, which are more expensive [90]. On the other hand, due to the increased expressivity in polyqubits, it is possible to implement stabiliser measurements with fewer two-body gates. There is evidence to suggest that this may lead to lower logical error rates, despite physical errors being multi-qubit [48]. It may also be possible to make native polyqubit error-correcting codes.

Indeed, the use of multi-level systems can also bring advantages for error correction. Access to multiple states allows for a full logical qubit to be encoded within a single information carrier instead of being spread out across multiple ones [28], reducing overheads in physical register size and two-body gates.

#### 2.5.1.6 Scalability

The total Hilbert space dimension $D$ of $n$ $d$-level systems is $D = d^n$. It is clear that increasing the qudit dimension only increases the register Hilbert space dimension polynomially. However, the number of control parameters typically increases linearly with qudit dimension [17]. In contrast, in a monoqubit system of $n$ qubits, a crude estimate of the number of control parameters for single- and two-qubit gates yields $O(n)$ and $O(n^2)$ respectively, while the total Hilbert space dimension increases as $2^n$. It is clear that achieving scalability by increasing the qudit dimension only is totally infeasible [17]. Nevertheless, this does not negate the advantages that can be brought about by making use of small qudits of dimension $2-10$, or polyqubits with small numbers $(2-3)$ of qubits per ion [48].

#### 2.5.1.7 Other uses of multi-level computation

The large information-carrying capacity of multi-level systems has found a plethora of uses outside of pure computation. Qudits have been shown to yield benefits for quantum cryptography and key distribution protocols [91–93]. Additionally, the rich entanglement structure that is exhibited in bi-partite and multi-partite multi-level entanglement is an area of active study [94, 95].

Finally, the use of auxiliary states in monoqubit systems (thereby essentially turning them into multi-level systems) can be used to simplify multi-qubit operations. They are

essentially used as temporary caches, a role that would otherwise be used by auxiliary monoqubits, thus reducing the size of the register [51, 96–100].

### 2.5.2 Protocol comparison

#### 2.5.2.1 Use of qubits

The main point of comparison between qudits and polyqubits is in their computational use. The primary advantage of polyqubits over qudits is that they allow qubit-based computation, even though the hardware is multi-level. Thus, we can take advantage of the theory and algorithms that have been developed for qubit-based computation, which are more mature than their qudit-based equivalents. This is why we consider polyqu*b*its and not polyqu*d*its: while it would be perfectly possible to, for example, encode two qutrits in a 9-dimensional qudit, there is no apparent good reason to prefer 3-dimensional over 9-dimensional qudits for generic algorithms. Indeed, whether an algorithm is expressed in qubits or qudits, the number of two-qubit/qudit gates is $O(D)$, where $D$ is the total Hilbert space dimension [78][15]. Contrastingly, the simplicity of two-state systems and their ubiquity in the QIP literature means that intuitive understanding of qubit circuits is more widespread than qudit-based ones. Indeed, qubit circuit identities are used numerous times throughout this thesis.

Furthermore, because qubit-based computation has been almost universal in the development of QIP, most existing algorithms have been developed for qubits. While many common algorithms have been transpiled (or naturally extend) to native qudit computation [76], to the author's knowledge, no prescriptive recipe for doing so has been developed. Thus, implementing new algorithms on qudit devices will require manual transpilation, since they will most likely be developed for qubits. Hence, while the natural representation of multi-valued quantities that is so tailored to qudits is lost on polyqubits (see Section 2.5.2.2), the latter have access to all the tools of qubit-based computation. Many existing algorithms are agnostic to the numeric base used [76] and it is reasonable to assume most future ones will too. In these cases, computing with qubits is likely to be favourable, since circuit optimisation and compilation tools are much more mature [38,

[15] However, the coefficient must be dimension-dependent, since if all $D$ states are in a single carrier, no two-body gates are necessary. This is not discussed in the reference.

41–43] than qudit ones [44, 45]. We also point out that any device capable of polyqubit computation is also capable of generic qudit computation, since arbitrary unitaries within the high-dimensional subspace can be applied. While the native gates that can be applied may not exactly coincide with those that optimise qudit algorithms as in Section 2.3, algorithms that are best suited to qudits can still be executed on the same device.

#### 2.5.2.2 Multi-valued problems

On the other hand, many relevant problems in physics deal with quantities that can take on more than just two values and are thus best described with multi-valued computational units. Simulating these systems using qubits naturally carries an overhead in qubit number and two-qubit gate count, since more than one qubit is required to store these multi-valued quantities. Clearly, directly using qudits to encode these quantities reduces these overheads. This is particularly true of quantum simulation problems in high-energy physics [39, 81, 101], and chemical dynamics [102]. Spectacular reductions in gate count of over 90% can be demonstrated in certain cases [39].

#### 2.5.2.3 Polyqubits vs monoqubits

Finally, it is worth pointing out an obvious consequence of the increase in carrier Hilbert space dimension in 2-polyqubits: the total number of qubits is twice that of a monoqubit system with the same number of information carriers. In addition, as shown in Chapter 4, this can be done with minimal hardware overheads. While this appears extremely promising for achieving a large, near-term increase in current devices, this is only advantageous as long as it doesn't introduce significant errors. It is especially important to keep inter-carrier two-qubit gate errors low, despite the fact that some multi-qubit gates are intra-carrier and thus likely to be lower error. Indeed, the fraction of two-qubit gates that are intra-ion is $O(1/N)$ for a register of $N$ $n$-polyqubits[16].

However, we can choose the placement of qubits to minimise the number of inter-carrier gates: indeed, we can clearly always find a placement where at least *some* two-qubit

[16] Because the total number of qubits is $nN$, the total number of possible two-qubit gates is $\binom{2}{nN}$. However, the total number of intra-ion gates is $N\binom{2}{n}$, so the fraction of intra-ion gates is $N\binom{2}{n}/\binom{2}{nN} = (n-1)/(nN-1)$.

gates are intra-ion. This qubit placement task is understudied in the context of polyqubits, although early results do suggest that significant reductions in inter-carrier gate counts are possible [45, 103]. In fact, this problem is similar to designing compilers for distributed quantum computing [104–108], where two distinct types of multi-qubit gates are also present – those acting within nodes or across them. Thus, if the error and number of inter-carrier operations can be suitably reduced, one can be hopeful that the multiplicative increase in the number of qubits in the register may outweigh the impact of a greater operational complexity, thereby increasing the computational power of the device.

### 2.5.3 Entanglement in polyqubits

Polyqubits raise an interesting question regarding entanglement: can two qubits within a single polyqubit be considered to be entangled? What about many qubits across a few carriers?

This depends primarily on whether *locality* is considered a fundamental prerequisite for entanglement. Many practical uses of entanglement explicitly require non-locality, namely any protocol that requires separation of two parties. In addition, certain properties increase with the number of entangled, non-local parties, such as superdecoherence [109] and enhanced frequency sensitivity [110] in GHZ states. In Chapter 8, we will form two- and four-qubit GHZ states across two ions, but it would be unreasonable to expect that their physical properties will differ. Indeed, when viewing the two polyqubits as two qudits, these two- and four-qubit GHZ states are both equivalent to simple two-level qudit entanglement of the form $1/\sqrt{2}(|i:i\rangle + |j:j\rangle)$. Thus, despite it appearing like the two- and four-qubit GHZ states across the two polyqubits have different amounts of entanglement, physically, they are equivalent.

On the other hand, it has been proposed [53, 54] that entanglement should be defined according to how a Hilbert space is partitioned, given that each partition can be independently manipulated and measured. This partitioning of the Hilbert space is precisely what polyqubits are. The intra- and inter-ion gates described in Chapter 4 allow us to manipulate the individual partitions, and a single-qubit readout scheme is proposed in Section 4.4. Thus, there may be scope to suggest that we *do* generate qubit entanglement

using polyqubit gates, despite it not being non-local. Indeed, from a very abstract point of view, non-separable states are just particular examples of superposition states in the full Hilbert space of a register. This is the entanglement resource that is used in *local* quantum computation, and what is displayed by non-separable qubit states in a polyqubit.

Nevertheless, since the interest of this thesis is to use polyqubits for computation, for which locality or lack thereof is irrelevant, the author will heed caution and refrain from using the term "entanglement" or its variants to describe polyqubit states or gates going forward.

## 2.6 Summary

This chapter has introduced the notation and the fundamentals of qubits, qudits and polyqubits, which will be necessary for the remainder of this thesis. In addition, a qualitative comparison of the advantages and disadvantages of monoqubit, qudit and polyqubit architectures was carried out.

*Sometimes, you just need to sit down with a damp cloth.*

— Chris Ballance, giving practical advice for doing theory work.

# 3 Ion trapping theory

In this chapter, we discuss the physics of the operations that induce single- and two-ion gates, though a discussion of the *logical* polyqubit operations they can be used for is reserved to Chapter 4.

We begin by introducing some useful concepts in the evolution of quantum states, followed by a discussion of the trapping mechanism and motional quantum dynamics of the ions. This is followed by exploring the coupling between lasers and single ions, in the context of two states per ion, which is then extended to consider effects that arise in multi-level systems with cyclic connectivity graphs, as used in later chapters. Methods to calculate the Rabi frequencies, which are useful for simulations, are then given. The chapter concludes with the physics of two-ion light-shift interactions with more than two states per ion.

## 3.1 State evolution

The time evolution of a pure quantum state under a Hamiltonian $H(t)$ is given by the Schrödinger equation $\frac{\partial|\psi\rangle}{\partial t} = -\frac{i}{\hbar}H(t)|\psi\rangle$. This can be integrated to obtain the state at arbitrary times, $|\psi(t_f)\rangle = U(t_f;t_i)|\psi(t_i)\rangle$, with the *time evolution operator*, or *propagator*,

$$U(t_f;t_i) = \mathcal{T}\left(\exp\left[-\frac{i}{\hbar}\int_{t_i}^{t_f} \mathrm{d}t' H(t')\right]\right) \tag{3.1}$$

where $\mathcal{T}$ is the time-ordering operator, which is important if $H(t)$ does not commute with itself at different times. Often, we will drop one or both of the arguments in $U$.

The state evolution can also be computed in an *interaction frame* or *picture*, in which part of the state's time dependence is removed. This is useful when the Hamiltonian contains some background term that does not contribute any interesting dynamics, or the Hamiltonian has a time dependence that may be simplified by a change of frame [111]. This change of frame is done by means of a frame-change Hamiltonian $H_F(t)$, which generates a *frame-change unitary*[1] $F(t) = \exp\left(\frac{i}{\hbar}\int_0^t \mathrm{d}t' H(t')\right)$. The state in the interaction picture is $|\tilde{\psi}\rangle = F(t)|\psi\rangle$, which also obeys the Schrödinger equation $\frac{\partial|\tilde{\psi}\rangle}{\partial t} = -\frac{i}{\hbar}\tilde{H}(t)|\tilde{\psi}\rangle$ with the interaction-frame Hamiltonian

$$\tilde{H} = FHF^\dagger + i\hbar F^\dagger \frac{\mathrm{d}F}{\mathrm{d}t}. \tag{3.2}$$

Note that when the frame-change Hamiltonian is time-independent, $i\hbar F^\dagger \frac{\partial F}{\partial t} = -H_F$. Thus, if the unwanted time evolution in the Hamiltonian stems from a term $H_0$, it can be removed by going into the interaction frame with $H_F = H_0$.

The propagator $\tilde{U}$ for $|\tilde{\psi}\rangle$ is found using $\tilde{H}$ in equation 3.1. This can facilitate the calculation of exact propagators in the non-interaction frame[2], by using

$$U(t_f; t_i) = F^\dagger(t_f)\tilde{U}(t_f; t_i)F(t_i). \tag{3.3}$$

The structure of this operator is clear: the state at $t_i$ is rewritten in the interaction frame, evolved, then rewritten back to the original frame.

We point out that the interaction frame is just a mathematical tool, albeit a powerful one, and the choice of frame has no bearing on the observables of the state.

[1] The frame-change Hamiltonian will always commute with itself at different times in this thesis, so we drop the time-ordering operator.

[2] Note that this doesn't generally have to be done if a sequence of operators are calculated in the same interaction frame, since the frame change unitaries for consecutive operators will cancel. Furthermore, if the frame change unitary commutes with the measurement operators (as is often the case) and $|\psi(0)\rangle$ is an eigenstate of $F$, we can forget about the frame change unitaries entirely, and calculate the state evolution in the interaction frame without worry.

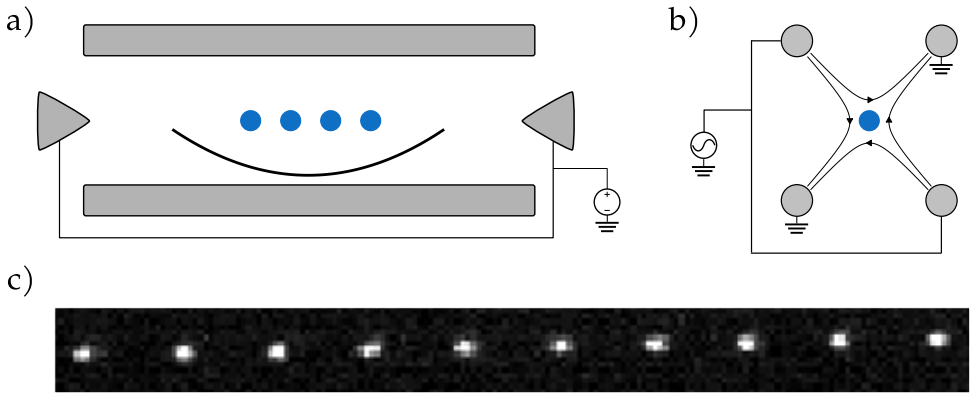



**Figure 3.1:** Sketch of a traditional rod ion trap. a) A string of ions (blue) lies along the trap axis. Positive voltages applied to the trap endcaps confine the ions, with a parabolic potential shown. b) Side view of the trap. An RF voltage is applied to two diagonally opposed electrodes, which set up electric fields as shown (these are the fields on the positive RF cycle). The time average of these fields creates a confining pseudopotential. c) Picture of 10 ions in a chain, which is rotated due to misalignment of the imaging system.

## 3.2 Trapping mechanism

The first step in any trapped ion quantum information processing (QIP) experiment is trapping the ions themselves. The fact that ions are charged is profoundly advantageous in this task, since this allows us to exert large forces on them by applying voltages on nearby electrodes. However, Gauss' law forbids an electrostatic potential that is confining in all directions. Instead, a combination of static and time-varying electric fields can be used to generate confinement; this is the operating principle of Paul, or RF, traps [112].

While modern traps often make use of complex design and manufacturing techniques, almost all RF traps derive from the linear design that is shown in Figure 3.1. A set of four RF electrodes, which are parallel to the $z$-axis (the "trap" axis) in the figure, are used to generate confinement in the $x-y$ "radial" plane. The confining mechanism can be understood with an intuitive picture. First, note that applying a positive voltage on two diagonally opposed electrodes, while grounding the other two, produces a potential with a saddle point at the trap axis. This potential would push a positively charged ion away from the charged electrodes towards the trap axis, but would not be able to confine the ion because it would be simultaneously expelled towards the two grounded electrodes. However, reversing the sign of the voltage on the electrodes would flip the direction of the electric forces on the ion. If we did this just as the ion was being pushed towards

the grounded electrodes, the initially anticonfining force would become confining, and the ion would be directed back towards the trap axis. By continually flipping the sign of the voltage (typically at ~ 10 MHz), the ion would on average be confined to the vicinity of the trap axis. The overall motion primarily consists of slow oscillations (the *secular* motion ~ 1–5 MHz) that can be described by an effective, time-averaged harmonic *pseudopotential* [113–115]. The oscillating RF potential also drives small residual motion at the RF frequency, the *micromotion*. Excess micromotion is typically detrimental for quantum information applications, since it can cause heating of the ion's motion and introduce sidebands on the atomic resonances [116]. An ion located exactly on the potential's saddle point at the trap axis does not experience any force, since the electric fields there vanish, and hence does not experience any micromotion. Thus, radial DC fields are often used to push the ions onto the trap axis.

These electrodes provide no confinement along the trap axis, since no force is exerted in that direction[3]. For this, a positive DC voltage is applied onto the two "endcap" electrodes that are placed along the trap axis, which prevents the ion from escaping in this direction[4]. Typically, this potential is made significantly weaker than the radial potential, so that if many ions are trapped together, their Coulomb repulsion will spread them out along the RF null (see Figure 3.1).

The resulting time-averaged potential is a harmonic, confining potential, in which a single ion with mass $m$ undergoes simple harmonic motion along the three principal directions:

$$U(t) = \frac{m}{2}\left(\omega_x^2 x^2 + \omega_y^2 y^2 + \omega_z^2 z^2\right). \tag{3.4}$$

The frequencies $\omega_i$ ($i \in \{x, y, z\}$) are the oscillation frequencies of the secular motion along the three principal directions of the trap[5]. They depend on the magnitude of the voltages applied, the ion's charge to mass ratio and the trap electrode geometry.

This description also applies when many ions are simultaneously trapped. If the axial confinement is made sufficiently smaller than the radial confinement ($\omega_z < \omega_x, \omega_y$) then

[3] Unless there is axial micromotion, but this is detrimental.

[4] Due to Gauss' law, this DC potential must be anticonfining along the radial directions, but this is countered by the radial pseudopotential.

[5] The principal axes of oscillation do not have to coincide with the coordinate axes shown here and can be modified by applying further DC voltages with the correct spatial structure [117].

the ions will spread out in a line along the RF null, minimising the micromotion they experience. The axial equilibrium positions $\tilde{z}_n$ of the ions can be calculated by minimising the electrostatic energy of the entire chain along the axial direction [118]:

$$U_a = \sum_{n=0}^{N-1} \left[ \frac{m\omega_z^2}{2} z_n^2 + \frac{e^2}{4\pi\varepsilon_0} \sum_{m<n} \frac{1}{|z_n - z_m|} \right]. \tag{3.5}$$

This yields the ion separation in a two-ion chain as[6]

$$\Delta z_2 = \left( \frac{e^2}{2\pi\varepsilon_0 m\omega_z^2} \right)^{\frac{1}{3}}. \tag{3.6}$$

### 3.2.1 Quantised motion

Another effect of the Coulomb repulsion between the ions in the chain is to couple their motion, which is then described by normal modes in which all the ions participate. If the motional energy of a mode is cooled near to the ground state, its amplitude becomes quantised [119]. These quantised modes are invaluable for QIP experiments, since they enable the internal electronic states of different ions in the chain to couple indirectly via the shared motional bus [85, 87]. As will be described in Section 3.6, these mechanisms are the backbone for implementing multi-qubit gates. Furthermore, since the modes generally involve the motion of all ions, these mechanisms natively enable all-to-all connectivity, which is difficult to achieve in most other platforms.

The motion along each principal axis is independent, so we will only consider one axis. While the coulomb repulsion between ions is highly non-linear, the potential can be approximated as harmonic in the neighbourhood of the ions' equilibrium positions, and any deviations from this can be dealt with perturbatively [120]. This harmonic approximation means that the coupled motion of all ions in the chain can be decomposed into normal modes. Indeed, the vector of the displacement of each of the $N$ ions along one of the principal axes $\mathbf{q}(t) = (q_0(t), q_1(t), ..., q_{N-1}(t))^T$ is decomposed into motional modes according to $\mathbf{q} = \sum_m \boldsymbol{\xi}^{(m)} Q_m(t)$. The $Q_m(t)$ are $N$ motional modes, which undergo simple harmonic motion at a frequency $\omega_m$. The vectors $\boldsymbol{\xi}^{(m)}$ are the mode participation vectors for the $m^{\text{th}}$ mode, whose components are the normalised extremal displacement of the corresponding ion in the mode oscillations.

[6] This assumes that the axial potential is perfectly harmonic.

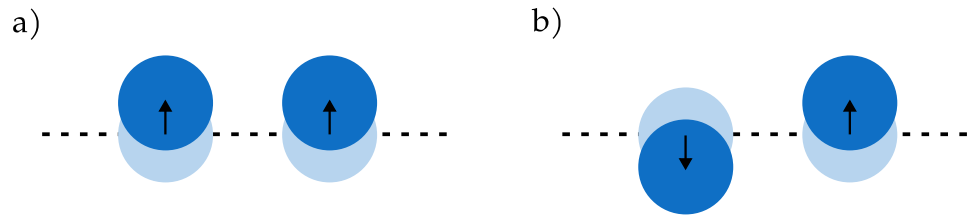



**Figure 3.2:** Sketch of the motion of a two-ion a) CoM and b) rocking mode.

These modes, and their conjugate canonical momenta $P_m = m\dot{Q}_m$, can be quantised and written in terms of bosonic creation and annihilation operators $\hat{a}_m^\dagger$, $\hat{a}_m$ [118]:

$$\begin{aligned} Q_m \to \hat{Q}_m &= \sqrt{\frac{\hbar}{2m\omega_m}}\left(\hat{a}_m + \hat{a}_m^\dagger\right), \\ P_m \to \hat{P}_m &= i\sqrt{\frac{\hbar m\omega_m}{2}}\left(\hat{a}_m^\dagger - \hat{a}_m\right) \end{aligned} \tag{3.7}$$

with the usual commutator relations $\left[\hat{a}_m, \hat{a}_n^\dagger\right] = \delta_{m,n}$.

An $N$-ion chain has $3N$ modes, $N$ for each principal axis. Along all three directions there exists one mode in which all ions move together[7]. These centre-of-mass (CoM) modes oscillate at the secular motion frequencies in (3.4), which are the three mode frequencies of a single trapped ion. In the radial directions, the other modes oscillate at lower frequencies than the CoM mode, while in the axial direction they oscillate at higher frequencies. This discrepancy between the two directions occurs because the Coulomb repulsion acts as a restoring force for axial displacement, but acts as an *anti*-restoring force in the radial direction.

### 3.2.2 Two-ion chains

The experiments in this thesis only used the radial motion of two-ion chains. There are two modes in each radial direction, the CoM mode and the *rocking* mode, shown schematically in Figure 3.2. These give us four radial modes in total. The participation vectors of these modes are $\boldsymbol{\xi}^{(\mathrm{CoM})} = \frac{1}{\sqrt{2}}(1,1)$ and $\boldsymbol{\xi}^{(\mathrm{Roc})} = \frac{1}{\sqrt{2}}(1,-1)$.

We refer to the two radial directions as the high- and low-frequency directions (HF, LF respectively) according to the frequency of the CoM mode along these principal

[7] In a CoM mode, the ions move in the same direction, but not by the same amount [121].

axes[8]. Of the two modes along each direction, the CoM is always the highest-frequency one, for reasons discussed. The properties of the modes in our trap are discussed in detail in Section 8.2.

## 3.3 Ion-laser interactions

Electromagnetic (EM) radiation is an immensely powerful tool for ion trappers, since it enables the manipulation of the electronic and motional state of single ions through the control of macroscopic fields. Laser light ($\sim 100$ THz), microwaves ($1-10$ GHz) or radio waves ($1-100$ MHz) can be used depending on the experimental implementation. The experiments described in this thesis only use lasers, in which case the interaction is mediated by the coupling between the radiation's electric field[9] and the spatial distribution of the wavefunction of the ion's single valence electron[10].

We are interested in using these fields to drive TSRs, which were introduced in Section 2.3. Thus, we will presently consider the coupling between only two states and introduce effects from the presence of other states later.

### 3.3.1 Resonant driving

We will treat the light from a laser beam entirely classically, which at the intensities typically used in experiments is a very good approximation. It will be assumed to be a plane wave travelling in the $\hat{\mathbf{k}}$ direction, with frequency $\omega_l$ and phase $\phi_l$. Its electric field is $\mathbf{E}(\mathbf{r}) = \frac{E_0}{2}\left(\hat{\boldsymbol{\epsilon}} e^{i(\mathbf{k}\cdot\mathbf{r}-\omega_L t+\phi_l)} + h.c.\right)$ where $\mathbf{k} = k\hat{\mathbf{k}} = \frac{\omega_l}{c}\hat{\mathbf{k}}$ and $\hat{\boldsymbol{\epsilon}}$ is the beam polarisation, which will be defined in Section 3.5.2. The lab-frame Hamiltonian of two atomic states in the presence of this beam is

$$H_{Lab} = H_0 + \frac{\hbar}{2}\left[\left(\Omega_{0,1} e^{i(\mathbf{k}\cdot\mathbf{r}-\omega_l t+\phi_l)} + \bar{\Omega}_{0,1} e^{-i(\mathbf{k}\cdot\mathbf{r}-\omega_l t+\phi_l)}\right)|1\rangle\langle 0| + h.c.\right] \tag{3.8}$$

where $H_0 = \hbar\omega_1 |1\rangle\langle 1|$ is the atomic Hamiltonian (the states are labelled in increasing energy and the energy reference is set to be energy of $|0\rangle$) and $\Omega_{0,1}$, $\bar{\Omega}_{0,1}$ are the co- and

[8] The direction along which the frequency is highest can be controlled by using DC voltages to modify the confinement along these directions [117, 121], so which axis is the HF or LF one is generally not well-defined. However, these directions are consistent throughout this thesis.

[9] An analogous treatment can be carried out by microwaves, which are mediated by the radiation's magnetic field.

[10] We will exclusively consider transitions in alkali earth ions. To a very good approximation, the light does not couple to the electrons in the closed inner shell [122].

counter-rotating Rabi frequencies[11] respectively, defined in Section 3.5. We point out that these are complex, so $\Omega_{0,1} = |\Omega_{0,1}|e^{i\phi_\Omega}$. In addition, the quantities $e^{\pm i\mathbf{k}\cdot\mathbf{r}}$ depend on the ion's position operator $\mathbf{r}$ and allow the laser to couple to the motional states, adding or removing motional quanta by driving *motional sidebands*. However, motional transitions will barely be used in the remainder of this thesis, since the motional coupling of the 1762 nm laser that will be used to drive transitions in later chapters is very small due to its long wavelength. Indeed, this coupling is characterised by the Lamb-Dicke parameter $\eta = k\sqrt{\hbar/2m\omega_m}$, where $k$ is the beam's wavenumber, $m$ is the ion mass and $\omega_m$ the frequency of the mode coupled to. Thus, we will set $e^{\pm i\mathbf{k}\cdot\mathbf{r}} \approx \mathbb{1}$: the interested reader is referred to [83, 112, 123, 124] for details.

We now go into an interaction picture, the *drive frame*, which removes the time dependence and mostly cancels $H_0$ if the laser is close to resonance. This uses the frame change Hamiltonian $H_F = \hbar\omega_l |1\rangle\langle 1|$, which transforms the operators in 3.8 as[12]

$$|1\rangle\langle 0| \to e^{i\omega_l t}|1\rangle\langle 0| \quad , \quad |0\rangle\langle 1| \to e^{-i\omega_l t}|0\rangle\langle 1|. \tag{3.9}$$

With this, it can be seen that the drive frame Hamiltonian will be split into one part that has no time dependence and contains the co-rotating Rabi frequency; and another that rotates at $e^{\pm 2i\omega_l t}$ and contains the counter-rotating Rabi frequency. Since for a laser $\omega_l \sim 100$ THz, which is much larger than the Rabi frequency, the counter-rotating terms average out and have negligible effect on the dynamics. Thus, we invoke the rotating wave approximation (RWA) and discard these terms, which yields the laser-frame Hamiltonian

$$H_D = -\hbar\tilde{\delta}|1\rangle\langle 1| + \frac{\hbar}{2}\left(\Omega_{0,1}e^{i\phi_l}|1\rangle\langle 0| + h.c.\right) \tag{3.10}$$

where we have defined the detuning from the bare transition $\tilde{\delta} = \omega_l - \omega_1$. The rightmost term drives the transition and can be written as $\frac{\hbar}{2}|\Omega_{0,1}|\sigma_\phi^{0,1}$, with the equatorial angle $\phi = \phi_l + \phi_\Omega$.

We can rewrite (3.10) as

$$H_D = \frac{\hbar}{2}\tilde{\Omega}_{0,1}\left(\sin\nu\,\sigma_z^{0,1} + \cos\nu\,\sigma_\phi^{0,1}\right) - \frac{\hbar\tilde{\delta}}{2}\mathbb{1}^{0,1} \tag{3.11}$$

[11] The co-propagating Rabi frequency is defined such that at the $\pi$-time $t_\pi \triangleq \frac{\pi}{\Omega_{0,1}}$ the measured populations flip state.

[12] The frame change unitary for this operator is $F(t) = e^{i\omega_l t}|1\rangle\langle 1| + |0\rangle\langle 0|$, see Appendix A.1.

where $\tilde{\Omega}_{0,1} = \sqrt{\tilde{\delta}^2 + |\Omega_{0,1}|^2}$ and $\tan\nu = \frac{\tilde{\delta}}{\Omega_{0,1}}$. The propagator for this Hamiltonian is

$$U(t+\tau;t) = e^{i\tilde{\delta}\tau/2} R^{0,1}(\theta,\phi,\nu) \tag{3.12}$$

with $\theta = \tilde{\Omega}_{0,1}\tau$ and $R^{0,1}(\theta,\phi,\nu)$ as in (2.26). Thus, driving a transition induces TSRs. If this TSR is equatorial ($\nu = 0$) we say the transition is driven *on resonance*. In the case of (3.10), this occurs when $\tilde{\delta} = 0$; we will see that this condition is modified in the presence of other states. Furthermore, the global phase has been explicitly kept, since in the context of a multi-level system, the phase obtained when exponentiating the generalisation of (3.11) will no longer be global.

Note that the previous discussion has explicitly defined $|1\rangle$ to have higher energy than $|0\rangle$, meaning that the process $|0\rangle \to |1\rangle$ *absorbs* a photon. This implicitly fixes the relationship between the laser's phase and the equatorial angle of the resulting *logical* TSR along $\sigma_\phi$. Indeed, had $|1\rangle$ been the *lower* energy state, the transition would proceed by the *emission* of a photon, the term in equation 3.8 whose time dependence vanishes is the one proportional to $\bar{\Omega}$, since the sign of $H_F$ would need to be flipped to cancel $H_0$. Consequently, $\bar{\Omega}$ would appear in (3.10) and the equatorial phase would be $\phi = \phi_{\bar{\Omega}} - \phi_l$. This will be important when considering multi-level systems.

We have also been explicit in the inclusion of the phase of the Rabi frequency. This is not necessary in monoqubit systems, since a constant phase offset has no effect on the dynamics. This can be seen by the following identity [125]:

$$R_{\phi-\Delta\phi}(\theta) = R_z\left(-\Delta\phi\right) R_\phi(\theta) R_z\left(\Delta\phi\right). \tag{3.13}$$

Furthermore, if all pulses in a sequence had a phase offset $\Delta\phi$, undoing these phases would simply require prepending and appending the circuit with $R_z\left(\pm\Delta\phi\right)$. However, since the state is initially prepared in a computational basis state, and we also measure in this basis, these rotations only add an unmeasurable global phase. An alternative view of this is that the first pulse *defines* the phase that corresponds to a rotation about the $x$-axis (even if the rotation is about some other axis). Only subsequent phases *relative* to this pulse have meaning. Equivalently, this defines the "origin" $\phi = 0$ of the phase in a superposition $|\psi\rangle = \cos(\theta/2)|0\rangle + e^{i\phi}\sin(\theta/2)|1\rangle$. We will see in Section 3.4 that in multi-level systems with cyclic connectivity graphs, such phase offsets do lead to measurable effects.

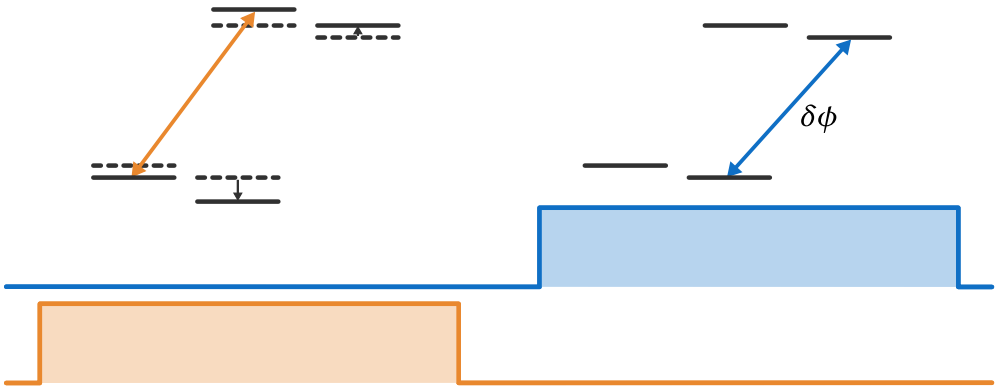



**Figure 3.3:** The effect of light shifts on multi-level systems. Pulsing one transition (orange) shifts the frequency of all states (including the ones addressed), making them acquire a phase $\delta\phi$. In any given two-state subspace, this appears like an unwanted $z$-rotation which will add an error. This can be corrected by the method of virtual rotations (Section 4.1.2), which involves changing the phase of the next pulse on that transition (blue), for which accurate knowledge of the phase $\delta\phi$ is necessary.

### 3.3.2 Light shifts

The previous discussion has dealt with the action of a beam on a resonant transition, but the beam *also* interacts off-resonantly with the multitude of other states in the ion. The form of the resulting interaction is very different. Instead of driving population transfer (a $\sigma_x$-like interaction), off-resonant interactions alter the state energies (a $\sigma_z$-like interaction). These energy shifts are called *light shifts* (LS), or *AC Stark shifts*.

Even when a transition is being driven on resonance, its frequency is usually light-shifted, because the beam couples to off-resonant transitions that involve the driven states. In most cases[13], this only has a minor impact since the laser frequency can be shifted to compensate. However, when the transition is *not* being driven – because the laser is off, or driving some other transition – the state energies change. Thus, in the drive frame, they will accrue phase during the time that the background "LS environment" is modified, as shown in Figure 3.3.

LSs have a smaller impact in monoqubits than multi-level systems, since in the former, the driving laser is resonant with the transition for almost the full duration of a circuit. The laser is only turned off briefly between pulses, or for inter-ion gates, so the LS environment is unchanged for most of the circuit. However, in multi-level systems, each transition

[13]We point out that, for multi-level systems with cyclic connectivity graphs, LSs may force the multi-photon resonance condition to be broken, see Sections 3.4.3 and 5.2.1, which can lead to large, but correctable, errors.

spends most of the time idle while *other* transitions are being driven; the LS environment is different while each transition is being addressed, which we will capture later in the LS matrix. Thus, larger phases can accumulate in multi-level systems for the same LS. Nonetheless, these phases can be accounted for by updating the phase of the driving lasers every pulse, which, as described in Section 4.1.2, implements virtual diagonal gates[14]. To do so, we require accurate knowledge of their magnitude. This can either be measured, which is laborious and error-prone for systems of many states, or calculated from experimental parameters, which is the approach taken in Chapter 7.

To calculate the LSs on each state, we start with the Hamiltonian in the lab frame, with a single, off-resonant beam. We consider many states, possibly across multiple levels and indexed by increasing energy:

$$H_L = \hbar \left[ \sum_\nu \omega_\nu |\nu\rangle\langle\nu| + \frac{1}{2} \sum_{\nu,\mu>\nu} \left( (\Omega_{\nu,\mu} |\mu\rangle\langle\nu| + \bar{\Omega}^*_{\nu,\mu} |\nu\rangle\langle\mu|) e^{-i\omega_l t} + h.c. \right) \right]. \tag{3.14}$$

This is analogous[15] to (3.8). Now, it is not generally possible to find an interaction frame in which all time dependences vanish (see 3.4.3) so we go into an interaction picture with respect to the atomic Hamiltonian. That is, $H_F = \hbar \sum_\nu \omega_\nu |\nu\rangle\langle\nu|$, in which case $|\mu\rangle\langle\nu| \to e^{i\omega_{\nu,\mu} t} |\mu\rangle\langle\nu|$ with $\omega_{\nu,\mu} \triangleq \omega_\mu - \omega_\nu$. Thus, we obtain the atomic frame Hamiltonian

$$H_A = \frac{\hbar}{2} \sum_{\nu,\mu>\nu} \Omega_{\nu,\mu} e^{-i(\omega_l - \omega_{\nu,\mu})t} |\mu\rangle\langle\nu| + \bar{\Omega}^*_{\nu,\mu} e^{-i(\omega_l + \omega_{\nu,\mu})t} |\nu\rangle\langle\mu| + h.c. \tag{3.15}$$

This Hamiltonian does not commute with itself at arbitrary times, so directly calculating the propagator is non-trivial. Instead, we use the James-Jerke approximation[16] [119] to calculate an effective, time-averaged Hamiltonian. This states that the time-averaged effect of a Hamiltonian $H = \sum_n h_n e^{-i\omega_n t} + h.c.$, with operators $h_n$ and frequencies $\omega_n > 0$, is given by the effective Hamiltonian

$$H_{\text{Eff}} = \frac{1}{\hbar} \sum_{n,m} \frac{\omega_n + \omega_m}{2\omega_n \omega_m} [h_n^\dagger, h_m] e^{-i(\omega_m - \omega_n)t}. \tag{3.16}$$

[14] The LSs are quadratic in the Rabi frequency, so by making these smaller, the phase acquired on spectator states over a TSR linearly reduces. This can also be used to mitigate LS errors.

[15] The $\bar{\Omega}^*_{\nu,\mu}$ comes from the Hermitian conjugate in (3.8). Additionally, the laser phases have been dropped, since they have no effect.

[16] This approximation also assumes that the frequencies are of similar order, which is not the case in (3.15). However, we only take the interaction of terms with themselves and discard the rest, so the approximation is valid.

We can see that (3.15) has the correct form to apply this. Keeping only the commutators of the form $[h_n^\dagger, h_n]$, which have no time dependence, we obtain

$$H_{\mathrm{LS}} = \frac{\hbar}{4} \sum_{\nu,\mu>\nu} \left( \frac{|\Omega_{\nu,\mu}|^2}{\omega_l - \omega_{\nu,\mu}} + \frac{|\bar{\Omega}_{\nu,\mu}|^2}{\omega_l + \omega_{\nu,\mu}} \right) \left( |\nu\rangle\langle\nu| - |\mu\rangle\langle\mu| \right). \tag{3.17}$$

The term containing $\omega_l - \omega_{\nu,\mu}$ is the standard LS term. We can observe that this reduces the frequency of the $|\nu\rangle \leftrightarrow |\mu\rangle$ transition if $\omega_l > |\omega_{\nu,\mu}|$ and increases it otherwise. The other term is the Bloch-Siegert shift [126, 127]. This is only relevant if the beam is very off-resonant from the transition.

Rearranging, we find the LS shift on state $|\nu\rangle$ to be[17]

$$\Delta^{|\nu\rangle} = \frac{\hbar}{4} \sum_{\mu\neq\nu} s_{\nu\mu} \left( \frac{|\Omega_{\nu,\mu}|^2}{\omega_l - \omega_{\nu,\mu}} + \frac{|\bar{\Omega}_{\nu,\mu}|^2}{\omega_l + \omega_{\nu,\mu}} \right) \tag{3.18}$$

with the sign $s_{\nu\mu} = +1$ for $\mu > \nu$ and $-1$ otherwise.

## 3.4 TSR sequences

So far, the state dynamics under the action of a single laser pulse have been discussed. However, a quantum circuit on a multi-level system is implemented by a series of pulses, generally on different transitions. We will see in Sections 3.4.2 and 3.4.3 that if the connectivity graph is *cyclic*, such that population can be moved around a closed loop of transitions, the phase of the lasers that drive each TSR affects the dynamics non-trivially.

We will thus consider such cyclic graphs, limited to a single loop with no "dangling" states, and also the simpler situation of a *linear* connectivity graph. These are shown in Figure 3.4: cyclic graphs have $d$ states and $d$ transitions, while linear graphs have $d-1$ transitions. It will be convenient to use a notation that links the index of a transition to the pair of states it involves: we will say that transition $T$ will drive population between $|T\rangle \leftrightarrow |T+1\rangle$. In linear graphs, one of the two end states is chosen to be state $|0\rangle$, while in cyclic graphs, the choice is arbitrary. Furthermore, it will be convenient to abstractly consider each transition as being driven by an entirely different laser, even though in practice usually a single laser is used, whose frequency and phase are modulated as needed. In this picture, the RF synthesisers that are used to modulate the beam could be thought of as the "drive", as far as the frequency and phase control is concerned.

[17] This also uses $\Omega_{\mu,\nu} = \bar{\Omega}^*_{\nu,\mu}$, which can be seen by swapping the indices in 3.14.

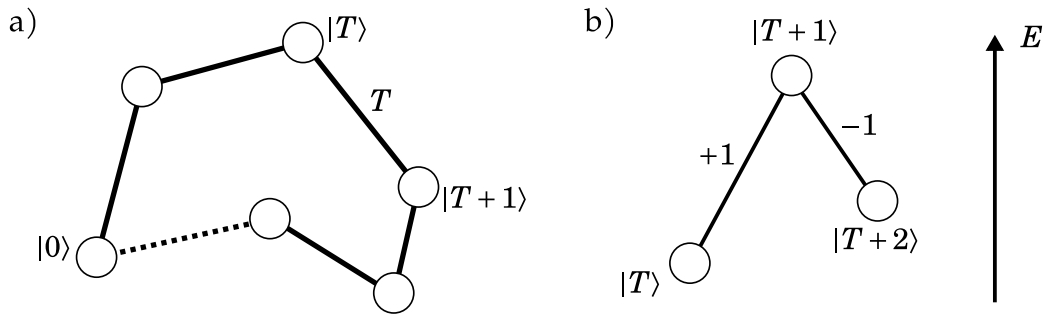



**Figure 3.4:** a) Sketch of a computational manifold, with states as circles and transitions as edges; it is cyclic if the dashed transition can be driven and linear otherwise. State $|0\rangle$ is picked as one of the transition extremes if the graph is linear, and arbitrarily otherwise. Each transition $T$ drives $|T\rangle \leftrightarrow |T+1\rangle$. b) Section of a graph, with higher states being higher energy. The signs $s_T$ for each transition are shown, which are $+1(-1)$ if $|T\rangle \rightarrow |T+1\rangle$ results in an increase (decrease) in energy, by absorbing (emitting) a photon.

### 3.4.1 Linear connectivity

First, we consider the linear connectivity case. We write the Hamiltonian of the full sequence in the lab frame as $H_{Lab}(t) = H_0 + \sum_n f_n(t) H_{n,Lab}(t)$, where $H_0 = \hbar \sum_{T=0}^{d-1} \omega_T |T\rangle\langle T|$ with the state energies $\hbar\omega_T$ and $\omega_0 = 0$; the $f_n(t)$ are top-hat functions that are 1 while the $n^{\text{th}}$ pulse is driven (between the start of the pulse $t_{n,i}$ and $t_{n,i} + \tau_n$, where $\tau_n$ is the pulse duration) and 0 otherwise; and the *pulse* Hamiltonians are

$$H_{n,Lab} = \frac{\hbar\Omega^{(T_n)}}{2}\left(e^{-i(\omega_l^{(T_n)}t - \phi_n^{(T_n)})}|T_n+1\rangle\langle T_n| + h.c.\right) + \hbar\sum_{T=0}^{d-1}\Delta_{T_n}^{|T\rangle}|T\rangle\langle T| \tag{3.19}$$

in which terms that will be counter-rotating have been neglected. $T_n$ is the transition driven in the $n^{\text{th}}$ pulse. The laser that drives the $T^{\text{th}}$ transition has a frequency $|\omega_l^{(T)}|$; the *signed* laser frequency $\omega_l^{(T)} = s^{(T)}|\omega_l^{(T)}|$ takes into account whether the energy of $|T+1\rangle$ is higher (lower) than that of $|T\rangle$, in which case $s^{(T)} = +1(-1)$ and the transition $|T\rangle \rightarrow |T+1\rangle$ absorbs (emits) a photon (see Section 3.3.1). Likewise, the laser phase at the $n^{\text{th}}$ pulse is $|\phi_n^{(T_n)}|$ and the *signed* phase is $\phi_n^{(T_n)} = s^{(T_n)}|\phi_n^{(T_n)}|$. We implicitly include the phase of the Rabi frequency[18] in $\phi_n^{(T_n)}$ and thus treat $\omega^{(T)}$ as a real number. Hence, if $s^{(T)} = +1(-1)$, $\Omega^{(T)} = |\Omega^{(T)}|(|\bar{\Omega}^{(T)}|)$.

The quantities $\Delta_{T'}^{|T\rangle}$ form the *state LS matrix*, which are the LS on $|T\rangle$ when transition $T'$ is driven. It will also be convenient to define the *transition LS matrix* $\Delta_{T'}^{T} \triangleq \Delta_{T'}^{|T+1\rangle} - \Delta_{T'}^{|T\rangle}$,

[18] If $s^{(T)} = -1$, the Rabi frequency in (3.19) corresponds to $\bar{\Omega}$ in (3.8).

which is the LS on the $T^{\text{th}}$ transition when driving $T'$ (this will often be referred to as *the* LS matrix). We can use this to rewrite the LS contributions to (3.19) as[19]

$$H_{LS}^{(T_n)} = \sum_{T=0}^{d-1} \Delta_{T_n}^{|T\rangle} |T\rangle\langle T| = \sum_{T=0}^{d-1} \left( \sum_{T'=0}^{T-1} \Delta_{T_n}^{T'} \right) |T\rangle\langle T| + \Delta_{T_n}^{|0\rangle} \mathbb{1}. \tag{3.20}$$

The term proportional to the identity only adds global phases and is thus dropped.

We now go into an interaction picture that is the analogue of the previous drive interaction picture, with the frame change Hamiltonian [128]

$$H_F = \hbar \sum_{T=0}^{d-1} \left( \sum_{T'=0}^{T-1} \omega_n^{(T')} \right) |T\rangle\langle T|. \tag{3.21}$$

The operators in (3.19) are then transformed in an obvious generalisation of (3.9). The time dependence in the pulse Hamiltonians is removed, and the total Hamiltonian during the $n^{\text{th}}$ pulse becomes

$$H_{n,D} = \frac{\hbar\Omega^{(T_n)}}{2} \sigma_{\phi_n^{(T_n)}}^{(T_n)} - \hbar \sum_{T=0}^{d-1} \left( \sum_{T'=0}^{T-1} \delta_{T_n}^{(T')} \right) |T\rangle\langle T| \tag{3.22}$$

where $\sigma_{\phi_n^{(T_n)}}^{(T_n)}$ is a two-state Pauli matrix in the $\{|T\rangle, |T+1\rangle\}$ subspace (with the obvious state ordering) and the (signed) *LS detunings* $\delta_{T'}^{(T)} = \omega_l^{(T)} - (\omega_{T+1} - \omega_T + \Delta_{T'}^{T})$. The $T^{\text{th}}$ transition is driven resonantly when $\delta^{(T)} \triangleq \delta_T^{(T)} = 0$; all other $\delta_{T'}^{(T)}$ are not related to whether a transition is driven resonantly or not. Note that $\omega_l^{(T)} - (\omega_{T+1} - \omega_T)$ would be the generalisation of the bare transition detuning from 3.3.1.

The only part of the diagonal operator in (3.22) that does not commute with $\sigma_{\phi_n^{(T_n)}}^{(T_n)}$ is $\frac{\delta^{(T_n)}}{2}\sigma_z^{(T_n)}$, so we can write

$$H_{n,D} = \frac{\hbar}{2}\left( \Omega^{(T_n)} \sigma_{\phi_n^{(T_n)}}^{(T_n)} + \delta^{(T_n)} \sigma_z^{(T_n)} \right) - \hbar \left( \sum_{T=0}^{d-1} \left( \sum_{T'=0}^{T-1} \delta_{T_n}^{(T')} \right) |T\rangle\langle T| + \frac{\delta^{(T_n)}}{2} \sigma_z^{(T_n)} \right) \tag{3.23}$$

where the two operators in brackets act on disjoint subspaces, and thus commute, so they can easily be integrated over the pulse duration $\tau_n$

We can also include the effect of a small inter-pulse gap of duration $\tau_n^{(Int)}$, during which the laser is turned off. During this time, the Hamiltonian is identical to (3.22),

[19] We abuse notation in this equation and include $T = 0$ in the outer sum, in which case it is considered 0. This will be used repeatedly.

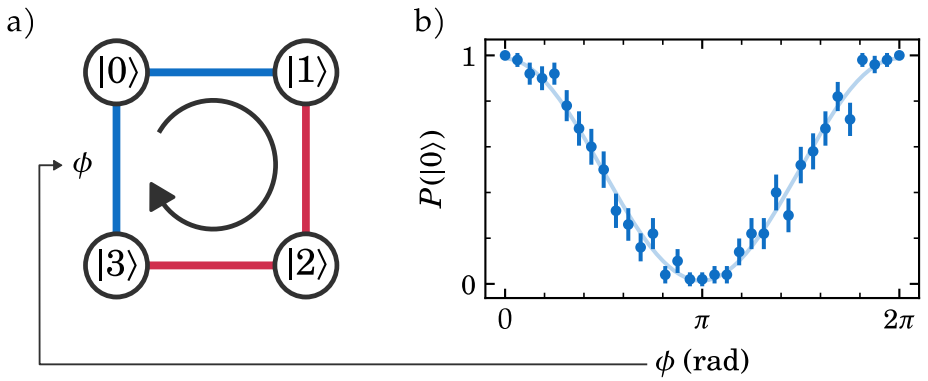



**Figure 3.5:** a) Diagram of a loop interferometer experiment. Half of the population is driven around the loop of transitions. $\pi/2$ pulses are driven on the red transitions and $\pi$ pulses on the blue ones, in the order which causes population to move in the direction of the arrow. The phase $\phi$ of the $|3\rangle \leftrightarrow |0\rangle$ transition is scanned b) Despite this transition only being pulsed once, its phase affects the dynamics.

without the $\sigma^{(T_n)}_{\phi_n^{(T_n)}}$ term and with $H_{LS}^{(T_n)}$ subtracted from it. Then, the unitary for a single pulse $U_n \triangleq U(t_{n,i} + \tau_n + \tau_n^{(Int)}; t_{n,i})$ can be found to be

$$U_n = \mathscr{U}_n^{(LS)} \mathscr{U}_n^{(\delta)} R^{(T_n)}\left(\theta_n, \phi_n^{(T_n)}, \nu^{(T_n)}\right) \tag{3.24}$$

where $\theta_n = \tau_n \sqrt{\Omega^{(T_n)^2} + \delta^{(T_n)^2}}$ and $\tan \nu^{(T_n)} = \frac{\delta^{(T_n)}}{\Omega^{(T_n)}}$, analogously to (3.12) and

$$\mathscr{U}_n^{(\delta)} = R_z^{(T_n)}\left(-\delta^{(T_n)}\tau_n\right) \exp\left(i\left[\tau_n + \tau_n^{(Int)}\right] \sum_{T=0}^{d-1} \sum_{T'=0}^{T-1} \delta^{(T')} |T\rangle\langle T|\right), \tag{3.25}$$

$$\mathscr{U}_n^{(LS)} = \exp\left(i \sum_{T=0}^{d-1} \left( \sum_{T'=0}^{T-1} \Delta_{T'}^{T'} \left[\tau_n + \tau_n^{(Int)}\right] - \Delta_{T_n}^{T'} \tau_n \right) |T\rangle\langle T| \right). \tag{3.26}$$

Furthermore, if $\tau_n^{(Int)} = 0$, the action of $\mathscr{U}_n^{(\delta)}$ on the $\{|T_n\rangle, |T_n + 1\rangle\}$ subspace is the equivalent of the global phase in (3.12). The total unitary for a sequence of pulses is $C = \prod_n U_n$.

### 3.4.2 Closed-loop interferometers

Before discussing arbitrary sequences of pulses in cyclical maps, we will build intuition by considering a pulse sequence that drives population around a loop. Despite its simplicity, it will be seen that this displays interference effects *between* the different (and independent) laser tones, which are mediated by the state. Such interference would be expected when all transitions in a loop are *simultaneously* driven. This has been theoretically [128–130] and experimentally [131] explored[20]. In such situations, the *eigenvalues* of the

[20] In contrast, the author has not seen discussion of interference effects in sequences of pulses in the literature.

Hamiltonian depend on the phase of the lasers, not just its eigenstates as with a single tone. Specifically, they depend on the phase $\Theta \triangleq \sum_T \phi^{(T)}$. Changing $\Theta$ can lead to effects such as coherent population trapping [129, 131].

In our experiments, transitions are driven sequentially, not simultaneously. Nevertheless, we still observe effective interference effects, because the phase of the driving tones is imparted onto the atomic state. This temporal interference is certainly present in two-level systems: the dynamics brought about by a sequence of two rotations clearly depends on the phase of the second rotation relative to the first. However, as discussed in 3.3.1, the phase of the *first* laser has no effect on the dynamics, and can be thought as simply "defining" the axes of the Bloch sphere, or the "phase origin" of superposition states.

In a multi-level system which does not have closed loops, the situation is similar: the first pulse on each transition "defines" the axes of the effective two-state Bloch sphere and thus the relative phase of those two states in the full state vector. Because there are no closed loops, these "definitions" are unique. However, if transitions can be driven in a loop, the Bloch sphere axes of a two-state subspace can be defined in more than one way, which may contradict. Indeed, in a cyclically connected graph, the $|d-1\rangle \leftrightarrow |0\rangle$ transition can be driven as well as all transitions $|T\rangle \leftrightarrow |T+1\rangle$ for $0 \le T \le d-2$. Thus, a superposition between states $|0\rangle$ and $|d-1\rangle$ can be set up by traversing all $|T\rangle$ states. The phase of this superposition is defined by the phase of all the tones that have been driven. However, the superposition can be closed by doing a $\pi/2$ pulse on the $|0\rangle \leftrightarrow |d-1\rangle$ transition, which is then the *first* pulse on that transition. The final state then depends on the difference between the *absolute* phase of the final drive and the predefined phase of the state.

The above procedure is implemented by a sequence of TSRs $R^{(T)}_{\phi^{(T)}}(\theta_T)$ for $0 \le T \le d-2$, where $\theta_0 = \pi/2$ and $\theta_T = \pi$ otherwise. The final rotation is $R^{(d-1)}_{\phi^{(d-1)}}(\pi/2)$. The phases $\phi^{(T)}$ depend on the absolute phase of the tone that drives the corresponding transition. Then, the resulting state is

$$\begin{aligned} |\psi\rangle &= R^{(d-1)}_{\phi^{(d-1)}}(\pi/2) \times R^{(d-2)}_{\phi^{(d-2)}}(\pi) \ldots \times R^{(1)}_{\phi^{(1)}}(\pi) \times R^{(0)}_{\phi^{(0)}}(\pi/2)\,|0\rangle \\ &= e^{i\frac{\Theta_d}{2}} \cos\left(\frac{\Theta_d}{2}\right)|0\rangle - i e^{-i(\phi^{n-1}+\frac{\Theta_d}{2})} \sin\left(\frac{\Theta_d}{2}\right)|d-1\rangle \end{aligned} \tag{3.27}$$

for $\Theta_d = \Theta - d\frac{\pi}{2}$. Thus, the probability of measuring the state in $|0\rangle$ is $P_{|0\rangle} = (1+\cos\Theta_d)/2$. This means that there are more stringent requirements on the necessary experimental

phase control when a cyclic connectivity graph is used. Indeed, in the latter, the transitions need to maintain *temporal* coherence, but their absolute phase at the start of the experiment is irrelevant. However, with a cyclic graph, $\Theta_d$ must be controlled (Figure 3.5). This is trivial if a single laser (or some other source) is modulated using RF from a single synthesiser, as is often the case. However, if transitions are driven with different mechanisms, achieving the necessary phase coherence between the drives may be challenging.

Non-trivial dynamics can occur if $\Theta_d$ changes over a sequence of pulses, as will be seen in the next section.

### 3.4.3 Cyclic connectivity

We now derive the full unitary for a circuit when the connectivity graph is cyclic. The lab frame Hamiltonian is identical to 3.19, with the addition of the transition between $|d-1\rangle \leftrightarrow |0\rangle$. However, the frame-change Hamiltonian (3.21) does not remove all time dependences, since the operator $|0\rangle\langle d-1|$ does not obey (3.9), instead transforming as $|0\rangle\langle d-1| \rightarrow \exp(-\sum_{T=0}^{d-2}\omega_l^{(T)}t)|0\rangle\langle d-1|$. The time dependence can be symmetrised across all states using the frame change Hamiltonian[21]

$$H_F = \hbar\sum_{T=0}^{d-1}\left(\sum_{T'=0}^{T-1}\left(\omega_n^{(T')} - \bar{\omega}_l\right)\right)|T\rangle\langle T| \tag{3.28}$$

with the *mean signed laser frequency* $\bar{\omega}_l \triangleq \frac{1}{d}\sum_{T=0}^{d-1}\omega_l^{(T)}$. The energy $\hbar\bar{\omega}_l$ is the sum of all the photons absorbed or emitted in the process of traversing a full loop. If $\bar{\omega}_l = 0$, we say the laser drives obey the *multi-photon resonance condition* [128].

In this modified drive frame, the laser-ion Hamiltonians are

$$H_{n,D} = \frac{\hbar\Omega^{(T_n)}}{2}\left(e^{-i(\bar{\omega}_l t - \phi_n^{(T_n)})}|T_n+1\rangle\langle T_n| + h.c.\right) - \hbar\sum_{T=0}^{d-1}\left(\sum_{T'=0}^{T-1}\left(\delta_{T_n}^{(T')} - \bar{\omega}_l\right)\right)|T\rangle\langle T|. \tag{3.29}$$

This still contains a time dependence. However, we can use (3.3) to calculate the propagator for the pulse in this interaction frame by "hopping" to an interaction picture in which the Hamiltonian is time-independent for the duration of the pulse. The frame change Hamiltonian for this is $H_F = -\frac{\hbar\bar{\omega}_l}{2}\sigma_z^{(T_n)}$. In this frame, the Hamiltonian is the same

[21] The author was not able to find a frame change Hamiltonian that removed the time dependence and was diagonal in the computational basis (a frame change Hamiltonian that is *not* diagonal can be found using Floquet theory [111], but the measurements wouldn't commute with them). While it was not proven that this is *not* possible, the author conjectures this to be so.

as 3.29 with the addition of $\hbar\left(\sum_{T=0}^{d-1}\sum_{T'=0}^{T-1}\bar{\omega}_l |T\rangle\langle T| + \frac{\bar{\omega}_l}{2}\sigma_z^{(T_n)}\right)$, which is diagonal in the $\{|T\rangle, |T+1\rangle\}$ subspace. Then, after calculating the propagator and multiplying by the appropriate frame change unitaries (see Section 3.1) we find that the propagator for the $n^{\text{th}}$ pulse is given by[22]

$$U_n = R_z^{(T_n)}\left(-\bar{\omega}_l t_{n,i}\right)\mathscr{U}_n^{(\bar{\omega}_l)}\mathscr{U}_n^{(LS)}\mathscr{U}_n^{(\delta)}R^{(T_n)}\left(\theta_n, \phi_n, \nu^{(T_n)}\right)R_z^{(T_n)}\left(\bar{\omega}_l t_{n,i}\right) \tag{3.30}$$

where $\mathscr{U}_n^{(\delta)}$ and $\mathscr{U}_n^{(LS)}$ are as per (3.25) and (3.26), and

$$\mathscr{U}_n^{(\bar{\omega}_l)} = \exp\left(-i\bar{\omega}_l\left[\tau_n + \tau_n^{(Int)}\right]\sum_{T=0}^{d-1} T|T\rangle\langle T|.\right) \tag{3.31}$$

We see that (3.30) depends on the time at which the pulse started, which is not the case for the unitaries with linear connectivity graphs. Indeed, this can be linked to the intuition from Section 3.4.2: if $\bar{\omega}_l \neq 0$, then $\Theta_d$ advances over time. Thus, the result of the experiment described there would depend on *when* that experiment was carried out! We explore the consequences of these dynamics in more detail in Sections 5.2.1 and 7.3.1.4.

### 3.4.4 Discussion

We can gain deeper intuition about why detunings affect graphs with linear and cyclic connectivity differently by analysing the problem in a different interaction picture, which we call the *atomic* interaction picture. This uses the atomic Hamiltonian $H_0$ as the frame-change Hamiltonian, which removes the state evolution due to the atomic eigenergies of the states: the only evolution then comes from the drive tones. Here, we qualitatively discuss the behaviour in this frame, with a full mathematical treatment given in Appendix B.1. For simplicity, we will ignore any light shifts in the remainder of the section.

In the atomic frame, an idle state does not evolve, unlike in the drive frame (Equation (3.21), but the pulse Hamiltonians retain some time dependence if there are detunings. Indeed, in the two-state Bloch sphere of a transition, the axis of the TSR induced by the drive precesses at a rate equal to the detuning, both when the drive is on and off. The precession while the drive is on tilts the final TSR away from the Bloch-sphere equator

[22] The final $R_z^{(T_n)}$ operator would depend on $t_{n,i} + \tau_n$, but a factor of $R_z^{(T_n)}\left(-\bar{\omega}_l\tau_n\right)$ cancels elsewhere. Note that we do not have to go into the frame defined by (3.29) during the inter-pulse gap.

($\nu^{(T_n)} \neq 0$ in (3.12), (3.24) and (3.30)) and, in the atomic frame, adds an additional $z$-rotation. The precession while the drive is off is absent in the drive frame, but in the atomic frame, it causes the equatorial angle $\phi$ of TSRs to depend on when they are applied. Independently of connectivity, the unitary for the $n^{\text{th}}$ pulse in the atomic frame is (in the absence of LSs)

$$\begin{aligned}\tilde{U}_n &= R_z^{(T_n)}\left(-\delta^{(T_n)}\tau_n\right) R_z^{(T_n)}\left(-\delta^{(T_n)} t_{n,i}\right) R^{(T_n)}\left(\theta_n, \phi_n^{(T_n)}, \nu^{(T_n)}\right) R_z^{(T_n)}\left(\delta^{(T_n)} t_{n,i}\right) \\ &= R_z^{(T_n)}\left(-\delta^{(T_n)}\tau_n\right) R^{(T_n)}\left(\theta_n, (\phi_n^{(T_n)} - \delta^{(T_n)} t_{n,i}), \nu^{(T_n)}\right).\end{aligned} \tag{3.32}$$

This appears markedly different to Equation (3.24) in that it depends on the absolute time $t_{i,n}$ at which the pulses are driven. However, as shown in Appendix B.1, the $R_z^{(T_n)}\left(\pm\delta^{(T_n)} t_{n,i}\right)$ rotations can be distributed across other pulses in a circuit if the connectivity is linear. In this case, the full unitary of a circuit can be expressed as $C = \prod_n \tilde{U}_n = D_f \prod_n U_n D_i$ where $U_n$ are as per (3.24) and the $D_{f/i}$ are diagonal unitaries which, since they act on a computational basis state or just before a measurement, have no observable effect and can be ignored. Thus, the unitary applied by each pulse becomes independent of the absolute time at which they are applied, and depend only on the control parameters and the pulse duration. However, the techniques used to do so cannot be applied if the connectivity graph is cyclic, suggesting that, in that case, the pulses do maintain some dependence on the absolute time as per Equation (3.30).

Some intuition on this can be gained by considering a detuning $\delta^{(\tilde{T})}$ on a single transition $\tilde{T}$. Suppose that an even superposition is produced in which all states have the same phase, using a suitable sequence of pulses[23] that does not include the $\tilde{T}^{\text{th}}$ transition[24]. After this, at time $t$ (the time taken to drive all previous pulses), a pulse is applied on the $\tilde{T}$ transition with a drive phase $\phi_n^{(\tilde{T})} = 0$ and rotation angle $\theta$. Thus,

[23] This sequence of pulses can be exactly the same whether the connectivity is linear or cyclic, since all transitions in the linear connectivity graph are allowed in the cyclic one.

[24] Generating an even superposition in this way would generally not be possible if the system begins in a computational state, but it would be possible if it begins in a superposition of at least two states that include one state below $|\tilde{T}\rangle$ and above $|\tilde{T+1}\rangle$. In order to do this, the drive tones would have to maintain phase coherence with the phase of the superposition over different shots of the experiment. However, any other initial state $|\psi\rangle$ would also work for this argument.

neglecting the effects of the TSR precession during the pulse[25] the state becomes

$$|\psi\rangle = \frac{1}{\sqrt{d}}\left[|0\rangle + ... + |\tilde{T}-1\rangle + \left(\cos\left(\frac{\theta}{2}\right) - ie^{i\delta^{(\tilde{T})}t}\sin\left(\frac{\theta}{2}\right)\right)|\tilde{T}\rangle \right. \\ \left. + \left(\cos\left(\frac{\theta}{2}\right) - ie^{-i\delta^{(\tilde{T})}t}\sin\left(\frac{\theta}{2}\right)\right)|\tilde{T}+1\rangle + |\tilde{T}+2\rangle + ... + |d-1\rangle\right]. \tag{3.33}$$

A sequence of pulses on other transitions is then carried out before another pulse on this transition or a measurement occurs.

The previous paragraph assumed nothing about the connectivity graph, but we will now show that using the expression for the pulse unitaries (3.24), which does not depend on the absolute time, we obtain the same state only if the connectivity graph is linear. With this expression, TSRs on transitions other than $\tilde{T}$ (which do not have a detuning) have an additional diagonal unitary after them. Since only transition $\tilde{T}$ has a detuning and there are no LSs, these are[26]

$$\mathscr{U}_n^{(\delta)} = \mathrm{diag}\{\underbrace{1,...,1}_{\tilde{T}},\underbrace{e^{i\delta^{(\tilde{T})}\tau_n},...,e^{i\delta^{(\tilde{T})}\tau_n}}_{d-\tilde{T}}\}. \tag{3.34}$$

That is, all states above and including $|\tilde{T}+1\rangle$ acquire a phase of $e^{i\delta^{(\tilde{T})}\tau_n}$ (where $\tau_n$ is the duration of the $n^{\text{th}}$ pulse) and all below and including $|\tilde{T}\rangle$ acquire no phase. If the connectivity graph has no loops, these operations commute with all TSRs on transitions other than $\tilde{T}$. Thus, the sequence of pulses before the pulse on this transition will produce an even superposition $1/\sqrt{d}\left(\sum_{T=0}^{\tilde{T}}|T\rangle + \sum_{T=\tilde{T}+1}^{d-1}e^{i\delta^{(\tilde{T})}t}|T\rangle\right)$, since the sum of the duration of all previous pulses is $t$. The state after the pulse on the $\tilde{T}$ transition will now be[27]

$$|\psi\rangle = \frac{1}{\sqrt{d}}\left[|0\rangle + ... + |\tilde{T}-1\rangle\left(\cos\left(\frac{\theta}{2}\right) - ie^{i\delta^{(\tilde{T})}t}\sin\left(\frac{\theta}{2}\right)\right)|\tilde{T}\rangle \right. \\ \left. + e^{i\delta^{(\tilde{T})}t}\left\{\left(\cos\left(\frac{\theta}{2}\right) - ie^{-i\delta^{(\tilde{T})}t}\sin\left(\frac{\theta}{2}\right)\right)|\tilde{T}+1\rangle + |\tilde{T}+2\rangle + ... + |d-1\rangle\right\}\right] \tag{3.35}$$

since the $\pi$-pulse was done with $\phi_n^{(\tilde{T})} = 0$.

If the connectivity graph is linear then, since the $\tilde{T}$ transition is not used in the subsequent pulses, the qudit can be thought of as being split into two different subspaces

[25] This amounts to ignoring the $R_z^{(T_n)}\left(-\delta^{(T_n)}\tau_n\right)$ rotation in (3.32) and setting $\nu^{\tilde{T}} = 0$.

[26] We have also assumed no inter-pulse delays, for brevity.

[27] We have again set $\nu^{\tilde{T}} = 0$ and do not include the effect of $\mathscr{U}_n^{(\delta)}$ on the detuned transition. In the latter, the $R_z^{(T_n)}\left(-\delta^{(T_n)}\tau_n\right)$ rotation is also included in 3.32, so along $\nu^{\tilde{T}} \neq 0$ will produce the same result as if Equation 3.32 were used; the remainder of $\mathscr{U}^{(\delta)}$ will be included in subsequent diagonal unitaries.

$\{|T \leq \tilde{T}\rangle\}$, $\{|T \geq \tilde{T}+1\rangle\}$ that do not interact. Within these subspaces, the states (3.33) and (3.35) are the same. Thus, the action of subsequent pulses on transitions other than $\tilde{T}$ results in the same state as if they acted on the state (3.33), up to a phase multiplying the states $|T > \tilde{T}\rangle$[28]. It can be shown that the state after a subsequent pulse on $\tilde{T}$ is the same (up to a diagonal unitary[29]) whether the absolute-time-dependent (3.32) or the absolute-time-independent (3.24) unitaries are used for the calculation. Because measurements are unaffected by the phase on each state, the observables of the states obtained with each expression are indistinguishable. Thus, it is valid to consider the unitary of each pulse to be independent of the absolute time.

However, this process does not work if the connectivity graph is cyclic. This is because the phase between the $|d-1\rangle$ and $|0\rangle$ is not the same in the states (3.33) and (3.35). Thus, the states output when the $|d-1\rangle \leftrightarrow |0\rangle$ transition is driven will generally differ in more than just phase, so the two expressions for the unitaries give different observables. This can also be seen from the fact that the unitary (3.34) does not commute with this transition, but it would need to for the previous argument to hold. Thus, in this case, evolving the state using the absolute-time-dependent unitaries (3.32), which is the "raw" evolution of the state, is *not* equivalent to evolution under the absolute-time-independent unitaries (3.24). Thus, the unitary applied by each pulse retains some dependence on the absolute time[30], as per (3.30).

## 3.5 Calculating the Rabi frequency

It will be necessary throughout this thesis to be able to calculate the Rabi frequency of a transition between two states, under a known laser geometry and quantisation magnetic field. We will be most concerned with driving transitions between states in levels whose angular momentum quantum numbers differ by $\Delta L = 1$ (dipole transitions) or $\Delta L = 2$ (quadrupole transitions). However, with little additional complexity, we calculate the general case of a transition with $\Delta L = K$, a rank-$K$ transition. The approach

[28] Due to the $\tilde{U}_n^{(\delta)}$ unitaries applied with these pulses, this phase increases to $e^{i\delta^{(\tilde{T})}t_2}$.

[29] This unitary has the same form as (3.34) using the time $t_2$ at which the second pulse on $\tilde{T}$ is carried out.

[30] It could not be proven that a *different* approach to that taken in Appendix B.1 which can remove the absolute time dependences does not exist. However, the author conjectures this to be so.

that will be followed is that of [127]. The reader is referred to [118, 124, 132, 133] for alternative derivations if desired.

We assume the beam is a plane wave with electric field $\mathbf{E} = \frac{E_0}{2}\left(\hat{\boldsymbol{\varepsilon}} e^{i(\mathbf{k}\cdot\mathbf{r}-\omega_l t)} + c.c.\right)$, where $\omega_l$ is the frequency and $\mathbf{k}$ is the beam's wavevector (see Section 3.5.2 for conventions). The Hamiltonian that drives rank-$K$ transitions[31] between the levels containing the states $|\nu\rangle, |\mu\rangle$ (neglecting any terms that arise from detunings) is[32]

$$H = -\sqrt{\frac{2K+1}{K!(2K+1)!!}} \sum_{q=-K}^{K} (-1)^q \mathscr{M}_q^{(K)} \left( B_{-q}^{(K)} e^{i(\mathbf{k}\cdot\mathbf{r}-\omega_l t+\phi)} + \tilde{B}_{-q}^{(K)} e^{-i(\mathbf{k}\cdot\mathbf{r}-\omega_l t+\phi)} \right) \tag{3.36}$$

where the $\mathscr{M}_q^{(K)}$ is the $q^{\text{th}}$ component of the rank-$K$ *multipole moment operator*, which characterises the electron's spatial wavefunction; and the $B_{-q}^{(K)}$, $\tilde{B}_{-q}^{(K)}$ are proportional to what we refer to as the *beam tensor components* $\beta_{-q}^{(K)}$, which depend on the beam's $\hat{\mathbf{k}}$ and $\hat{\boldsymbol{\varepsilon}}$. Using their definitions (which are given later in (3.43) and (3.46)) and comparing to equation (3.10) after neglecting counter-rotating terms, we find the resonant[33] Rabi frequency[34]

$$\Omega_{\nu,\mu} = (-1)^{q+1} \frac{2}{\hbar} \sqrt{\frac{2K+1}{K!(2K+1)!!}} \langle\mu| \mathscr{M}_q^{(K)} |\nu\rangle B_{-q}^{(K)} \tag{3.37}$$

$$= (-1)^{q+1} i^{K-1} \frac{eE_0}{\hbar} \sqrt{\frac{2\pi}{\alpha c}\left(\frac{c}{\omega_l}\right)^3 (2J_\mu+1) A_{J_\mu,J_\nu}} \langle\mu| \mathsf{T}_q^K |\nu\rangle \beta_{-q}^{(K)}(\hat{\mathbf{k}}, \hat{\boldsymbol{\varepsilon}}) \tag{3.38}$$

where $E_0$ is the electric field magnitude of the beam; $A_{J_\mu,J_\nu}$ is the Einstein coefficient for decay from the level containing $|\mu\rangle$ to the one containing $|\nu\rangle$ (or vice-versa depending on the state energies); $q = m_\mu - m_\nu$, where $m_i$ is the quantum number for the $z$-projection of the angular momentum of state $|i\rangle$; and $\alpha$ is the fine structure constant. The atomic properties of the coupling between the two states are encoded in $\langle\mu| \mathsf{T}_q^K |\nu\rangle$ and the beam parameters in $\beta_{-q}^{(K)}(\hat{\mathbf{k}}, \hat{\boldsymbol{\varepsilon}})$. We now give explicit expressions for these.

### 3.5.1 Electronic multipole moments

The components of the rank-$K$ multipole moments are [127, 134]

$$\mathscr{M}_q^{(K)} = -e\sqrt{\frac{4\pi}{2K+1}} \rho^K Y_{K,q}(\vartheta, \varphi) \tag{3.39}$$

[31] The most common transition rank considered are dipole transitions, where the Hamiltonian is often written as $H = -\hat{\mathbf{d}}\cdot\mathbf{E} = -E_0/2\left(\mathbf{d}\cdot\hat{\boldsymbol{\varepsilon}} e^{i(\mathbf{k}\cdot\mathbf{r}-\omega_l t)} + \mathbf{d}\cdot\hat{\boldsymbol{\varepsilon}}^* e^{-i(\mathbf{k}\cdot\mathbf{r}-\omega_l t)}\right)$, where $\hat{\mathbf{d}}$ is the dipole moment operator. The matrix elements can be obtained by comparing Equation (3.37) with the familiar expression $\Omega_{\nu,\mu} = E_0 \langle\mu|\mathbf{d}\cdot\hat{\boldsymbol{\varepsilon}}|\nu\rangle/\hbar$.

[32] The double-factorial is defined as $X!! = X(X-2)(X-4)...$

[33] This assumes that $\omega_l = \omega_{\nu,\mu}$: we neglect any light shifts.

[34] The expression for the counter-rotating Rabi frequency is identical up to a sign of $(-1)^{(K-1)}$ and the transformation $\hat{\boldsymbol{\varepsilon}} \to \hat{\boldsymbol{\varepsilon}}^*$.

where the $Y_{K,q}$ are spherical harmonics and the coordinates $(\rho, \vartheta, \varphi)$ are *operators* for the coordinates of the electron relative to the atomic nucleus, which is why we explicitly use $\rho$ for the electron's radial position.

We now look for their matrix elements that couple $|\nu\rangle$, $|\mu\rangle$. The Wigner-Eckart theorem [132, 135] can be used to write the matrix elements in terms of their wavefunctions' angular distribution and the reduced matrix element, which depends on all other quantum numbers. We first write this in the absence of hyperfine structure. Consider two states, $|\alpha_{1,2}, J_{1,2}, m_{1,2}\rangle$, where $J_{1,2}$ and $m_{1,2}$ are the quantum numbers for the total and the $z$-projection of the angular momentum of each state, and $\alpha_{1,2}$ are other quantum numbers[35]:

$$\langle \alpha_2, J_2, m_2 | \mathcal{M}_q^{(K)} | \alpha_1, J_1, m_1 \rangle = \langle \alpha_2, J_2 || \mathcal{M}^{(K)} || \alpha_1, J_1 \rangle (-1)^{J_2 - m_2} \begin{pmatrix} J_2 & K & J_1 \\ -m_2 & q & m_1 \end{pmatrix}. \quad (3.40)$$

The first symbol on the right-hand-side is the reduced matrix element, which can be written in terms of the measurable Einstein coefficient $A_{J_2,J_1}$ for decay from the level containing $|\alpha_2, J_2, m_2\rangle$ to the one containing $|\alpha_1, J_1, m_1\rangle$:

$$\langle \alpha_2, J_2 || \mathcal{M}^{(K)} || \alpha_1, J_1 \rangle = e \sqrt{\frac{K(2K-1)!!(2K+1)!!}{2(K+1)} \frac{1}{\alpha c} \left( \frac{c}{\omega_{\nu,\mu}} \right)^{2K+1} (2J_2 + 1) A_{J_2,J_1}} \quad (3.41)$$

where $\alpha$ is the fine-structure constant.

We can write the Wigner-3j symbols[36] (the matrix-like structure in (3.40)) as the matrix elements of a unitless tensor operator $\mathsf{T}_q^K$,

$$\langle J_2, m_2 | \mathsf{T}_q^K | J_1, m_1 \rangle \triangleq (-1)^{J_2 - m_2} \begin{pmatrix} J_2 & K & J_1 \\ -m_2 & q & m_1 \end{pmatrix}. \quad (3.42)$$

This allows us to find the matrix elements when there is hyperfine structure for any value of the magnetic field (see Section 6.2.2). Indeed, any state in a level with total angular momentum $J_\nu$ can be written as $|\nu\rangle = \sum_{\tilde{m}_\nu} c_{\tilde{m}_\nu} |\alpha_\nu, J_\nu, \tilde{m}_\nu\rangle \otimes |I, m_\nu - \tilde{m}_\nu\rangle$, where $m_\nu$ is the magnetic quantum number $m_F$ of $|\nu\rangle$ and the coefficients $c_{\tilde{m}_\nu}$ depend on the magnetic field. Then, since the reduced matrix element is a scalar, it can be seen that

$$\langle \mu | \mathcal{M}_q^{(K)} | \nu \rangle = \langle \alpha_\mu, J_\mu || \mathcal{M}^{(K)} || \alpha_\nu, J_\nu \rangle \langle \mu | \mathsf{T}_q^K | \nu \rangle \quad (3.43)$$

[35] The Racah convention is taken for the reduced matrix element, following [127].
[36] The Wigner-3j symbols vanish unless $q + m_1 - m_2 = 0$ and $J_2 + J_1 \geq K \geq |J_2 - J_1|$.

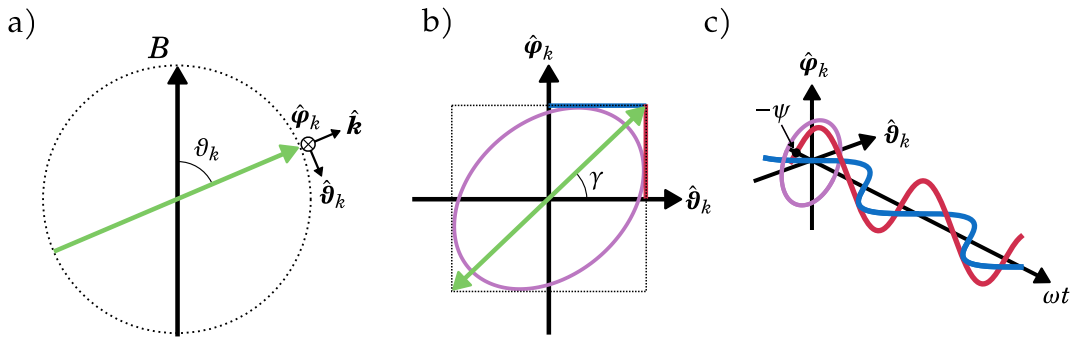



**Figure 3.6:** Beam geometry. a) The angle $\vartheta_k$ is the angle between the beam (green) and the $z$-axis, which lies along the quantisation field. The beam travels along $\hat{\mathbf{k}}$, which defines the $\hat{\boldsymbol{\vartheta}}_k$ and $\hat{\boldsymbol{\varphi}}_k$ directions, with the latter being into the page. The angle $\varphi_k$ is not shown, since it is irrelevant for a single beam. b) Beam polarisation angles. The angle $\gamma$ sets the amplitude between the electric field components about $\hat{\boldsymbol{\vartheta}}_k$ and $\hat{\boldsymbol{\varphi}}_k$. A linearly polarised beam is shown in green, as well as an elliptically polarised beam with $\psi \neq 0$. Note that the polarisation ellipse axes do *not* lie along $\gamma$, but rather, the ellipse is tangent to the square shown. The length of the blue and red lines is $\cos\gamma$ and $\sin\gamma$, respectively. c) Electric field over time at a point. There is a phase difference between the polarisation components, set by $\psi$.

where the operator in the matrix element is implicitly the identity over all degrees of freedom not addressed in (3.42) and can be found with knowledge of the $c_{\tilde{m}_\nu}$, which can be numerically calculated[37].

### 3.5.2 Beam geometry

We now define the geometry of the laser beam from before. The $z$-axis is parallel to the magnetic field that breaks the atomic degeneracy and the $x$-axis is usually defined such that the beam travels in the $x-z$ plane[38], though this is not necessary (see Figure 3.6). We shall work in polar coordinates $(r, \vartheta, \varphi)$ where $\vartheta$ and $\varphi$ are the polar and equatorial angles, respectively. This defines the usual unit vectors

$$\hat{\mathbf{r}} \triangleq \begin{pmatrix} \sin\vartheta\cos\varphi \\ \sin\vartheta\sin\varphi \\ \cos\vartheta \end{pmatrix} \quad , \quad \hat{\boldsymbol{\vartheta}} \triangleq \begin{pmatrix} \cos\vartheta\cos\varphi \\ \cos\vartheta\sin\varphi \\ -\sin\vartheta \end{pmatrix} \quad , \quad \hat{\boldsymbol{\varphi}} \triangleq \begin{pmatrix} -\sin\varphi \\ \cos\varphi \\ 0 \end{pmatrix} \tag{3.44}$$

along the relevant directions. Then, the beam direction is fixed to be $\hat{\mathbf{k}} \triangleq \hat{\mathbf{r}}(\vartheta_k, \varphi_k)$, where $(\vartheta_k, \varphi_k)$ are the polar and equatorial angles that define the beam direction. The polarisation vector $\hat{\boldsymbol{\varepsilon}}$ is perpendicular to $\hat{\mathbf{k}}$:

$$\hat{\boldsymbol{\varepsilon}} \triangleq \cos\gamma\,\hat{\boldsymbol{\vartheta}}_k + e^{i\psi}\sin\gamma\,\hat{\boldsymbol{\varphi}}_k. \tag{3.45}$$

[37] In the low-field regime, an exact expression can be found using the Wigner-6j symbols [127, 132].

[38] Defining the $x-z$ plane to contain the beam is equivalent to setting $\varphi_k = 0$, which has no effect when there is just one beam – when there are two, the angle *between* them does affect the dynamics.

The angles $\gamma$, $\psi$ respectively set the amplitude and relative phase of the polarisation components along the $\hat{\boldsymbol{\vartheta}}_k \triangleq \hat{\boldsymbol{\vartheta}}(\vartheta_k, \varphi_k)$ and $\hat{\boldsymbol{\varphi}}_k \triangleq \hat{\boldsymbol{\varphi}}(\vartheta_k, \varphi_k)$ directions (see Figure 3.6). In our setup, the quantisation field is parallel to the plane of the optical table, so we will often refer to the $\hat{\boldsymbol{\vartheta}}_k$ and $\hat{\boldsymbol{\varphi}}_k$ polarisation components as the in-plane (IP) and out-of-plane (OOP) components respectively.

### 3.5.3 Beam tensor components

The rank-$K$ components of the electric multipole moment couple to the $(K-1)^{\text{th}}$ derivative of the beam's electric field $\overbrace{\nabla\nabla...\nabla}^{K-1}\mathbf{E}(\mathbf{r})$ at the ion's position $\mathbf{r}$. More specifically, they couple to the rank-$K$ spherical tensor of these derivatives. We do not derive these in detail and instead refer the reader to [127] for details.

The quantities $B_{-q}^{(K)}$ and $\tilde{B}_{-q}^{(K)}$ from (3.36) are[39]

$$B_{-q}^{(K)} = \frac{E_0}{2}\sqrt{\frac{4\pi(K-1)!(K+1)}{(2K+1)!!}}(ik)^{K-1}\beta_{-q}^{(K)}(\hat{\mathbf{k}}, \hat{\boldsymbol{\varepsilon}}). \tag{3.46}$$

Here, we have introduced $\beta_{-q}^{(K)}(\hat{\mathbf{k}}, \hat{\boldsymbol{\varepsilon}}) \triangleq \hat{\boldsymbol{\varepsilon}} \cdot \mathbf{Y}_{K,-q}(\vartheta_k, \varphi_k)$, which we call the *beam tensor components*; the vector fields $\mathbf{Y}_{K,-q}$ are vector spherical harmonics (see [127]). The expression for $\tilde{B}_{-q}^{(K)}$ is obtained by setting[40] $ik \to -ik$ and $\hat{\boldsymbol{\varepsilon}} \to \hat{\boldsymbol{\varepsilon}}^*$.

Some intuition of this equation can be gained by realising that each derivative $\nabla$ brings down a factor of $\pm ik\hat{\mathbf{k}}$ from the exponent, which is the reason behind the $(\pm ik)^{K-1}$. Furthermore, the vector spherical harmonics $\mathbf{Y}_{K,-q}(\vartheta, \varphi)$ are vector fields on the unit sphere, which are proportional to the electric field of the light emitted along the $(\vartheta, \varphi)$ direction when a decay event occurs on the driven transition. Thus, Equation (3.46) shows that the coupling between a beam and the transition it drives depends on $\hat{\mathbf{k}}, \hat{\boldsymbol{\varepsilon}}$ and this emission pattern.

The beam tensor components that drive rank-1 (dipole) transitions are[41]

$$\beta_0^{(1)}(\hat{\mathbf{k}}, \hat{\boldsymbol{\varepsilon}}) = -\sqrt{\frac{3}{8\pi}}\sin\vartheta_k \cos\gamma, \tag{3.47}$$

$$\beta_{\pm 1}^{(1)}(\hat{\mathbf{k}}, \hat{\boldsymbol{\varepsilon}}) = \sqrt{\frac{3}{16\pi}}e^{\pm i\varphi_k}\left(\mp\cos\vartheta_k\cos\gamma - i\sin\gamma e^{i\psi}\right) \tag{3.48}$$

[39] This uses the assumption that the beam is a plane wave.

[40] Note that we *do not* take the complex conjugate of $\mathbf{Y}_{K,-q}$ in $\tilde{B}_{-q}^{(K)}$.

[41] The dependence on $\varphi_k$ is irrelevant when only one beam is present, since rotations of the coordinate systems do not change the dynamics. However, if two beams are present (for example, for Raman transitions) the angle between the beams does affect the dynamics.

and those that drive rank-2 (quadrupole) transitions are

$$\beta_0^{(2)} = -\sqrt{\frac{15}{8\pi}}\cos\vartheta_k \sin\vartheta_k \cos\gamma, \tag{3.49}$$

$$\beta_{\pm1}^{(2)} = \sqrt{\frac{5}{16\pi}} e^{\pm i\varphi_k}(\mp\cos 2\vartheta_k \cos\gamma - i\cos\vartheta_k \sin\gamma e^{i\psi}), \tag{3.50}$$

$$\beta_{\pm2}^{(2)} = \sqrt{\frac{5}{16\pi}} e^{\pm 2i\varphi_k}(\sin\vartheta_k \cos\vartheta_k \cos\gamma \pm i\sin\vartheta_k \sin\gamma e^{i\psi}). \tag{3.51}$$

## 3.6 Two-ion light shift gates

We now turn to describing interactions that couple the atomic states of two separate ions, which are the backbone of the two-polyqubit gates demonstrated in later chapters. Generating this coupling directly is challenging, since the coupling strength of these interactions is extremely weak for typical inter-ion separations of $\sim 5$ μm[42]. Instead, an effective two-ion coupling is mediated by the normal modes of the ion chain. There exist numerous interactions that make use of similar principles; we will focus on the light shift (LS) interaction. This, in turn, is just one of a broader class of *geometric phase* interactions [86, 137, 138], which notably includes the Mølmer-Sørensen (MS) interaction [139, 140] though, for brevity, it will not be discussed.

Intuitively, the mechanism behind geometric phase gates is the following. We apply a force on the two ions which depends on their joint atomic state: this is a *state-dependent force* (SDF), also referred to as a *spin-dependent force*. The resulting motional states are thus coupled to the atomic states, thereby entangling them. It is possible to create and then undo this entanglement, in such a way that the two-ion atomic states acquire different phases. The unitary that describes this evolution is generally not separable into a tensor product of single-ion unitaries, and is instead a true two-ion unitary.

All geometric gate mechanisms work according to this principle; they only differ in the mechanism used to generate the state-dependent force, and the basis of two-ion states on which the forces depend on – which is the gate's eigenbasis. As the name suggests, LS gates use light with oscillating intensity (or polarisation) gradients to exert forces via the induced LS (see Section 3.3.2). This makes them diagonal in the computational

[42] A notable exception to this rule are gates that use direct dipole interactions between Rydberg states to implement Rydberg-blockade gates [136].

basis, so they commute with many sources of noise (e.g. magnetic field noise). This reduces the impact of these noise sources and allows the gates to be embedded in dynamical decoupling sequences.

We will now explain the physics behind this gate in detail. The existence and form of the geometric phase will first be derived, after which the driving mechanism via spatially varying light shifts will be explained. We will thus arrive at the general form of the LS gate unitary. This derivation follows primarily from References [83, 86, 140]. All of these references consider each ion to host only two computational states; we extend their derivations to consider the full effect on multi-level systems. A theoretical study of LS gates on multi-level systems was also published during the writing of this manuscript [141].

We only explain the physical mechanism behind the LS interaction, leaving a discussion on its computational application to Section 4.2.2. In addition, we will only consider two-ion chains.

### 3.6.1 The geometric phase

Most often, geometric phase gates excite only a single mode of motion with a periodic driving force, whose frequency $\omega_d = \omega_m + \delta$ is off-resonant from the motional frequency $\omega_m$ by a detuning $\delta$. Most of the relevant physics is thus identical to that of a quantum harmonic oscillator which is driven by a state-independent force. The Hamiltonian of this system is [142]

$$H(t) = H_0 - F\hat{x}\sin(\omega_d t - \phi) = H_0 - Fx_0\left(\hat{a} + \hat{a}^\dagger\right)\sin(\omega_d t - \phi), \tag{3.52}$$

where $F$ is the force amplitude, $H_0 = \hbar\omega_m\left(\hat{a}^\dagger\hat{a} + 1/2\right)$, $x_0 = \sqrt{\hbar/2m\omega_m}$ is the zero-point wavefunction spread (with $m$ the mass of the oscillator), $\phi$ is the initial phase of the force and $\hat{a}, \hat{a}^\dagger$ are the motional annihilation and creation operators respectively.

We can now go into the interaction picture with respect to $H_0$, so that $\hat{a} \rightarrow \hat{a}e^{i\omega_m t}$, and we invoke the RWA to neglect terms oscillating at $\omega_d + \omega_m$. Defining $\mathscr{F} \triangleq Fe^{-i\phi}$, the driving Hamiltonian is

$$H(t) = \frac{ix_0}{2}\left(\mathscr{F}\hat{a}^\dagger e^{i\delta t} - \mathscr{F}^*\hat{a}e^{-i\delta t}\right). \tag{3.53}$$

We now calculate the propagator, which is complicated by the fact that the Hamiltonian does not commute with itself at arbitrary times. To get around this, we make use of the Magnus expansion [143, 144]. This expresses the propagator as the exponential of an infinite sum $U(t) = \exp\left[\sum_{n=1}^{\infty} \mathscr{H}_n(t)\right]$ where the $\mathscr{H}_n$ are integrals of nested commutators of $H$. The first two terms are

$$\mathscr{H}_1(t) = -\frac{i}{\hbar}\int_0^t dt_1 H(t_1), \tag{3.54}$$

$$\mathscr{H}_2(t) = -\frac{1}{2\hbar^2}\int_0^t \int_0^{t_1} dt_1 dt_2 [H(t_1), H(t_2)]. \tag{3.55}$$

All further terms depend on commutators of the form $[H(t_1),[H(t_2),H(t_3)]]$. However, $[H(t_1),H(t_2)]$ is a scalar for (3.53), so the expansion up to $\mathscr{H}_2$ is exact. This also means that $\mathscr{H}_1$ and $\mathscr{H}_2$ can be exponentiated separately. We find

$$\mathscr{H}_1(t) = \hat{a}^\dagger \alpha - \hat{a}\alpha^* \tag{3.56}$$

with $\alpha = \frac{\mathscr{F}x_0}{2\hbar}\int_0^t dt' e^{i\delta t'} = \frac{\mathscr{F}x_0}{\hbar\delta} e^{i\delta t/2}\sin(\delta t/2)$. Exponentiating this yields a displacement operator $\mathscr{U}_1(t) = D(\alpha(t))$, with $\alpha(t)$ such that the vacuum state traverses loops in phase space (see Figure 3.7). The "velocity" is $\dot{\alpha} = \frac{\mathscr{F}x_0}{2\hbar} e^{i\delta t}$, whose direction at $t = 0$ depends on the phase of $\mathscr{F}$. This allows us to change the orientation of the loops, which can be useful for error suppression (see Section 8.1.3.2). We also point out that the handedness of the circular trajectory depends on the sign of $\delta$.

One key feature of these trajectories is that at times $\tau = \frac{2K\pi}{\delta}$ for integer $K$, $D(\alpha(\tau)) = \mathbb{1}$: the oscillator is returned to its initial state. The integer $K$ is the number of loops that are traversed in motional space while the force is applied. Crucially, the loop closure times are independent of the force $\mathscr{F}$[43]; thus, even when we let the force depend on the ions' state later, all loops will close simultaneously if we pulse for the correct time. This behaviour is in fact entirely classical (see Figure 3.7).

The truly quantum component of the dynamics arises from $\mathscr{H}_2$, which is not surprising since it contains all the non-commutative behaviour. A little bit of algebra following

[43] Assuming it is constant in time.

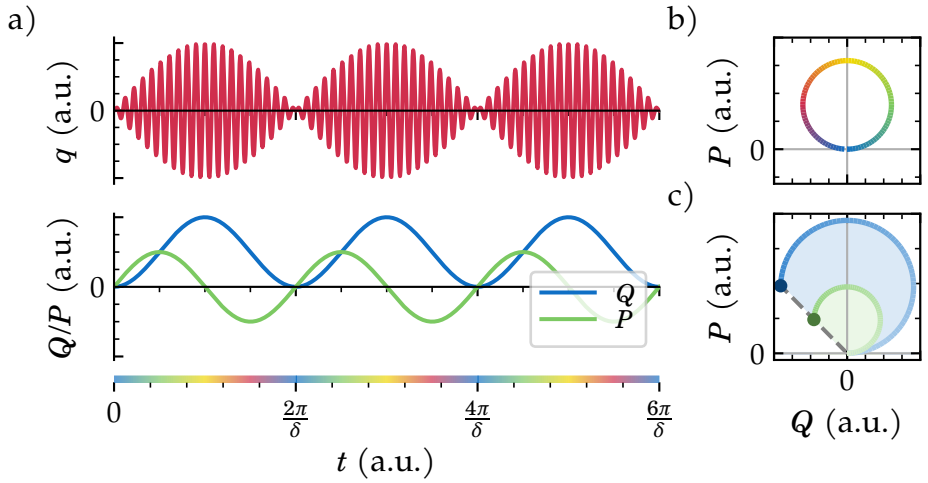



**Figure 3.7:** Most of the dynamics of a driven QHO are shared with a classical harmonic oscillator. a) Top: position $q$ of a classical harmonic oscillator (red) driven with a detuning $\delta$ from its resonance frequency. Bottom: the corresponding position $Q$ and momentum $P$ in the rotating frame, whose phase space trajectory is shown in b). The colour shows the time according to the axis in a). Phase space loops close at $\tau = \frac{2K\pi}{\delta}$, which is when the oscillator returns to its initial state momentarily. c) Driving the oscillator with different force means that different trajectories sweep out different areas, even though they will reach the origin at the same time. This will be the mechanism by which different atomic states acquire different geometric phases, proportional to the area, yet decouple together.

substitution of (3.53) into (3.55) yields[44]

$$\mathscr{H}_2(t) = i\Im\left\{\int_C \alpha^* d\alpha\right\} \tag{3.57}$$

$$= i\left(\frac{|\mathscr{F}|x_0}{2\hbar\delta}\right)^2 (\delta t - \sin\delta t) \triangleq i\Phi(t). \tag{3.58}$$

This is a scalar, so when exponentiated will simply yield $\mathscr{U}_2(t) = e^{i\Phi(t)}$. The form of Equation (3.57) clearly shows that $\Phi$ depends only on the curve $C$ traversed; in particular, if $C$ is a closed curve, we can convert the contour integral into an area integral to yield $i\Im\{\int_C \alpha^* d\alpha\} = iA/\hbar$ where $A$ is the (signed) area[45] enclosed by $C$ [86]. Thus, $\Phi$ is a geometric phase. This phase can also be seen as a direct consequence of the non-commutativity of displacement operators that are not along parallel directions, yielding [3]

$$D(\alpha)D(\beta) = D(\alpha+\beta)\exp\left(i\Im(\alpha\beta^*)\right). \tag{3.59}$$

Traversing the loop can be seen as a long sequence of such non-commuting displacements.

[44] In (3.57) we have used $\frac{d\alpha}{dt_1}dt_1 = d\alpha$.

[45] This is in the units of the canonical variables $\hat{x}$ and $\hat{p}/m\omega$, in terms of which we can write $\alpha = 1/(2x_0)(\hat{x} + i\hat{p}/m\omega)$ [86].

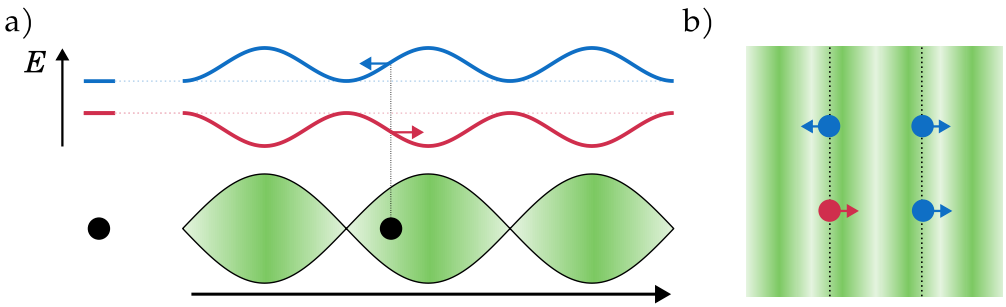



**Figure 3.8:** Sketch of the LS forces on an ion chain. a) Two atomic states which are light-shifted differently by off-resonant light (green): the blue (red) state increases (decreases) in energy in the presence of the light. If the ion is at an intensity gradient, the two states will feel different forces, denoted by the arrows, since the energy landscapes observed by each state have different gradients. As the travelling intensity wave passes over the ion (in the direction of the black arrow), the forces will change direction at a rate dictated by the speed of the intensity wave, which in turn depends on the difference frequency of the beams that set it up. b) The joint state of *both* ions determines the coupling to the motional mode, due to the direction of the forces. Two ions in different states (left) will maximally couple to the rocking mode, since the force is in the opposite direction; if they are in the same state (right) there is *no* coupling to the rocking mode, since forces are the same in magnitude and direction. Thus, the two states $|r:b\rangle$ and $|b:b\rangle$ will acquire different geometric phases if the force is near-resonant with just that mode.

The overall propagator for a driven harmonic oscillator is thus

$$U_D(t) = e^{i\Phi(t)} D(\alpha(t)). \tag{3.60}$$

Clearly, when $\alpha(t) = 0$ this only imparts the geometric phase, which is a trivial global phase when only the motion is considered. However, once we drive the motion with a force $\mathscr{F}$ that depends on the atomic state of the two ions, these phases will become relative phases on each state, leading to a two-ion coupling.

### 3.6.2 Generating the state-dependent force

#### 3.6.2.1 Intuition

To begin with, consider a single ion illuminated by a laser whose frequency is far off-resonant from an atomic transition. As shown in Section 3.3.2, this light-shifts the state energies by an amount proportional to the laser's intensity. If this has spatial structure[46], the shifted energy of the levels will depend on the ion's position, effectively setting up a potential landscape. The ion will feel a force proportional to the gradient of this potential.

This effect can be used to create a periodic driving force. As shown in Figure 3.8, a light field with a periodically varying intensity results in a periodic potential. If we were

[46]The SDF can also be set up by a field with spatially-varying polarisation.

able to move this light field over the ion at a constant speed, a force that is periodic in time would be exerted due to the changing potential gradient at the ion's location. Setting up this moving, structured light field is surprisingly straightforward[47], since it is the interference pattern set up by two non-collinear beams whose frequencies are slightly detuned from each other. Thus, the frequency (and phase) of the force can be controlled using AOMs and made to be close to the frequency of a motional mode. This allows us to excite just that mode, as in the previous section.

Crucially, the magnitude of these light shifts depends on the atomic state $|v\rangle$ (see Section 3.3.2). Thus, a different force is exerted on each state in a single ion, making the force state-dependent. However, the force that excites a mode of a *two*-ion chain must depend on the *joint* state of both ions $|v:\mu\rangle$. This is because the effective force that excites the $j^{\text{th}}$ mode depends on whether the direction of the forces on each ion align with the mode oscillations or not (Figure 3.8). Explicitly, the effective force is $\sum_i \xi_i^{(j)} \mathscr{F}_i$, where $\mathscr{F}_i$ is the force on the $i^{\text{th}}$ ion and $\xi_i^{(j)}$ is the corresponding component of the $j^{\text{th}}$ mode participation vector. This depends on both the phase and amplitude of $\mathscr{F}_i$ and thus the phase of the interference pattern at the location of the two ions.

One disadvantage of light shift gates, and geometric phase gates in general, is that the atomic and motional degrees of freedom become entangled during the gate due to the state-dependent nature of the displacements. This has two detrimental effects. Firstly, decoherence on the motional state due to various sources, which are difficult to eliminate, affects the electronic state while they are entangled. Secondly, any residual motional entanglement will lead to errors, as subsequent operations on the electronic state as well as measurements are independent of the motion. Thus, the appropriate description of the electronic state is that found by taking the partial trace over the motion, which will yield a mixed state if there is residual entanglement. This may occur due to miscalibration of pulse timing and detuning, or due to fluctuations in trap or drive parameters during the gate. We will discuss such errors in more detail in Section 5.3.

[47] At least compared to the numerous terrible ways of doing so that occurred to the author when first hearing of this.

#### 3.6.2.2 Derivation

The notation in derivations of the LS force is often cluttered, since similar quantities that act as a "drive" must be discussed: Rabi frequencies between single-ion states $|\nu\rangle$, $|\mu\rangle$ due to a single beam; two-beam LSs on a single-ion state $|\nu\rangle$; and the magnitude of the SDF force on the two-ion state $|\nu:\mu\rangle$, which is related to the two-beam LS on each ion and acts as an effective Rabi frequency. For beam $i$ and ion $j$, these will be notated as $\tilde{\Omega}^{(i)}_{\nu\epsilon,j}$, $\Delta^{(j)}_{\nu}$ and $\Omega_{\nu,\mu}$, respectively. Note that the meaning of the superscripts change between the Rabi frequency and the two-beam LS, which is done to maintain consistency in the context around where each term is used.

We begin by writing the Hamiltonian on both ions as a sum of the Hamiltonian on each ion:

$$H_T(t) = H_2(t)\otimes\mathbb{1} + \mathbb{1}\otimes H_1(t). \tag{3.61}$$

Each single-ion Hamiltonian off-resonantly couples the computational states $|\nu\rangle$ to a set of excited states $|\epsilon\rangle$[48] via two lasers, the "red" and "blue" lasers, which are very far detuned from any allowed atomic transition. Their relative detuning is $\omega^{(b)} - \omega^{(r)} = \omega_\delta$, which we assume to be close to the frequency of one of the motional modes, but far away from any transition. Furthermore, all $|\nu\rangle \leftrightarrow |\varepsilon\rangle$ are assumed to be dipole (rank-1) transitions. Then, in the interaction picture with respect to the atomic energies, each single-ion Hamiltonian is given by[49]

$$H_j = -\frac{\hbar}{2}\sum_{i,\nu,\epsilon}\tilde{\Omega}^{(i)}_{\nu\epsilon,j}e^{-i\left(\delta^{(i)}_{\nu\epsilon}t - \mathbf{k}^{(i)}\cdot\mathbf{r}_j - \phi^{(i)}_j\right)}|\epsilon\rangle\langle\nu| + h.c. \tag{3.62}$$

Here, $\tilde{\Omega}^{(i)}_{\nu\epsilon,j}$ is the Rabi frequency for the $|\nu\rangle \leftrightarrow |\epsilon\rangle$ transition due to the $i^{\text{th}}$ beam ($i \in \{r,b\}$) in the $j^{\text{th}}$ ion; $\delta^{(i)}_{\nu\epsilon} = \omega^{(i)} - \omega_{\nu\epsilon}$ is the detuning of the $i^{\text{th}}$ beam to the transition; $\mathbf{k}^{(i)}$ is the wavevector of the $i^{\text{th}}$ beam; $\mathbf{r}_j$ is the position operator of the $j^{\text{th}}$ ion; and $\phi^{(i)}_j$ is the initial phase of the $i^{\text{th}}$ beam at the position of the $j^{\text{th}}$ ion.

We can now take the James-Jerke approximation as in Section 3.3.2. This yields diagonal terms due to light shifts, and terms proportional to $|\nu\rangle\langle\nu'|$ that would drive

[48] We will assume that all the $|\epsilon\rangle$ are in the same atomic level, so that the detunings between all states are similar. However, the derivation can be easily modified to change this.

[49] The counter-rotating terms have been dropped, which would lead to a Bloch-Siegert shift. They can be easily included in the derivation and just modify the strength of the final SDF [145].

Raman transitions. Since we are assuming that $\omega_\delta$ is far away from any transition frequency, we neglect the latter. The light shift terms include single beam light shifts of the form (3.18) due to each beam. As described in Chapter 8, they can be echoed out, since they commute with the final light shift unitary, so they will be ignored for brevity. The relevant terms that generate the state-dependent force are then

$$\begin{aligned} H_j &= \hbar \sum_\nu \frac{\sum_\epsilon 2\Re\left\{\left(\tilde{\Omega}^{(b)}_{\nu\epsilon,j}\right)^* \tilde{\Omega}^{(r)}_{\nu\epsilon,j} e^{i(\omega_\delta t - \boldsymbol{\delta k}\cdot\mathbf{r}_j - \delta\phi_j)}\right\}}{4\delta_l} |\nu\rangle\langle\nu| \\ &= \hbar \sum_\nu \frac{\sum_\epsilon \left|\left(\tilde{\Omega}^{(b)}_{\nu\epsilon,j}\right)^* \tilde{\Omega}^{(r)}_{\nu\epsilon,j}\right| \cos\left(\omega_\delta t - \boldsymbol{\delta k}\cdot\mathbf{r}_j - \delta\phi_j - \tilde{\phi}_{\nu\epsilon,j}\right)}{2\delta_l} |\nu\rangle\langle\nu| \end{aligned} \quad (3.63)$$

with $\boldsymbol{\delta k} \triangleq \mathbf{k}^{(b)} - \mathbf{k}^{(r)}$, $\delta\phi_j \triangleq \phi_j^{(b)} - \phi_j^{(r)}$ and approximating $\delta^{(i)}_{\nu\epsilon} \approx \delta_l$ in the denominator, since both lasers are approximately equally detuned from all transitions. The phases[50] $\tilde{\phi}_{\nu\epsilon,j}$ appear because the Rabi frequencies are generally complex (see 3.5) so, for arbitrary beam polarisations, $\left(\tilde{\Omega}^{(b)}_{\nu\epsilon,j}\right)^* \tilde{\Omega}^{(r)}_{\nu\epsilon,j} = \left|\left(\tilde{\Omega}^{(b)}_{\nu\epsilon,j}\right)^* \tilde{\Omega}^{(r)}_{\nu\epsilon,j}\right| e^{-i\tilde{\phi}_{\nu\epsilon,j}}$. These phases generally depend on the change in $m_F$ in the $|\nu\rangle \leftrightarrow |\epsilon\rangle$ transition, so the inner sum in (3.63) contains interfering terms, which affects the amplitude and phase of each state-dependent force. The state-dependent phase shift also can affect the force amplitude via the coupling strength to the motional mode (see Equation (3.67) later). In general, since the extent of the motional wavefunction is small over a wavelength, we can write

$$\begin{aligned} H_j &= \hbar \sum_\nu \Delta^{(j)}_\nu \cos\left(\omega_\delta t - \boldsymbol{\delta k}\cdot\mathbf{r}_j - \delta\phi_j - \phi_{\nu,j}\right) |\nu\rangle\langle\nu| \\ &\approx \hbar \sum_\nu \Delta^{(j)}_\nu \left[\cos\left(\omega_\delta t - \delta\phi_j - \phi_{\nu,j}\right) + \boldsymbol{\delta k}\cdot\mathbf{r}_j \sin\left(\omega_\delta t - \delta\phi_j - \phi_{\nu,j}\right)\right] |\nu\rangle\langle\nu| \end{aligned} \quad (3.64)$$

where the two-beam LSs $\Delta^{(j)}_\nu$ and the phases $\phi_{\nu,j}$ are functions of $\tilde{\Omega}^{(b,r)}_{\nu\epsilon,j}$ and $\tilde{\phi}_{\nu\epsilon,j}$. Nonetheless, for specific beam geometries, $\left(\tilde{\Omega}^{(b)}_{\nu\epsilon,j}\right)^* \tilde{\Omega}^{(r)}_{\nu\epsilon,j} \in \mathbb{R}$ independent of $|\nu\rangle, |\epsilon\rangle$, which makes $\tilde{\phi}_{\nu\epsilon} = 0$. In particular, this occurs for counter-propagating beams whose polarisation vectors are the same at the ion[51]. In that case, $\phi_\nu = 0$ and $\Delta^{(j)}_\nu = \sum_\epsilon \left(\tilde{\Omega}^{(b)}_{\nu\epsilon,j}\right)^* \tilde{\Omega}^{(r)}_{\nu\epsilon,j}/2\delta_l$.

The term proportional to the cosine in (3.64) leads to a time-varying shift in the energy of the atomic states due to the beating intensity of the beams. This term depends

[50] The author has not come across these phases in previous derivations (see [83, 146, 147]). This is because they implicitly assume that the Rabi frequencies are real, which does not hold in general. However, in interactions between an ion and a single beam, or for specific polarisations of multiple beams, these phases have no measurable physical consequences.

[51] This can be found from Equations (3.47), (3.48) from which we obtain $\beta^{(1)}_q(\varphi+\pi, \pi-\vartheta, \gamma, \psi+\pi) = \beta^{(1)}_q(\varphi, \vartheta, \gamma, \psi)$ and the vector spherical harmonics are the same for the coupling in both beams.

on the initial phase of the two-beam beat note, which is difficult to control [144]. It is usually dealt with by ramping the beam intensity into and out of each pulse, which effectively nulls its effect by averaging over this initial phase [140]; we will thus drop it from further discussion.

The second term includes the dependence on the ion's position. We will assume that the difference wavevector $\boldsymbol{\delta k}$ is aligned with just one of the principal trap axes[52] so that $\boldsymbol{\delta k}\cdot\mathbf{r}_j = \sum_{\tilde{m}} \eta_{\tilde{m}} \xi_j^{(\tilde{m})} (\hat{a}_{\tilde{m}} + \hat{a}_{\tilde{m}}^\dagger)$ where $\xi_j^{(\tilde{m})}$ is the participation of the $j^{\text{th}}$ ion on the $\tilde{m}^{\text{th}}$ mode, $\eta_{\tilde{m}} = |\boldsymbol{\delta k}|\sqrt{\hbar/m\omega_{\tilde{m}}}$ is the Lamb-Dicke parameter for the mode, and $\hat{a}_{\tilde{m}}$, $\hat{a}_{\tilde{m}}^\dagger$ are the creation and annihilation operators for each mode. Next, we transform to the interaction picture with respect to the ion's motion and invoke the RWA, as per Section 3.6.1. We now further assume that the beam detuning is close to the oscillation frequency of just the $m^{\text{th}}$ mode, so that $\omega_\delta = \omega_m + \delta$, and all other modes are multiplied by fast-rotating terms and thus negligible. Thus, the single-ion Hamiltonians are reduced to

$$H_j = -\frac{i\hbar}{2}\sum_\nu \eta \Delta_\nu^{(j)} \xi_j \left(\hat{a}^\dagger e^{i(\delta t - \delta\phi_j - \phi_{\nu,j})} - \hat{a} e^{-i(\delta t - \delta\phi_j - \phi_{\nu,j})}\right) |\nu\rangle\langle\nu| \tag{3.65}$$

where we have dropped the label of the motional mode for brevity. Then, we can write the full two-ion Hamiltonian (3.61) as

$$H = -\frac{i\hbar\eta}{2}\sum_{\nu,\mu}\left(\Omega_{\nu,\mu} e^{i\delta t}\hat{a}^\dagger - \Omega_{\nu,\mu}^* e^{-i\delta t}\hat{a}\right)|\nu{:}\mu\rangle\langle\nu{:}\mu| \tag{3.66}$$

with the effective Rabi frequencies

$$\Omega_{\nu,\mu} \triangleq \Delta_\nu^{(2)}\xi_2 e^{-i(\delta\phi_2+\phi_{\nu,2})} + \Delta_\mu^{(1)}\xi_1 e^{-i(\delta\phi_1+\phi_{\mu,1})}. \tag{3.67}$$

Each term in the sum is of exactly the same form as Equation (3.53), with a state-dependent driving force $x_0\mathscr{F}_{\nu\mu} = -\hbar\eta\Omega_{\nu,\mu}|\nu{:}\mu\rangle\langle\nu{:}\mu|$. These forces are operator-valued, but since they all commute with each other and with the creation and annihilation operators, they can be treated as scalars. The derivation from Section 3.6.1 can then be followed exactly, yielding the full propagator for the light shift interaction[53]:

$$U_{LS}(t) = \sum_{\nu,\mu} D\left(\alpha_{\nu,\mu}(t)\right) e^{i\Phi_{\nu,\mu}(t)} |\nu{:}\mu\rangle\langle\nu{:}\mu| \tag{3.68}$$

[52] If the beams and the axes are at an angle $\theta$, the effective Lamb-Dicke parameter is simply multiplied by $\cos\theta$.

[53] Here, we have used $\prod_{\nu,\mu} e^{i\hat{O}_{\nu,\mu}\otimes|\nu:\mu\rangle\langle\nu:\mu|} = \sum_{\nu,\mu} e^{i\hat{O}_{\nu,\mu}} \otimes |\nu{:}\mu\rangle\langle\nu{:}\mu|$ for any operators $\hat{O}_{\nu,\mu}$ that commute with $|\nu{:}\mu\rangle\langle\nu{:}\mu|$.

with

$$\alpha_{\nu,\mu}(t) = -\frac{\eta\Omega_{\nu,\mu}}{\delta} e^{i\delta t/2} \sin\left(\frac{\delta t}{2}\right), \tag{3.69}$$

$$\Phi_{\nu,\mu}(t) = \frac{\eta^2|\Omega_{\nu,\mu}|^2}{4\delta^2}(\delta t - \sin(\delta t)). \tag{3.70}$$

At times $\tau_g = 2K\pi/\delta$, at which the motional loops close, this operator reduces to $U_{LS}(\tau_g) = \sum_{\nu,\mu} e^{i\Phi_{\nu,\mu}(\tau_g)} |\nu{:}\mu\rangle\langle\nu{:}\mu|$. This provides a coupling between the electronic state of the two ions, while leaving the motional state untouched. In many experimental scenarios (such as Chapter 8), it is convenient to traverse more than one motional loop during the gate, so $K > 1$. This allows for a weaker excitation of the motion, and for the implementation of dynamical decoupling protocols on the atomic and motional states [148]. We thus call $\tau_g$ the gate duration and $\tau_l = \tau_g/K$ the loop duration.

## 3.7 Summary

We have given the necessary background physics required for all intra- and inter-ion operations.

Intra-ion operations are carried out by sequences of laser pulses. The resulting state evolution was analysed taking into account frequency miscalibrations on the driving lasers for linear and cyclic connectivity graphs. Furthermore, expressions for the Rabi frequency in terms of the atomic properties of the states in the transition and the geometry of the laser that drives it are given in order to aid numerical simulations in subsequent chapters.

Inter-ion operations make use of the LS gate mechanism, which was derived from first principles for multi-level systems. The necessary physics behind the motion of ions in a Paul trap was given at the start of the chapter.

*I am not going to die on this hill.*

— Jamie Leppard, before invariably fighting to the bitter end.

# 4 Primitive Polyqubit operations

Chapter 2 described a universal gate set for qubits. Here, we explain how to implement the gates in this set in a trapped ion system. These will naturally split into intra-ion and inter-ion gates (previously intra-carrier and inter-carrier). Other necessary operations for universal quantum computation [149], such as state-preparation and readout, are also discussed.

Because these operations involve manipulating many levels within an ion, techniques previously developed for qudits can be directly applied [48, 50, 75]. The novel contribution presented here is a comprehensive computational analysis of all TSRs in a polyqubit (Section 4.1) and a proposal for efficient inter-ion gates using a light shift mechanism (Sections 4.2.2 and 4.2.3).

One natural question to pose is how many qubits to store in each ion. This is equivalent to asking how many states do we want to control. Recently, control over a 25-state qudit [26] was demonstrated, which is large enough to host the Hilbert space of 4 qubits. Nevertheless, as discussed in Section 2.4 and elsewhere [17, 48], using more than $\sim 2-3$ qubits per ion with high fidelity is likely to be infeasible, as the number of control parameters and decoherence rates increase[1]. Since our aim is to demonstrate a proof-of-principle polyqubit gate set, we restrict ourselves to just two qubits per ion.

[1] A discussion on whether suitable atomic states can be found to host more than two qubits per ion is presented in Section 6.3.

The discussions that follow focus on this case, except when the generalisation to $n$ qubits per ion is trivial.

## 4.1 Intra-ion gates

Before explaining in detail how intra-ion gates are implemented, it is worth pointing out that all operations act on a 4-dimensional space (or generally $2^n$ dimensional). This must be kept in mind even when addressing just a single qubit. For example, to implement a unitary

$$\begin{pmatrix} \alpha & \beta \\ \gamma & \delta \end{pmatrix}$$

on the MSB or LSB qubits in a 2-polyqubit, we would actually apply the following gates on the full 4-dimensional system:

$$U_{LSB} = \mathbb{1} \otimes U = \begin{pmatrix} \alpha & \beta & & \\ \gamma & \delta & & \\ & & \alpha & \beta \\ & & \gamma & \delta \end{pmatrix} \qquad U_{MSB} = U \otimes \mathbb{1} = \begin{pmatrix} \alpha & & \beta & \\ & \alpha & & \beta \\ \gamma & & \delta & \\ & \gamma & & \delta \end{pmatrix}. \tag{4.1}$$

The ensuing section then discusses how to efficiently implement such operations as well as two-qubit ones, taking into account the nuances associated with working in this large Hilbert space. At times, it will be convenient to refer to a polyqubit state $|\mathsf{q}_{(n-1)}...\mathsf{q}_1\mathsf{q}_0\rangle$ using a more qudit-like notation $|i\rangle$, where $\mathrm{bin}(i) = \mathsf{q}_{(n-1)}...\mathsf{q}_1\mathsf{q}_0$. The use-case should be clear from context.

As discussed in Section 2.3, intra-ion gates in multi-level systems (whether qudits or polyqubits) are commonly driven by sequentially driving equatorial and polar two-state rotations (TSRs). We use an analogous notation to that in Section 2.3: a TSR about the $x$-axis in the $\{|\mathsf{pq}\rangle, |\mathsf{sr}\rangle\}$ subspace is written $R^{\mathsf{pq},\mathsf{sr}}(\theta, x)$ and the two-state Pauli matrices are defined using an obvious extension of (2.21).

In trapped ion systems, these are applied by performing Rabi oscillations on transitions within the computational manifold. These can be quadrupole [25, 26, 28, 150], Raman [100] or microwave transitions [27, 52], or a combination of them [99, 151]. The following discussion is agnostic to the driving mechanism used. However, for clarity and because it was used in the experiments presented in Chapters 7 and 8, we will say that transitions are driven by a resonant quadrupole laser.

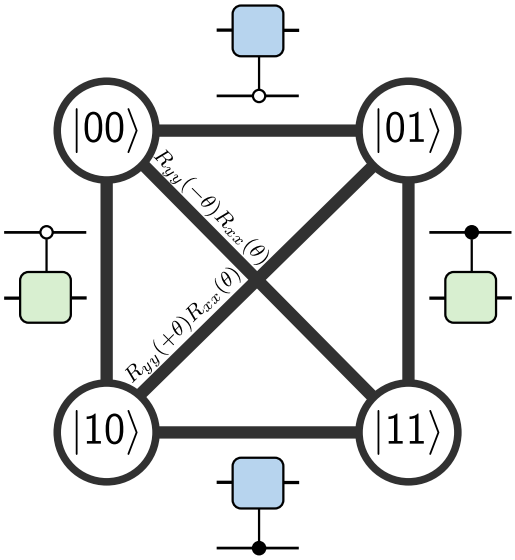



**Figure 4.1:** A sketch of the full connectivity graph of a 2-polyqubit. The family of gates implemented by a TSR on each edge is shown as a circuit diagram, or written next to the edge. To drive a single-qubit gate on the LSB (MSB) qubit, the same TSR is applied on the two horizontal (vertical) edges. The diagonal edges implement more complex two-qubit gates.

To implement a universal intra-ion gate set, one must find the sequence of pulses that applies each unitary in the gate set. This can be easily done irrespective of the number of qubits in the ion by using a Givens decomposition of the target unitary [74, 75], which is now a standard procedure in the field. However, this merely queries a black-box process that spits out an answer: greater insight, which may also influence experiment design, can be reached by analysing the action of individual TSRs.

For this, we make use of the connectivity graph (see Section 2.3) shown in Figure 4.1. This shows a fully connected graph, which describes the rare situation in which all transitions between the states can be driven. The extension to graphs with reduced connectivity will be discussed in Section 4.1.1.

Driving any single edge in the graph applies a two-qubit gate. It is easy to see that driving any edge on the perimeter of the graph applies an equatorial unitary on one qubit controlled on the state of the other. With reference to the arrangement in Figure 4.1, the two vertical (horizontal) edges apply gates controlled on the states $|0\rangle$ and $|1\rangle$ of the LSB (MSB) qubits. For example, applying a unitary $R_\phi^{10,11}(\theta)$ on the $\{|10\rangle, |11\rangle\}$ subspace drives the LSB qubit *only if* the MSB qubit is in state $|1\rangle$. Thus, we've applied a controlled-$R(\theta, \phi)$

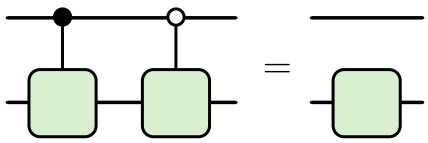


**Figure 4.2:** Decomposition of a single-qubit gate in terms of two controlled unitaries, which are each applied with a single TSR.

operation. In particular, a $\pi$-pulse $R_x^{10,11}(\pi)$ implements a `CNOT` gate with a *single* laser pulse (up to a diagonal gate, which we'll explain how to account for in Section 4.1.2).

The remaining diagonal edges are more exotic, implementing products of Ising gates $R_{\phi_0\phi_1}(\theta) = \exp\left[-i\theta/2\,\sigma_{\phi_0} \otimes \sigma_{\phi_1}\right]$ [69]. Driving the $\{|01\rangle, |10\rangle\}$ edge applies $R_{yy}(\theta/2)R_{xx}(\theta/2)$ unitaries, which includes gates like the $\texttt{iSWAP} = R_{yy}(-\pi/2)R_{xx}(-\pi/2)$ [69, 152]. Driving the $\{|00\rangle, |11\rangle\}$ edge applies $R_{yy}(-\theta/2)R_{xx}(\theta/2)$ gates.

#### 4.1.0.1 Intra-ion gates in $n$-polyqubits

Thus, we see that, in contrast to monoqubit systems, the native gates in 2-polyqubits are two-qubit. Single-qubit gates require two pulses and are constructed using the circuit in Figure 4.2. A single-qubit gate is equal to two controlled gates that apply the same unitary on the target qubit, controlled on the two states of the control qubit. The intuition is that applying a single-qubit gate means that the target unitary must be applied for *any* value of the spectator qubits. Each controlled unitary is a TSR. Since each TSR acts on orthogonal subspaces, they commute.

The generalisation to an $n$-polyqubit is straightforward. For convenience, let us embed the connectivity graph in $n$-dimensional Cartesian space by placing the nodes at the coordinates corresponding to the state's bit-string $(|q_{n-1}...q_1q_0\rangle \to (q_{n-1}, ..., q_1, q_0))$. Driving any single edge applies an $n$-qubit gate. While the gates implemented by diagonals of the resulting hypercube are difficult to interpret, the exterior edges implement conditional gates just like in the 2-polyqubit case. These edges connect two points that share $n-1$ bits; the control qubits are those that correspond to the shared bit-string, while the target qubit is the remaining one. Applying a single-qubit gate thus involves applying sequential controlled unitaries, conditioned on all possible control bit-strings. This requires $2^{(n-1)}$ TSRs, which again shows that storing many qubits per ion results in exponentially increasing complexity [48].

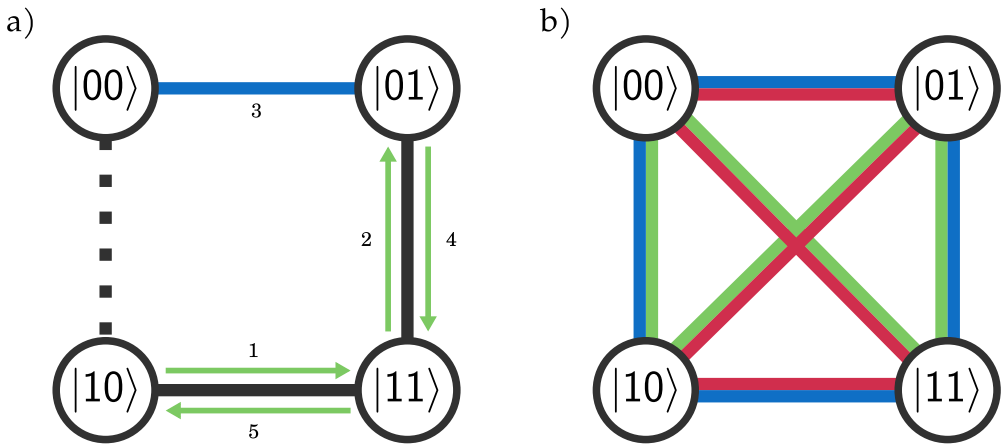



**Figure 4.3:** a) The protocol for synthesising a TSR on a forbidden transition (the dashed edge). Only solid edges are allowed. We transfer the state $|10\rangle$ to $|01\rangle$ through $\pi$ pulses on allowed edges (green inner arrows) before applying the desired TSR (blue). The transfer pulses are then undone (green outer arrows). The order of each operation is marked next to it. b) If the transitions between the four atomic states that form the polyqubit form a closed loop, three possible connectivity graphs can be constructed by choosing which atomic state hosts which computational basis state. Two of these (red and green) include the diagonal edges instead of one pair of exterior edges. In experiments, we choose the graph that does not include any diagonals (blue).

### 4.1.1 The impact of connectivity

As discussed in Section 2.3, a fully connected connectivity graph like the one in Figure 4.1 is not required for applying a universal gate set. The only requirement is that the graph is minimally connected, so that there exists at least one path connecting any two nodes [74, 75]. Reduced connectivity often arises due to selection rules, which forbid transitions from being driven.

If the edge connecting states $|i\rangle$ and $|j\rangle$ is forbidden (where $i, j$ are the decimal representations of some polyqubit bit-strings), we can synthesise a TSR between them (Figure 4.3). We start by swapping one of the states (say, $|j\rangle$) with another state $|k\rangle$ that is connected to $|i\rangle$. This swap can always be carried out by a sequence of $\pi$-pulses on allowed edges[2]. Then, we can apply the desired TSR on the $\{|i\rangle, |k\rangle\}$ subspace and swap back.

The number of pulses in the swap operation depends heavily on the connectivity graph and which TSR we wish to synthesise [48]. The worst-case scenario is that of the two extremal points in a linearly connected graph, which are separated by $2^n - 1$ edges in an $n$-polyqubit graph. Thus, a total of $2 \times (2^n - 2)$ pulses are needed to move one of the

[2]These rotations will induce unwanted phases as in (2.27), but these can be dealt with by applying virtual diagonal gates (Section 4.1.2)

states there and back, and the remaining edge implements the TSR. However, if more than one forbidden TSR is to be driven, the number of transfer pulses could be reduced by not returning to the original arrangement after each TSR. We also point out that, while the specific shape of the graph is determined by the physics of the drive mechanism used, how the computational states are distributed over the nodes is up to the experimenter. This can also greatly affect the number of transfer pulses required in each operation [48]. The design of optimal transfer pulse routines is left for future work.

In the experiments of later chapters, the connectivity graph is such that the transitions form a closed loop. This gives us the option to either include or exclude the diagonal edges, depending on where we place the polyqubit states (Figure 4.3). From our previous analysis, we can see that excluding the diagonals favours single-qubit gates at the expense of the more exotic $R_{yy}(\pm\theta)R_{xx}(\theta)$ gates. Single-qubit gates are crucial for a universal gate set and are more common in quantum circuits, so we choose the graph that includes all transitions on the perimeter. Synthesising the missing TSRs only requires 2 transfer pulses.

### 4.1.2 Diagonal gates

So far, we have only considered gates that are equatorial, in the sense that all of them involve $\sigma_\phi$; what about diagonal gates, involving $\sigma_z$?

In monoqubit devices, $z$ rotations can be implemented *virtually*, without applying any pulses [125]. This is because a $z$ rotation can equivalently be viewed as either a polar rotation of the qubit vector with respect to a fixed Bloch sphere, or a polar rotation of the sphere relative to the fixed qubit. The latter interpretation simply means that the angle $\phi$ of all equatorial rotations following the *virtual* $z$ rotation are shifted by this angle [125], which is clearly displayed by (3.13). That is, we can effectively commute $z$ rotations through equatorial rotations until a measurement is made (which is agnostic to the phase[3]). The axis angle of equatorial rotations is set by the optical phase of the laser at the ion[4], which in turn can be controlled by the phase of an RF tone via an

[3]These virtual $z$ rotations also must be commuted through two-body interactions. This can be done by choosing a diagonal two-body gate like the CZ, which naturally commutes with all $z$ rotations, or by ensuring that the drive tones for intra-ion and inter-ion gates are phase-locked.

[4]Relative to the optical phase at the start of the experiment, which is random.

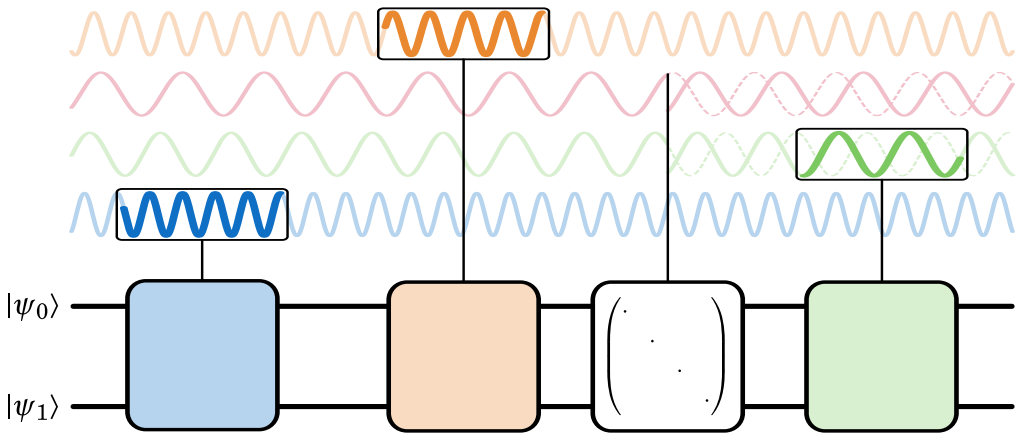



**Figure 4.4:** A sketch of the RF tones used to implement a short circuit consisting of three TSRs (coloured squares) and one diagonal matrix (white square). Each sinusoid represents the RF that modulates a laser to drive one of the transition in an encoding (the specific transitions involved are irrelevant for this example). The individual RF tones are only output by the DDS for the duration of the TSR (represented by a darker colour on the sinusoid) but the phase is constantly increasing even if no RF is generated (light coloured sinusoids). The diagonal matrix is implemented by shifting the phase of some tones, which shifts the phase of subsequent gates. This is done while the output is off to prevent phase glitches.

acousto-optic (AOM) or electro-optic (EOM) modulator[5]. This RF tone is generated by a direct digital synthesiser (DDS) or arbitrary waveform generator (AWG), so its phase can be controlled in software.

The situation in polyqubits is more complicated, because monoqubits only have a single control field – there is only one transition to drive. In polyqubits, we can conceptually consider each transition to be driven by independent drive tones, even though the same *hardware* (the same laser and AOM, for example) is used for all of them. We can do this by associating each transition to the RF tone that modulates the laser when driving the transition, as the RF phase is imparted onto the laser. It is the phase of these independent RF tones that sets the rotation angle of TSRs.

This allows us to generalise virtual monoqubit $z$ rotations to high-dimensional systems[6] (Figure 4.4). Say that we wish to virtually apply a diagonal gate $D = \mathrm{diag}\{e^{\phi_0}, e^{\phi_1}, ...\}$, after which we must apply a two-state-rotation $R_\phi^{i,j}(\theta)$ (where $i, j$ are again the decimal representation of some polyqubit bit-string). We now factor $D$ into two operators. One of these, $D_\perp$, acts non-trivially only *outside* the $\{|i\rangle, |j\rangle\}$ subspace, and thus commutes with $R_\phi^{i,j}(\theta)$. The other operator can always be written as $D_\parallel R_z^{i,j}(\Delta\phi)$, with $\Delta\phi = \phi_j - \phi_i$.

[5] If microwaves are used, their phase can be changed directly.
[6] These are often referred to as virtual SNAP gates [35]

The diagonal operator $D_\parallel$ is 1 in all entries on the main diagonal except for the $(i,i)$ and $(j,j)$ entries, which are $e^{i\bar{\phi}}$, with $\bar{\phi} = (\phi_i + \phi_j)/2$. This is just a global phase in the $\{|i\rangle, |j\rangle\}$ subspace and thus commutes with $R_\phi^{i,j}(\theta)$. The two-state $z$ rotation $R_z^{i,j}(\Delta\phi)$ can be dealt with using an obvious generalisation of (3.13) to TSRs. Thus, we have:

$$R_\phi^{i,j}(\theta)D = R_\phi^{i,j}(\theta)D_\perp D_\parallel R_z^{i,j}(\Delta\phi) = D_\perp D_\parallel R_z^{i,j}(\Delta\phi)R_{\phi-\Delta\phi}^{i,j}(\theta) = DR_{\phi-\Delta\phi}^{i,j}(\theta). \tag{4.2}$$

The same operation is then carried out with all subsequent TSRs in the circuit. This is a more powerful technique in polyqubits than in monoqubits. It means that all intra-ion diagonal gates can be executed with *no* laser pulses. This includes two-qubit gates like the `CZ`, making these the natural candidate for inclusion in our universal gate set. Furthermore, the unwanted "global" phases introduced by TSRs (see (2.27)) can also be immediately removed. Finally, other unwanted $z$ rotations, such as those arising from off-resonant light shifts (see Section 3.3.2), can be undone if the unitary they apply is known.

## 4.2 Inter-ion gates

It is clear that, while intra-ion gates enable multi-qubit gates, these alone are not sufficient for a universal gate set: we also need *inter-ion* gates that act on qubits in different ions. These are akin to two-qubit gates in monoqubit systems, which typically are at least an order of magnitude lower fidelity and slower than intra-ion gates. This is also observed in qudit systems [25]. Thus, it is crucial to make sure that they can be efficiently implemented, to minimise the number of expensive operations required.

There are various two-ion coupling mechanisms available to ion trappers for implementing inter-ion gates, which include the Cirac-Zoller [87], Mølmer-Sørensen (MS) [85, 139] or the Light Shift (LS) [86] mechanism[7]. They use the quantised motion of the ion chain to mediate the coupling between the atomic state of different ions, since they typically don't couple directly[8]. All three mechanisms have been applied to multi-level systems, in [39, 100], [25, 150] and [153] respectively.

[7] In monoqubits, all three mechanisms result in gates which are equivalent up to local operations [69]. However, in multi-level systems, these mechanisms produce different interactions. Thus, having access to all three mechanisms in a polyqubit or qudit system can greatly increase the available gate set, which is a unique advantage of multi-level systems.

[8] Rydberg-blockade gates have been proposed as two-atom polyqubit gates in neutral atom architectures [151] and could thus also be used in ions. However, since their error rates in ion traps are currently much higher than in other mechanisms, we will omit them from this discussion.

Except in certain situations, the two-ion Hamiltonians implemented by these mechanisms act non-trivially on all four qubits in the ions. Thus, the unitaries that they generate are generally multi-qubit gates, rather than two-qubit ones. Access to such exotic gates is often valuable, since they are useful in many algorithms [154, 155] and expensive to synthesise from two-qubit gates [42]. However, pure two-qubit gates are ubiquitous in algorithms and optimisers. Thus, it is crucial to make pure two-qubit inter-ion gates part of our polyqubit toolbox.

In order for a two-ion unitary to act non-trivially on only two out of four qubits, it must act as the identity on the remaining spectator qubits – we say that the unitary is *partitioned*. This naturally occurs if the unitary is generated by a Hamiltonian which itself is partitioned. In monoqubit systems, this partitioning occurs natively, since the qubits are located in spatially separated ions and can be individually addressed. However, the Hamiltonians of the three mechanisms mentioned previously are not generally partitioned for polyqubit systems. There are generally two methods to generate partitioned unitaries from non-partitioned Hamiltonians, although both come at a cost.

Firstly, if certain interactions are applied for very particular durations, the resulting unitary may be partitioned, even though the generating Hamiltonian is not[9]. However, the required durations are generally long, leading to large error rates. In addition, the errors induced by timing miscalibrations necessarily involve more qubits than those targeted, a feature not present in partitioned Hamiltonians. Furthermore, because the partitioning only occurs for certain durations, only particular unitaries can be generated, limiting the expressivity of these protocols.

Secondly, a partitioned two-ion unitary could also be synthesised by an appropriate sequence of multi-qubit two-ion and single-ion unitaries. Such schemes also suffer from a larger prevalence of multi-qubit errors, and an increase in the number of errors due to the many pulses required.

Most previous polyqubit two-qubit gate proposals make use of the MS interaction, whose Hamiltonian is not partitioned. Both tactics for generating two-qubit unitaries

[9]This is exactly what occurs in geometric phase gates. The underlying Hamiltonian is not partitioned between the atomic and motional degrees of freedom, but the duration of the interaction is chosen so that the resulting unitary *is*: it only acts on the atomic states.

from this have been explored: Reference [50] shows that, for particular (long) gate durations, the MS interaction can generate a two-qubit CZ gate; References [48] and [52] give decompositions for various two-qubit gates in terms of multiple MS pulses. Alternatively, Reference [47] proposes a modification of the MS Hamiltonian that *is* partitioned, although with significant experimental overhead. These proposals are briefly reviewed in Section 4.2.1.

In Section 4.2.2, a novel scheme for two-qubit intra-ion polyqubit gates based on the LS mechanism is presented. We show that, if the light shifts imparted on each of the atomic states that encode the polyqubit take a specific form, the resulting Hamiltonian is partitioned. As such, we can generate arbitrary two-qubit Ising $R_{zz}$ interactions optimally, in the sense that the gate durations are the same as for the equivalent monoqubit gates. In Chapter 6, we show that states which exhibit these light shifts can be readily found in ion species with hyperfine structure, meaning that this interaction can be implemented with no technical overhead, other than taking care of laser polarisations. Furthermore, it will be shown that the resulting gate is also equivalent to certain multi-qubit gates up to local operations.

The LS gate mechanism has been used to demonstrate maximal qudit entanglement [153]. Furthermore, in the writing of this manuscript, the author became aware of a related proposal using microwave gradients in Reference [52]. There they considered the nuclear and electronic spin as the two qubits, rather than encoding them across an arbitrary four-level system. Furthermore, their scheme does not produce a partitioned Hamiltonian. To the author's knowledge, this is the first proposal for applying a laser-based LS mechanism on polyqubits, as well as the first proposal that implements a partitioned Hamiltonian without significant technical overhead.

Because these interactions depend heavily on the atomic states used to encode the polyqubit, in the following discussion, we will often refer to the atomic states $|v\rangle$ that encode the polyqubit states $|\mathtt{pq}\rangle$.

### 4.2.1 Review of Mølmer-Sørensen decompositions

For brevity, the physical interaction behind this mechanism will not be explained here; the interested reader is referred to [144, 156].

The interaction works by shining two beams (a *bichromatic tone*), whose frequency is equally detuned by $\delta$ from the red and blue motional sidebands of a transition. This couples the electronic state of the two ions via the corresponding motional mode addressed. If the transition couples the states $\{|v\rangle, |\mu\rangle\}$ in both the MSB and LSB ions[10], the Hamiltonian implemented is (neglecting the motional phase [147, 156]):

$$H_{MS}^{v,\mu:v,\mu}(t) = i\frac{\hbar\eta\Omega}{2}\left(\sigma_{\phi_{\mathsf{MSB}}}^{v,\mu}\otimes\mathbb{1} + \mathbb{1}\otimes\sigma_{\phi_{\mathsf{LSB}}}^{v,\mu}\right)\left(\hat{a}e^{i\delta t} - \hat{a}^\dagger e^{-i\delta t}\right) \tag{4.3}$$

where $\Omega$ is the Rabi frequency, $\eta$ is the Lamb-Dicke parameter of the addressed mode, $\hat{a}$ is the annihilation operator of that mode and $\phi_{\mathsf{MSB}}$, $\phi_{\mathsf{LSB}}$ are related to the laser phases on the MSB and LSB ions. Regardless of how the polyqubit states are arranged over the atomic states, this Hamiltonian cannot partition. This is because the terms containing $\sigma_{\phi_{\mathsf{MSB}}}^{v,\mu}$ and $\sigma_{\phi_{\mathsf{LSB}}}^{v,\mu}$ drive a TSR, but as discussed in Section 4.1, these implement two-qubit gates, rather than a single-qubit gate.

Analogously to light-shift gates as discussed in Section 3.6, if the gate detuning $\delta$ and gate time $\tau_g$ are chosen such that $\delta = 2K\pi/\tau_g$ for $K \in \mathbb{Z}$, the motional and atomic states disentangle, and the unitary affects only the atomic state. In this case, the resulting unitary is, up to single-ion diagonal gates [25]:

$$\begin{aligned} MS^{v,\mu:v,\mu}(\Phi) &= \exp\left(-i\frac{\Phi}{2}\sigma_{\phi_{\mathsf{MSB}}}^{v,\mu}\otimes\sigma_{\phi_{\mathsf{LSB}}}^{v,\mu}\right) \\ &= \cos\left(\frac{\Phi}{2}\right)\mathbb{1}^{v,\mu}\otimes\mathbb{1}^{v,\mu} - i\sin\left(\frac{\Phi}{2}\right)\sigma_{\phi_{\mathsf{MSB}}}^{v,\mu}\otimes\sigma_{\phi_{\mathsf{LSB}}}^{v,\mu} + \tilde{\mathbb{1}}^{\alpha,\beta}\otimes\tilde{\mathbb{1}}^{\alpha,\beta}. \end{aligned} \tag{4.4}$$

This can be interpreted as a regular Ising $R_{xx}(\Phi)$ interaction, but only acting on the subspace spanned by $\{|v:v\rangle, |v:\mu\rangle, |\mu:v\rangle, |\mu:\mu\rangle\}$[11]. This is the entire computational manifold in two-level systems, but clearly not in multi-level systems. The angle $\Phi = \eta^2\Omega^2\tau_g^2/(4\pi K)$ is the geometric phase [139, 140] acquired in the gate. A maximally entangling monoqubit

[10] MS interactions can still be driven if different states are addressed in each ion [157], although this is not necessary: by surrounding the gate with appropriate TSRs, MS gates between any pair of states can be synthesised even if only one transition can be addressed.

[11] We note that, even if only one transition can be addressed, effective MS gates between any pair of qudit states in the two ions can be synthesised by mapping qudit states before and after the gate. This is analogous to implementing TSRs on forbidden transitions.

gate locally equivalent to a CNOT or CZ gate is achieved by setting $\Phi = \pi/2$ [139]. Gate error typically increases linearly with geometric phase [37].

Because the Hamiltonian (4.3) is not partitioned, the unitary (4.4) is generally a four-qubit gate on 2-polyqubits. As discussed previously, true two-qubit gates can be synthesised by applying sequences of MS gates and single-ion TSRs, or by acquiring particular values of the geometric phase $\Phi$.

**Sequences of MS pulses** A CNOT gate decomposition using two MS gates and a total geometric phase of $\Phi = 2\pi$ as well as intra-ion gates is given in [48]. This reference also shows how to implement inter-ion gates between a 2-polyqubit and a monoqubit using sequences of a few MS gates. In addition, a decomposition for an Ising $R_{xx}$ gate was proposed in [52], which uses the same geometric phase as a monoqubit $R_{xx}$ gate. However, the author was unable to replicate the theoretical results presented in that work.

**Acquiring specific geometric phases** Reference [50] points out that the unitary applied by a single pulse with $\Phi = 2\pi$ is identical to a CZ gate. This can be seen from equation (4.4) using $|\text{bin}(\nu)\rangle = |01\rangle, |\text{bin}(\mu)\rangle = |11\rangle$: the term $\mathbb{1}^{\nu,\mu} \otimes \mathbb{1}^{\nu,\mu}$ acquires a phase of -1, thus flipping the phase of all states $|\text{p1}:\text{q1}\rangle$. This is exactly a CZ gate with two spectators. Furthermore, by using an additional auxiliary state, this same mechanism results in three- and four-qubit CCZ and CCCZ gates. However, the decomposition of the two-, three- and four-qubit gates all use four times the geometric phase of a regular two-qubit monoqubit gate. Thus, all decompositions are likely to be higher error than monoqubit gates, which is problematic for the two-qubit gates. However, the scheme for the CCZ and CCCZ gates is favourable over the monoqubit equivalents, which require 5 MS gates with total $\Phi = 7\pi/4$ and 11 MS gates[12] respectively [42].

An alternative proposal was put forth in Reference [47], which modifies the MS mechanism to generate a Hamiltonian that *does* partition and thus generates an Ising unitary. To do so, two pairs of bichromatic tones must be simultaneously applied, instead of one. This brings with it significant technical overhead, as exquisite control over the amplitude of four beams is required to perform this with low error.

[12] Required geometric phases were not reported.

### 4.2.2 Inter-ion two-qubit light shift gates

We now turn to inter-ion two-qubit gates using the light shift mechanism. The physics behind this was explained in Section 3.6, where it was found that the Hamiltonian is given by

$$H_{LS}(t) = i\frac{\hbar\eta}{2}\sum_{\nu,\mu}\Omega_{\nu,\mu}\left|\nu:\mu\right\rangle\left\langle\nu:\mu\right|\left(\hat{a}e^{i\delta t}-\hat{a}^{\dagger}e^{-i\delta t}\right). \tag{4.5}$$

The effective Rabi frequencies are as per Equation (3.67) and depend on the two-beam light shift $\Delta_{\nu}^{(\mathsf{MSB/LSB})}$ experienced by each atomic state in the MSB and LSB ion, as well as the mode participation vector $\boldsymbol{\xi} = (\xi_{\mathsf{MSB}}, \xi_{\mathsf{LSB}})$. In the experiments in Chapter 8 we use a two-ion radial rocking mode, for which $\boldsymbol{\xi} = 1/\sqrt{2}(1,-1)$. We also assume that the beam directions and polarisation are chosen to null all the phases in the effective Rabi frequencies, as described in Section 3.6.2. We assume that the atomic states $|\nu\rangle$ used to encode the polyqubit are the same in both ions – though we do *not* assume that the assignment of the polyqubit states over the atomic states is necessarily the same. In addition, we assume that the two-beam light-shifts on the same atomic state in each ion are the same; that is, $\Delta_{\nu}^{(\mathsf{MSB})} = \Delta_{\nu}^{(\mathsf{LSB})} \triangleq \Delta_{\nu}$. This is the case if the intensity of the two beams at each ion is the same[13]. All in all, we have:

$$\Omega_{\nu,\mu} = \frac{1}{\sqrt{2}}(\Delta_{\nu} - \Delta_{\mu}) \tag{4.6}$$

As before, in order to correctly apply the gate, the gate detuning $\delta$ and duration $\tau_g$ must be chosen to disentangle the electronic state from the motion, for which we must have $\delta = 2K\pi/\tau_g$. Then, the gate unitary is:

$$U_{LS}(\tau) = \sum_{\nu,\mu} e^{-i\Phi_{\nu,\mu}}\left|\nu:\mu\right\rangle\left\langle\nu:\mu\right| \quad , \quad \Phi_{\nu,\mu} = \frac{\eta^2\Omega_{\nu,\mu}^2\tau_g^2}{4K\pi} \tag{4.7}$$

If we chose any arbitrary atomic states for the computation, there would be no particular pattern to the effective Rabi frequencies $\Omega_{\nu,\mu}$. As such, the Hamiltonian (4.5) will not be partitioned. However, we can ask the following question: is there a set of light shifts $\Delta_{\nu}$ on the atomic states (a *light shift structure*) such that the resulting Hamiltonian does partition in the desired way?[14]

[13] An imbalance in illumination in the monoqubit case results in the acquisition of single-qubit phases, which can be echoed out. The qudit/polyqubit case is more complex and will be discussed in Section 5.3.4.

[14] This idea of using a specific light shift structure that generates a target unitary was first introduced in [153]. Here, this is adapted for use across two 2-polyqubits.

#### 4.2.2.1 Monoqubit LS gate

Before discussing the full polyqubit unitary, it is useful to first derive the gate behaviour in monoqubits, since we will replicate this in polyqubits. The evolution of the target qubits under this gate is an $R_{zz}(\Phi)$ gate, which is

$$\begin{aligned} |00\rangle &\rightarrow |00\rangle, \\ |01\rangle &\rightarrow e^{-i\Phi}|01\rangle, \\ |10\rangle &\rightarrow e^{-i\Phi}|10\rangle, \\ |11\rangle &\rightarrow |11\rangle, \end{aligned} \tag{4.8}$$

up to a global phase $e^{-i\Phi/2}$.

We will now see how this is generated from the Hamiltonian (4.5) in the qubit case. If the atomic states which encode the $|0\rangle$ $|1\rangle$ states in each ion are the same, the two computational states will always observe light shifts of the form $\Delta_{0,1} = \mp\Delta$[15]. The effective Rabi frequencies for each two-ion state are $\Omega_{0:0} = \Omega_{1:1} = 0$ and $\Omega_{1:0} = -\Omega_{0:1} = \sqrt{2}\Delta$. Substituting these into Equation (4.5), we obtain the monoqubit LS Hamiltonian:

$$H_{LS}^{(Mono)}(t) = i\frac{\hbar\Delta\eta}{\sqrt{2}}\left(|1:0\rangle\langle 1:0| - |0:1\rangle\langle 0:1|\right)\left(\hat{a}e^{i\delta t} - \hat{a}^{\dagger}e^{-i\delta t}\right). \tag{4.9}$$

The evolution of the states (choosing the detuning to disentangle the electronic and motion at the gate time $\tau_g$) is[16]

$$\begin{aligned} |0:0\rangle &\rightarrow |0:0\rangle, \\ |0:1\rangle &\rightarrow e^{i\frac{\eta^2\Delta^2\tau_g^2}{4K\pi}}|0:1\rangle, \\ |1:0\rangle &\rightarrow e^{i\frac{\eta^2\Delta^2\tau_g^2}{4K\pi}}|1:0\rangle, \\ |1:1\rangle &\rightarrow |1:1\rangle. \end{aligned} \tag{4.10}$$

This coincides with (4.8) with

$$\Phi = -\frac{\eta^2\Delta^2\tau^2}{4K\pi}. \tag{4.11}$$

Just as in the MS gate case, the rotation angle $\Phi$ is the geometric phase. Setting $\Phi = -\pi/2$, we obtain a gate $R_{zz}(-\pi/2)$, which can generate a Bell state from the $|0:0\rangle$ state, alongside single-qubit gates [69, 158].

[15] There may be a common light shift component $\Delta_c$, which shifts the mean energy equally. This cancels when using a radial rocking mode, and only results in single-ion Z rotations when using a radial CoM mode, which can be echoed out (see Section 8.1.3.1).

[16] The sign of the geometric phase depends on the detuning, see Section 3.6.2.

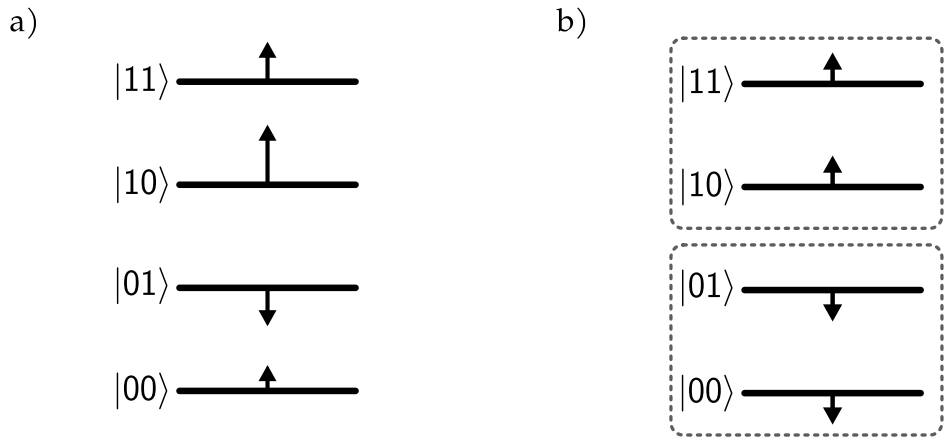



**Figure 4.5:** Two-beam light shifts induced on a 2-polyqubit for different choices of atomic states (it is assumed that the second ion in a 2-ion interaction has the same encoding). The magnitude and sign of the shift is indicated by the length and direction of each arrow, respectively. a) Shifts induced on the polyqubit basis states when four arbitrary atomic states are chosen to encode them. Because there is no particular structure to the shifts, the Hamiltonian will not be partitioned. However, if the atomic states (and laser polarisation) are chosen such that the light shifts have the structure shown in b), a partitioned Hamiltonian can be implemented. Note that the light shift on each basis state does not depend on the LSB qubit (rightmost in each ket). If the states in both ions observe these light shifts, the unitary generated is an $R_{zz}$ Ising gate on the MSB qubits.

In multi-level systems, different tensor product states $|v{:}\mu\rangle$ may acquire different geometric phases, as can be seen from Equation (4.7). Thus, there is generally no *one* geometric phase that can be defined.

#### 4.2.2.2 Polyqubit LS gate between MSB qubits

We will now aim to find a light shift structure that partitions the Hamiltonian (4.5). We will find that this generates the unitary which evolves the MSB qubits in both ions as per (4.10) and acts as the identity on the LSB qubits.

To do so, we need the evolution of each state $|\mathsf{qr}{:}\mathsf{st}\rangle$, or equivalently, the effective Rabi frequencies $\Omega_{\mathsf{qr:st}}$, to be independent of the states $\mathsf{r},\mathsf{t}$ of the LSB qubit. This will clearly be the case if the single-ion light shifts $\Delta_{\mathsf{qr}}$ are themselves independent of the LSB qubit, so that $\Delta_{00} = \Delta_{01} = -\Delta$ and $\Delta_{10} = \Delta_{11} = +\Delta$. Thus, the atomic states that encode the polyqubit must feel "pairwise" light shifts, as in Figure 4.5. In this case, the Hamiltonian is given by:

$$H_{LS}(t) = i\frac{\hbar\eta\Delta}{\sqrt{2}}(|1{:}0\rangle\langle 1{:}0|_{\mathsf{MSB}} - |0{:}1\rangle\langle 0{:}1|_{\mathsf{MSB}})(\mathbb{1}_{\mathsf{LSB}}\otimes\mathbb{1}_{\mathsf{LSB}})\left(\hat{a}e^{i\delta t} - \hat{a}^\dagger e^{-i\delta t}\right). \tag{4.12}$$

This Hamiltonian is clearly partitioned. Furthermore, the action on the MSB qubits across the two ions coincides exactly with the monoqubit Hamiltonian (4.9). This means the

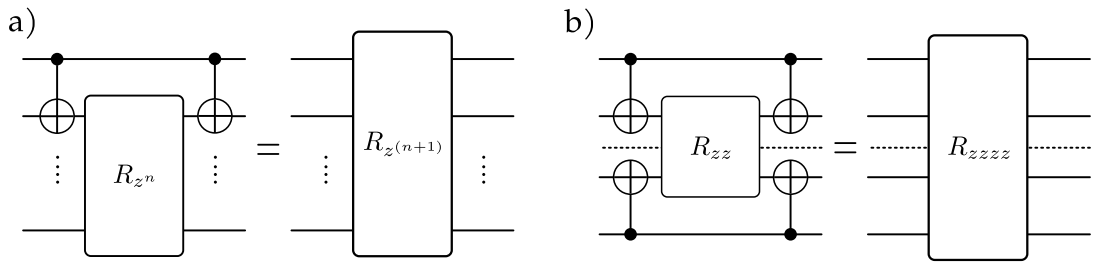



**Figure 4.6:** Circuits that make use of the identities (4.13). a) Surrounding an $R_{z^{\otimes n}}(\theta)$ gate with two CNOT gates synthesises an $R_{z^{\otimes(n+1)}}(\theta)$ (or an $R_{z^{\otimes(n-1)}}(\theta)$ one, by using the fact that the CNOT is its own inverse to surround the rightmost circuit in CNOTs). b) Example circuit showing how intra-ion CNOT gates can convert a two-qubit $R_{zz}(\theta)$ (in this case between the MSB qubit in the top ion and the LSB qubit in the bottom ion) into a four-qubit $R_{zzzz}(\theta)$ gate.

evolution of the states will be exactly as per Equations (4.10), with the replacement $|\mathsf{p{:}q}\rangle \to |\mathsf{p{:}q}\rangle_{\mathsf{MSB}} \otimes |\mathsf{r{:}s}\rangle_{\mathsf{LSB}}$ independent of the state of the LSB qubits $|\mathsf{r{:}s}\rangle_{\mathsf{LSB}}$.

We point out that the geometric phase $\Phi$ is acquired at the same rate as for monoqubits without needing any additional beams. Indeed, the gate time required to implement an $R_{zz}(-\pi/2)$ gate on the MSB qubits, and thus generate a Bell state, is exactly the same as for the monoqubit case. This is in contrast with the Mølmer-Sørensen implementations of Section 4.2.1, which either quadrupled the gate duration, or doubled the number of laser beams required. Instead, the LS mechanism relies on the existence of states which exhibit the light shift structure of Figure 4.5; we will see in Chapter 6 that these states can be found in ions with hyperfine structure.

#### 4.2.2.3 The Sleepy Gates

The fact that this scheme produces an $R_{zz}$ interaction between the MSB qubits in each ion arises not only from the existence of atomic states with particular light shifts, but also from how the logical polyqubit states are encoded over them. For example, if we swapped states $|01\rangle \leftrightarrow |10\rangle$ in Figure 4.5, then the light shifts would now only depend on the LSB qubit not the MSB one. Thus, the roles of the LSB and MSB qubits in (4.12) would swap, so the target of the gate would now be the LSB qubits. We can effectively change the polyqubit encoding over the atomic states on the fly by swapping pairs of states before and after the gate operation using TSRs.

Computationally, these $\pi$-pulse TSRs are equivalent to intra-ion CNOT gates[17] applied

[17]Any extra phases that are introduced by the TSRs will commute with the LS gate, and thus can be cancelled by applying the inverse rotation before and after the gate.

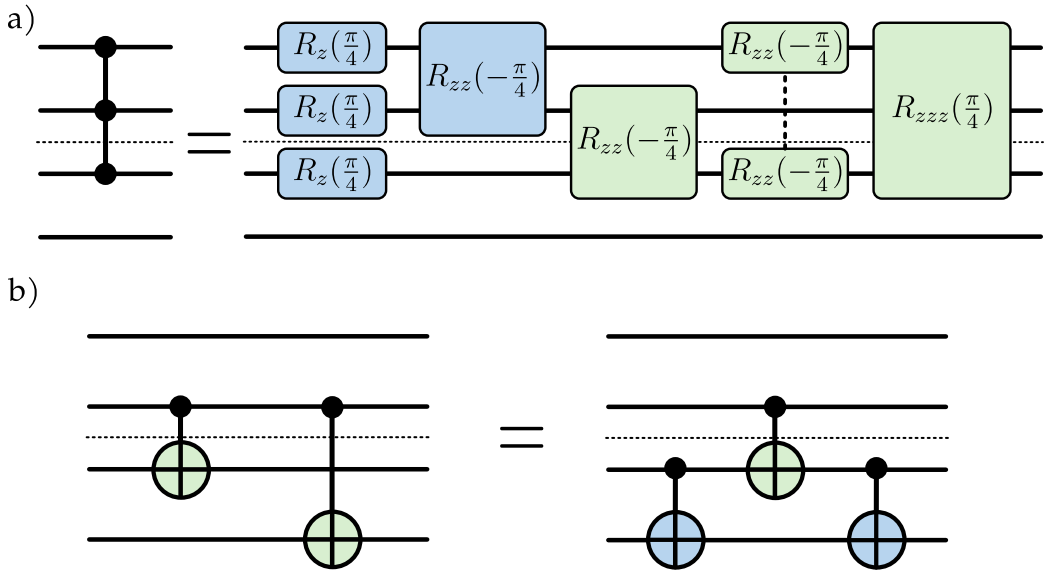



**Figure 4.7:** Decomposition of some useful gates. Inter-ion gates are shaded green, while intra-ion gates are shaded blue. a) Decomposition for a CCZ gate, requiring only three inter-ion gates with a total geometric phase of $3\pi/4$. b) Decomposition for two sequential CNOT gates (which is equal to a CXX gate), which can be done using a single inter-ion gate equivalent to an $R_{zz}(-\pi/2)$ gate.

before and after the LS interaction (Figure 4.6a). We can thus make use of the following Pauli identities [46] (where the subscripts 0, 1 are used to indicate which qubit is the control and target of the CNOT gates)

$$\begin{aligned} \mathtt{C_0NOT_1}\left(\mathbb{1}_0 \otimes \sigma_{z,1}\right)\mathtt{C_0NOT_1} &= \sigma_{z,0} \otimes \sigma_{z,1}, \\ \mathtt{C_1NOT_0}\left(\mathbb{1}_0 \otimes \sigma_{z,1}\right)\mathtt{C_1NOT_0} &= \mathbb{1}_0 \otimes \sigma_{z,1}. \end{aligned} \tag{4.13}$$

With these, we can construct circuits like those in Figure 4.6b, which turn an $R_{z^{\otimes n}}$ gate into an $R_{z^{\otimes(n\pm1)}}$ one using only intra-ion CNOT gates. Thus, all two-ion $R_{zz}$, $R_{zzz}$ and $R_{zzzz}$ gates, which we affectionately refer to as the Sleepy Gates, are locally equivalent in 2-polyqubit systems! Figure 4.6 gives an explicit construction of an $R_{zzzz}$ gate from a single inter-ion $R_{zz}$ gate, which can generate a four qubit GHZ state $\frac{1}{\sqrt{2}}(|00{:}00\rangle + |11{:}11\rangle)$.

#### 4.2.2.4 Other multi-qubit gates

We can use the previous gates to simplify decompositions of more complex gates. A decomposition for a three-qubit CCZ gate is shown in Figure 4.7. This requires three equal LS gates with a total geometric phase of $\Phi = 3\pi/4$. A similar decomposition for a CCCZ gate requires 9 pulses with a total geometric phase of $9\pi/8$; we will show a more efficient decomposition later. For comparison, the best monoqubit CCZ decomposition [42] uses 5

LS gates with a total geometric phase of $\Phi = 7\pi/4$. Previous polyqubit proposals using MS gates require just one pulse, but with a total geometric phase of $\Phi = 2\pi$ [50].

In addition, a decomposition for a pair of `CNOT` gates conditioned on the same qubit (equivalent to a `CXX` gate) is shown in Figure 4.7. This requires only one two-ion gate instead of two, as required in monoqubits. Such gates can be used to perform $XX$ or $ZZ$ measurements on the two qubits in the ion, which are useful for syndrome measurements in error correction.

We also point out that the scheme above can be used to drive $R_{z^{\otimes n}}$ gates between polyqubits hosting different, and arbitrary, numbers of qubits, as long as the atomic states in each ion can be split into two halves that each see the same light-shift. This is the natural extension of the light shift structure in Figure 4.5. Finding these states in the structure of typical ions is unlikely for large $n$. However, gates between a 2-polyqubit and a monoqubit can be implemented with this method. This is particularly useful, as they enable QND measurements of individual qubits in a polyqubit, as described in Section 4.4.

### 4.2.3 General inter-ion LS gates

#### 4.2.3.1 Decomposition of a diagonal gate into generalised rotations

We now turn to a mathematical formalism for understanding the action of a general LS gate (4.7), when the light shifts on each state in each ion are allowed to take any arbitrary value. Indeed, this unitary implements *some* diagonal two-ion gate, but it is generally difficult to interpret its computational "meaning" and find its relation to standard gates; these are the problems we aim to alleviate. The procedure is also rather general: it can be used to rewrite any $d$-dimensional diagonal unitary matrix $U \in \mathcal{DU}_d$ as a product of simpler diagonal gates, making its action easier to interpret.

First, note that due to the unitarity constraint, the entries along the diagonal of $U$ are complex numbers of unit modulus,$U_{ii} = e^{-i\phi_i\sqrt{d}/2}$ (with a normalisation factor chosen for convenience). As such, we can associate a real $d$-dimensional vector $\mathbf{u} \in \mathbb{R}^d$ to every such

$U$[18], whose components are proportional to the argument of each diagonal element:

$$U = \text{diag}\left\{e^{-i\frac{\phi_0\sqrt{d}}{2}}, e^{-i\frac{\phi_1\sqrt{d}}{2}}, ...\right\} \rightleftharpoons \mathbf{u} = \begin{pmatrix}\phi_0\\ \phi_1\\ \vdots\end{pmatrix}. \tag{4.14}$$

As a concrete example, a single-qubit $Z$ rotation $R_z(\theta) = \begin{pmatrix}e^{-i\theta/2} & 0\\ 0 & e^{i\theta/2}\end{pmatrix}$ has a corresponding vector of $\frac{\theta}{\sqrt{2}}(1,-1)^T$.

Because all elements of $\mathscr{DU}_d$ commute, matrix multiplication $UV$ and scalar exponentiation $U^\alpha$ correspond to vector addition $\mathbf{u}+\mathbf{v}$ and scalar multiplication $\alpha\mathbf{u}$. We can thus construct a basis $\{\mathbf{e}_0, \mathbf{e}_1, ...\}$ (which we also choose to be orthonormal for convenience) and write $\mathbf{u} = \sum_{i=0}^{d-1} c_i \mathbf{e}_i$ for $c_i \in \mathbb{R}$. This allows us to write $U$ as a product of the diagonal matrices associated with the basis vectors:

$$U = e^{-i\frac{\sqrt{d}}{2}\text{diag}\{\mathbf{u}\}} = \prod_{j=0}^{d-1} \exp\left(-ic_j\frac{\sqrt{d}}{2}\text{diag}\{\mathbf{e}_j\}\right). \tag{4.15}$$

We point out that the components $c_j = \mathbf{u}\cdot\mathbf{e}_j$ are proportional to an effective rotation angle $\theta_j$ of a gate $\exp\left(-i\frac{\theta_j}{2}\ \text{diag}\{\mathbf{e}_j\}\right)$.

We can now choose the basis $\{\mathbf{e}_j\}$ that allows us to express $U$ as a product of computationally meaningful gates using the above decomposition. For polyqubits, a convenient choice is to decompose the gate as a product of what we call the $n$-qubit generalised $Z$ rotations $R_z^{\otimes\mathbf{b}}(\theta_\mathbf{b})$,

$$U = \prod_{\mathbf{b}\in B} R_z^{\otimes\mathbf{b}}(\theta_\mathbf{b}) = \exp\left[-\frac{i}{2}\sum_{\mathbf{b}\in B}\theta_\mathbf{b}\Sigma_z^{\otimes\mathbf{b}}\right] \tag{4.16}$$

where we define the generalised Pauli rotations as

$$R_\alpha^{\otimes\mathbf{b}}(\theta) = \exp\left(-i\frac{\theta}{2}\Sigma_\alpha^{\otimes\mathbf{b}}\right), \quad \Sigma_\alpha^{\otimes\mathbf{b}} \triangleq \bigotimes_j \sigma_\alpha^{b_j}, \quad \alpha\in\{x,y,z\} \tag{4.17}$$

with $\mathbf{b} = (b_{(n-1)}, b_{(n-2)}, ..., b_1, b_0)$ a string of $n$ bits. The generalised Pauli operators $\Sigma_\alpha^{\otimes\mathbf{b}}$ apply $\sigma_\alpha$ on all qubits $j$ for which $b_j = 1$, so the generalised Pauli rotations $R_\alpha^{\otimes\mathbf{b}}(\theta)$ are gates that act on all these qubits.

[18] More formally, the Lie algebra $\mathfrak{du}_d$ of the Lie group $\mathscr{DU}_d$ is the vector space of purely real $d$-dimensional diagonal matrices (using the physicist's definition from Section 3.4 in [159]). Then, we can identify $\mathbf{u}$ as vectors whose components are the diagonal entries of matrices in $\mathfrak{du}_d$, times a factor of $-\frac{2}{\sqrt{d}}$ (with our choice of normalisation factor). The Hilbert-Schmidt inner product $[A,B] = \text{Tr}(A^\dagger, B)$ [46] for $A, B \in \mathfrak{du}_d$ then corresponds to the usual dot product $\mathbf{u}\cdot\mathbf{v}$ for the corresponding $\mathbf{u},\mathbf{v}\in\mathbb{R}^d$ associated to the diagonal matrices $U = \exp(A)$, $V = \exp(B)$.

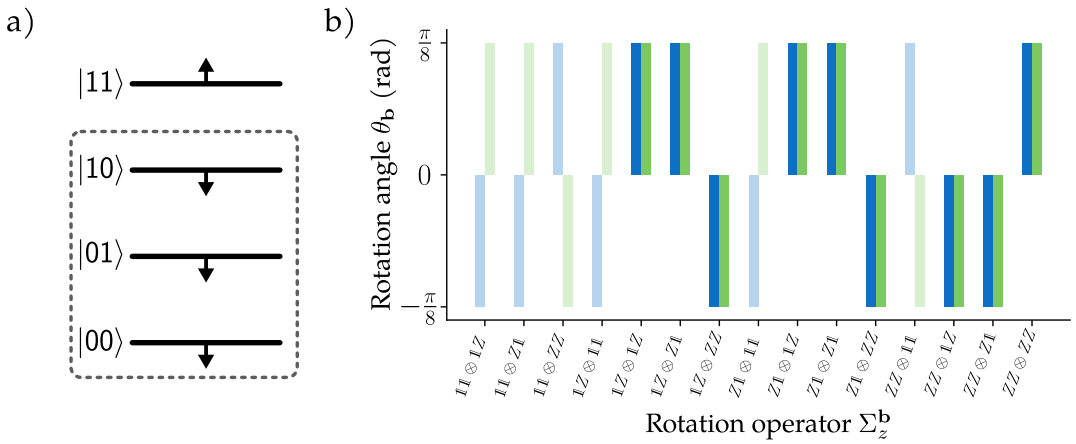



**Figure 4.8:** a) Light shift structure for implementing a CCCZ gate in a single pulse. The $\{|00\rangle, |01\rangle, |10\rangle\}$ states all observe the same light shift $\Delta$ relative to the state $|11\rangle$. b) Decomposition of two diagonal inter-ion gates as a product of generalised $z$ rotations $U = \prod_{\mathbf{b}} R_z^{\otimes \mathbf{b}}(\theta_{\mathbf{b}})$ (see text) for all 4-bit strings $\mathbf{b}$ – excluding $\mathbf{b} = (0,0,0,0)$, which generates a global phase. The (signed) height of the bars indicates the rotation angles $\theta_{\mathbf{b}}$. Rotations corresponding to intra-ion gates are in lighter colours. The bars in blue show the decomposition for a CCCZ gate, while the ones in green show the decomposition of the unitary $V(\pi)$ obtained when the light-shift interaction with the structure shown in a) is applied for a duration $\tau_g$ such that $\eta^2\Delta^2\tau_g^2/(2K\pi) = \pi$ (as usual, choosing the gate detuning such that $\delta\tau_g = 2K\pi$). The two unitaries differ only in intra-ion gates, which can be shown to be equal to $\sqrt{\mathrm{CZ}}^\dagger \otimes \sqrt{\mathrm{CZ}}^\dagger$. If the light-shift interaction were driven for a different duration, the height of the green bars would be scaled by a constant factor.

The choice of orthonormal basis $\mathbf{e_b}$ over which the components of $\mathbf{u}$ are exactly the rotation angles[19] $\theta_{\mathbf{b}} = \mathbf{u} \cdot \mathbf{e_b}$ is that for which $\mathrm{diag}\{e_{\mathbf{b}}\} = \frac{1}{\sqrt{2^n}}\Sigma_z^{\otimes \mathbf{b}}$. These vectors have components[20] $(\mathbf{e_b})_i = \frac{(-1)^{\mathbf{b}\cdot\mathbf{i}}}{\sqrt{2^n}}$ where $\mathbf{i}$ is the ($n$-bit) binary representation of $i$.

#### 4.2.3.2 Decomposition of arbitrary LS gates

With this tool, we can now decompose the general light shift gate (4.7). For two $n$-polyqubits, the components of the corresponding vector are $u_{\nu n+\mu} = -\frac{2}{\sqrt{2^{2n}}}\Phi_{\nu,\mu}$. The generalised rotation angles are then explicitly given by

$$\theta_{\mathbf{b}} = -\frac{2}{2^{2n}}\sum_{\nu\mu}(-1)^{\mathbf{b}\cdot(\boldsymbol{\nu},\boldsymbol{\mu})}\Phi_{\nu,\mu} \tag{4.18}$$

where $(\boldsymbol{\nu},\boldsymbol{\mu})$ is the concatenation of the bit-string representations of $\nu, \mu$.

Furthermore, we can explore what other two-ion gates are implemented when the polyqubits are encoded in atomic states that exhibit a different light shift structure to that in Figure 4.5. These can be accessed by temporarily transferring the polyqubit

[19] The normalisation factors in (4.14) were chosen to simplify this equation.

[20] We point out that the matrix formed by stacking these basis vectors in an obvious order is the tensor product of $n$ Hadamards[46].

states to auxiliary atomic states for the duration of the two-ion gate. For example, a CCCZ gate can be implemented in a single pulse. This can be done using the light shift structure shown in Figure 4.8: three of the atomic states observe the same light shift $\Delta$ relative to the fourth state[21]. This results in a gate $V_{LS}(\Phi)$ with $\Phi$ given by (4.11) like the previous scheme, although it is picked up by different tensor product states than the ones in the Sleepy Gates. The rotation angles of the decomposition of $V_{LS}(\pi)$ into generalised $z$ rotations are shown in Figure 4.8, alongside the same decomposition for a CCCZ gate. These gates are equal up to intra-ion gates. Indeed, it can be shown that $V_{LS}(\pi) = \mathtt{CCCZ} \cdot \sqrt{\mathtt{CZ}}^\dagger \otimes \sqrt{\mathtt{CZ}}^\dagger$ where the $\sqrt{\mathtt{CZ}}^\dagger = \mathrm{diag}\{1,1,1,-i\}$ gates are intra-ion. Thus, we can apply a CCCZ gate in a single pulse, and requiring only half of the geometric phase required in the MS decompositions of Section 4.2.1.

#### 4.2.3.3 Expressivity of LS gates

We can clearly see that the ability to change the light shift structure gives us access to a much larger family of diagonal gates that can be implemented with a single laser pulse of some duration. This begs the following question: for any arbitrary diagonal $U$, does there exist a light shift structure across the two ions that implements it in just one pulse?

We can see that the answer is "no" purely from a degrees-of-freedom argument. If we lift the restriction that the same set of states is used on each ion, the effective "degrees of freedom" that we can "modify" are the light shifts on the states on the two ions $\Delta_v^{(\mathrm{MSB})}, \Delta_v^{(\mathrm{LSB})}$, plus the gate duration $\tau$. Across two $n$-polyqubits, there are clearly $2 \times 2^n$ such light shifts. However, some of these light shifts include global shifts, which generate the identity; thus, the number of non-trivial degrees of freedom is $N_{DoF} < 2^{n+1} + 1$, where we include the gate duration as an extra degree of freedom.

We can also count the number of possible generalised $z$ rotations that correspond to inter-ion gates. It is clear that there is a total of $2^{2n} - 1$ non-trivial rotations, as that is the number of possible bit-strings of length $2n$, minus the bit-string corresponding to the identity. We can also see that the number of intra-ion rotations must be $2^n - 1$ on each ion, for the same reason. Thus, the total number of two-ion generalised rotations is $N_{Rot} = (2^{2n} - 1) - 2(2^n - 1) = (2^n - 1)^2$.

[21] This is the same structure as used in [153].

Because of the inequality in $N_{DoF}$, we see that $N_{Rot} > N_{DoF}$ whenever there is more than one qubit per ion. Thus, there are always some two-polyqubit gates which cannot be implemented with a single light shift interaction. A full analysis of which gates *can* be implemented is left as future work.

## 4.3 State preparation

When using alkali earth ions to store quantum information, the computational manifold is chosen from states in the ground $S_{1/2}$ and metastable $D_{5/2}$ levels, as discussed in Sections 6.1.3 and 6.2.3. State preparation then involves fiducially transferring all the population to a state in the manifold. This is exactly the same requirement as for monoqubit state preparation, so existing techniques can be used without modification [47, 48].

Usually, population is transferred to a state in the $S_{1/2}$ level, which is either already in the computational manifold, or from which population can be coherently mapped to some computational state. This can be done via optical pumping through dipole-allowed transitions to a $P_{1/2}$ or $P_{3/2}$ level[22] [160], or with techniques involving coherent operations [161].

The specific scheme used in the experiments of later chapters is discussed in detail in [18] and makes use of the $\Delta m_F = 0 \nleftrightarrow 0$ if $\Delta F = 0$ dipole selection rule in species with hyperfine structure. It pumps population to the $|F = F = 2, m = m_F = 0\rangle$ state in the $S_{1/2}$ level.

## 4.4 Readout

While reading out a monoqubit reveals 1 bit of information, reading out a polyqubit reveals $n$ bits; it is reasonable to expect that the increase in information gained comes at the cost of a more complex readout operation.

In typical trapped-ion setups, this is the case, but only insofar as it requires multiple fluorescence detection (FD) operations instead of just one. These distinguish whether the electronic population is in the $S_{1/2}$ or $D_{5/2}$ level, by illuminating the ion with a beam resonant with the $S_{1/2} \leftrightarrow P_{1/2}$ transition[23], which is very short-lived. Population in the

[22] Since decay to the $D_{3/2}$ or $D_{5/2}$ levels can occur from the $P_{1/2}$ or $P_{3/2}$ levels, repumping lasers resonant with the relevant $D \leftrightarrow P$ transitions are necessary.

[23] Since decay to the $D_{3/2}$ level can also occur, leading to population trapping, a repumping laser resonant with the $D_{3/2} \leftrightarrow P_{1/2}$ transition is also necessary.

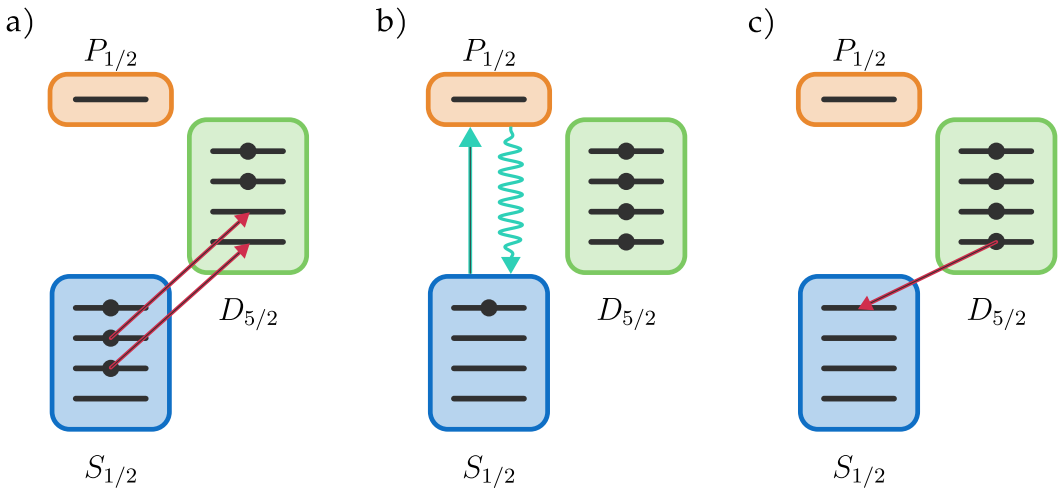



**Figure 4.9:** Scheme for reading out a multi-level system (which can be a qudit or a polyqubit). a) We set up the measurement, for which all states except one are hidden in the $D_{5/2}$ level. b) An FD operation is performed on the cycling $S_{1/2} \leftrightarrow P_{1/2}$ transition. If there is population in the $S_{1/2}$ level, this will scatter light which can be detected with a camera, resulting in a bright outcome; this projects the population onto a mixed state over the states in the $S_{1/2}$ level. Otherwise, no light is scattered, so the outcome is dark; the population is coherently projected onto the states in the $D_{5/2}$ level. c) The next state to be measured is prepared by transferring it to the $S_{1/2}$ level. Steps b) and c) are repeated for all states except one.

$S_{1/2}$ level will be excited, emitting a photon upon each decay. This happens many times, producing an observable signal (a bright measurement) *only* if the population was in the $S_{1/2}$ level; otherwise, the ion is dark. After a bright measurement, the population is scattered over the states in the $S_{1/2}$ level, while after a dark measurement, the populations and coherences of the states in the $D_{5/2}$ level are kept intact[24].

The scheme for reading out an $n$-polyqubit is shown in Figure 4.9 [75]. We start with just one state in the $S_{1/2}$ level, with all other states hidden in the $D_{5/2}$ level. Depending on how the states are arranged in the ion, mapping pulses with a quadrupole laser may be required. Then, an FD operation is carried out. If the outcome is dark, then we know that the polyqubit was not in that state and its population has been projected onto the remaining states in the $D_{5/2}$ level. Then, another state is mapped down, and another FD operation is carried out. This is repeated with each of the remaining states. The measurement outcome is the *first* state for which a bright outcome is observed [25]. If we reached the last state with no previous bright outcomes, then we know that the

[24] Up to the normalisation factor changing after the measurement.

[25] Since the bright measurement scatters population incoherently across the $S_{1/2}$ level, subsequent FD operations are most likely bright. However, the transfer pulses that would map the next computational state down will map the population in the target state in the $S_{1/2}$ level, so the outcome could be dark.

population is entirely in this state, so this is the readout outcome. Thus, a full readout operation requires $2^n - 1$ FD operations[26].

In an $n$-polyqubit, this yields the populations in each of the $2^n$ computational basis states of the $n$ qubits, $P_{|q_{(n-1)},\ldots,q_1,q_0\rangle}$. To find the probability that a particular qubit is found in state $|0\rangle$, we simply sum the populations of all the states in which the qubit is in that state. For example, the probability that the LSB qubit in a 2-polyqubit is in $|0\rangle$ is simply $P_{\mathsf{LSB}}(|0\rangle) = P_{|00\rangle} + P_{|10\rangle}$.

#### 4.4.0.1 Reading out a subset of qubits

This procedure reads out all $n$ qubits in the ion simultaneously, collapsing their state. To the author's knowledge, no scheme has been proposed for natively reading out a subset of qubits in the ion. Indeed, reading out a single qubit in a 2-polyqubit (say, the MSB one) involves a measurement with the following projectors [46]:

$$E_{|0\rangle} = |0\rangle\langle 0|_{\mathsf{MSB}} \otimes \mathbb{1}_{\mathsf{LSB}} \qquad E_{|1\rangle} = |1\rangle\langle 1|_{\mathsf{MSB}} \otimes \mathbb{1}_{\mathsf{LSB}} \tag{4.19}$$

This generalises to $n$-polyqubits in an obvious way. The key point is that, whatever the outcome of the measurement on the MSB qubit, the LSB qubit must survive. We can *almost* do this via FDs. Indeed, if we were to place the two states with the MSB qubit in $|1\rangle$ (the states $|10\rangle$, $|11\rangle$) in the $S_{1/2}$ level, then a single FD distinguishes the MSB $|0\rangle$ and $|1\rangle$ states with dark or bright outcome, respectively. This implements $E_{|0\rangle}$, since a dark outcome projects the polyqubit into the $D_{5/2}$ manifold, maintaining the superposition of $|00\rangle$, $|01\rangle$. However, a bright outcome destroys the superposition in the $S_{1/2}$ level and generates a maximally mixed state, which does not correspond to $E_{|1\rangle}$. To avoid this, we would need the FD operation to maintain coherence even after a bright outcome, which, due to the stochastic nature of the decay from the $P_{3/2}$ level, is difficult to engineer. Whether the necessary coherent bright measurement could be implemented by other means is an open question.

However, we can perform a quantum non-demolition measurement [3, 162] on any subset of qubits in a single $n$-polyqubit using a single auxiliary $(n-1)$-polyqubit. As shown

[26] If the control system can react to a measurement outcome in real time, the readout operation can be terminated after a bright outcome, so on average only $(2^n - 1)/2$ FDs are needed.

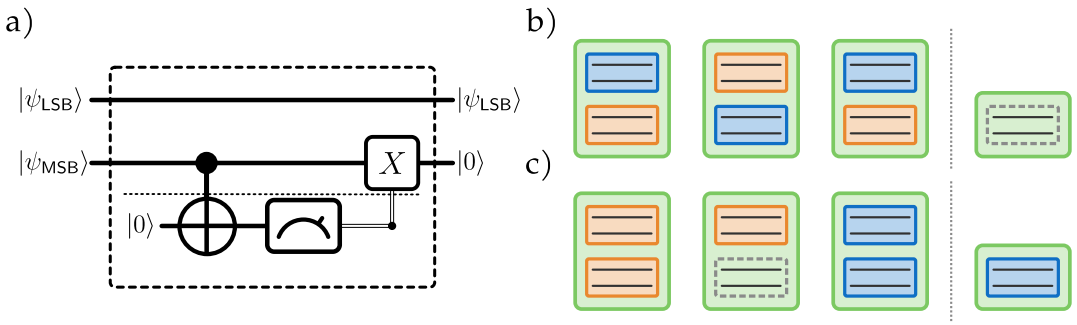



**Figure 4.10:** a) Circuit to implement a QND measurement on the MSB qubit using an auxiliary monoqubit. The MSB qubit can be reset coherently by the operation. In the general case of measuring any set of qubits in an $n$-polyqubit, the auxiliary ion would host an $(n-1)$-polyqubit and up to $n-1$ `CNOT` gates would be necessary. b), c) Scheme to measure any subset of qubits in a register of 2-polyqubits, using just one auxiliary ion (the generalisation to $n$-polyqubits is straightforward). We wish to read out all blue qubits and keep all orange qubits intact. In the arrangement in b), this cannot be done, because the qubits to be read out and kept are all in the same ion. However, using a sequence of `SWAP` gates, we can always rearrange the qubits such that no ion contains both a qubit to be read out and one to be kept, shown in c). This makes use of one auxiliary ion, which is to the right of the dotted line, and contains a single qubit initialised to $|0\rangle$.

in Figure 4.10 for 2-polyqubits, this is implemented by applying `CNOT` gates between the data qubits to be measured and those in the auxiliary ion, which is subsequently read out. Using classical feedback, the measured qubits can be reset coherently.

Furthermore, by rearranging qubits in the register using `SWAP` gates, this single auxiliary $(n-1)$-polyqubit can be used to perform any partial measurement of the register, assuming that individual ions can be measured [163]. The scheme is also shown in Figure 4.10 for 2-polyqubits; the extension to $n$-polyqubits is straightforward.

### 4.4.1 Heralded SPAM protocol for leakage detection

By the addition of up to three more FD steps, we can extend the previous state-preparation procedure to allow for the detection of leakage errors. These involve population exiting the computational manifold, due to bad state preparation or off-resonant excitation, for example. They account for the vast majority of state-preparation and measurement (SPAM) errors[27]. This is particularly relevant for multi-level systems, because the many transitions that need to be driven could each excite multiple spectator transitions.

[27] There may be errors misclassifying a fluorescing ion as dark and vice-versa. These errors depend on the device used to collect photons and are typically at least an order of magnitude lower than any other error source [18].

A SPAM protocol was proposed in [18] that can herald whether a leakage error occurred within a shot, allowing it to be rejected and effectively nulling the effect of these errors. This has resulted in the highest SPAM fidelity reported to date. We naturally extend this protocol to multi-level systems. The protocol separately allows one to herald leakage errors in state-preparation and leakages into both the $S_{1/2}$ and $D_{5/2}$ levels during the computation or measurement. This scheme is closely linked to erasure conversion error correction protocols [164–167].

State preparation errors are detected as follows. We start by preparing one of the states in the $S_{1/2}$ level, for example by optical pumping. After this, the population in the state that has been prepared is mapped to some state in the $D_{5/2}$ level. The optical pumping may have been imperfect, so some population may remain in the $S_{1/2}$ level. An FD is carried out to check this: if it measures dark, all the population has been projected to the single state in the $D_{5/2}$ level. The population in this state can then be transferred to the desired initial computational state, if needed, and the ensuing algorithm proceeds. However, a bright outcome heralds a leakage, so the shot is discarded.

Then, the readout procedure is able to detect leakages in either the $S_{1/2}$ or $D_{5/2}$ levels that occurred during the calculation. It starts by transferring the entire computational manifold to states in the $D_{5/2}$ level[28]. Then, we check for leaked population in the $S_{1/2}$ level by performing an FD. A bright outcome heralds a leakage error, in which case the shot is discarded. After this, we carry out the readout procedure described above. Finally, we can check for leakages in the $D_{5/2}$ level by transferring the final computational state (which otherwise would only be implicitly measured) to the $S_{1/2}$ level and performing an FD. Because now *all* computational states have been measured, at least *one* of them must have yielded a bright outcome. If not, we know that population has leaked in the metastable level. So we discard shots in which all readout FDs yield dark outcomes.

## 4.5 Summary

This chapter has discussed the computational protocols that will be used in the rest of this thesis to compute using 2-polyqubits. This includes a universal gate set of intra-

[28] Unless it already was there for the computation

and inter-ion gates, as well as SPAM operations.

The intra-ion gate set proposed in Section 4.1 was chosen to form a minimal universal gate set, but was optimised for computation using polyqubits rather than generic qudits. This was done by identifying which transitions in the connectivity graph are the most important when implementing single-qubit gates and harnessing virtual rotations to implement two-qubit gates. The inter-ion gate mechanism proposed in Section 4.2 (the Sleepy Gates) takes advantage of atomic states with a particular LS structure to natively implement gates between only two qubits, while leaving the remaining spectator qubits in the ions untouched. Simple circuits for constructing gates on more than two qubits were identified, and the computational effect of gates in which the LS structure of the states is arbitrary was analysed. Finally, protocols to prepare (Section 4.3) and read out (Section 4.4) a polyqubit while simultaneously detecting leakage errors were discussed.

*Nadlingus, Fixify!*

— Ana Sotirova, invoking a powerful force for when things get *really* interesting – in a bad way.

# 5 Sources of Error

This chapter discusses and presents expressions for many sources of experimental error in multi-level systems. These will be used in the experimental analyses of Chapters 7 and 8. The work presented in this chapter is based on the author's contribution to Reference [48] and considerably extends it.

Most errors in multi-level systems are a direct extension of the corresponding monoqubit errors, which are comprehensively studied. The generalisation of many error sources can be found in existing works [25, 26, 75], but some of the analyses presented here, such as those on two-ion gates, have not been deeply explored in the literature to the author's knowledge. The author is also not aware of a detailed treatment of detuning errors in multi-level systems, which are found to have particularly unique properties.

The chapter begins by briefly summarising the necessary theory to analyse the effect of Hamiltonians with stochastic classical terms. This is then applied to intra- and inter-ion gates. Where meaningful comparison is possible, the relative effect of an error on monoqubit and multi-level systems is discussed. Overall, it is found that, as expected, the impact of intra-ion errors is larger on multi-level systems. In many cases, this is not fundamental, but rather due to the likelihood of finding states that are insensitive to noise sources decreasing. Contrastingly, we find that the errors in inter-ion gates are in many cases identical. Furthermore, the computational impact of some errors on a polyqubit, rather than an abstract multi-level system, is discussed. Finally, an attempt has been made

to express the errors in a form that lends itself to numerical simulations, in particular giving explicit expressions for the Lindblad operators where possible. The author hopes that this will enable easy integration into existing simulation frameworks.

## 5.1 Background theory

### 5.1.1 Quantum processes

Some errors in a quantum computer can be described by unitary processes: instead of applying a target unitary $U_T$, a unitary $U_E$ is applied instead, which is the same every shot. The error can then be described by how similar the unitary $U_T^\dagger U_E$ is to the identity. Such processes can only capture a small set of errors, since unitary transformations can never map an initially pure density matrix to a mixed one.

A much broader class of errors can be described by *quantum processes*, which are mappings $\Lambda$ between density matrices, $\rho \to \Lambda(\rho)$ [46]. Such maps are very general and allow for the description of processes such as interactions with an environment in an unknown state [3], or those in which the Hamiltonian contains a classical stochastic variable [168]. These maps are subject to the requirements that all density matrices they output must be physical, which imposes two conditions [46]:

- **Complete positivity (CP)** For all input density matrices, the output density matrix must be positive-semidefinite, so the probabilities of measuring any observable are non-negative.

- **Trace Preserving (TP)** For all input density matrices, the trace of the output density matrix (which is the sum of the probabilities of measuring each observable) must[1] be 1.

Maps that obey both conditions are termed CPTP.

There are many equivalent ways to express quantum processes [170], each of which is useful in its own context. Those used throughout this thesis will be introduced as and when needed. For now, we introduce just one of these representations, the Kraus

[1] There do exist relevant, non-TP processes, such as leakage out of the computational subspace [169]. Since the heralded SPAM protocol allows for the detection of leakage events, allowing for shots in which they occur to be discarded, we neglect such errors in the following discussion.

sum. It can be shown [3] that any arbitrary quantum process on a $d$-dimensional system can be written as

$$\Lambda(\rho) = \sum_i K_i \rho K_i^\dagger \tag{5.1}$$

for at most $d^2$ Kraus operators $\{K_i\}$. Remarkably, the only condition they must obey to describe a CPTP map is $\sum_i K_i^\dagger K_i = \mathbb{1}$. As a specific example, a map describing unitary evolution $\Lambda(\rho) = U\rho U^\dagger$ has a single Kraus operator $U$.

Sequentially carrying out two quantum processes $\Lambda_1$, $\Lambda_2$ generates a third quantum process, $(\Lambda_2 \circ \Lambda_1)\rho = \Lambda_2(\Lambda_1(\rho))$, which is the composition of the two processes. This, amongst other things, enables the calculation of a process consisting of a series of gates, in analogy to the description by a product of unitaries.

### 5.1.2 Fidelity and error metrics

A characterisation of a quantum computer should yield a set of quantities that allow us to predict the likelihood that an arbitrary algorithm will return the correct result, for a given input. In order to be useful, this set of quantities should be small. Indeed, one could obtain a complete characterisation of the device by running every possible algorithm and comparing the measured and theoretical results, but this would be both unwieldy to analyse and entirely infeasible to measure experimentally. Instead, one can consider errors on individual gates, that is, how "close" their implementation in hardware is to the ideal gate. With this information, we may hope to be able to extrapolate how closely the physical implementation of *any* algorithm run on the hardware approximates the theoretical one. Indeed, we can ask the following: is it possible to quantify the likelihood that an error will occur in an algorithm by ascribing a *single* error to each gate in the device's gate set?

One way to approach this question is to realise that the experimental implementation of a quantum gate is associated with a set of gate parameters, such as the time that a laser is on for, and its frequency and phase. Thus, we can meaningfully talk about the error in a gate if every time the set of parameters for this gate is keyed in, the same quantum operation $\Lambda$ (which does not have to correspond to the target gate or be unitary) is always implemented [171]. Then, a metric that characterises the similarity of the map $\Lambda$ to the ideal map would serve to quantify the error. This quantity is the *fidelity* $\mathscr{F}$, from which

the error can be defined as[2] $\varepsilon = 1 - \mathscr{F}$. Note that the fidelity and errors derived from it do not yield any information on what type of errors occur - for example, whether the errors will result in a bit-flip or a phase flip. This requires knowledge of the full quantum process $\Lambda$, obtained through quantum process tomography or related protocols [46, 169].

It will be useful to define the *error process* $\mathscr{E}$ of the process $\Lambda$ applied when implementing a gate $U$. This is defined by[3] $\mathscr{E} \triangleq (\mathscr{U}^\dagger \circ \Lambda)$, where $\mathscr{U}^\dagger$ is the process that perfectly applies $U^\dagger$ [172]. If the gate is applied perfectly, $\mathscr{E}$ is the identity map.

There exist many ways to define the fidelity [173–175] which differ in their ability to describe the effect of the gate on general states, and their ease of experimental measurement. We clearly should choose a fidelity metric that is as descriptive as possible, yet feasible to extract from the experiments of Chapters 7 and 8.

The measurements of Chapter 7 allow us to directly measure the *average gate fidelity* $\bar{\mathscr{F}}$ for each gate. This is the average squared overlap between the state output by a process $\Lambda(|\psi\rangle\langle\psi|)$ and the one output by the ideal process $U|\psi\rangle$ [175]:

$$\bar{\mathscr{F}} \triangleq \int d\psi \, \langle\psi|U^\dagger \Lambda(|\psi\rangle\langle\psi|)U|\psi\rangle = \int d\psi \, \langle\psi|\mathscr{E}(|\psi\rangle\langle\psi|)|\psi\rangle \tag{5.2}$$

where the integral is taken over the Haar metric[4] [175]. It can be shown that the average gate fidelity of a quantum map on a $d$-dimensional system is related to its Kraus operators by[5] [170]

$$\bar{\mathscr{F}} = \frac{d + \sum_j \left|\mathrm{Tr}(K_j)\right|^2}{d(d+1)}. \tag{5.3}$$

It is worth pointing out that errors derived from this fidelity *do not* necessarily add up linearly! Indeed, suppose that a gate is implemented with an over-rotation of $\delta\theta$, whose error is proportional to $\delta\theta^2$ as shown in Appendix A.2. If two such operations are applied sequentially, then the net over-rotation angle will be $2\delta\theta$, so the error will be proportional to $4\delta\theta^2$. However, in many cases, small errors do add linearly.

[2] A fidelity of 1 corresponds to a perfect gate, under the relevant metric.

[3] An equivalent definition of the error process is $\mathscr{E} \triangleq (\lambda \circ \mathscr{U}^\dagger)$, which will be used in Chapter 7. They behave almost identically [172].

[4] The Haar metric defines a probability distribution over unitary matrices such that sampling has an unbiased probability of returning any unitary. This can then be used to define a uniform probability distribution over quantum states by writing $|\psi\rangle = U|\phi\rangle$ where $U$ is a random matrix sampled from the Haar metric and $|\phi\rangle$ is an arbitrary fixed state [176, 177].

[5] The quantity $\mathscr{F}_e = \frac{\left|\mathrm{Tr}(K_j)\right|^2}{d^2}$ is the *entanglement* or *process* fidelity [176, 178].

The inter-ion experiments in Chapter 8 are more complex and, due to technical reasons, it is not possible to extract the average gate fidelity for those experiments. Instead, what we term the *single-state gate fidelity*[6] $\mathcal{F}_{|\psi\rangle}$ is used. This fidelity is common in the monoqubit two-ion gate literature [109, 140, 179, 180], so it also allows for easy comparison with existing works. It is defined as the squared overlap between a single state output by the process $\Lambda$ and the ideal output for that state[7]:

$$\mathcal{F}_{|\psi\rangle} \triangleq \langle\psi|U^\dagger\Lambda(|\psi\rangle\langle\psi|)U|\psi\rangle = \langle\psi|\mathcal{E}(|\psi\rangle\langle\psi|)|\psi\rangle\,. \tag{5.4}$$

This fidelity depends strongly on $|\psi\rangle$, so it is important to select an adversarial state, for which the fidelity will be significantly affected by the expected errors in the gate[8]. A good choice is a state that is orthogonal to the eigenbasis of $U$, since it will be sensitive to many types of errors. Going forward, the dependence on $|\psi\rangle$ will often be dropped for clarity, instead writing $\mathcal{F}_s$.

#### 5.1.2.1 Markovian errors

The previous discussion relied on the ability to associate a single quantum process $\Lambda$ to a gate's experimental implementation. This is by no means trivial, since it means that what happens in the device depends on nothing other than the experimental parameters that determine which gate to implement – in particular, it does not depend on the time at which the gate is driven. Such errors are *Markovian* [171]. However, many processes (if not most!) *do* depend on time: this happens if there is a dependence on variables that change during a computation (such as the ions' temperature) or on a noise process that shows temporal correlations. This can also occur if the Hamiltonian that describes the gate implementation shows complex time dependence, as we will see. Such processes are *non-Markovian* [182] and cannot be generally described by associating a unique quantum process to a gate [183, 184]. Thus, defining a single fidelity that can be associated to such processes is challenging [185].

[6] Sometimes just the *gate fidelity* [170].

[7] The expression for the state fidelity in the RHS is the same whether the error process $\mathcal{E}$ is defined with $U^\dagger$ applied after the process $\Lambda$ (as defined here) or whether it is applied after the process (as in Section 7.1.2).

[8] Though finding the state that is most adversarial for a given gate and expected errors is a challenging problem [181].

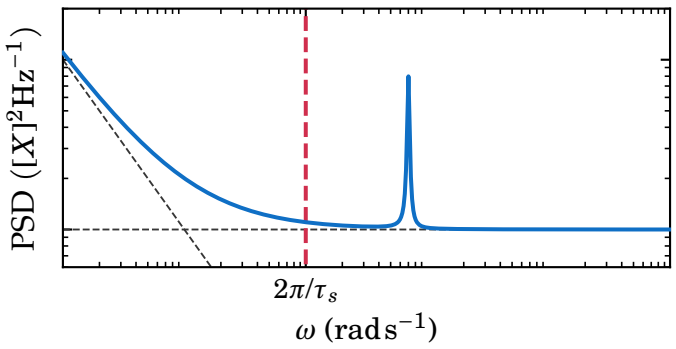



**Figure 5.1:** Sketch of a typical experimental noise PSD, in units of $[X]^2\mathrm{Hz}^{-1}$, where $[X]$ are the units of $X$. The noise is large at low frequencies and drops off (in this case with a slope of $1/\omega$) until it reaches a "white noise" plateau. A noise spike, or spur, can also be observed. The low-frequency noise is concentrated below $2\pi/\tau_s$, so it can be approximated as static.

### 5.1.3 Evolution under stochastic Hamiltonians

We now briefly outline some necessary results regarding the evolution of a quantum system under Hamiltonians of the form

$$H(t) = H_c(t) + X(t)H_n(t) \tag{5.5}$$

where $X(t)$ is a stochastic classical variable, assumed to be zero mean and stationary – the noise statistics are invariant under time-translation [186]. Both $H_c$ – the *control* Hamiltonian – and $H_n$ –the *noise* Hamiltonian, which couples the noise to the system – are deterministic operators. For brevity, the necessary results will be presented with little background discussion. The reader interested in a clear, in-depth treatment is referred to [168, 187], as well as classic texts such as [186].

The statistics of the experimentally measured outcomes are determined not by the state $\rho(t)$ produced in a given run of the experiment, but rather the average state $\langle\rho(t)\rangle$, where the average is taken over many realisations of the noisy process $X$. However, for notational ease, the brackets will be dropped, with the understanding that $\rho(t)$ is an average state.

For a given $H_c$ and $H_n$, the state evolution is determined by the noise process' power spectral density (PSD) $S_X(\omega)$ [147, 188], which measures the average power in the noise signal within the bandwidth $(\omega,\ \omega + \mathrm{d}\omega)$. The spectra of experimentally relevant noise sources (see Figure 5.1) often contain large low-frequency contributions, whose PSD below some cutoff frequency often go as $1/\omega$ or $1/\omega^2$ (termed $1/f$ or $1/f^2$ noise) until

reaching a flat (broadband) plateau, referred to as a "white" noise region. There also may be a noise "spur", characterised by a narrow spike in the PSD around some frequency. In future chapters, it will often not be possible to explicitly determine the exact form of the spectrum, so we will typically assume some generically low-frequency noise, and a white noise plateau. Ignoring the specific form of the low-frequency noise is justified when it is concentrated at frequencies below $2\pi/\tau_s$, where $\tau_s$ is the duration of an experimental shot. In such cases, the noisy parameter will be constant over the shot, but will change shot-to-shot; we refer to this as *static* noise.

A closely related quantity to the PSD, which can be viewed as its time-domain analogue, is the autocorrelation function

$$R_X^{(t)}(\tau) \triangleq \langle X(t)X(t+\tau)\rangle = \langle X(0)X(\tau)\rangle \tag{5.6}$$

where, as usual, the angled brackets denote an average over noise realisations. In the second equality we have invoked the assumption that $X$ is stationary, so the superscript $(t)$ will be dropped. This function provides a measure of how similar a noise process is to a shifted copy of itself, thereby measuring how correlated the value of the noise at time $t+\tau$ is to the value at $t$. It is worth pointing out that the noise's variance $\langle X^2\rangle$ is equal to $R_X(0)$. The autocorrelation function and the PSD can be related by[9] [147, 188]

$$R_X(\tau) = \frac{1}{2\pi}\int_{-\infty}^{\infty} S_X(\omega)e^{i\omega\tau}\,\mathrm{d}\omega \tag{5.7}$$

From this, it can be observed that the autocorrelation of white noise with PSD $S_X(\omega) = \Gamma$ is $R_X(\tau) = \Gamma\delta(\tau)$. Indeed, white noise is perfectly uncorrelated[10] and thus Markovian [186]. In this case, the evolution of a quantum state under the stochastic Hamiltonian (5.5) can be described by a Lindblad master equation[11] [168, 187, 189]. In general, if the system is subject to many independent white noise sources, so (5.5) becomes $H(t) = H_c(t) + \sum_i X_i H_{n,i}(t)$ for some $\{X_i\}$ and $\{H_{n,i}\}$, then

$$\frac{\mathrm{d}\rho}{\mathrm{d}t} = -\frac{i}{\hbar}[H_c(t),\rho] + \sum_i l_i\rho l_i^\dagger - \frac{1}{2}\left(l_i^\dagger l_i\rho + \rho l_i^\dagger l_i\right). \tag{5.8}$$

[9] The PSD as defined here is the two-sided PSD.

[10] One can also observe that white noise has an infinite RMS!

[11] The master equation can also describe couplings between a system and an environment described by a quantum state [3].

with the Lindblad operators $l_i \triangleq \frac{\sqrt{\Gamma_i}}{\hbar} H_n$. Integrating the master equation over a duration $\Delta t$ yields a quantum process[12] $\Lambda_{\Delta t}(\rho)$. It can be shown that, to first order in $\Delta t$, the Kraus operators for time-independent $H_c$ and $H_n$ are [3]

$$K_0 = \mathbb{1} - \Delta t \left( \frac{i}{\hbar} H_c + \frac{1}{2} \sum_i l_i^\dagger l_i \right) \quad , \quad K_{i\neq 0} = \sqrt{\Delta t}\, l_i . \tag{5.9}$$

This can be useful for calculating the form and average fidelity of small errors.

Calculating the effect of noise with arbitrary correlations is more involved. In Reference [168], a perturbative approach is used to show that, for weak noise, and in the interaction picture with respect to the deterministic Hamiltonian $H_c$, the evolution is given by

$$\rho(t) \approx \rho(0) - \frac{1}{\hbar^2} \int_0^t \mathrm{d}t_1 \int_0^{t_1} \mathrm{d}t_2 R_X(t_1 - t_2) [H_n(t_1), [H_n(t_2), \rho(0)]]. \tag{5.10}$$

Many experimentally relevant autocorrelation functions can be approximated with a decaying exponential $R_X(\tau) = \langle X^2 \rangle e^{-\gamma|\tau|}$ with a correlation time $\tau_c = 1/\gamma$ [190]. If, in addition, the noise Hamiltonian $H_n$ is time-independent, then by directly evaluating the integral $\int \mathrm{d}t_1 \int \mathrm{d}t_2 R_X(t_1 - t_2)$, one finds

$$\rho(t) = \rho(0) - \langle X^2 \rangle \frac{e^{-\gamma t} + \gamma t - 1}{\gamma^2} [H_n, [H_n, \rho(0)]]. \tag{5.11}$$

The PSD corresponding to this autocorrelation function can also be easily found to be[13]

$$S_X(\omega) = 2\langle X^2 \rangle \frac{\gamma}{\gamma^2 + \omega^2}. \tag{5.12}$$

Note that this is a Lorentzian centred at $\omega = 0$. An identical PSD is often used to model noise spurs at frequency $\omega_0$, setting $\omega \to \omega - \omega_0$ and $\gamma \to \Gamma/2$, where $\Gamma$ is the Lorentzian FWHM. For a spur, $\frac{\Gamma}{\omega_0} \ll 1$.

It is useful to explore the extremal limits of the correlation time. The short $\tau_c$ limit ($\gamma \to \infty$) is the white noise limit, which we expect to be closely related to evolution under a master equation. Evaluating (5.11) in this limit directly yields the Kraus representation

[12] The quantum process generated by a master equation generally depends on the start and end times of the integration, but this will not be relevant in the cases considered.

[13] The normalisation of this Lorentzian PSD ensures consistency with $R_X(0) = \langle \delta X^2 \rangle$.

(5.9) with $l = \sqrt{\frac{2\langle X^2\rangle}{\gamma}} H_n$. The long coherence time case ($\gamma \to 0$) approximates low-frequency spectra. Indeed, $\gamma = 0$ exactly corresponds to static noise [190]. Expanding the exponential in (5.11) to second order in $\gamma t$ we find

$$\rho(t) = \rho(0) - \frac{t^2\langle X^2\rangle}{2}[H_n,[H_n,\rho(0)]]. \tag{5.13}$$

The Kraus operators for this process are

$$M_0 = \mathbb{1} - \frac{t^2\langle X^2\rangle}{2} H_n^2 \quad , \quad M_1 = t\sqrt{\langle X^2\rangle} H_n. \tag{5.14}$$

#### 5.1.3.1 Filter function formalism

An alternative method to numerically calculate a stochastic evolution is to employ a filter function formalism. For brevity, this formalism is not discussed in any depth, and the reader is referred to References [191, 192] for a deeper discussion, as well as the accompanying Python software package [193] for calculations.

By treating the control and noise Hamiltonians from (5.5) in the frequency domain, the full quantum process of the evolution under arbitrarily correlated noise can be calculated from coefficients of the form $\Gamma_{k,l} = \int_{-\infty}^{\infty} \frac{\mathrm{d}\omega}{2\pi} S_X(\omega) F_{k,l}(\omega)$. The functions $F_{k,l}$ are the Hamiltonian's filter functions, which contain the "sensitivity" of the system to noise at a particular frequency $\omega$, which is exactly the information contained in the PSD $S_X$. The filter functions depend strongly on both the control and noise Hamiltonian. For example, if the control Hamiltonian implements a dynamical decoupling sequence, the impact of a noise source will clearly be reduced.

## 5.2 Intra-ion gates

A discussion of the errors relevant to intra-ion gates is now given. Equations to calculate the evolution of a density matrix are given – usually as Lindblad operators for a master equation treatment. Where possible, a simple form of the average error due to the described process is also given.

### 5.2.1 Detuning and LS miscalibration

The evolution of a multi-level system over a sequence of laser pulses was calculated in Section 3.4.3, taking into account detunings on the drive lasers, as well as any light shifts they induce on all states in the manifold. We are primarily interested in multi-level systems with cyclic connectivity graphs, since this is the connectivity of the manifold chosen in future chapters. In this case, the unitary applied at every pulse was calculated to be[14]

$$U_n = R_z^{(T_n)}\left(-\bar{\omega}_l t_{n,i}\right)\mathscr{U}_n^{(\bar{\omega}_l)}\mathscr{U}_n^{(LS)}\mathscr{U}_n^{(\delta)}R^{(T_n)}\left(\theta_n,\phi_n,\nu^{(T_n)}\right)R_z^{(T_n)}\left(\bar{\omega}_l t_{n,i}\right) \tag{5.15}$$

where $\mathscr{U}_n^{(\delta)}$ from (3.25) contains phase shifts due to the drive tones being off-resonant with the (light-shifted) transitions they drive; $\mathscr{U}_n^{(LS)}$ from (3.26) contains phase shifts due to the fact that the state energies are light-shifted at every pulse; and $\mathscr{U}_n^{(\bar{\omega}_l)}$ from (3.31) and the $R_z^{(T_n)}\left(\pm\bar{\omega}_l t_{n,i}\right)$ rotations are due to breaking the multi-photon resonance condition, so $\bar{\omega}_l = \frac{1}{d}\sum_{T=0}^{d-1}\omega_l^{(T)} \neq 0$. Here, we discuss the form of the errors induced by these effects, as well as how to coherently correct some of them. Quantitative expressions are not given, since they are lengthy, not enlightening and, in the case of multi-photon resonance errors, of questionable value. Where errors are calculated in this thesis, the expressions of Section 5.1 are calculated numerically.

We now discuss the errors due to the different contributions in (5.15) separately. Errors due to breaking the multi-photon resonance condition are not present if the connectivity graph is linear, while the remaining ones are. Despite how common the control miscalibrations that induce them are, the errors take a surprisingly non-trivial form.

#### 5.2.1.1 Pure detuning errors

The unitary $\mathscr{U}_n^{(\delta)}$ encodes the phase that is accrued between states that are not driven in the $n^{\text{th}}$ TSR and the tone that drives the transitions they are involved in. Such errors are entirely absent in monoqubit systems, since at no point is any transition idle (other than short delays between pulses). The effect of detunings that *is* shared with monoqubits the modification of the TSR $R_{\theta_n}^{(T_n)}\left(\phi_n\right) \to R^{(T_n)}\left(\theta_n,\phi_n,\nu^{(T_n)}\right)$: the rotation axis is rotated away from the equator by $\nu^{(T_n)}$.

[14] If the connectivity graph is linear, the unitary is $U_n = \mathscr{U}_n^{(LS)}\mathscr{U}_n^{(\delta)}R^{(T_n)}\left(\theta_n,\phi_n,\nu^{(T_n)}\right)$, see Section 3.4.1.

#### 5.2.1.2 Breaking multi-photon resonance

A striking and unique error occurs if the connectivity graph is cyclic and the laser frequencies break the multi-photon resonance condition $\bar{\omega}_l = 0$ (see Figure 5.2c). The error is induced by $\mathscr{U}_n^{(\bar{\omega}_l)}$ and the two $Z$ rotations in (5.15). As discussed in Section 3.4.2, the ability to connect a pair of states via two independent paths sets up an effective interferometer involving all drive tones. Indeed, it was shown that the effect of a pulse sequence depends on the sum of the laser phases going around the loop, which evolves at a rate $\bar{\omega}_l t$. This is the reason behind the two $Z$ gates that surround the TSR and rotate its phase $\phi_n \to \phi_n - \bar{\omega}_l t_{n,i}$ by an amount that depends on the absolute time $t_{n,i}$ at which the pulse is driven. Thus, under the definition of Section 5.1.2.1, this induces non-Markovian errors! As such, it is difficult to meaningfully associate a gate error, since the unitary implemented in hardware will differ more from the target unitary the later it is implemented in the circuit.

However, these $Z$ rotations, as well as $\mathscr{U}^{(\bar{\omega}_l)}$, depend only on $\bar{\omega}_l$ and the time at which each pulse is executed. The former is always known to the experimentalist exactly and, in most situations, so is the latter. This is the case if all transitions are driven by microwaves, so all transition frequencies $\omega_l^{(T)}$ are known exactly, or if the loop has an even number of transitions and each of them is driven by modulating a common laser. Indeed, then the (unknown) unmodulated laser frequency drops out of $\bar{\omega}_l$ and only the (known) modulation frequencies contribute. Thus, the inverse of the $Z$ rotations and $\mathscr{U}^{(\bar{\omega}_l)}$ can be exactly calculated and applied with virtual rotations, thereby coherently cancelling these errors[15]. Unfortunately, this phenomenon was only found at the time of writing, so such corrections could not be done in the experiments of future chapters.

We point out that it is possible for the multi-photon resonance condition to be broken *even if* all drive tones are on-resonance with the transition they drive, $\delta^{(T)} = 0$. This occurs if the light shifts induced when driving each transition shift the states by different amounts. Thus, each laser tone must be detuned from the *bare* frequency of the transition that it drives by a different amount in order to be on resonance, in a way that does not in general obey $\bar{\omega}_l = 0$. This is shown in Figure 5.2.

[15]The author is grateful to David Nadlinger for initially pointing this out.

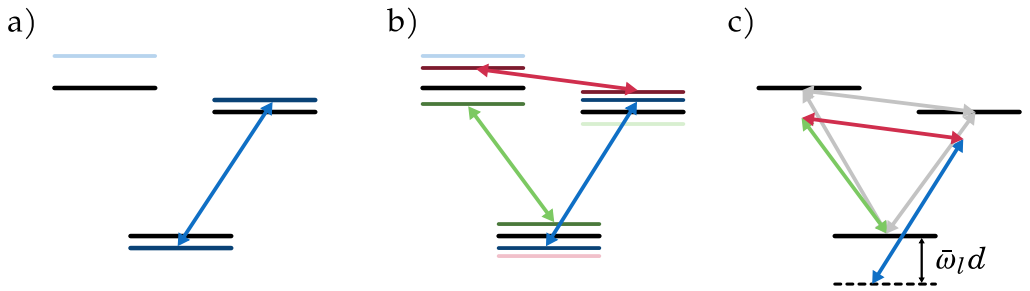



**Figure 5.2:** a) Since the laser that drives a TSR induces a LS on the states it addresses, driving the transition on resonance requires it to be tuned to the frequency of the shifted states (dark blue) rather than the bare states (black). The third state is also shifted (light blue). The shifts induced by each laser do not need to match, as shown in b) where each laser in a closed loop induces a different LS. c) Because of this, the lasers break the multi-photon resonance condition ($\bar{\omega}_l \neq 0$) even though all transitions are driven resonantly ($\delta^{(T)} = 0$). If there were no LS, driving the transition on resonance would imply that the laser frequency corresponds to the frequency between bare states, so the multi-photon resonance condition would be met, as shown in gray.

#### 5.2.1.3 Light shift miscalibration

The LS unitary $\mathscr{U}_n^{(LS)}$ can also be corrected with knowledge of the transition LS matrix $\Delta_{T'}^{T}$, whose entries are the LS on transition $T$ when driving $T'$. Indeed, given some measured LS matrix $\tilde{\Delta}_{T'}^{T}$ one could apply $\tilde{\mathscr{U}}_n^{\dagger(LS)}$, which has the same form as $\mathscr{U}_n^{\dagger(LS)}$ with $\Delta_{T'}^{T} \to \tilde{\Delta}_{T'}^{T}$. An LS miscalibration error occurs when $\tilde{\Delta}_{T'}^{T} \neq \Delta_{T'}^{T}$, which results in a unitary

$$\mathscr{U}_n^{(LS)} = \exp\left( i \sum_{T=0}^{T_{\text{Max}}} \left( \sum_{T'=0}^{T-1} \nabla_{T'}^{T'} \left[ \tau_n + \tau_n^{(Int)} \right] - \nabla_{T_n}^{T'} \tau_n \right) |T\rangle\langle T| \right) \tag{5.16}$$

with $\nabla_{T'}^{T} \triangleq \Delta_{T'}^{T} - \tilde{\Delta}_{T'}^{T}$.

#### 5.2.1.4 Comparison with monoqubits

It is clear that the impact of LS and detuning errors in multi-level systems is larger than in monoqubits. Not only do entirely new types of error arise, which are not present in monoqubits, but they are also more likely, since more transitions and light shifts need to be correctly calibrated to avoid them.

#### 5.2.1.5 Compensating LS through the TSR phase

The LS compensation procedure from the previous section was not known at the time of the experiments. Instead, the phase of each TSR was individually modified by the right amount to compensate the accrued LS phase. The phase of the $n^{\text{th}}$ TSR is updated by

$$\phi_n \to \phi_n + \left( \tilde{\Delta}_{T_n}^{T_n} (t_{n,i} - \mathscr{T}_n^{(T_n)}) - \sum_{T \neq T_n} \tilde{\Delta}_{T}^{T_n} \mathscr{T}_n^{(T_n)} \right) \tag{5.17}$$

where $\mathcal{T}_n^{(T)}$ is the total amount of time that transition $T$ has been on for before the start of the $n^{\text{th}}$ pulse. This is the difference between phase accrued by a laser oscillating at the transition's resonance frequency between the start of the circuit and the start of the $n^{\text{th}}$ gate, minus the expected total phase accrued by the pair of states in $T_n$ as the frequency between them changes throughout the circuit.

This equation can also be derived from (5.15) for linear connectivity graphs using similar techniques to those in Appendix B. However, the derivation cannot easily be generalised to cyclic connectivity graphs. The author conjectures that this generalisation in fact *cannot* be done, because these phase updates may also correct for the effects due to $\bar{\omega}_l \neq 0$. This is supported by simulations, which show that applying the inverses of $\mathscr{U}^{(LS)}$, $\mathscr{U}_n^{(\bar{\omega}_l)}$ and the $R_z^{(T_n)}\left(\pm\bar{\omega}_l t_{n,i}\right)$ TSRs has the same effect as applying these phase corrections.

### 5.2.2 Sources of dephasing

Many common errors in trapped ions arise from noise that imparts random phases onto states in a superposition. Such processes are termed "dephasing" and lead to a decay of the state's coherences (the off-diagonal terms in the density matrix). Common sources of dephasing involve fluctuating magnetic fields; laser frequency and phase noise; and time-varying light shifts that arise from fluctuations in laser intensity. We first give an overview of dephasing in a multi-level system before focusing on each source.

Dephasing processes are described by the general Hamiltonian

$$H(t) = H_c + XH_n = H_c + \hbar X \sum_v \Xi_v |v\rangle\langle v| \tag{5.18}$$

where $X$ is the classical stochastic variable that generates the noise, and the $\Xi_v$ are sensitivities of each atomic state to the noise. These two quantities entirely characterise the effect of the noise.

If the spectrum of $X$ is white, then a master equation can be used with the Lindblad operator

$$l = \sqrt{\Gamma} \sum_v \Xi_v |v\rangle\langle v| \tag{5.19}$$

where $\Gamma$ is given by $\langle X(\tau)X(0)\rangle = \Gamma\delta(\tau)$.

An important special case is that in which the only evolution is due to the noise process, $H_c = 0$; this is referred to as free-induction decay (FID). The master equation can then be integrated exactly to yield

$$\rho_{\nu,\mu}(t) = \rho_{\nu,\mu}(0) e^{-\Gamma_X (\Xi_\nu - \Xi_\mu)^2 t}. \tag{5.20}$$

This solution is also applicable to situations in which the control and noise Hamiltonians commute, since this allows us to move into the interaction picture with respect to the control Hamiltonian. The control and noise Hamiltonians in this frame would be $\tilde{H}_c = 0$, $\tilde{H}_n = H_n$.

The FID evolution can also be found for correlated noise, such as static noise. Using equation (5.11) in the static noise limit, we obtain

$$\rho_{\nu,\mu}(t) = \rho_{\nu,\mu}(0)\left(1 - \langle X^2 \rangle (\Xi_\nu - \Xi_\mu)^2 t^2\right) \approx \rho_{\nu,\mu}(0) e^{-\langle X^2 \rangle (\Xi_\nu - \Xi_\mu)^2 t^2} \tag{5.21}$$

where the Gaussian evolution can in fact be shown to be exact at arbitrary times [190].

The discussion so far has considered a general multi-level system, but some additional intuition about the effect of the noise on polyqubits can be gained. Indeed, we can rewrite the noise Hamiltonian in terms of generalised $Z$ rotations

$$H_n = \hbar X \sum_{\mathbf{b}} \zeta_{\mathbf{b}} \Sigma_z^{\otimes \mathbf{b}} \tag{5.22}$$

with the sensitivities to $Z$ rotations[16] $\zeta_{\mathbf{b}} = \frac{1}{2^n} \sum_\nu (-1)^{\mathbf{b}\cdot\boldsymbol{\nu}} \Xi_\nu$ where, as usual, $\boldsymbol{\nu}$ is the binary string corresponding to atomic state $|\nu\rangle$. When only one of the $\zeta_{\mathbf{b}}$ is non-zero, we say that the noise is polarised about $\Sigma_z^{\otimes \mathbf{b}}$. Then, since ${\Sigma_z^{\otimes \mathbf{b}}}^2 = \mathbb{1}$, the master equation takes the simple form

$$\dot{\rho} = -\frac{i}{\hbar}[H_c, \rho] + \Gamma \zeta_{\mathbf{b}} \left( \Sigma_z^{\otimes \mathbf{b}} \rho \Sigma_z^{\otimes \mathbf{b}} - \rho \right). \tag{5.23}$$

It is also worth noting that any common-mode contribution of the sensitivities (any contribution from $\zeta_{\mathbf{0}} = \frac{1}{2^n} \sum_\nu \Xi_\nu$) is inconsequential, since only differences between the sensitivities affect the state.

[16] This makes use of the identity $|\boldsymbol{\nu}\rangle\langle\boldsymbol{\nu}| = \bigotimes_i \frac{\mathbb{1} + (-1)^{\nu_i} \sigma_z}{2} = \frac{1}{2^n} \sum_{\mathbf{c}} (-1)^{\boldsymbol{\nu}\cdot\mathbf{c}} \Sigma_z^{\otimes \mathbf{c}}$.

#### 5.2.2.1 Comparison to monoqubits

We wish to make statements about how the same noise source $X$ affects monoqubits and multi-level systems for general dephasing processes. This is made complicated by the fact that $H_n$ depends on many parameters - the sensitivities. We thus require some way to characterise the magnitude of the ion's sensitivity to the dephasing noise, separate from the relative sensitivity between each state.

A "sensitivity magnitude" can be defined by considering how small errors accumulate under FID. We assume that the PSD of $X$ is white, though an identical definition would be reached with static noise. Using (5.9), we find that the Kraus operators for FID ($H_c = 0$) over short times $t$ are

$$K_0 = \mathbb{1} - \frac{\Gamma t}{2}\sum_v \Xi_v^2 |v\rangle\langle v| \quad , \quad K_1 = \sqrt{\Gamma t}\sum_v \Xi_v |v\rangle\langle v| . \tag{5.24}$$

The fidelity of this process is

$$\bar{\mathscr{F}}(t) = 1 - \Gamma t \frac{\sum_{v,\mu}\left(\Xi_v - \Xi_\mu\right)^2}{d(d+1)} \triangleq 1 - \Gamma t |\Xi|^2 \tag{5.25}$$

where we have defined the sensitivity magnitude $|\Xi|^2 = \frac{\sum_{v,\mu}\left(\Xi_v - \Xi_\mu\right)^2}{d(d+1)}$. This single parameter quantifies the effect of the atomic properties on the average dephasing error, which accumulates at a rate $\Gamma|\Xi|^2$. The structure of the sensitivities is entirely contained in the normalised sensitivities $\xi_v \triangleq \frac{\Xi_v}{|\Xi|}$, which do not affect the size of the error. With this, we can meaningfully compare errors across systems with different sensitivities and dimensions.

The sensitivity magnitude likely increases with dimension, since states with small relative sensitivities to a noise source (such as magnetic field noise) usually exhibit particular symmetries. Such symmetries are generally rare, so finding many states that exhibit them is challenging. Thus, we expect that dephasing errors will generally increase with dimension[17].

The structure of the normalised sensitivities $\xi_v \triangleq \frac{\Xi_v}{|\Xi|}$ determines the computational impact of the error, through the Kraus operators (5.24). For example, noise polarised about a generalised $Z$ rotation will induce an error process $\Lambda(\rho) = (1-\varepsilon)\rho - \varepsilon\Sigma_z^{\otimes \mathbf{b}}\rho\Sigma_z^{\otimes \mathbf{b}}$.

[17] The factor of $d(d+1)$ in the denominator of $|\Xi|^2$ does not generally reduce the sensitivity with $d$, since there are $d^2$ terms in the sum.

Knowledge of the normalised sensitivities can thus be used to inform error correction protocols or to identify decoherence-free subspaces within a polyqubit, or a general multi-level system. In general, errors on a polyqubit will contain a mixture of all generalised rotations, including single- and multi-qubit contributions.

#### 5.2.2.2 Magnetic field noise

Magnetic fields change the energy of the atomic states according to their magnetic field sensitivity, thereby leading to phase accrual between states. The Hamiltonian is $H_B = \hbar B \sum_\nu \frac{\mathrm{d}\omega_\nu}{\mathrm{d}B} |\nu\rangle\langle\nu|$, where $\hbar\omega_\nu$ is the energy of state $|\nu\rangle$. This noise is characterised by

$$X = B \quad , \quad |\Xi|^2 = \frac{1}{d(d+1)} \sum_T \left( \frac{\mathrm{d}\omega_T}{\mathrm{d}B} \right)^2 \quad , \quad \xi_\nu = \frac{1}{|\Xi|} \frac{\mathrm{d}\omega_\nu}{\mathrm{d}B} \tag{5.26}$$

where $\omega_T$ is a transition connecting two states, and the sum is over all transitions (whether they can be driven or not).

#### 5.2.2.3 Light shift noise

As was discussed in Section 3.3.2, an off-resonant beam of intensity $I$ shifts the energy of each state by

$$\Delta\omega_\nu = \sum_\mu \frac{\Omega_{\nu,\mu}^2}{4(\omega_L - \omega_{\nu,\mu})} = I\Xi_\nu \tag{5.27}$$

where $\Omega_{\nu,\mu}$ is the Rabi frequency between states $|\nu\rangle, |\mu\rangle$, $\omega_L$ is the laser frequency and $\Xi_\nu \triangleq \frac{\Delta\omega_\nu}{I}$ is the LS sensitivity of state $|\nu\rangle$. These sensitivities can be calculated using the expressions from Section 3.5 and depend on the beam's polarisation. Thus, LS noise is characterised by $X = \delta I$, where $\delta I$ is a fluctuation in the laser intensity about its mean value, alongside the LS sensitivities.

#### 5.2.2.4 Laser frequency noise

The phase of a laser that drives a TSR determines the equatorial axis about which the TSR is driven. Thus, it does not directly impart random phases onto the atomic states; instead, these arise when viewing the system from an interaction picture that tracks the rotation axis, in which case it is the state vector that rotates randomly. This is analogous to the effect of a frequency error in a monoqubit: in the atomic interaction frame, the

rotation axis precesses, but in the drive's frame, the qubit precesses. The effect of such noise is derived in Reference [168] for monoqubits; it is extended here to multi-level systems with cyclic connectivity, under reasonable assumptions.

We begin with the circuit Hamiltonian (3.29) without LS or detuning miscalibrations, so it can safely be written in the drive interaction frame:

$$H = \frac{\hbar}{2}\sum_n \Omega^{(T_n)}\left(e^{i(\phi_n + s^{(T_n)}\varphi^{(T_n)}(t))}|T_n+1\rangle\langle T_n| + h.c.\right) \tag{5.28}$$

where $\varphi^{(T)}(t)$ is the random phase of the drive for transition $T$, which is accumulated due to frequency fluctuations $2\pi\delta f^{(T)} = \dot{\varphi}^{(T)}$, and $s^{(T_n)} = +1(-1)$ if the energy of $|T+1\rangle$ is higher (lower) than that of $|T\rangle$ (see Section 3.4). A second frame change using the unitary $F = \exp[i\frac{1}{\hbar}\int \mathrm{d}t H_I(t)]$ with[18]

$$H_I(t) = 2\pi\hbar\sum_{T=1}^{d-1}\sum_{T'=0}^{T-1} s^{(T')}\delta f^{(T')}|T\rangle\langle T| \tag{5.29}$$

can now be carried out. Assuming that the connectivity graph is cyclical[19], this results in

$$e^{i\varphi^{(T)}(t)}|T_n+1\rangle\langle T| \to \begin{cases} |T_n+1\rangle\langle T| & \text{for } T \neq d-1 \\ e^{i\sum_{T=0}^{d-1} s^{(T)}\varphi^{(T)}}|0\rangle\langle d-1| & \text{for } T = d-1 \end{cases} \tag{5.30}$$

as well as an additional term added to the Hamiltonian (see Section 3.1)

$$i\hbar F^\dagger \frac{\mathrm{d}F}{\mathrm{d}t} = -2\pi\hbar\sum_{T'=0}^{T-1} s^{(T')}\delta f^{(T')}|T\rangle\langle T|. \tag{5.31}$$

We now make two assumptions. Firstly, the computational states are considered to be spread evenly across two atomic levels $L$ and $U$, with transitions being driven only across them and the energy of $U$ being higher than $L$. In this case, $s^{(T)} = -s^{(T+1)}$, that is computationally consecutive transitions must either go up, then down in energy or down, then up. This assumption also forces the number of states to be even. Secondly, we assume that the drives for each transition stem from a common source whose frequency is what is fluctuating. This implies $\delta f^{(T)} = \delta f$ is the same for all transitions.

[18] As pointed out in [168], this transformation adds random phases to the density matrix coherences. This may be relevant if two-ion gates do not commute with diagonal gates (LS-based ones do), or are driven with different sources.

[19] The phase dependence for all $|T+1\rangle\langle T|$ vanishes in linear connectivity graphs, in analogy to Section 3.4.3.

Under these assumptions, the time dependence in (5.30) vanishes and Equation (5.31) simplifies, so the Hamiltonian in this frame is

$$H = \frac{\hbar}{2}\sum_n \Omega^{(T_n)}\sigma_{\phi_n}^{(T_n)} - 2\pi\hbar\delta f \sum_{v\in U} |v\rangle\langle v|. \tag{5.32}$$

That is, all states in level $U$ observe effective noisy frequency shifts. Thus, laser frequency noise is characterised by $X = 2\pi\delta f$ and sensitivities $\Xi_v = 1(0)$ for $|v\rangle \in U(L)$. We point out that, since the sensitivities split into two equal halves, laser phase noise with this arrangement of atomic states will *always* be polarised along a generalised $Z$ rotation in 2-polyqubits, although this is not the case for $n$-polyqubits with $n > 2$.

### 5.2.3 Rotation angle miscalibration

To implement a TSR of rotation angle $\theta$, the relevant transition – whose Rabi frequency is $\Omega_{v,\mu}$ – must be driven for a duration $t_\theta = \theta/\Omega_{v,\mu}$. Usually, the pulse durations for a few rotation angles (typically $t_{\pi/2}$ and $t_\pi$, called the $\pi$- and $\pi/2$-times) are calibrated, from which the correct time for arbitrary rotations can be interpolated. Miscalibrations in these times can lead to over- or under-rotations by small angles $\delta\theta$. As shown in Appendix A.2, the error per laser pulse for small $\delta\theta$ obtained from the average fidelity is

$$\bar{\varepsilon} = \frac{\delta\theta^2}{2(d+1)} \tag{5.33}$$

where $d$ is the Hilbert space dimension. The error in a 2-polyqubit is found by setting $d = 4$.

The relative effect of these errors in multi-level and monoqubit systems depends on the number of TSRs needed to drive an inter-ion gate. Thus, the particular unitary being compared and the gate decomposition have a large impact. As a baseline, an angle miscalibration in a monoqubit leads to an error of $\delta\theta^2/6$. In contrast, the single-gate decompositions presented in Section 4.1, which require two TSRs on orthogonal subspaces, would have an error of $2\times\delta\theta^2/10$ if both rotations have the same miscalibration. Clearly, while the error per TSR is lower, the total error per single-qubit gate is higher. Additionally, unequal miscalibrations in each TSR would result in two-qubit errors. In general, an arbitrary unitary requires a maximum of $d(d-1)/2$ TSRs [75], so in the worst case scenario, these errors increase linearly with dimension for the same miscalibration in all pulses. Furthermore, many Rabi frequencies must be calibrated in multi-level systems, thereby increasing the likelihood that errors will occur.

### 5.2.4 Off-resonant excitation

The laser tone that drives a TSR can off-resonantly couple to a spectrally nearby transition, leading to undesired population transfer. While in monoqubits this can only lead to excitation outside the computational manifold, this is not so in multi-level systems, since spectator transitions within the manifold can be excited. Furthermore, excitation outside the computational manifold is more likely, since a larger number of transitions are available. Nonetheless, the heralded SPAM protocol of Section 4.4.1 allows us to detect and discard shots in which such leakage outside the manifold has occurred. Thus, the effect of these leakages can often be considered negligible, at most decreasing the experimental data rate.

A full treatment that considers all possible couplings of a single laser to an arbitrary number of transitions is involved [194]. In addition, if the manifold has been chosen to ensure sufficient spectral separation between transitions, such generality is unnecessary. Instead, we employ an estimate involving the sum of all excitation probabilities of each spectator transition individually. For a spectator transition with Rabi frequency $\Omega$, which is detuned from the laser by $\Delta$, the off-resonantly excited population (which we treat as equal to the error) is bounded by [112]

$$\varepsilon \approx \left(\frac{\Omega}{\Delta}\right)^2. \tag{5.34}$$

We consider the full excitation error per laser pulse as the sum over all spectator transitions – which may be within or outside the manifold.

If the states in the encoding are well-separated in frequency, this error is usually $\sim 10^{-4}$. If such separation is not possible, the Rabi frequency can be reduced, or pulse shaping techniques can be employed to make the pulses more adiabatic [195, 196].

### 5.2.5 Spontaneous decay

Spontaneous decay arises from a coupling of the atomic states to the continuum of electromagnetic modes, causing excited states to decay with the emission of a photon. This is only relevant for states stored in the atomic $D_{5/2}$ level, which can decay to the $S_{1/2}$ level; decay rates between states in the same level are negligible in comparison.

The decay can leave population in states inside or outside the computational manifold. The latter case corresponds to a leakage error, which can be corrected with the heralded SPAM protocol, as before. This process can be described using a master equation with the following Lindblad operators for decay from an excited state $|\nu\rangle$ to a lower state $|\mu\rangle$[20] [124, 197, 198]:

$$l_{\text{Scat}}^{\nu\to\mu} = \sqrt{\Gamma^{\nu\to\mu}}\,|\mu\rangle\langle\nu| \tag{5.35}$$

with a decay rate $\Gamma^{\nu\to\mu} = A_{\nu,\mu}(2J_\nu+1)\left|\langle\nu|\,\mathsf{T}_q^K\,|\mu\rangle\right|^2$ where $A_{\nu\mu}$ is the Einstein $A$ coefficient for decay from the level containing $|\nu\rangle$ to the one containing $|\mu\rangle$; $\mathsf{T}_q^K$ is a component of the rank-$K$ tensor operator defined in (3.42), with $q = m_\nu - m_\mu$ where $m$ is the magnetic quantum number; and $J_\nu$ is the total electronic angular momentum of the level containing $|\nu\rangle$.

As a comparison between multi-level and monoqubit systems, Figure 5.3 shows the decay error on an even superposition in the four-state encoding chosen in Section 6.2.4. It contains two states in the $D_{5/2}$ level that can decay to two states in the $S_{1/2}$ level. The decay errors on every pair of states across the levels are also plotted. It can be seen that the error in the four-state system is dominated by decay via the fastest-decaying transition – the one with the largest error. However, the error in the four-state system is always below the worst two-state system. Furthermore, the fairest comparison should pitch a four-level system against a two-monoqubit system, whose errors are twice as large as for a single monoqubit.

In $Ba^+$ ions, the decay lifetime on the $D_{5/2} \to S_{1/2}$ transition is $\tau = 1/\sum_\mu \Gamma^{\nu\to\mu} = 1/A \approx 30$ s, meaning that the contribution from this error is usually negligible. Indeed, the error rate extracted from a linear fit to the four-state errors in Figure 5.3 is $2.78 \times 10^{-3}$ s$^{-1}$. We note that this is significantly less than what may be expected from the 30 s $D_{5/2}$ level lifetime, since only decays to computational levels are considered.

### 5.2.6 Raman and Rayleigh scattering

Spontaneous atomic decay can be viewed as the direct coupling between an ion and the electromagnetic vacuum modes. The presence of an intense, off-resonant laser light mediates a second coupling mechanism, which is identical to a two-photon Raman transition in which the second "beam" is a mode of the electromagnetic vacuum. This

[20] The operator is zero if $|\nu\rangle$ is a state of lower energy than $|\mu\rangle$.

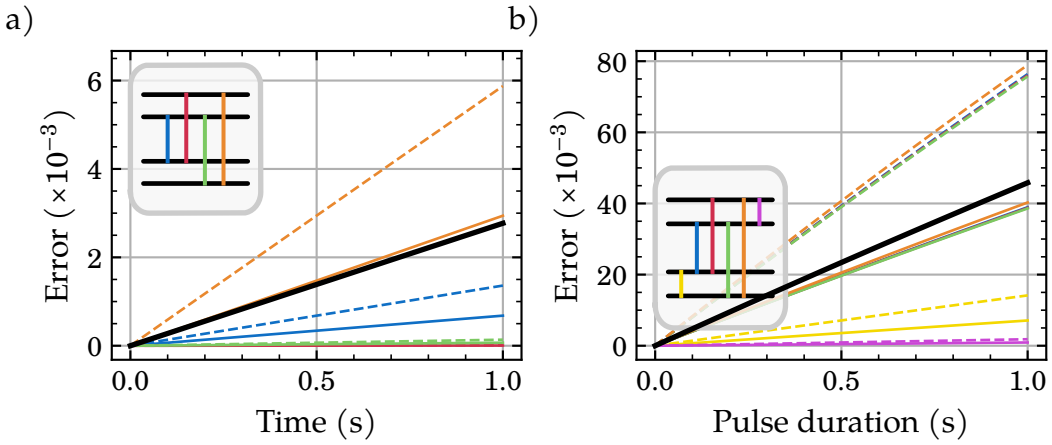



**Figure 5.3:** Simulated error on even superpositions of states due to a) spontaneous decay and b) scattering due to intense, off resonant laser light. The states are those chosen in Chapter 6. Two states are in the metastable $D_{5/2}$ level (top two black lines in the insets), which in a) can weakly decay to the two remaining states in the $S_{1/2}$ level (bottom two black lines). The thick black lines show the error on an even superposition of the four states, while solid (dashed) coloured lines show the error on one (two) monoqubit(s) encoded across the two states connected by the vertical line in the inset of the same colour. The two-ion simulations use independent Lindblad operators for the process on each ion.

coupling can either return the ion to the same state (termed Rayleigh or elastic scattering, since there is no change in the ion's energy) or leave the ion in some other state (Raman or inelastic scattering).

Inelastic scattering causes population transfer across all states, though, as before, only leakages to other computational states are considered due to the heralded SPAM protocol. Elastic scattering does not change the atomic populations, but instead acts as a dephasing term.

A master equation description of these processes was developed for monoqubits in Reference [199]. The Lindblad operators for elastic scattering via vacuum modes that couple via dipole transitions with $\Delta m = q$ (from the low- to the high-energy state) are

$$l_{El,q} = \chi_q^{0\to 0} |0\rangle\langle 0| + \chi_q^{1\to 1} |1\rangle\langle 1| \tag{5.36}$$

and inelastic scattering from $|\nu\rangle \to |\mu\rangle$ is modelled by

$$l_{In,q}^{0\to 1} = \chi_q^{0\to 1} |1\rangle\langle 0| \quad , \quad l_{In,q}^{1\to 0} = \chi_q^{1\to 0} |0\rangle\langle 1| \tag{5.37}$$

with [145]

$$\chi_q^{\nu\to\mu} = \frac{eE}{2\hbar}\sqrt{\frac{2\pi c^2(\omega_L-\omega_{\mu\nu})^3}{\alpha}}\sum_\kappa (2J_\kappa+1)\sqrt{\frac{A_{\kappa,\nu}A_{\kappa,\mu}}{\omega_{\kappa\nu}^3\omega_{\kappa\mu}^3}} \times\left(\frac{\langle\mu|\,\mathsf{T}^1_{-q}\,|\kappa\rangle\langle\kappa|\,\mathsf{T}^1_{q_{\kappa\nu}}\,|\nu\rangle\,\beta^{(1)}_{-q_{\kappa\nu}}(\hat{\mathbf{k}},\hat{\boldsymbol{\varepsilon}})}{\omega_{\kappa\nu}-\omega_L}+\frac{(\beta^{(1)}_{-q_{\kappa\mu}}(\hat{\mathbf{k}},\hat{\boldsymbol{\varepsilon}}))^*\langle\mu|\,\mathsf{T}^1_{-q_{\kappa\mu}}\,|\kappa\rangle\langle\kappa|\,\mathsf{T}^1_{q}\,|\nu\rangle}{\omega_{\kappa\nu}+\omega_L}.\right) \quad (5.38)$$

Here, $E$, $\hat{\mathbf{k}}$ and $\boldsymbol{\varepsilon}$ are the beam's electric field, direction unit vector and polarisation unit vector; $\omega_L$ and $\omega_{\nu\mu}$ are the laser frequency and the frequency between $|\nu\rangle$ and $|\mu\rangle$; $\alpha$ is the fine structure constant; $q_{i,j} = m_i - m_j$; and other quantities are as defined in Section 5.2.5. The inelastic scattering rate from $|\nu\rangle \to |\mu\rangle$ is $\Gamma^{\nu\to\mu} = \sum_q \left|\chi_q^{\nu\to\mu}\right|^2$.

This master equation generalises to multi-level systems in the obvious way[21]:

$$l_{El,q} = \sum_\nu \chi_q^{\nu\to\nu}\,|\nu\rangle\langle\nu| \quad , \quad l_{In,q}^{\nu\to\mu} = \chi_q^{\nu\to\mu}\,|\mu\rangle\langle\nu| \quad (5.39)$$

Simulated scattering errors in an even superposition of the four-state manifold chosen in Section 6.2.4 are shown in Figure 5.3, alongside errors in pairwise superpositions of the states. A 532 nm beam was considered instead of a 1762 nm one, which would be used to drive intra-ion gates, since 532 nm is much closer to dipole-allowed transitions and thus results in significantly larger scattering errors. Furthermore, these errors are relevant to inter-ion gates, since high intensities are used over long pulse durations. The error on the four-level system slightly exceeds that on each two-level subsystem, although as for decay errors, a fairer comparison for intra-ion gates would consider the errors on two monoqubits. A linear fit to the four-level error yields a rate of $47.8\times10^{-3}\mathrm{s}^{-1}$, which, as for decay errors, is usually negligible.

## 5.3 Inter-ion gates

Now we turn towards analysing errors that act on intra-ion gates. Most of these errors are related to the ion motion and the resulting back-action on the atomic states which causes the decoherence. Thus, one may expect that, as a multi-level system may intuitively be

[21] Scattering in multi-level systems was considered in Reference [75], although only inelastic scattering was considered, and not in a master equation formalism.

"more" entangled with the motion[22] the errors that arise from the motion may worsen with dimension. Surprisingly, we find that, in general, the asymptotic dependence of these errors on dimension is weak[23]. Furthermore, the errors for the Sleepy Gate scheme proposed in Chapter 4, in which the atomic states are evenly distributed across two levels within which all states couple equally to the motion, are found to be identical to the equivalent in monoqubits! This is not entirely surprising, since, as shown in Appendix D.1, the structure of the resulting unitary does not depend on the dimensionality of the atomic system. A convenient consequence of this is that well-known results from monoqubit analyses can then be used without modification.

For brevity, we will focus on the errors in Sleepy Gates with 2-polyqubits. However, we do generalise to arbitrary numbers of qubits and light shift structures when this is straightforward.

### 5.3.1 Control errors

An important source of errors in geometric two-ion gates occurs when the motional trajectories associated with each atomic state do not return to the origin at the end of the gate – the loops don't close. Since the atomic states will remain entangled with the motion, their reduced state will be mixed, leading to uncorrectable errors. Additionally, if the laser power is not set correctly, the states may acquire a different geometric phase over the gate duration to that which implements the target gate. These errors, which stem from imperfect control, are grouped together, since an expression for the gate error in terms of all these parameters will be obtained. This expression can also be used to deduce the error due to some other noise sources.

We first consider the effect of an arbitrary LS gate on two ions containing $d$ states. The target state will then just be the atomic state at the nearest loop closure point, which we

[22]The author makes no attempt to formally quantify this statement, but merely points out that if only $d$ states of the motional mode are considered (in other words, the mode is regarded as a second $d$-level system) states with "more" entanglement than a Bell pair can be formed. This is in the sense that certain states (e.g. $\frac{1}{\sqrt{d}}\sum_{i=0}^{d-1}|ii\rangle$) can be converted to a qubit Bell pair $\frac{1}{2}(|00\rangle+|11\rangle)$ using only local operations and classical communication, but not the other way around [178, 200].

[23]The scheme for qudit entanglement in Reference [153] does show errors that increase with qudit dimension. However, this was found to be primarily due to the increase in complexity of the gate operation and the effect of local errors.

write as

$$\rho_{Id} = \frac{1}{d^2} \sum_{\nu\mu\xi\chi} e^{i(\tilde{\Phi}_{\nu,\mu} - \tilde{\Phi}_{\xi,\chi})} |\nu:\mu\rangle \langle\xi:\chi| \tag{5.40}$$

for some target geometric phases $\tilde{\Phi}_{\nu,\mu}$ acquired on state $|\nu:\mu\rangle$. The errors for the Sleepy Gates are then obtained as a special case.

#### 5.3.1.1 Errors on arbitrary LS gates

The ions are initialised to the state $\rho(0) = \rho_A \otimes \rho_T$, with $\rho_A = \frac{1}{d} \sum_{\nu\mu\xi\chi} |\nu:\mu\rangle \langle\xi:\chi|$ an even superposition of atomic states and $\rho_T = \sum_n \frac{\bar{n}^n}{(1+\bar{n})^{n+1}} |n\rangle \langle n|$ a thermal motional state with mean occupation $\bar{n}$ [3]. This is then evolved by the gate unitary $U(t)$ from (3.68), yielding the state

$$U(t)\rho(0)U^\dagger(t) = \frac{1}{d^2} \sum_{\nu\mu\xi\chi} e^{i(\Phi_{\nu,\mu} - \Phi_{\xi,\chi})} |\nu:\mu\rangle \langle\xi:\chi| \otimes D\left(\alpha_{\nu,\mu}(t)\right) \rho_T D\left(-\alpha_{\xi,\chi}(t)\right) \tag{5.41}$$

where the $\Phi_{\nu,\mu}$ are the actual geometric phases imparted in the erroneous operation. The reduced atomic state is obtained by taking the partial trace with respect to the motion [201]. Using $\mathrm{Tr}\left(D(\alpha)\rho_T D\left(-\beta\right)\right) = e^{-i\Im(\beta\alpha^*)} \mathrm{Tr}\left(\rho_T D(\alpha-\beta)\right)$ alongside $\mathrm{Tr}\left(\rho_T D(\alpha)\right) = e^{-(\bar{n}+1/2)|\alpha|^2}$ [202, 203], the reduced atomic state is

$$\rho_A(t) = \frac{1}{d^2} \sum_{\nu\mu\xi\chi} e^{i\left(\Phi_{\nu,\mu} - \Phi_{\xi,\chi} - \Im(\alpha_{\xi,\chi}\alpha^*_{\nu,\mu})\right)} e^{-(\bar{n}+1/2)|\alpha_{\nu,\mu} - \alpha_{\xi,\chi}|^2} |\nu:\mu\rangle \langle\xi:\chi|. \tag{5.42}$$

The single-state gate fidelity with respect to the target state (5.40) is then

$$\mathscr{F} = \mathrm{Tr}\left(\rho_A(t)\rho_{Id}\right) = \frac{1}{d^4} \sum_{\nu\mu\xi\chi} \cos\left(\Delta\Phi_{\nu\mu,\xi\chi} - \Delta\tilde{\Phi}_{\nu\mu,\xi\chi} - \Im(\alpha_{\xi,\chi}\alpha^*_{\nu,\mu})\right) e^{-(\bar{n}+1/2)|\Delta\alpha_{\nu\mu,\xi\chi}|^2} \tag{5.43}$$

where $\Delta X_{\nu\mu,\xi\chi} \triangleq X_{\nu,\mu} - X_{\xi,\chi}$. From this, one can see that the fidelity has no strong dependence on the dimension: the sum over the four indices contributes $d^4$ terms, which exactly cancels with the factor in front.

This appears counter-intuitive, since one would expect that, due to the large number of parameters involved in the gate (the phases acquired by each two-ion state), control errors could have a large effect on the fidelity. However, we can observe that there are two sources of infidelity in Equation (5.43): contributions from residual motional entanglement and from not acquiring the correct geometric phase. Both terms are of a similar form, in that they depend on miscalibrations in the gate duration, detuning or

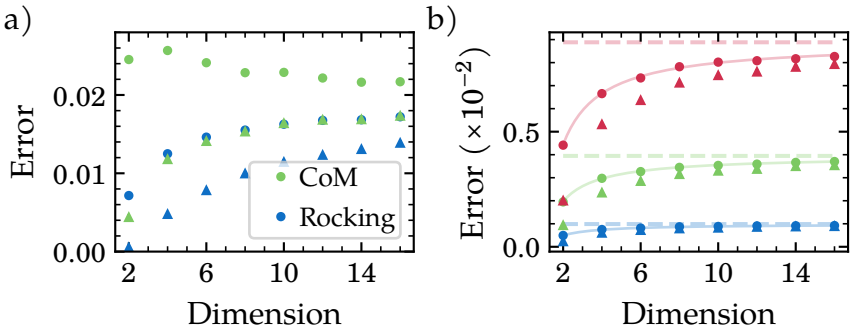



**Figure 5.4:** a) Mean (circles) and median (triangles) errors from 10000 samples of small, LS-type gates as a function of the single-ion Hilbert space dimension $d$. $d^2$-dimensional unitaries of the form $\mathrm{diag}\{e^{i\phi_{\nu,\mu}}\}$ were generated, with the phases $\phi_{\nu,\mu} = (\xi^{(1)}\theta_\nu + \xi^{(2)}\theta_\mu)^2$ having the same structure as the LS unitary (Equation (3.70)). The $d$ angles $\theta_\alpha$ were independently sampled from the same normal distribution in all simulations. Blue points used the mode participation vector $\boldsymbol{\xi}$ for a CoM mode and green points used that for a rocking mode. In both cases, the mean and median appear to converge to the same error at large $d$. b) Mean and median errors from 10000 samples of structureless $d$-dimensional diagonal unitaries $\mathrm{diag}\{e^{i\phi_\nu}\}$, where the $\phi_\nu$ were independently sampled from Gaussian distributions. Different colours correspond to distributions with standard deviations $\sigma_\phi$ of $\{0.01\pi, 0.02\pi, 0.03\pi\}$. The analytical solution for the mean (see text) is shown as a solid line. In all cases, the mean and median tend to an error of $\sigma_\phi^2$ at large $d$.

SDF magnitude, times a factor that depends on the two-beam LS on the relevant states. Thus, we can consider the control miscalibration as a scale, times a factor that depends on the LS structure. To gain some intuition about the dependence of the error in arbitrary LS gates (not just Sleepy Gates) on dimension, we can average the errors that occur with different LS structures for the same control miscalibration.

The primary contribution to the motional errors is from the $e^{-(\bar{n}+1/2)|\Delta\alpha_{\nu\mu,\xi\chi}|^2}$ coefficients[24]. We can expect that, when averaging over all possible LS structures, the mean of these coefficients will be approximately independent of the state indices[25]. This mean will depend on the average motional space excursion for each state, which is independent of dimension. Thus, these motional contributions should approximately act as a constant factor that multiplies all terms in the sum in (5.43), so the error due to these will be independent of the Hilbert space dimension.

[24]The contribution from $\Im(\alpha_{\xi,\chi}\alpha^*_{\nu,\mu})$ is small, since the trajectories $\alpha_{\nu,\mu}$ can be chosen to lie on the same line through the origin with appropriate control of the SDF phases on each ion, in which case $\Im(\alpha_{\xi,\chi}\alpha^*_{\nu,\mu}) = 0$. Thus, even if the phases are set imperfectly, this factor will be small.

[25]This is not exact: the average coefficients do depend on whether any of the indices $\{\nu,\mu,\xi,\chi\}$ are the same. For example, $\left|\Delta\alpha_{\nu\mu,\xi\chi}\right|^2$ independently of the underlying two-beam LSs. However, the proportion of $\Delta\alpha_{\nu\mu,\xi\chi}$ for which indices coincide decreases to zero with dimension, so we can consider most such coefficients to have no coincidences. In that case, the dependence on the indices should vanish.

The contribution from the geometric phase error could be described as an additional small LS gate[26] on top of the ideal unitary, which encodes all the error. This error unitary would add phases of the form[27] $\phi_{\nu,\mu} = (\theta_\nu \xi_1 + \theta_\mu \xi_2)^2$, where the $\theta_\nu$ depend on the two-beam LS on state $|\nu\rangle$ and the control miscalibration, and $\boldsymbol{\xi} = (\xi_1, \xi_2)$ is the mode participation vector of the two ions (see Equation (3.70)). Thus, we can consider the average effect of these small rotations when the $\theta_\nu$ on each state are sampled from independent zero-mean normal distributions with the same standard deviation. Numerical calculations of the mean error as a function of dimension for arbitrary gates with the LS gate structure for a CoM and rocking mode ($\boldsymbol{\xi} = 1/\sqrt{2}(1,1)$ and $\boldsymbol{\xi} = 1/\sqrt{2}(1,-1)$ respectively) are shown in Figure 5.4. It can be seen that the error in both cases asymptotes to a common value at large single-ion dimension $d$. We can also compare this to the fidelity of small diagonal gates with arbitrary structure, $U = \text{diag}\{e^{i\phi_0}, e^{i\phi_1}, ...\}$, where the phases $\phi_i$ are independently sampled from the same zero-mean normal distribution with standard deviation $\sigma_\phi$ (Figure 5.4). It is shown in Appendix A.3 that the average error over these gates when the total Hilbert space dimension is $d$ is $\sigma_\phi^2 d(d-1)/d^2$. Thus, the error becomes asymptotically independent of the dimension and tends to $\sigma_\phi^2$. It seems reasonable that the behaviour of an average LS gate is similar.

#### 5.3.1.2 Errors on the Sleepy Gates

The fidelity for the Sleepy Gates can now be found by substituting the values for $\Delta\Phi_{\nu,\mu}(t)$ and $\Delta\alpha_{\nu,\mu}(t)$ with the LS structure from Figure 4.5. Furthermore, we assume that the motional mode and the phase of the LS force on each ion are chosen[28] to make the SDFs $\Omega_{\nu,\mu}$ from Equation (3.67) zero if the states in each ion are in the same level. We also assume that the two beams used have the same polarisation vector and intensity at each ion, so that $\Omega_{\nu,\mu} = -\Omega_{\mu,\nu}$. In that case, if $|\nu\rangle$, $|\mu\rangle$ are in different levels, $\alpha_{\nu,\mu} = -\alpha_{\mu,\nu} \triangleq \alpha$, $\Phi_{\nu,\mu} = \Phi_{\mu,\nu} \triangleq \Phi$ and $\tilde{\Phi}_{\mu,\nu} = \pi/2$, and all quantities are zero if they are in the same level. Then, we obtain

$$\mathscr{F} = \frac{1}{8}\left(3 + e^{-4(\bar{n}+1/2)|\alpha|^2} + 4\sin\Phi e^{-(\bar{n}+1/2)|\alpha|^2}\right). \tag{5.44}$$

[26] This "phase error" unitary would ignore all motional effects.

[27] Here, we consider all quantities to be real, for brevity.

[28] This is the most common arrangement, often achieved by correctly setting the ion separation if an axial mode is used to mediate the gate [140, 204] or by coupling to a radial rocking mode using lasers perpendicular to the ion chain, as per Chapter 8.

This is the same expression as found in Reference [140] for monoqubits. Thus, we deduce that miscalibration errors in the Sleepy Gates are in fact independent of the number of qubits stored in each ion! Additionally, many of the errors considered in [140] make use of this result, so they can be directly applied. As well as detuning and power miscalibrations, these include errors from variations in the effective Rabi frequency due to a hot spectator mode, or due to Kerr cross-coupling. For brevity, these are not reproduced here.

Again, it appears surprising that control errors in the Sleepy Gates are entirely independent of dimension, and agree exactly with the monoqubit case. However, as shown in Appendix D.2, the unitary for a Sleepy Gate can be expressed as a simple sum over few generalised Pauli operators $\Sigma_z^{\otimes \mathbf{b}}$ (Section 4.2.3). Indeed, suppose that we arrange the states in each ion such that the states with even and odd parity are contained in separate levels, called $\uparrow$ and $\downarrow$ respectively, in which all states observe the same two-beam LS[29]. Then, there are only four possible geometric phases $\Phi_{ij}$ and motional displacements $\alpha_{ij}$ with $i, j \in \{\uparrow, \downarrow\}$ that can be accrued by each two-ion computational state. The $n$-polyqubit Sleepy Gate unitary at arbitrary times can thus be expressed as

$$\begin{aligned} U = \frac{1}{4}\Big[ & D(\alpha_{\uparrow\uparrow}) \otimes e^{i\Phi_{\uparrow\uparrow}} \left(\Sigma_z^{\otimes(\mathbf{0},\mathbf{0})} + \Sigma_z^{\otimes(\mathbf{0},\mathbf{1})} + \Sigma_z^{\otimes(\mathbf{1},\mathbf{0})} + \Sigma_z^{\otimes(\mathbf{1},\mathbf{1})}\right) \\ & + D(\alpha_{\downarrow\downarrow}) \otimes e^{i\Phi_{\downarrow\downarrow}} \left(\Sigma_z^{\otimes(\mathbf{0},\mathbf{0})} - \Sigma_z^{\otimes(\mathbf{0},\mathbf{1})} - \Sigma_z^{\otimes(\mathbf{1},\mathbf{0})} + \Sigma_z^{\otimes(\mathbf{1},\mathbf{1})}\right) \\ & + D(\alpha_{\uparrow\downarrow}) \otimes e^{i\Phi_{\uparrow\downarrow}} \left(\Sigma_z^{\otimes(\mathbf{0},\mathbf{0})} - \Sigma_z^{\otimes(\mathbf{0},\mathbf{1})} + \Sigma_z^{\otimes(\mathbf{1},\mathbf{0})} - \Sigma_z^{\otimes(\mathbf{1},\mathbf{1})}\right) \\ & + D(\alpha_{\downarrow\uparrow}) \otimes e^{i\Phi_{\downarrow\uparrow}} \left(\Sigma_z^{\otimes(\mathbf{0},\mathbf{0})} + \Sigma_z^{\otimes(\mathbf{0},\mathbf{1})} - \Sigma_z^{\otimes(\mathbf{1},\mathbf{0})} - \Sigma_z^{\otimes(\mathbf{1},\mathbf{1})}\right)\Big]. \end{aligned} \tag{5.45}$$

where $(\mathbf{i},\mathbf{j})$ is the concatenation of the two bit-strings $\mathbf{i}$, $\mathbf{j}$ and the bit-strings $\mathbf{0}$, $\mathbf{1}$ are the $n$-bit strings that contain only 0 and 1.

First, we point out that the structure is independent of the number of qubits per ion (and thus the Hilbert space dimension); only the generalised Pauli matrices change with dimension. Thus, it is reasonable that miscalibrations of the same magnitude have the same impact for any number of qubits.

Second, we can also consider the effect on a computational basis state when the gate is rotated into the $x$-basis by surrounding it with appropriate intra-ion gates (see Section 8.1). In that case, we can see that the computational basis is split into disjoint subspaces of

[29] In this case, the gate induced acts on all $2n$ qubits: with 2-polyqubits, this is a $ZZZZ$ gate. Other gates have a very similar structure.

four states that are all mapped between each other[30]. Thus, errors act within these disjoint subspaces equally, independently of the *number* of such subspaces that can be formed.

### 5.3.2 Motional heating

Noisy electric fields, arising mainly from the nearby trap electrodes [205], exert forces on the ion chain, which can be thought of as inducing random, infinitesimal kicks onto the motional state [206]. The Hamiltonian for this process is that of a driven harmonic oscillator (3.52), with a random force $\delta F(t)$.

If the ions are left idle, the average phonon population increases linearly at a rate of $\dot{\bar{n}}$ quanta per second. In addition, since these displacements do not commute, a random phase is acquired, which is global if the atomic and motional states are not entangled. This is not the case during the gate operation so, despite the atomic and motional states disentangling at the end of the gate[31], the atomic states pick up random phases, leading to dephasing.

It can be shown [168, 206] that the evolution of the atomic and motional states is given by the master equation with the Lindblad operators[32]

$$l_{h,1} = \sqrt{\dot{\bar{n}}}\hat{a} \quad , \quad l_{h,2} = \sqrt{\dot{\bar{n}}}\hat{a}^{\dagger}. \tag{5.46}$$

We do not attempt to solve this analytically and instead numerically solve the master equation with the LS Hamiltonian (3.66). The resulting error is shown in Figure 5.5 for a polyqubit and a monoqubit. It is clear that the errors for the same heating rate are identical, and follow the error derived in [140]

$$\varepsilon = \frac{\Delta\bar{n}}{2K} \tag{5.47}$$

where $\Delta\bar{n} = \dot{\bar{n}}\tau_g$ is the change in the mean phonon occupation over the gate time $\tau_g$ and $K$ is the number of loops in the gate.

[30] For example, in 2-polyqubits, population in the $|00{:}00\rangle$ state is constrained to the subspace $\{|00{:}00\rangle, |00{:}11\rangle, |11{:}00\rangle, |11{:}11\rangle\}$.

[31] This occurs even if there is heating. Indeed, since the kicks are independent of the atomic states, they are displaced by the same amount, so as long as the loops would have closed in the absence of noise, they do so with noise too. The errors arise because each atomic state takes a different route in motional phase space.

[32] As argued in Reference [168], since the $Q$ of the motional resonator is very high, only noise in a narrow band around the motional frequency couples to the motion. Thus, even if the noise spectrum is not white, over this band, approximating the spectrum as white is valid, allowing us to use a master equation.

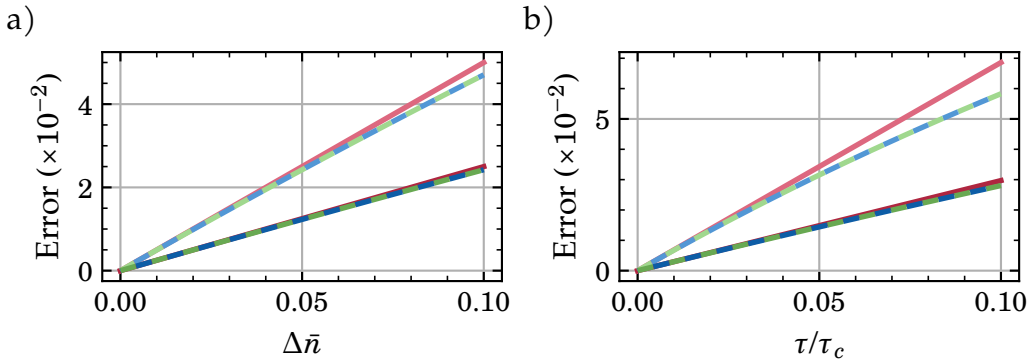



**Figure 5.5:** Simulated errors due to a) motional heating as a function of the change in the thermal population $\Delta\bar{n}$ over a gate and b) motional decoherence as a function of the gate duration normalised to the motional coherence time $\tau_c$. Dashed blue and green traces show errors on 2-polyqubits and monoqubits, respectively, while the red traces show the approximations from Reference [140] (Equations (5.47) and (5.50)). Light and dark traces indicate gates with $K = 1, 2$ loops, respectively. It can be seen that in all cases, monoqubit and polyqubit errors agree exactly.

### 5.3.3 Motional dephasing

Fluctuations in the RF and DC trapping voltages can change the mode frequency by a random amount $\delta\omega$. This is described by the Hamiltonian

$$H = \hbar\,\delta\omega(t)(\hat{a}^\dagger\hat{a} + 1/2) \tag{5.48}$$

whose effect is to change the energy spacing between Fock states. This imparts random phases $\delta\phi_n = n\int\delta\omega dt$ onto the state $|n\rangle$, which leads to motional dephasing. Since the atomic states are entangled with the motion during the gate, the reduced atomic state becomes mixed.

If the spectrum of the frequency fluctuations is white, so that the autocorrelation of the frequency fluctuations is $\langle\delta\omega(t+\tau)\delta\omega(t)\rangle = \Gamma\delta(\tau)$, a master equation can be used to calculate the state evolution, using the Lindblad operator [168]

$$l_d = \sqrt{\Gamma}\hat{a}^\dagger\hat{a}. \tag{5.49}$$

If the motion is left idle, this causes the motional state coherences $\rho_{nm}$ to decay exponentially with a time constant $\tau_{nm} = \tau_c/(n-m)^2$. The coherence time $\tau_c = 2/\Gamma$ is the time constant of the coherence between neighbouring Fock states.

The errors calculated by numerically solving the resulting master equation with the gate Hamiltonian are shown in Figure 5.5 for a polyqubit and a monoqubit. As

with the heating results, the errors in both cases are identical, and agree well with the result from [140]

$$\varepsilon = \alpha_K \frac{\tau_g}{\tau_c} \tag{5.50}$$

where $\alpha_K$ is a coefficient for a $K$-loop gate, found numerically.

Nonetheless, often the noise cannot be accurately described as white. Unfortunately, since the control and noise Hamiltonians do not commute, analytical approaches using Equation 5.10 are intractable. We thus consider static noise via a different approach and describe it as a detuning miscalibration $\Delta_\delta$ that changes every shot according to a normal distribution with RMS $\sqrt{\langle \Delta_\delta \rangle}$. By the results of 5.3.1, we can use the expression for a detuning miscalibration in monoqubits from [140] to calculate the error in a single shot for a polyqubit:

$$\varepsilon_D(\Delta_\delta) = \frac{1 + 2K(1+2\bar{n})}{16K^2} \tau_g^2 \Delta_\delta^2 \tag{5.51}$$

Then, the average error over many shots is

$$\bar{\varepsilon}_D = \frac{1}{\sqrt{2\pi\langle \Delta_\delta^2 \rangle}} \int_{-\infty}^{\infty} e^{-\Delta_\delta^2 / 2\langle \Delta_\delta^2 \rangle} \varepsilon_D(\Delta_\delta) \mathrm{d}\Delta_\delta = \frac{1 + 2K(1+2\bar{n})}{16K^2} \tau_g^2 \langle \Delta_\delta^2 \rangle \tag{5.52}$$

Once again, this expression is identical in monoqubit and polyqubits.

### 5.3.4 Polarisation

In general, the unitary applied by the LS interaction will be a product of generalised $Z$ rotations $R_z^{\otimes \mathbf{b}}(\Omega_{\mathbf{b}} \tau_g)$, whose effective Rabi frequencies depend on the polarisation of the two beams that set up the optical interference pattern. The gate is only a pure generalised rotation (such as an $R_{zz}$ gate) if the polarisation is set to give the correct Sleepy Gates LS structure. Thus, mis-set polarisations will lead to unwanted rotations, which is a coherent error. In monoqubits, this is of little consequence, since all stray rotations are single-ion and can be removed with virtual rotations or using echo sequences. However, in polyqubits, these are generally two-ion, and thus not correctable with virtual rotations.

Making very general statements about these errors is challenging because the SDF coefficients $\Omega_{\nu,\mu}$ (Equation 3.67) depend non-trivially on many parameters - the polarisation angles and directions of two beams. Instead, we provide a general recipe

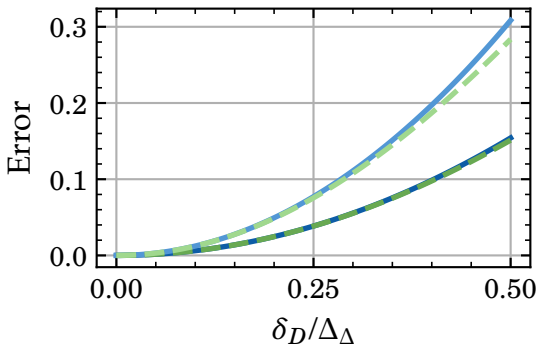



**Figure 5.6:** Simulated error in a 2-polyqubit $ZZZZ$ gate due to non-zero two-beam LS $\delta_D$ between states in the $D$ level, normalised to the differential two-beam LS between states across the $S$ and $D$ levels, $\Delta_\Delta$. The dark blue line is the analytical approximation (5.54) when only $ZZZ$ errors are considered, and the dark green dashed line is a numerical calculation of the GHZ state fidelity, having filtered out single-ion rotations. The light green dashed line is a numerical calculation that includes single-ion rotations, which contribute the same error as $ZZZ$ terms; the light blue line is twice the analytical $ZZZ$ error.

to numerically calculate these errors, and yield some intuition using a specific, yet broadly applicable, case.

The general error is easy to calculate numerically: the effective Rabi frequencies $\Omega_{\nu,\mu}$ are calculated using Equations (3.63), (3.64) and (3.67) from which the gate unitary[33] (3.68) is found. With this, the fidelity of a GHZ state generated using the gate[34], is easily found. Furthermore, the decomposition into generalised $Z$ rotations (4.18) can be used to understand the structure of the errors. This also easily enables the removal of single-ion gates from the final unitary (whose effect can be removed in experiment), if desired.

We now consider having two qubits per ion, under similar assumptions to Section 5.3.1: we assume that the two beams have the same polarisation vectors, in which case all two-beam LSs are real; that the motional mode and LS phase at each ion is chosen so that $\Omega_{\nu,\mu} = \frac{1}{\sqrt{2}}\left(\Omega_\nu^{(1)} - \Omega_\mu^{(2)}\right)$, where $\Omega_\nu^{(i)}$ is the 2-beam LS on state $|\nu\rangle$ in the $i^{\text{th}}$ ion; and that the beam intensity and polarisation at both ions is the same, so $\Omega_\nu^{(1)} = \Omega_\nu^{(2)}$. In this case, mis-set polarisations can only add LSs $\delta_{S/D}$ between the two states in each level, on top of the differential LS $\Delta_\Delta$ across the two levels and a potential common-mode LS $\Delta_\Sigma$. In anticipation of Chapter 8, we will place states $\{|00\rangle, |11\rangle\}$ and $\{|01\rangle, |10\rangle\}$ in the $S$ and $D$ levels, respectively, and we label the atomic states which encode them by the

[33] Assuming loop closure, so $\alpha_{\nu,\mu} = 0$.
[34] See Section 8.1

appropriate decimal number. The two-beam LS on each state is

$$\Omega_{0/3}^{(i)} = \frac{\Delta_\Sigma - \Delta_\Delta \pm \delta_S}{2} \quad , \quad \Omega_{1/2}^{(i)} = \frac{\Delta_\Sigma + \Delta_\Delta \pm \delta_D}{2}. \tag{5.53}$$

With ideal polarisations ($\delta_{S,D} = 0$), this results in a $ZZZZ$ rotation.

The effective Rabi frequencies $\Omega_{\nu,\mu}$ can be calculated from this, which yields the full LS unitary. The full unitary can then be decomposed into generalised $Z$ rotations and the rotation angles $\Phi^{\otimes \mathbf{b}}$ can be found. These are given in Appendix E. The key takeaway is that the $ZZZ$ rotation angles[35] are of order $\frac{\delta_D \pm \delta_S}{2\Delta_\Delta}\Phi$ where $\Phi \triangleq \Phi_{ZZZZ} = \pi/2$ is the $ZZZZ$ rotation angle, and the $ZZ$ terms are of order $\frac{\delta_{S/D}^2}{4\Delta_\Delta^2}\Phi$, which is negligible in comparison for small $\delta_{S/D}$. Then, after evaluating the single-state gate fidelity on $|{+}{+}:{+}{+}\rangle$ using the expression for the $ZZZ$ rotations from Appendix E, we find an error

$$\varepsilon \approx \frac{\pi^2}{16}\frac{\delta_D^2 + \delta_S^2}{\Delta_\Delta^2} \tag{5.54}$$

Figure 5.6 shows the error as a function of stray LS, assuming $\delta_S = 0$ (which is the case with the chosen encoding, see Section 6.2.4). If $\delta_S/\Delta_\Delta \lessapprox 0.01$, the error is small, $\varepsilon \lessapprox 10^{-4}$.

It can be shown that the spin-echo sequence of Chapter 8 eliminates the two $ZZZ$ rotations that do not involve one of the MSB qubits. In this case, the error would be

$$\varepsilon \approx \frac{\pi^2}{32}\frac{(\delta_D + \delta_S)^2}{\Delta_\Delta^2}. \tag{5.55}$$

If $\delta_S = 0$, the echo sequence halves the polarisation error.

## 5.4 Summary

A detailed survey of multiple error sources has been presented. It is found that the effect of intra-ion errors is generally larger on multi-level systems than on monoqubits, which is not surprising [17, 26]. Nonetheless, in many cases, the differences are not vast, particularly with a good choice of atomic states. Detuning miscalibrations are a notable exception to this, since they can lead to non-Markovian errors in many experimentally relevant scenarios. Such errors can be coherently eliminated, but this could not be implemented in the experiments of future chapters, since it was not known at the time.

[35] The $Z$ rotations have identical coefficients to the $ZZZ$ ones, but since they are intra-ion they are not considered.

Contrastingly, we find that the expected errors in multi-level inter-ion gates are very similar to those in monoqubit gates. In fact, the errors for the Sleepy Gates mechanism of Chapter 4 are found to be almost identical. The only additional source of error not present in monoqubit gates arises from mis-set polarisations, which is found to be small.

*The least predictable part of a quantum computing lab is the classical computer.*

— Fabian Pokorny, on the nature of classical and quantum uncertainty.

# 6

# Experimental apparatus and choice of states

In this chapter, we discuss the details of the states that will be used to encode a 2-polyqubit in the experiments of subsequent chapters, and the laser systems used to manipulate it. The experimental apparatus has previously been described in depth in theses written by previous members of the experiment [123, 207], so we will focus primarily on the most relevant systems for the experiments in this thesis.

## 6.1 The $^{137}Ba^{+}$ ion

### 6.1.1 Choice of species

With some exceptions, ions used in QIP experiments are often chosen from the Group 2 alkali-earth metals. The reason behind this is simple: after removing one of the two valence electrons, the remaining single valence electron has a hydrogen-like structure, enabling straightforward Doppler cooling and optical pumping. A noteworthy exception to this rule is the lanthanide $Yb^{+}$. For use in quantum computation, at least two long-lived states must exist in the ion's atomic structure, which is the case with all these species. Most, if not all, contain more than two long-lived states, and thus can be used for multi-level computation[1].

[1] $Lu^{+}$, which has been used in precision spectroscopy [208], is also recently being considered for multi-level computation.

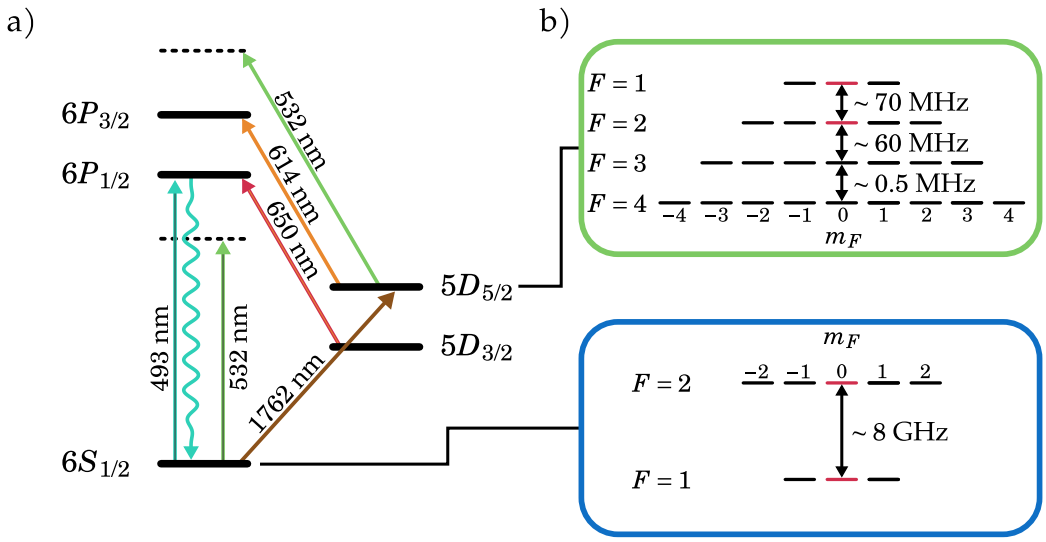



**Figure 6.1:** $^{137}Ba^+$ level structure. a) Coarse level structure showing the fine structure levels and the lasers used to drive them. The 532 nm lasers are not resonant with any transition. b) Hyperfine structure of the $D_{5/2}$ (top) and $S_{1/2}$ (bottom) levels. The states shown in red are used for the polyqubit encoding (see Section 6.2.4 later). The two states chosen in the $S_{1/2}$ level are "clock" states.

The alkali-earth ions all have the same gross level structure, which is shown for $Ba^+$ in Figure 6.1. Long-lived states suitable for computation exist in the ground $S_{1/2}$ level and the metastable $D_{5/2}$ and $D_{3/2}$ levels. The latter cannot decay via dipole-allowed transitions and thus have lifetimes of order 100 ms – 10 s, depending on the species. QIP experiments typically store all computational states in one of the $S_{1/2}$ or $D_{5/2}$ levels, or across them. Transitions between the states are driven using Raman processes or microwaves in the former case, or by directly driving quadrupole transitions using a narrow-linewidth laser in the latter.

Dipole-allowed transitions can be driven between the $S_{1/2}$ level and the $P_{1/2}$ or $P_{3/2}$ levels, which are used for cooling and SPAM – the *dissipative* operations. Which transition is used depends on the choice of ion, available lasers, and compatibility with other experimental protocols. Population in the excited $P$ levels can decay to the metastable $D$ levels as well as the ground $S_{1/2}$ level, with some branching fraction. Thus, a *repumping* laser is needed to prevent population trapping in these levels during dissipative operations. If one of the $D$ levels is used for computation, these lasers can also be used to return the population to the $S_{1/2}$ level.

| Isotope | Nuclear spin $I$ | Abundance (%) | Half-life (years) |
|---|---|---|---|
| $^{130}Ba^+$ | 0 | 0.106(1) | Stable |
| $^{132}Ba^+$ | 0 | 0.101(1) | Stable |
| $^{133}Ba^+$ | 1/2 | Synth. | 10.5379(16) |
| $^{134}Ba^+$ | 0 | 2.417(18) | Stable |
| $^{135}Ba^+$ | 3/2 | 6.592(12) | Stable |
| $^{136}Ba^+$ | 0 | 7.854(24) | Stable |
| $^{137}Ba^+$ | 3/2 | 11.232(24) | Stable |
| $^{138}Ba^+$ | 0 | 71.698(42) | Stable |

**Table 6.1:** Table of nuclear spin, natural abundance and half-life for all $Ba^+$ isotopes with half-life greater than 1 year. Abundances are taken from Reference [210] and nuclear spins and half-lives from Reference [211].

The most important differences between species are the lifetime of the metastable $D$ levels, particularly the $D_{5/2}$ level, and the wavelength of the atomic transitions. The lifetime determines how feasible computation would be in this level. The wavelength influences how easily suitable high-quality optics and lasers can be acquired[2]. In both these respects, $Ba^+$ compares favourably to other species. Its $D_{5/2}$ lifetime is 30.14 s [209], the longest of all alkali-earth metals[3] [48]. This, alongside the heralded SPAM protocol of Section 4.4.1, makes decay errors almost negligible, as discussed in Section 5.2.5. Furthermore, all commonly used transitions are in the visible range, with the notable exception of the $S_{1/2} \leftrightarrow D_{5/2}$ quadrupole transition at 1762 nm. High-quality optics and lasers are cheap and readily available for these optical wavelengths, and do not damage fibre optics as much as UV light, which is needed for all other species. In addition, 1762 nm is sufficiently close to the telecommunication 1550 nm band to exploit the large availability of optics at this wavelength[4].

### 6.1.2 Choice of isotope

If the atomic nucleus has non-zero nuclear spin $\mathbf{I}$, it couples to the total angular momentum of the electron $\mathbf{J}$ via the hyperfine interaction between their magnetic moments. In $Ba^+$, which has an even number of protons, this occurs when the mass number $A$

[2]The transition wavelengths are also relevant to networking experiments, but this will not be discussed here.

[3]The $F_{7/2}$ level in $Yt^+$ is quadrupole-forbidden and thus has a much longer lifetime, but making use of this transition involves significant technical complexity.

[4]At least in theory; in practice, the proportion of optics in our experiment for which 1762 nm is *within* spec is vanishingly small. However, in most cases, this just reduces the efficiency and does not lead to errors.

is odd (making the number of neutrons odd). When the nuclear spin is non-zero, $I = (2n+1)/2$, so the number of atomic states available is thus multiplied by $2I+1$ compared to the spinless case.

Isotopes with hyperfine structure have attractive atomic properties, in particular clock transitions. These transitions are linearly insensitive to magnetic field fluctuations (see Section 6.2.2). Furthermore, when illuminated by light that is far off-resonant from a dipole-allowed transition, these clock states feel the same LS. This is crucial for the Sleepy Gate mechanism of Section 4.2.

Nonetheless, hyperfine structure also often comes at the cost of more complex cooling and state-preparation[5] operations [198, 212]. The larger number of atomic states also leads to larger spectral crowding, so off-resonant excitation and undesired LS are more problematic. For multi-level computation, as long as the nuclear spin is not too high, the advantages of hyperfine structure outweigh its disadvantages.

A list of isotopes of $Ba^+$ along with their natural abundance is shown in Table 6.1. Of the odd isotopes, the choice[6] is between the spin-1/2 $^{133}Ba^+$ and the spin-3/2 $^{137}Ba^+$.

The low nuclear spin of $^{133}Ba^+$ makes this species particularly attractive, as it enables simple frequency-selective optical pumping schemes for state preparation [160]. However, because it is a synthetic radioisotope, it is challenging to work with due to the low quantities that can be used while complying with safety guidelines.

Because of this, we use $^{137}Ba^+$, whose popularity for high-dimensional QIP experiments is rapidly increasing [26, 27]. Despite the sizeable nuclear spin, high-fidelity SPAM [18, 161] and efficient cooling [212] has been demonstrated. In fact, its large number of states has been used to demonstrate operations of qudits of dimension 8 [27] and 25 [26], the latter of which would have been impossible with $^{133}Ba^+$.

### 6.1.3 Level structure

The relevant level structure of $^{137}Ba^+$ is shown in Figure 6.1. Quantum information can be stored in the $S_{1/2}$ or $D_{5/2}$ levels, which contain 8 and 24 states each. Each of these levels

[5] Spin-$\frac{1}{2}$ species are an exception, since state-preparation into the single $F = 0$ state in the $S_{1/2}$ manifold can be easily done with frequency selectivity [160].

[6] $^{135}Ba^+$ has the same spin as $^{137}Ba^+$ but half the natural abundance, and so is ignored.

is further split into manifolds[7] of states with quantum number $F$, which is defined later. The $S_{1/2}$ level has $F = \{1,2\}$ and the $D_{5/2}$ level has $F = \{1,2,3,4\}$.

As will be discussed later, the polyqubit will be stored across the $S_{1/2}$ and $D_{5/2}$ levels, so the quadrupole transition between them is used for QIP. This is driven by a 1762 nm laser. At the end of a computation, population is flushed out of the $D_{5/2}$ level via the 614 nm transition to the $P_{3/2}$ level, which decays to the $S_{1/2}$ level. The $S_{1/2} \leftrightarrow P_{1/2}$ transition at 493 nm is driven for dissipative operations, while simultaneously driving the $D_{3/2} \leftrightarrow P_{1/2}$ transition at 650 nm to repump any population in $D_{3/2}$. Decay from the $P_{1/2}$ to this level has a particularly large branching ratio of $\sim 0.27$ in $Ba^+$ [213]. Furthermore, a 532 nm laser is also present in the system, which is off-resonant from the dipole transitions between the $S_{1/2}$ and the $P$ levels, as well as the $D_{5/2} \leftrightarrow P_{3/2}$ transition, by comparable detunings. Thus, light at this frequency induces large LSs on states in the $S_{1/2}$ and $D_{5/2}$ levels, which will be used in the implementation of the Sleepy Gates in Chapter 8. Pairs of 532 nm beams can also drive two-photon Raman transitions within either manifold, a feature that is unique to $Ba^+$ [18, 157]. Such transitions will only be used in this thesis for sideband cooling.

## 6.2 Choosing the computational manifold

### 6.2.1 Key design desiderata

Properly designing a polyqubit system involves, amongst other things, choosing the set of atomic states that will be used to encode the computational manifold. The best choice is that which minimises the intra-ion and inter-ion gate errors outlined in Chapter 5. While it is possible to choose separate manifolds for each type of operation and transfer population between them when needed, this would increase the number of calibrations required and introduce errors due to the mapping. Thus, a single manifold that can be used for both operations is desired.

The principal desiderata for driving intra-ion TSRs are the following:

[7] Due to intermediate-field effects, described later, $F$ is not a good quantum number, which is discussed in 6.2.2.

1. Low magnetic field sensitivity[8], to reduce decoherence. This is quantified by the sensitivity magnitude from (5.26).

2. Fast Rabi frequencies. By minimising the duration of pulse sequences, the time over which errors can affect the circuit is reduced. This also reduces the sensitivity to errors from breaking the multi-photon resonance condition, since their impact worsens over time.

3. Wide spectral separation between transitions, to prevent off-resonant excitation both within the manifold and to spectators. The latter can be mitigated with the heralded SPAM protocol (Section 4.4.1), though a large decrease in data rate would occur if there is too much excitation. This also reduces the magnitude of the terms in the LS matrix.

4. Sufficiently high connectivity. As shown in Section 4.1.1, a connectivity graph with four edges is able to implement single-qubit gates without additional transfer pulses. Additional transitions increase the native expressivity, but do not improve the ability to implement a minimal universal gate set. If only three transitions are present, either two or four additional pulses are required per single-qubit gate for star or linear connectivities.

We neglect errors due to state decay and laser scatter, since these are minor in comparison to the ones listed above. Other errors are independent of the choice of manifold.

The main desideratum for implementing intra-ion Sleepy Gates is that the states in the manifold exhibit the LS structure from Figure 4.5. This is determined both by the atomic states and the polarisation of the beams used to drive the gate. Ideally, the states would exhibit a large LS for a given laser intensity, since that allows lower laser powers to be used for the gate operation.

In practice, it may not be possible to find states that exactly replicate the Sleepy Gate LS structure, particularly for storing more than two qubits per ion. However, as discussed

[8]There is a $\mu$-metal enclosure in our experiment, which would alleviate most issues from magnetic field noise. However, we discovered that there is a source of noise *inside* the box, which we were not able to identify – it was present even with all the electronics other than the trap voltages off. It was easier to find field-insensitive states than to resolve this.

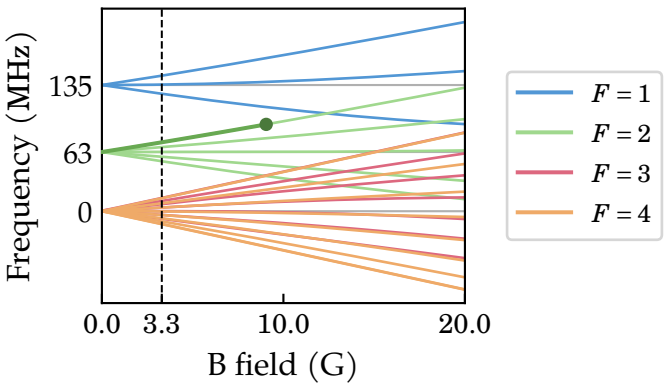



**Figure 6.2:** Breit-Rabi diagram for the $D_{5/2}$ level, which shows the frequency $\omega_\nu = E_\nu/\hbar$ of a state with energy $E_\nu$ (relative to the $F = 4$ manifold at 0 field). Each hyperfine manifold is coloured according to the legend. The frequency of each state relative to the $F = 4$ manifold at 0 field is shown (except for the $F = 3$ manifold, which is only separated by $\sim 0.5$ MHz from it). The magnetic field used in experiment is shown as a black dashed line. We can label a state in the intermediate field regime, whose energy is given by the green circle, by finding the state that it would be transformed to if the magnetic field were adiabatically turned off (thick green line).

in Section 5.3.4, the gate is quite tolerant to small deviations from the ideal LS structure, requiring a significant departure from it to induce large errors. Indeed, for 2-polyqubits, as long as the ratio of the intra-level LS $\delta$ to the LS between levels $\Delta$ is $\delta/\Delta \lesssim 1\%$, the error introduced is unlikely to be dominant (although, in a two-qubit gate, the error would be multi-qubit). If such a bound could not be reached, echo sequences such as those discussed in [141] could be used to filter out contributions from unwanted rotations.

### 6.2.2 The intermediate-field regime

The hyperfine splitting of states arises primarily[9] from a coupling between the magnetic field at the nucleus generated by the orbiting electron with total angular momentum $\mathbf{J}$, and the nuclear magnetic moment with angular momentum $\mathbf{I}$. This leads to a coupling Hamiltonian of the form $H_{HFS} = A_{HFS}\mathbf{J}\cdot\mathbf{I}$ with the hyperfine coefficient $A_{HFS}$ [122]. The atomic states are thus eigenstates $|F, m_F\rangle$ of the total angular momentum operator $F^2$ (with $\mathbf{F} = \mathbf{J} + \mathbf{I}$) and its $z$ projection $F_z$. The states are eigenstates of the electronic and nuclear angular momenta $J^2$, $I^2$, but not their $z$-projection. In this *low-field regime*, the states' magnetic field sensitivity is proportional to their $m_F$ quantum number, and transitions obey hyperfine selection rules.

[9] A coupling between the nuclear electric quadrupole moment and the electronic distribution is also present [214].

This is in the absence of any external magnetic field, which would couple to **J** and **I** independently. A strong field would overpower the hyperfine interaction Hamiltonian and decouple **I** and **J**. This would make the atomic states eigenstates of the $z$-components of the angular momenta, $|m_J, m_I\rangle$. In this case, $F$ and $m_F$ are not good quantum numbers. This is the *high-field* regime, where, since the nuclear magnetic moment is around three orders of magnitude smaller than the electronic one, the magnetic field sensitivity is proportional to $m_J$. Furthermore, transitions obey fine-structure selection rules, and the transition frequency between neighbouring states is the same for all states in an $F$ manifold.

Between these two extremes, neither of $F$, $m_F$ or $m_J$, $m_I$ are good quantum numbers – although $m$, the total $z$-projection of angular momentum always is. In this case, states become *mixed* and can be described as a superposition of high-field or low-field basis eigenstates. However, we can still label the states by $|F, m_F\rangle$, according to the state which would be reached if the magnetic field were adiabatically reduced to 0 (see Figure 6.2).

In this *intermediate-field* regime, the state energies depend non-linearly on the magnetic field. It can occur that two states have the same magnetic field sensitivity, in which case the frequency of the transition between them has no linear dependence on the field. Making use of these *clock* transitions greatly reduces errors due to magnetic field fluctuations. Clock transitions are present in the low-field regime between states with $m_F = 0$, since their energy does not depend on the magnetic field. Furthermore, transitions in this regime don't obey any particular selection rule. In general, useful clock manifolds of more than two states are very rare in alkali-earth metals, although approximate manifolds do exist.

The intermediate-field regime is entered when the energy of the hyperfine and magnetic coupling strengths become comparable. Crudely, this is when $\frac{2\mu_B B}{\hbar}$ is comparable to the hyperfine splitting between $F$ manifolds. In the $S_{1/2}$ level, whose manifolds are split by 8 GHz, this occurs at ~ 2800 G. However, the splittings in the $D_{5/2}$ level are much smaller, as can be seen in Figure 6.2: the $F = 3$ and $F = 4$ manifolds are only separated by ~ 0.5 MHz and thus mix almost immediately. The other manifolds are separated by ~ 70 MHz and thus mix at ~ 20 G.

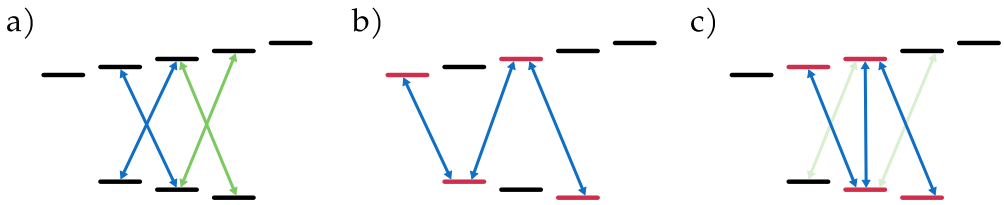



**Figure 6.3:** a) Because the $S_{1/2}$ manifold is in the low-field regime, transitions within the same $F$ manifold are degenerate in frequency, as are some transitions between manifolds, shown by arrows of the same colour. b) An option for a $S_{1/2}$ level manifold, where the chosen states are shown as red lines. It does not use the clock states at the centre, but no spectator transition is degenerate with a transition between states in the encoding. c) An option that does use the clock states, but some spectator transitions (shown in light green) are degenerate with the $\Delta m_F = -1$ transitions in the encoding. Exquisite polarisation control is required to avoid large leakages out of the manifold.

Thus, low-field intuitions can only be used for states in the $S_{1/2}$ level and for states in the $F = 1,2$ manifolds in the $D_{5/2}$ level at very low fields. For reasons discussed in Section 6.2.4, the magnetic field used in the experiment is $\sim 3.38$ G.

### 6.2.3 Ground, metastable or both?

The experimental apparatus is capable of manipulating a polyqubit stored entirely within the $S_{1/2}$ or $D_{5/2}$ levels, or across them. TSRs in the first two would be driven by Raman transitions, and by quadrupole transitions in the latter. Thus, we can search over all possible options to find a suitable manifold.

#### 6.2.3.1 Ground manifold

The $S_{1/2}$ level only contains 8 states and is firmly in the low-field regime, meaning that the number of experimentally viable manifolds of 4 states can be easily reasoned about. Firstly, transitions within the same $F$ manifold cannot be resolved, so they cannot be driven without coupling more than two states together, which is undesirable. Thus, only transitions *between* manifolds can be driven, which in most situations must obey $|\Delta m_F| = 0,1$ [75].

This restricts the choices to broadly two types of manifold [75], shown in Figure 6.3. One option only uses transitions with $\Delta m_F = 1$, which forbids the use of the clock transition between the $m_F = 0$ states, and forces the use of the extremal states that have a sensitivity of $\frac{\mu_B}{\hbar} = 2\pi \times 1.4$ MHzG$^{-1}$. Thus, the sensitivity magnitude is $|\Xi_B| = 0.70$ MHzG$^{-1}$. Alternatively, the clock transition could be included, though exquisite

polarisation purity is required to avoid driving spectator transitions, since the transitions to the two $\Delta m_F = 1$, or $\Delta m_F = -1$, are degenerate (see Figure 6.3). Furthermore, the magnetically sensitive $|m_F| = 1$ states must then be used, so the $|\Xi_B| = 0.31$ MHzG$^{-1}$.

Nonetheless, a manifold with the Sleepy Gate LS structure is present: the four $m_F = \pm 1$ states shift pairwise if illuminated by two counter-propagating beams of the same polarisation.

#### 6.2.3.2 Metastable manifold

Similar intuition is difficult to apply to manifolds encoded in the $D_{5/2}$ level. Firstly, there are many states available (24), which not only means that the number of possible manifolds is large ($\sim 10\,000$), but also makes avoiding very nearby spectator transitions challenging. Furthermore, the intermediate field effects modify the states' sensitivities and the transition strengths in non-trivial ways.

Thus, a cost-function is often used to find an optimal manifold according to certain criteria [26, 27], which was also done by the author in [48]. Even with this, finding encodings with low field sensitivities is non-trivial. Indeed, since states in the $D_{5/2}$ level have large values of $m_F$, the mean absolute sensitivity over all states in the $S_{1/2}$ and $D_{5/2}$ levels is 0.7 MHzG$^{-1}$ and 2.23 MHzG$^{-1}$ respectively (at 3.38 G). Thus, the encoding[10] used in [48] has a sensitivity magnitude of $|\Xi_B| = 1.11$ MHzG$^{-1}$.

#### 6.2.3.3 Optical manifold

Finally, the manifold could be spread across the two levels. Despite the fact that this *increases* the number of states to choose from, some physical intuition can be used to drastically reduce the number of reasonable options. Indeed, it seems reasonable to pick two states in each level, in which case we can pick the two $m_F = 0$ magnetically insensitive states in the $S_{1/2}$ level over a wide range of magnetic fields. Then, we must simply find a pair of states in the $D_{5/2}$ level that also have no magnetic field sensitivity.

This is less common than finding a clock transition, since we are not just imposing that the two states have the same sensitivity, but also that it is 0. Nonetheless, such states do exist: indeed, since the $F = 1$ and $F = 2$ manifolds in the $D_{5/2}$ level do not immediately mix,

[10] This used a field of 20 G.

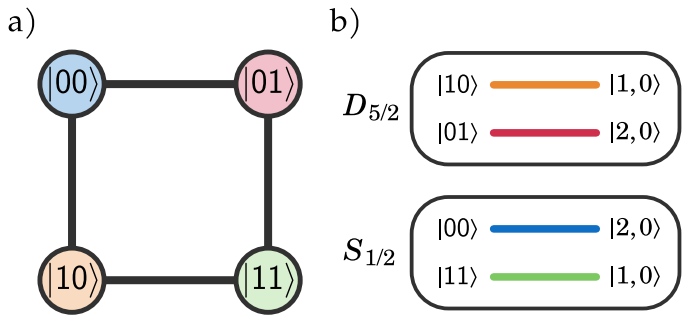



**Figure 6.4:** Sketch of the chosen computational manifold. a) The connectivity graph with the logical states. Colours match the logical state to the atomic state, shown in b). b) Map between the computational (left) and atomic states (right). The even parity $\{|00\rangle, |11\rangle\}$ are stored in the $S_{1/2}$ clock states, and the odd parity $\{|01\rangle, |10\rangle\}$ states are in the mirrored states in the $D_{5/2}$ level.

| Atomic transition | Logical transition | $\frac{d\omega}{dB}$ ( kHzG$^{-1}$) | $\Omega$ ( kHz) |
|---|---|---|---|
| $\|S_{1/2},2,0\rangle \leftrightarrow \|D_{5/2},2,0\rangle$ | $\|00\rangle \leftrightarrow \|01\rangle$ | $-1.3$ | 34.8 |
| $\|S_{1/2},2,0\rangle \leftrightarrow \|D_{5/2},1,0\rangle$ | $\|00\rangle \leftrightarrow \|10\rangle$ | 276.2 | 2.9 |
| $\|S_{1/2},1,0\rangle \leftrightarrow \|D_{5/2},2,0\rangle$ | $\|11\rangle \leftrightarrow \|01\rangle$ | 2.0 | 11.0 |
| $\|S_{1/2},1,0\rangle \leftrightarrow \|D_{5/2},1,0\rangle$ | $\|11\rangle \leftrightarrow \|10\rangle$ | 279.5 | 72.4 |

**Table 6.2:** Properties of the chosen manifold, calculated with the magnetic field and beam parameters measured in Sections 7.2.1.1 and 7.2.1.2 .

we may expect that the $m_F = 0$ states in these manifolds may *retain* their 0 field behaviour up to a few Gauss. In this case, they would remain approximately field insensitive.

Furthermore, clock states within the same manifold naturally experience the same dipole LS when illuminated with off-resonant light [123, 215]. However, this relies on symmetries in the electronic states, which are not present across levels. Thus, at 0 field, we expect the four states described above to exactly display the Sleepy Gate LS structure: clock states within each level will experience no differential LS, but an LS will be present between the *pairs* of states. Again, it can be hoped that this behaviour will be retained at low fields.

This intuition is in fact correct, as will be seen in the next section.

### 6.2.4 Properties of the chosen manifold

The states chosen for the manifold are shown in Figure 6.4. The polyqubit states are spread across these states in a way that optimises for driving single-qubit gates (see Section 4.1). In addition, relevant properties of the states are given in Table 6.2, using the magnetic field and beam parameters measured in Sections 7.2.1.1 and 7.2.1.2. All transitions have $\Delta m_F = 0$ and $|\Delta F| = 0, 1$. The $|\Delta F| = 0(1)$ transitions drive TSRs that

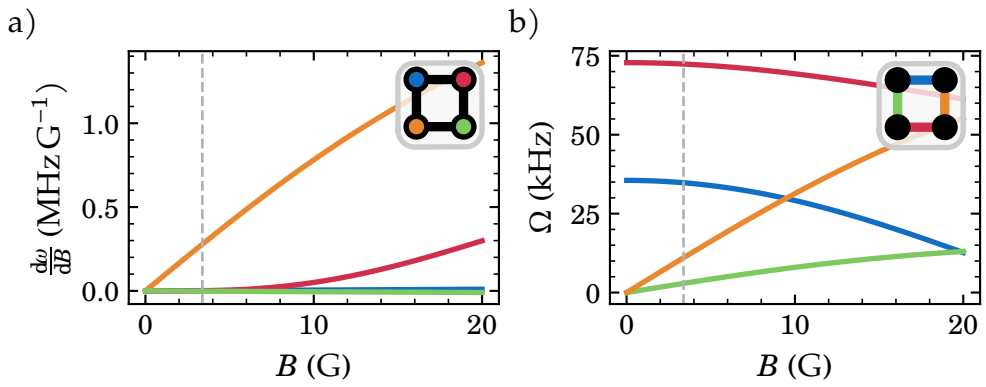



**Figure 6.5:** Calculated properties of the chosen manifold as a function of magnetic field. a) Magnetic field sensitivity of the state in the manifold (inset) with the same colour as the line, in angular units. b) Like a), but showing the Rabi frequency of the transition driven on the edge of the same colour in the manifold in the inset. The measured beam parameters of Figure 7.2 are used in the calculation.

implement single-qubit gates on the LSB (MSB) qubit.

Due to the intermediate field effects, the properties of the manifold change significantly over a small range of magnetic field. From the arguments in the previous section, it appears that the lowest field which enables sufficient spectral separation from spectator transitions is desired. However, the Rabi frequencies of the two $|\Delta F| = 1$ transitions vanish at 0 field[11] (Figure 6.5). As such, *some* amount of state mixing is necessary to allow these transitions to be driven. However, as expected, the magnetic field sensitivities of the states in the $D_{5/2}$ level quickly deviate from 0, particularly the $|D_{5/2}, 1, 0\rangle$ state. A field of ~ 3.4 G was found to be a good compromise between these two effects. At this field, the magnetic field sensitivity magnitude is $|\Xi| = 0.10$ MHzG$^{-1}$.

Nonetheless, the Rabi frequency of the $|S_{1/2}, 2, 0\rangle \leftrightarrow |D_{5/2}, 1, 0\rangle$ and to a lesser extent the $|S_{1/2}, 1, 0\rangle \leftrightarrow |D_{5/2}, 2, 0\rangle$ transition are still very small compared to the other transitions. This extends the duration of experiments, and makes driving each qubit asymmetric, since the two slower transitions drive the MSB qubit. This is the biggest disadvantage of this manifold.

The transitions are well resolved, both from each other and from spectators. Transitions from the same $S_{1/2}$ ($D_{5/2}$) state are separated by the splitting between the $D_{5/2}$ ($S_{1/2}$)

[11] The author believes this to be the quadrupole equivalent of the $m_F = 0 \nleftrightarrow m_F = 0$ for $\Delta F = 0$ selection rule for dipole transitions, but was unable to find further information on this.

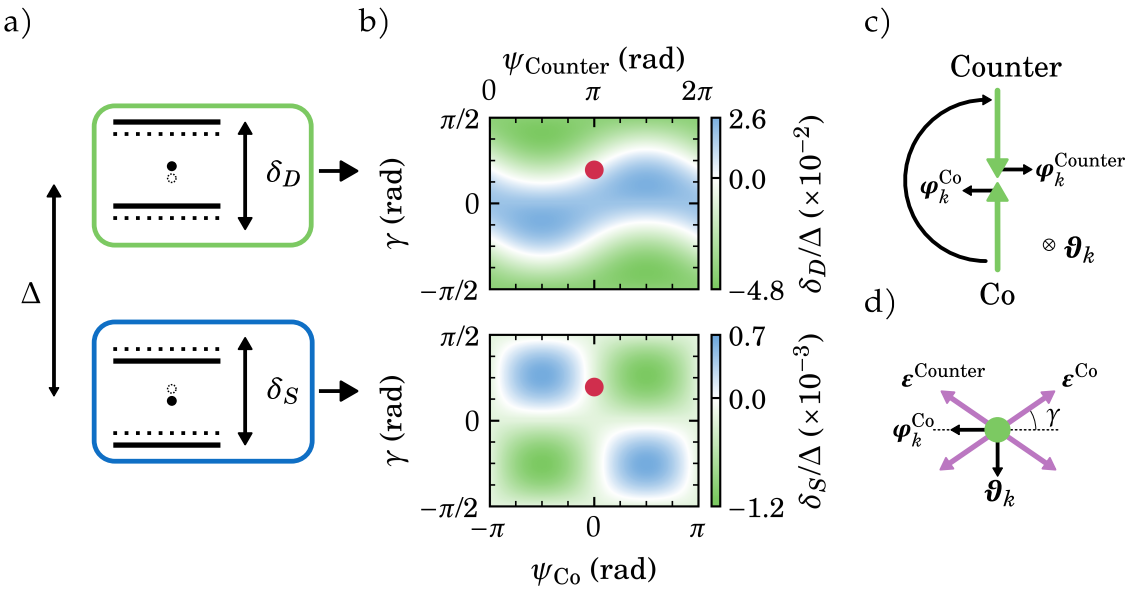



**Figure 6.6:** a) Sketch showing the differential LS between the two levels $\Delta$, which is the shift on the centre-of-mass energy of the two manifolds (shown as a dot). The LS within the levels are $\delta_{S/D}$. b) Ratio $\frac{\delta_D}{\Delta}$ (top) and $\frac{\delta_S}{\Delta}$ (bottom) as a function of the polarisation angle of two counter-propagating beams which are assumed to have the same polarisation vector $\hat{\boldsymbol{\varepsilon}}(\gamma, \psi_{\text{Co}}) = \hat{\boldsymbol{\varepsilon}}(\gamma, \psi_{\text{Counter}})$. The co-propagating beam is assumed to travel at an angle $\vartheta_k^{\text{Co}} = \frac{3\pi}{2}$ to the quantisation axis, as does the co-propagating 532 nm beam in our experiment. c) The $\hat{\boldsymbol{\varphi}}_k$ vector for two counter-propagating beams points in opposite directions. Because of this, two beams with the same $(\gamma, \psi)$ do not have the same $\hat{\boldsymbol{\varepsilon}}$, as shown in pink in the side-view in d). The $\hat{\boldsymbol{\vartheta}}_k$ vector for both beams does coincide, and point into the page in c) and downwards in d).

states, which is 72.2 MHz (8.04 GHz) respectively. Thus, the expected intra-encoding excitation error is $\approx 6.3 \times 10^{-7}$. The closest spectators are transitions to neighbouring $S_{1/2}$ level states, which are 2.37 MHz away. The nearest spectator state in the $D_{5/2}$ level is the $|D_{5/2}, 2, -1\rangle$ state, which is 5.15 MHz away from $|D_{5/2}, 2, 0\rangle$. The expected off-resonant excitation error to spectators is $4.62 \times 10^{-4}$.

#### 6.2.4.1 Two-beam light shifts

As discussed earlier, we expect the manifold to naturally display the correct LS structure for implementing the Sleepy Gates. Figure 6.6 shows that this is the case, at least in certain situations. It shows the calculated two-beam LS due to the intensity field set up by two beams travelling in opposite directions (a co- and a counter-propagating beam) which have the same polarisation vector $\hat{\boldsymbol{\varepsilon}}$. Note that, since the $\hat{\boldsymbol{\varphi}}$ vectors associated to each beam point in opposite directions, for the two beams to have the same $\hat{\boldsymbol{\varepsilon}}$, their angles $\psi$ must be offset by $\pi$ (see Figure 6.6c, d). The two-beam LS $\delta_S$ between the

$S_{1/2}$ level states is negligible and, for the correct choice of polarisation, the two-beam LS $\delta_D$ between the $D_{5/2}$ states is nulled. Even if the polarisation is mis-set, the largest two-beam LS between the $D_{5/2}$ states is $0.048\,\Delta$, where $\Delta$ is the differential two-beam LS between the pairs of $S_{1/2}$ and $D_{5/2}$ states. From Section 5.3.4 we expect this to induce a maximum error of $1.42 \times 10^{-3}$. However, Figure 6.6 is only a slice of a very large parameter space comprising all polarisation angles of both beams. There are combinations of polarisation, even for counter-propagating beams, which would lead to higher errors, as discussed in Section 8.6.1.5.

#### 6.2.4.2 Alternative choice of manifold

Two other states in the $D_{5/2}$ level, $|D_{5/2}, 3, -1\rangle$ and $|D_{5/2}, 4, 1\rangle$, also have very low magnetic field sensitivities – they are slightly lower than the sensitivity of $|D_{5/2}, 1, 0\rangle$. Additionally, their Rabi frequencies for transitions to the ground clock states are faster than from $|D_{5/2}, 1, 0\rangle$. However, they were not chosen because of the presence of very nearby spectators at $\sim 0.46$ MHz. As well as increasing the off-resonant excitation errors by about a factor of 5 (though this could be mitigated with the heralded SPAM protocol), the LS would become significantly larger. For intra-ion gates, shortening the duration of circuits may have reduced the impact of errors from breaking the multi-photon resonance condition, although since $\bar{\omega}_l$ may be made larger by the light shifts (Section 5.2.1), these effects could cancel.

## 6.3 More than two qubits per ion

The number of qubits that can be stored in a single ion for computation is limited not by the total number of states in the ion, but rather by the number of states in the $D_{5/2}$ level that can be used for hiding during readout[12] (Section 4.4). It must be possible to hide all but one of the states in this level, so the maximum number of qubits that can be stored is $n_{max} = \lfloor \log_2(n_D + 1) \rfloor$, where $n_D$ is the number of states in the $D_{5/2}$ level. In $Ba^+$, $n_{max} = 4$. Ions with higher nuclear spin such as the spin-7/2 $^{43}Ca^+$ or the spin-9/2 $^{87}Sr^+$

[12] In principle, this restriction could be sidestepped by not directly reading out the data ions and instead swapping one or more qubits to auxiliary ions. The number of qubits per ion is then limited by the total number of states across both levels. However, this requires inter-ion gates and the ability to individually read out ions, without resorting to frequency selectivity.

could store up to 5 qubits. While using such high-spin species can increase the complexity of operations such as SPAM, they bring other advantages, as will be discussed.

The primary difficulty in storing more than two qubits per ion arises from the fact that many of the desiderata in Section 6.2.1 rely on being able to find sets of states with comparatively rare properties. This is particularly the case when considering errors due to magnetic field noise, and finding a set of states that displays the Sleepy Gates LS structure. Thus, as the number of states necessary to host the computational manifold increases, the probability that all of them exhibit these rare properties diminishes. These considerations are identical to those involved when storing large-dimensional qudits in an ion [26].

### 6.3.1 Intra-ion gates

#### 6.3.1.1 Magnetic field sensitivity

We wish for the states in the computational manifold to have a low relative magnetic field sensitivity. However, as the number of states required to store many qubits increases exponentially, finding sets of states that all display this becomes rare, as discussed previously. Furthermore, in order to store many qubits, the number of computational states that are stored in the $D_{5/2}$ level is likely to increase. As mentioned in Section 6.2.3, these states tend to have larger magnetic field sensitivities than those in the $S_{1/2}$ level, which makes finding a set of states with low relative sensitivities challenging. Nonetheless, using species with a large nuclear spin can be beneficial for this. This is because while the number of states increases with $I$, the largest magnetic field sensitivity of any state in a given level does not. Thus, more states with comparatively low sensitivity exist [216]. As an example, the sensitivity of the ground-level $|m_F| = 1$ states in a spin-3/2 and spin-7/2 alkali-earth species is 700 kHzG$^{-1}$ and 350 kHzG$^{-1}$ respectively, while the maximum sensitivity in the $S_{1/2}$ level is 1400 kHzG$^{-1}$. If needed, these errors could also be mitigated by means of a $\mu$-metal shield or active stabilisation of the magnetic field [217].

#### 6.3.1.2 Rabi frequency

We also wish for fast Rabi frequencies. As long as the polarisation of the drive field is chosen to have roughly equal strengths for all the beam tensor components (See Section 3.5), the Rabi frequencies of most transitions are of a similar order of magnitude [26].

Thus, the average Rabi frequency of TSRs can likely be kept high as the number of qubits per ion increases.

#### 6.3.1.3 High connectivity

Connectivity graphs with high connectivity are likely to become rare with increased qubits per ion. Indeed, the generalisation to $n$ qubits of the connectivity graph that optimally drives single-qubit gates (the connectivity graph with a square) would be a graph in which all edges in an $n$-hypercube are allowed, so single-qubit gates can be driven in $2^{n-1}$ TSRs. For 3 qubits per ion, this already requires at least 12 transitions with a very particular structure. Indeed, if the states are spread across two levels and only transitions between them are allowed (as in an optical manifold), such a connectivity graph cannot be implemented. Thus, it is likely that a sub-optimal decomposition of single-qubit gates would be used with more than two qubits per ion, though even the optimal decomposition would require a large number of pulses per gate.

#### 6.3.1.4 Spectral separation and crosstalk

The spectral separation between transitions both within the encoding and to spectators is likely to increase with the number of qubits, as more transitions need to be driven. This would lead to larger off-resonant excitation errors. Nonetheless, previous studies found that these errors do not increase drastically with dimension [26].

#### 6.3.1.5 Discussion

Overall, it is likely that the errors in intra-ion operations will increase with the number of qubits in the ion, but this increase may not be drastic. Indeed, single-ion algorithms with 3-monoqubits have been demonstrated using $Ba^+$. In [27], Grover's algorithm was run, producing outcomes that were in close agreement with the ideal ones, and the Bernstein-Vazirani algorithm was shown in [26]. In the latter reference, Ramsey experiments with qudits up to 25 states were carried out, where it was found that the error with 16 states, sufficient to encode 4 qubits, was not yet dominated by magnetic field noise. This suggests that the atomic properties of the states were sufficiently close to the ideal to not be the main source of error.

### 6.3.2 Inter-ion gates

To drive the Sleepy Gates, the states in each ion must split into two halves that each observe the same LS. For 3-polyqubits, each half would contain 4 states.

While a natural choice for this would be to split the states evenly across the $S_{1/2}$ and $D_{5/2}$ levels, this may not be sufficient, because states within each level observe significant differential shifts. Indeed, the states in the $S_{1/2}$ level naturally split up into pairs of states with similar LSs (e.g. $\{|S_{1/2},1,0\rangle, |S_{1/2},2,0\rangle\}$, $\{|S_{1/2},1,+1\rangle, |S_{1/2},2,-1\rangle\}$) but the different pairs observe different LSs. Contrastingly, finding sets of states in the $D_{5/2}$ level with similar LSs is more likely, due to the many states available and intermediate-field effects. For example, the two $D_{5/2}$ states in the encoding alongside the alternative states from Section 6.2.4.2 form a set of 4 states with similar LSs.

Nonetheless, it may be possible to use other techniques to mitigate the inhomogeneity in the $S_{1/2}$ level LSs. As with the magnetic field sensitivity, choosing a high-nuclear-spin species may result in a smaller differential LS between the aforementioned pairs of states in the $S_{1/2}$ level, although this may be by an insufficient amount. Additionally, we can use the fact that the magnitude of the light shift is inversely proportional to the detuning between the beam and the dipole transitions it off-resonantly couples to (Section 3.3.2). Thus, if we choose a beam whose frequency is much closer to the $D_{5/2} \leftrightarrow P_{3/2}$ transition than to the $S \leftrightarrow P$ transitions, the LSs on the $S_{1/2}$ level states, and thus the *difference* between them, will be much smaller than those in the $D_{5/2}$ level. This idea was used in reference [153] in the context of qudit gates (although there the laser was tuned close to the $S_{1/2} \leftrightarrow P_{1/2}$ transition to minimise the LS on the $D_{5/2}$ level states). Because the frequency difference between the transitions from the $S_{1/2}$ and $D_{5/2}$ levels to the $P$ levels is particularly small in $Ba^+$, this species is likely not well-suited to this scheme. Alternatively, it may be possible to use multiple beams at different frequencies to null the differential LS in the $S_{1/2}$ level, at the cost of experimental complexity. Techniques like these may lighten the burden of finding states that natively exhibit the desired atomic properties. Nonetheless, finding states in the $D_{5/2}$ level that see no differential shift would be necessary, which may be difficult when going past 3-polyqubits.

Finally, if it is still not possible to engineer the correct LS structure, echo sequences such as those discussed in [141] can be used to generate a pure two-qubit gate.

## 6.4 Laser systems

We will now describe the laser systems used to drive intra- and inter-ion gates (the 1762 nm and 532 nm lasers, respectively).

### 6.4.1 Control system

The power in all lasers is controlled using an acousto-optic modulator (AOM). In addition, a photodiode pickoff near the trap is used to implement a PID feedback loop[13] to actively stabilise this power. The laser frequencies are also controlled through the frequency of the RF sent to these AOMs, with the notable exception of the 1762 nm beam, for which an electro-optic modulator (EOM) is used. The RF signals that drive these modulators are generated by direct digital synthesis (DDS) chips[14]. The exception to this is the RF that controls the power in the counter-propagating 532 nm beam path, which is generated by an AWG[15]. This allows for the power in the beam to be smoothly ramped at the start and end of pulses, which mitigates the coupling to spectator modes and optical-phase-dependent LS terms in inter-ion gates [140].

In turn, these synthesisers are controlled using a distributed, real-time control system that makes use of the ARTIQ ecosystem[16]. A central FPGA[17] sends instructions to hardware boards that are locked to an 8 ns grid. A clock is distributed to all boards to ensure synchronisation between potentially physically separate systems that is sufficiently accurate to ensure oscillators have deterministic phases relative to each other in different experimental sequences.

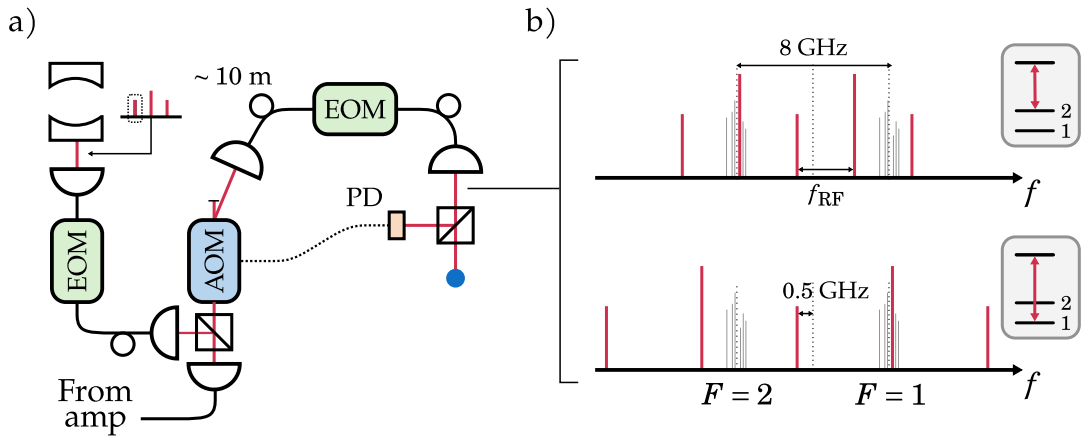



**Figure 6.7:** Sketch of the modulation for the quadrupole laser system. a) After amplification, the main laser path is passed through an AOM (blue) which is used to control the laser power at the trap. The frequency control is done using an in-fibre EOM (green) that is downstream from this. A photodiode (orange) near the trap monitors the power and feeds back to the RF signal sent to the AOM to stabilise it. Before the AOM, light is picked off for locking to a high-finesse cavity. An EOM is used to generate sidebands, which are locked instead of the carrier, allowing it to be placed arbitrarily with respect to the cavity reference. b) Transitions from the $F = 1,2$ manifolds of the $S_{1/2}$ level are driven using the $\pm 1$ sidebands of the downstream EOM. The carrier frequency near the centre, and the $\pm 1,2$ sidebands are shown; only one is ever resonant with transitions (shown as vertical gray lines) due to the carrier being placed away from the centre of the transitions.

### 6.4.2 Quadrupole laser system

The light is generated by a diode laser[18] and then amplified[19]. After the amplifier, it is locked to a high-finesse cavity[20] with a measured finesse of $\sim 500(20) \times 10^3$. This reduces the laser's linewidth enough to drive the narrow quadrupole transition. To allow the frequency to be set arbitrarily relative to the cavity's resonance, the light sent to the cavity is first passed through an EOM[21], and one of the sidebands is locked instead of the carrier (see Figure 6.7a). This EOM also applies the necessary PDH locking sidebands. Both this and the downstream EOM[22] (see later) are in-fibre.

All transitions in the encoding are $\Delta m_F = 0$ transitions. It can be seen from Figure 6.8

[13] Sinara Urukul and Sinara Sampler in an SUServo configuration.
[14] AD9910 on a Sinara Urukul board.
[15] Sinara Phaser.
[16] https://m-labs.hk/artiq/artiq/ (accessed 24/04/2026).
[17] Sinara Kasli.
[18] Toptica DL Pro.
[19] PreciLasers.
[20] Stable Laser Systems.
[21] iXblue MPZ-LN-01.
[22] iXblue MPZ-LN-10.

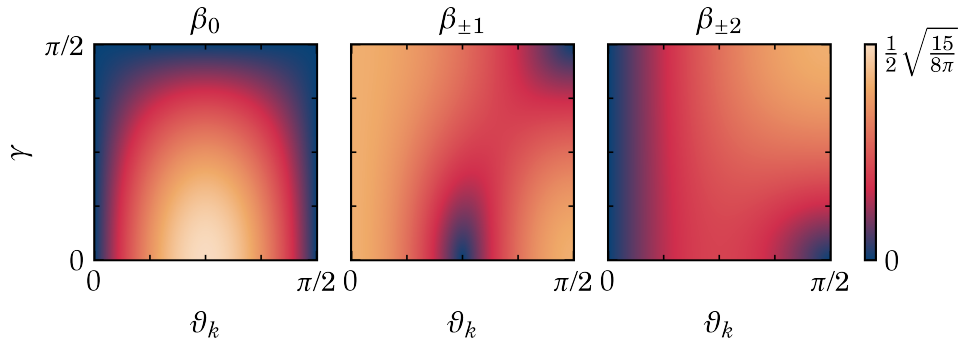



**Figure 6.8:** Magnitude of the geometric $\beta$ factors for quadrupole transitions, as defined in 3.49, for linear polarisation ($\psi = 0$). In that case $|\beta_q| = |\beta_{-q}|$. The patterns are symmetric about $\pi/2$ for both angles.

that these transitions are most strongly driven with the beam travelling at $\vartheta_k = \frac{\pi}{2}$ rad to the quantisation axis and linearly polarised with $\gamma = 0$ rad. The beam direction is chosen to match this. However, it is desirable to not be exactly aligned to this polarisation so that transitions of any $\Delta m_F$ can be driven. The reduction in Rabi frequency due to this is small, even for the weak $|S_{1/2}, 2, 0\rangle \leftrightarrow |D_{5/2}, 1, 0\rangle$ transition. A measurement of the beam direction and polarisation angles is given in Section 7.2.1.2.

#### 6.4.2.1 Spanning the $S_{1/2}$ hyperfine splitting

Transitions from the two ground hyperfine levels are split by 8.04 GHz, which is significantly outside the range of most available AOMs. However, EOMs usually have much higher modulation bandwidths in excess of 10 GHz, and thus allow us to address transitions from either manifold.

These elements phase-modulate the electric field of the light beam. Unlike an AOM, they do not spatially separate the modulation sidebands, and thus cannot be used to modulate the laser power. As such, an upstream AOM is used exclusively for this purpose. Furthermore, more than one frequency of light is present at the ion. Indeed, the phase-modulated electric field is

$$E_0 \cos\left(\omega_c t + \beta \sin(\omega_m t + \phi_m) + \phi_c\right) = E_0 \sum_{k=-\infty}^{\infty} J_k(\beta) \cos\left((\omega_c + k\omega_m)t + k\phi_m + \phi_c\right) \qquad (6.1)$$

where $J_k$ is the $k^{\text{th}}$ Bessel function of the first kind (see Figure 6.9); $\omega_c$ and $\phi_c$ are the unmodulated laser frequency – which acts as the "carrier" frequency – and phase; $\beta$

is the modulation depth, which is proportional to the amplitude of the RF voltage at the EOM; and $\omega_m$ and $\phi_m$ are the frequency and phase of the modulation signal. When driving a transition, we must ensure that all other sideband tones are not resonant with any atomic transition. This is achieved by using the $+1^{\text{st}}$ sideband to drive transitions from the $F = 1$ manifold, which are higher frequency than those from the $F = 2$ manifold, which are driven with the $-1^{\text{st}}$. In order to ensure only one set of transitions is addressed at a time, the carrier frequency is tuned using the cavity offset EOM to be ~ 500 MHz away from the midpoint between the $F = 1, 2$ transitions. Thus, whenever one sideband is resonant, the other is detuned by ~ 1 GHz, which is significantly larger than the span of the $D_{5/2}$ manifold, 160 MHz.

Thus, to span all quadrupole transitions from both manifolds, the EOM must be modulated at signals between $3.35 - 4.65$ GHz. This is well outside the range of the DDS used. Thus, we use a sequence of frequency multipliers[23] to multiply the DDS frequency by a factor of 12. Between each multiplication stage, the signal is bandpass-filtered and amplified, before a final amplifier after the frequency multiplication. The RF power sent to the EOM is 13.4 dBm.

The multiplier chain and an EOM add subtleties to the phase control. Firstly, the phase of the frequency multiplied signal is also multiplied by a factor of 12. Secondly, as is seen from (6.1) the phase of the $-1^{\text{st}}$ sideband has an additional minus sign. The phase of this sideband also acquires an offset of $\pi$ since $J_{-1}(\beta) = -J_1(\beta)$. These last two effects are only relevant because the connectivity graph is closed (see Section 3.4.2).

#### 6.4.2.2 Setting the modulation depth

As can be seen in Figure 6.9a, there is an optimal modulation depth $\beta_M \approx 1.84$ that maximises the electric field amplitude in the $\pm 1$ sidebands. At this modulation depth, the fraction of the total beam power in each of these sidebands is 0.338.

The RF power that generates this is found by maximising the Rabi frequency of the transitions (Figure 6.9b). As can be seen, the target modulation depth is reached at different DDS amplitudes for each transition, with larger differences between transitions

[23] MiniCircuits ZX90-2-13-S+, ZX90-2-11-S+, ZX-90-3-452-S+

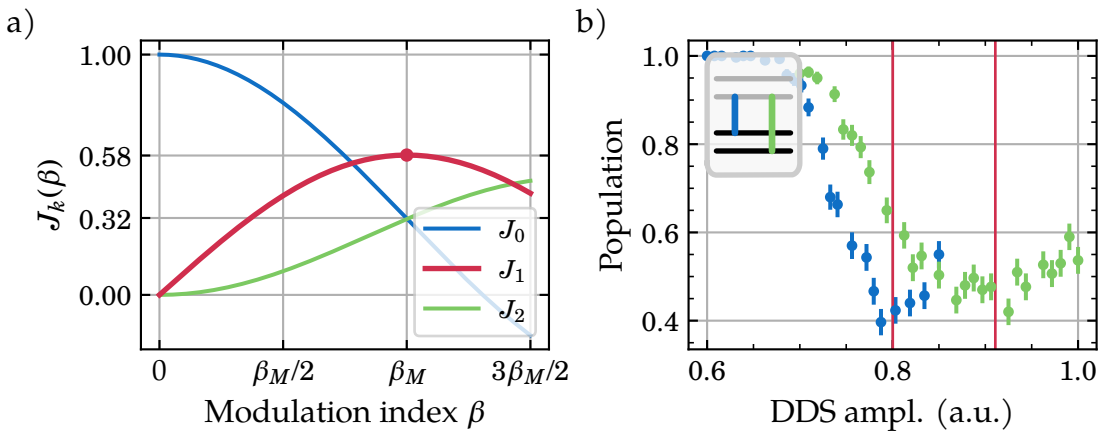



**Figure 6.9:** a) At a modulation index of $\beta_M \sim 1.84$ rad, the electric field amplitude in the $\pm 1$ sidebands is maximised, which maximises the Rabi frequency for a given total laser intensity. b) Transitions from the $F = 2$ (blue) and $F = 1$ (green) manifolds are pulsed for a duration approximately equal to $t_{\pi/2}$ while the amplitude of the DDS that modulates the EOM is scanned. At the voltage that generates a modulation index $\beta_M$ (which is not constant in frequency), maximum population transfer occurs, shown as red lines.

that address different manifolds. This is likely due to the RF chain's amplification not being uniform in frequency, as well as a frequency dependence of the EOM's $V_\pi$ – the voltage at which $\beta = \pi$.

#### 6.4.2.3 Phase control for cyclic connectivity graph

As discussed in Section 3.4.2, controlling a computational manifold with a cyclic transition graph requires more stringent phase control than manipulating one with a linear graph. In particular, we must have full control of $\Theta = \sum_T s^{(T)}\phi^{(T)}$, where $\phi^{(T)}$ is the phase of the light that drives the $T^{\text{th}}$ transition and $s^{(T)} = +1\,(-1)$ if state $|T\rangle$ has lower (higher) energy than $|T+1\rangle$ (see Section 3.4.2). One may worry that $\Theta$ may depend on the absolute laser phase $\phi_c$ from (6.1). This would entirely forbid any closed loop experiments, since this phase is entirely out of the experimentalist's control. Fortunately, this phase is common to all tones and, since when traversing a closed loop, as many photons are absorbed as emitted, it cancels in the sum.

Thus, $\Theta$ only depends on the modulation phase $\phi_m$, which is set by the modulation RF. A single DDS chip is used to generate this RF for all transitions, and its frequency is modified depending on the transition addressed. Thus, when changing the DDS's frequency, we must also set its phase to match that of a sinusoid whose phase at some

well-defined initial time was fixed. By doing this with all necessary frequencies, we can emulate the behaviour of four independent phase-locked tones, whose frequency we can arbitrarily control. Thus, control of $\Theta$ is possible.

### 6.4.3 532 nm laser system

When either driving Raman transitions, or generating the structured travelling light fields for inter-ion LS gates, two 532 nm beams must be present at the ion. Furthermore, in order to couple to the ions' radial motion, the difference wavevector $\Delta\mathbf{k}$ of the two beams must be non-zero along the radial direction. We maximise this coupling by making the two beams travel in opposite directions.

When driving LS gates, two beams whose frequency differs only by the motional frequency are applied in this configuration. These beams travel at angles of $\pi/2$ and $3\pi/2$ to the quantisation axis, respectively. The latter is referred to as the co-propagating beam, and the former is the counter-propagating beam. In addition, a second beam can be shone parallel to the co-propagating beam, whose frequency relative to the co- or counter-propagating beam can span a large fraction of the frequencies between $D_{5/2}$ level states[24]. Thus, Raman transitions are driven in the $D_{5/2}$ level by shining this beam plus one of the co- or counter-propagating beams. If the counter-propagating beam is used, the transition is motionally sensitive, which we use for sideband cooling the ion using a metastable transition [123].

## 6.5 Summary

This chapter has presented the design choices behind the experiments carried out in Chapters 7 and 8. The reasoning behind the selection of the atomic states that form the computational manifold is given in Section 6.2, with the necessary background on the level structure of $^{137}Ba^{+}$ discussed in Section 6.1. Section 6.3 explores the feasibility of storing more than two qubits per ion, focusing on whether a set of states suitable for storing a computational manifold capable of low-error computation is likely to be

[24] A beam can *also* be shone whose frequency relative to the co- and counter-propagating beams is equal to the $S_{1/2}$ level splitting, but this is not used in this thesis.

found in typical trapped-ion species. Finally, details of the laser setup used to drive intra- and inter-ion gates are provided in Section 6.4.

*This feels like such an European upgrade to scrambled eggs and ketchup*

— William Cutler, insightfully commenting on a dinner of Spanish omelette and ratatouille.

# 7 Experimentally implementing intra-ion gates

In this chapter, the universal intra-ion gate set described in Section 4.1 is experimentally implemented. These gates are characterised using randomised benchmarking (RBM) and quantum process tomography (QPT). We begin by explaining the necessary theory behind RBM and QPT. Following this, the routines used to calibrate the TSRs and compensate for the phases induced by light shifts are laid out. The RBM measurements are then presented, alongside an error analysis using the results and expressions of Chapter 5. The chapter concludes with the results of QPT experiments and some closing remarks.

## 7.1 Characterisation protocols

The theory behind RBM and QPT will be briefly reviewed here. They will be described in terms of abstract qubits without mention of the hardware architecture. Indeed, both can be directly implemented in polyqubits; polyqubit QPT has been demonstrated in ions [52] and RBM in superconductors [31]. Furthermore, both protocols can be extended to qudits [25, 29, 33].

### 7.1.1 Randomised Benchmarking

RBM works by applying long strings of random gates, chosen so that the net circuit should implement the identity operation. The probability that the qubits return to their initial

state – whether they *survive* or not – as a function of sequence length can be used to find the mean gate error, defined through the average fidelity (Section 5.1.2).

The gates are chosen from the Clifford set, which is the set of gates that normalises the Pauli matrices [56]. In other words, it is the set of $n$-qubit gates $C_i \in \mathscr{C}^{\otimes n}$ such that, for any $n$-qubit Pauli matrix $P$, the matrix $C_i P C_i^\dagger$ is also a Pauli matrix. The Clifford set is also a group, meaning that the product of any two Clifford gates is also a Clifford gate. To ensure a sequence implements the identity, the last gate is chosen to be the inverse of the product of all previous gates in the sequence[1].

The key point behind RBM is that the probability $P(N)$ of survival after a sequence of $N$ gates decreases exponentially,

$$P(N) = Ap^N + B. \tag{7.1}$$

As long as the errors are Markovian [218], $p$ depends only on the average fidelity of all Clifford gates[2]. In this case, the mean error per Clifford gate is $\varepsilon = \frac{d}{d+1}(p-1)$ where $d = 2^n$ is the Hilbert space dimension [218]. The remaining two parameters are independent of the fidelity: $A$ depends only on the SPAM error and $B = 1/2(1/4)$for one (two) qubit(s). This neatly separates SPAM errors from gate errors.

Since not all Clifford gates are native to the hardware, they must be compiled into sequences of native gates. We choose a decomposition which maximises the number of diagonal gates used, since they can be implemented using virtual rotations; all other rotations are $\pi/2$ rotations about the $x$ axis. The two-qubit Clifford gates are compiled from the single qubit ones, plus virtually applied `CZ` gates. The error per native gate can then be found by counting the average number of native gates per Clifford. In our case, the error per $\pi/2$ pulse is a more relevant quantity, since it excludes virtually applied gates that should not contribute to the error.

[1] This is enabled by the fact that Clifford gates can be efficiently calculated classically [56]. This is also precisely why a universal gate set must contain at least one non-Clifford gate: otherwise, all quantum circuits could be simulated efficiently on a classical computer!

[2] This is directly related to the fact that the Clifford group is a unitary 2-design. The interested reader is referred to [176] for an extensive and clear introduction.

### 7.1.2 Quantum Process Tomography

Quantum Process Tomography (QPT) measures the complete quantum process carried out when implementing a quantum gate [219, 220]. As such, it in theory provides all information about the process, so we can use it to analyse the structure of the errors in the gate in detail.

First, we will introduce the $\chi$-matrix (or process matrix) representation of a quantum map, which is often more convenient to work with than the Kraus sum from Section 5.1.1. This is obtained by expanding the Kraus operators as $K_i = a_{ij}P_j$, where $P_j$ is an $n$-qubit Pauli matrix, chosen with the normalisation condition[3] $\mathrm{Tr}(P_iP_j) \triangleq \delta_{ij}$. The coefficients are given by $a_{ij} = \mathrm{Tr}(K_iP_j)$. Inserting this into (5.1), we find

$$\Lambda(\rho) = \sum_{ij} \chi_{ij} P_i \rho P_j \tag{7.2}$$

with the entries of the $d^2 \times d^2$ matrix $\chi$ given by $\chi_{ij} = \sum_k a_{ki} a^*_{kj}$.

A QPT experiment involves measuring the complete density matrix of states output by the process $\Lambda$ when fed a known input state. If this is repeated with enough inputs to span the space of all density matrices then, by the linearity of quantum maps, the effect on any input state can be calculated. This is done by executing many experiments with identical form: a state $\rho_i$ out of the aforementioned spanning set is prepared, and the quantum process $\Lambda$ to be characterised is applied to it. The state is then measured, so the outcome associated with the projector[4] $|E_j\rangle\langle E_j|$ is observed with probability $p_{ij} = \mathrm{Tr}(|E_j\rangle\langle E_j|\Lambda(\rho_i))$. This is repeated with enough projectors to fully determine the density matrix $\Lambda(\rho_i)$, which again requires that the set of projectors spans the space of all density matrices. For $n$ qubits, this requires a minimum of $d^2$ measurement settings on $d^2$ different input states with $d = 2^n$, so a full tomography requires $d^4$ experiments.

We now relate the measured probabilities to the $\chi$-matrix:

$$p_{kl} = \sum_{ij} \mathrm{Tr}\left(|E_l\rangle\langle E_l| P_i \rho_k P_j\right) \chi_{ij} \triangleq \sum_{ij} \mathcal{M}_{kl,ij}\chi_{ij}. \tag{7.3}$$

[3] Note that this is not the convention used in the rest of this thesis. This normalisation requires multiplying the matrices from Section 2.2 by $\frac{1}{\sqrt{2}}$.

[4] In general, measurements are described by a set of POVM operators [46], but all measurements implemented in this work are projectors.

The quantities $\mathscr{M}_{kl,ij}$ are all known, since both $\rho_k$ and $|E_l\rangle\langle E_l|$ are chosen in advance. Now, by considering the tuple $(i,j)$ as well as $(k,l)$ as a single index (which is equivalent to reshaping the matrices $p_{kl}$, $\chi_{ij}$ into column vectors), equation (7.3) can be written as a matrix equation $\mathbf{p} = \mathscr{M}\boldsymbol{\chi}$. After measuring all $d^4$ entries in $\mathbf{p}$, the (vectorised) $\chi$-matrix can in principle be found by matrix inversion. In practice, the inversion is often done via maximum-likelihood estimators (MLE) to enforce physicality constraints; we use the algorithm of Reference [221].

In a single 2-polyqubit, the state preparation protocol of Section 4.3 only prepares the state $|00\rangle$. A spanning set of input states is prepared from this by applying one gate from the set $\{\mathbb{1}, R_x(\pi), R_x(\pm\pi/2), R_y(\pm\pi/2)\}$ on each qubit[5]. In this way, every Pauli eigenstate can be prepared. Similarly, the readout protocol of Section 4.4 implements all projectors $|\mathsf{pq}\rangle\langle\mathsf{pq}|$ for $\mathsf{p},\mathsf{q} = (0,1)$, which constitutes a full measurement in the $Z$ basis. A complete set of measurements is formed by applying one of $\{\mathbb{1}, R_x(\pi/2), R_y(\pi/2)\}$ to each qubit before the readout operation[6]. QPT assumes that the gates used to implement these SPAM operations, called *fiducials*, are perfect, but in practice they are not. This is one of the major drawbacks of QPT. More complex routines such as gate set tomography could be used instead [222], but were not implemented due to time constraints.

Once the $\chi$ matrix is found, the matrix $\mathscr{E}_\chi$ for the error process $\mathscr{E}(\rho) = \Lambda(U^\dagger \rho U)$, where $U$ is the target gate (Section 5.1.1) can now be found. Note that a slightly different definition of $\mathscr{E}$ to that given in Section 5.1.1 is used; here, we consider $U^\dagger$ to be applied *before* $\Lambda$. It is related to the $\chi$ matrix of the original process by[7] $\mathscr{E}_\chi = V\chi V^\dagger$, with $V_{ij} = \mathrm{Tr}(P_i P_j U^\dagger)$ [172].

#### 7.1.2.1 Interpreting the $\chi$ matrix

Firstly, assuming that the errors are small ($\lessapprox 10^{-2}$ [171]), the average fidelity can be easily extracted via $\bar{\mathscr{F}} = \frac{1+d\mathscr{E}_{\chi,00}}{d+1}$ [172, 176]. The term $\mathscr{E}_{\chi,00}$ is the $(0,0)$ entry in the matrix, corresponding to the identity coefficient[8].

[5] This in fact produces an overcomplete set, but is symmetric in the positive and negative eigenstates of the Pauli matrices.

[6] A smaller number of measurement settings is required since each measurement yields the probabilities associated to four projectors.

[7] The matrix for the error process of Section 5.1.1 can be calculated by using $V_{ij} = \mathrm{Tr}(P_i U^\dagger P_j)$.

[8] $\mathscr{E}_{\chi,00}$ is equal to the entanglement fidelity.

Next, since the errors are small, the error process is approximately the identity, plus a small error term. That is, $\mathscr{E}(\rho) \approx \rho + \mathscr{L}(\rho)$ for an error generator process $\mathscr{L}$, which should be interpreted as a first-order expansion of the process $\mathscr{E}(\rho) = e^{\mathscr{L}(\rho)}$. This generates error processes in the same sense that Hamiltonians generate unitary gates. The error generator for the measured process can be found by $\mathscr{L}(\rho) = \log\big(\mathscr{E}(\rho)\big)$.

An arbitrary error generator can be decomposed into *elementary generators*, which, as characterised in depth in [171], generate different types of error[9]. Dropping the argument $\rho$ for convenience, this is written as $\mathscr{L} = \sum_{P=1}^{d^2-1} h_P \mathscr{H}_P + s_P \mathscr{S}_P$. The *Hamiltonian* and *Stochastic* generators, $\mathscr{H}_P$ and $\mathscr{S}_P$, generate unitary errors and errors from stochastic noise, respectively[10]. For a given Pauli matrix $P$, they are defined by

$$\mathscr{H}_P(\rho) = -i[P, \rho] \quad , \quad \mathscr{S}_P(\rho) = P\rho P - \mathbb{1}\rho\mathbb{1}. \tag{7.4}$$

Their coefficients $h_P$, $s_P \in \mathbb{R}$ can be interpreted as effective error *rates* and can be extracted using the dual to the elementary generators, given in [171]. This will allow us to not only estimate the fraction of coherent and stochastic errors, but will also enable us to identify the Pauli matrix along which the errors are strongest.

## 7.2 Calibration routines

Running polyqubit circuits involves a sequence of pulses of the 1762 nm laser, which drive equatorial TSRs $R_\phi^{\alpha,\beta}(\theta)$. To do so, we must have accurate knowledge of the following quantities for each of the four transitions in the computational manifold:

- The laser frequency that drives each transition on resonance. In our system, this is determined by the RF drive frequency sent to the 1762 EOM (see Section 6.4.2).
- The duration $t$ of each laser pulse, which determines the rotation angle $\theta = \Omega_{v,\mu} t$ via the Rabi frequency $\Omega_{v,\mu}$ of each transition. For the experiments below and further calibrations, it is sufficient to calibrate the $\pi$ and $\pi/2$ times ($t_\pi$ and $t_{\pi/2}$).

[9] There are another two classes of elementary generators, but these do not affect the average fidelity and are harder to interpret, so we neglect them [171].

[10] This can be clearly seen by inserting $\sum_P h_P \mathscr{H}_P$ and $\sum_P \mathscr{S}_P$ into $\mathscr{E}(\rho) = \rho + \mathscr{L}(\rho)$. The former results in $\rho - i\sum_P h_P[P, \rho] \approx e^{-i\sum h_P \mathscr{H}_P} \rho e^{i\sum h_P \mathscr{H}_P}$, which is an evolution under the Hamiltonian $\hbar \sum h_P \mathscr{H}_P$. The latter results in the Kraus sum $(1 - \sum_P s_P)\rho + \sum_P s_P P\rho P$ which is a general depolarising error.

- The light shifts induced on each state in the qudit while the different transitions are addressed. With these values, the phase acquisition due to LS can be undone.

The methods used for calibrating these quantities are now described, starting with the LS, since the frequency calibration depends on it.

### 7.2.1 Calibrating light shifts

The LS compensation protocol from Section 5.2.1.5 requires knowledge of the LS matrix $\Delta^T_{T'}$, which contains the light shift on transition $T$ due to driving $T'$. Before discussing how this is measured, we discuss the transitions in the ion that contribute to it, since they do so in different ways.

There are broadly two sets of transitions that the polyqubit states off-resonantly couple to when addressing a quadrupole transition. These are dipole transitions connecting $S_{1/2} \leftrightarrow P_{1/2}$, $S_{1/2} \leftrightarrow P_{3/2}$ and $D_{5/2} \leftrightarrow P_{3/2}$; and other spectator quadrupole transitions. As shown in Figure 7.1, the shifts induced by dipole transitions are much greater than those due to off-resonant quadrupole transitions, since the matrix elements are so much larger (this compensates for the detuning being also much larger). However, they are independent of the laser frequency over the ~ 8 GHz span of the polyqubit transitions and thus only induce measurable phase shifts when the laser intensity changes, such as when the laser is turned off between pulses. We can in fact eliminate its effect altogether by keeping the laser on for the whole duration of an experimental shot and addressing different transitions only by changing the laser frequency. This is possible because the frequency is controlled using an EOM, which is independent of the upstream AOM that manages the power. This is left on throughout the entire shot. The EOM "pulses" are still separated by a $2-3$ μs due to technical reasons, during which the laser is not phase-modulated, but still on.

However, the contribution from spectator quadrupole transitions, while significantly weaker than the dipole contribution, does depend on the laser frequency, and thus the transition addressed. Nonetheless, these shifts are entirely determined by the beam's frequency and the Rabi frequencies of all transitions between the $S_{1/2}$ and $D_{5/2}$ levels (Equation 3.18). These Rabi frequencies in turn depend on the beam's polarisation and

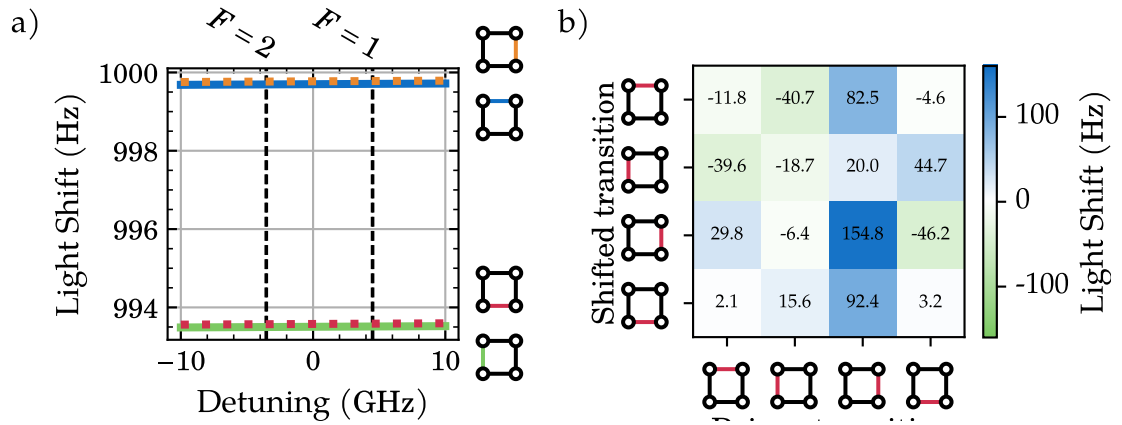



**Figure 7.1:** The total light shifts on polyqubit transitions have contributions from off-resonant coupling to spectator dipole and quadrupole transitions. a) The dependence of the dipole light shift on each polyqubit transition as a function of the detuning of the 1762 nm laser. The four colours correspond to the four transitions in the encoding, whose corresponding edge in the connectivity graph is highlighted next to the corresponding trace. A detuning of 0 GHz corresponds to the frequency of the EOM carrier (see Section 6.4.2). Dashed, black vertical lines show the detunings which drive transitions from the two ground manifolds. b) Quadrupole light shift matrix. Each entry is the shift on each polyqubit transition (along the $y$-axis) when one of the four transitions is driven (along the $x$-axis). The average magnitude of the entries in the matrix is 38.3 Hz.

intensity, as well as the quantisation magnetic field, which can all be accurately measured. This enables us to calculate the LS matrix, which can then be used in experiment[11].

#### 7.2.1.1 Measuring the quantisation field

In order to accurately measure the quantisation field, we use the fact that the states in the $S_{1/2}$ level are in the low-field regime until ~1000 G, which is far above the field we use in experiments (~3 G). In this regime, the magnetic field sensitivity of the state $|F, m_F\rangle$ is $\frac{g_F \mu_B}{\hbar} m_F$ with the Bohr magneton $\mu_B$ and the $g_F$-factor which can be easily calculated from the state's angular momentum quantum numbers [122]. As such, the detuning between the transitions $|S_{1/2}, 2, 0\rangle \rightarrow |D_{5/2}, 2, 0\rangle$ and $|S_{1/2}, F = 2, m = m_F\rangle \rightarrow |D_{5/2}, 2, 0\rangle$ is equal to $B \frac{g_F \mu_B}{\hbar} m_F$ (Figure 7.2). We thus measure their frequencies with high precision using the procedure in Section 7.2.2.2[12] and fit a straight line, which yields a field strength of 3.3903(8) G.

[11] When calculating the LS matrix, only the sideband that drives the transition in question is considered. It is found numerically that the carrier and remaining sidebands are too far off-resonant from any transition to contribute significantly.

[12] We neglect any effects due to light shifts in this measurement. Calculations show that this has a negligible effect on the measured field.

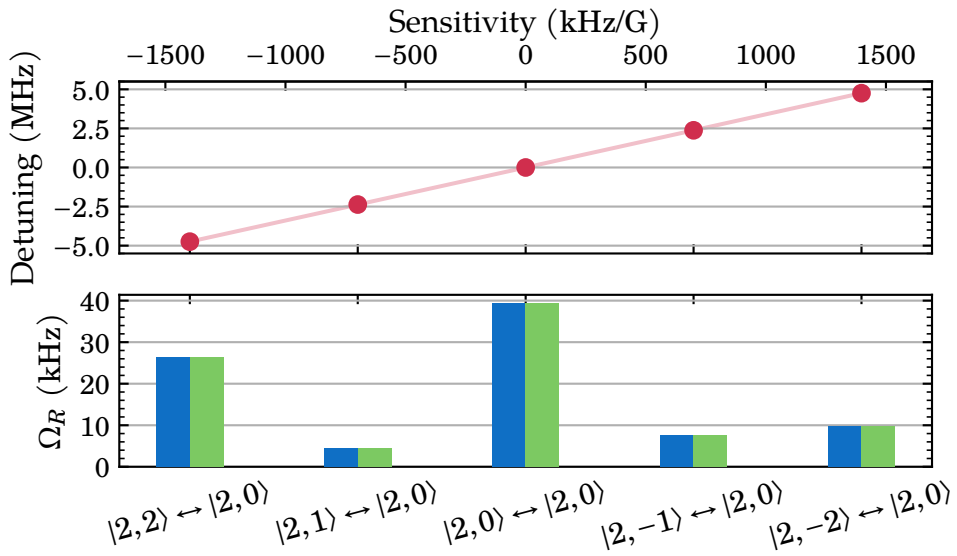



**Figure 7.2:** Top: detuning from the $|S_{1/2},2,0\rangle \leftrightarrow |D_{5/2},2,0\rangle$ transition frequency of each transition from the $F = 2$ manifold in the $S_{1/2}$ level to the $|D_{5/2},2,0\rangle$ state, against their magnetic field sensitivity. The gradient of the linear fit yields the quantisation field. Bottom: measured (blue) Rabi frequency $\Omega_R$ of each transition. These were used to extract a total beam intensity of 5.14 $\mathrm{Wmm}^{-2}$ (1.74 $\mathrm{Wmm}^{-2}$ in the $\pm 1^{\mathrm{st}}$ order phase-modulation sidebands) and beam angles $\vartheta = -43.66°$, $\gamma = -27.37°$ and $\psi = 54.90°$. These parameters are used to calculate the Rabi frequencies in blue.

#### 7.2.1.2 Measuring the beam polarisation and intensity

The five transitions discussed in the previous section span all values of $\Delta m$ that can be driven in quadrupole transitions. Their relative Rabi frequencies depend on the five rank-2 beam tensor components, while the beam intensity scales them equally. This dependence can be inverted to infer the beam parameters. We use the technique in Section 7.2.2 to measure the Rabi frequency[13] for the transitions chosen for measuring the quantisation field.

Equation 3.37 for the quadrupole Rabi frequency between the states $|\nu\rangle$ and $|\mu\rangle$, which are in the $S_{1/2}$ and $D_{5/2}$ levels respectively, can be expressed as

$$\Omega^{(q)} = X^{(q)}(B) E \beta^{(2)}_{-q} \tag{7.5}$$

with $q = m_\mu - m_\nu$. This splits into three parts. The quantity $X^{(q)}(B) \propto \langle \mu | \mathcal{M}^{(2)}_q | \nu \rangle$ depends on the atomic states and the quantisation field, and can be calculated; $E = \sqrt{2I/c\varepsilon_0}$ is the

[13] Again, neglecting light shifts.

magnitude of the beam's electric field; and $\beta^{(2)}_{-q}$ is the $-q^{\text{th}}$ component of the rank-2 beam tensor.

Once the $\Omega^{(q)}$ are measured, we can immediately extract the beam's electric field by using

$$\sum_q \frac{|\Omega^{(q)}|^2}{|X^{(q)}(B)|^2} = \sum_q E^2 |\beta^{(2)}_{-q}|^2 = \frac{5E^2}{8\pi} \tag{7.6}$$

since $\sum_q |\beta^{(2)}_{-q}|^2 = 5/8\pi$ as can be verified directly from Equations (3.49)-(3.51). With this, we can obtain the beam tensor components

$$\beta^{(2)}_{-q} = \frac{\Omega^{(q)}}{EX^{(q)}(B)} \tag{7.7}$$

The five beam tensor components $\beta^{(2)}_{-q}$are functions of the beam's direction and polarisation vectors $\hat{\mathbf{k}}$ and $\hat{\boldsymbol{\varepsilon}}$, which themselves depend on the beam angles $\vartheta_k, \gamma, \psi$ (see (3.45)). We obtain these by numerically inverting Equations (3.49)-(3.51) through minimising the cost function

$$C(\vartheta_k, \gamma, \psi) = \sum_q \left( |\beta^{(2)}_{q,\text{meas}}| - |\beta^{(2)}_{q,\text{calc}}(\vartheta_k, \gamma, \psi)| \right)^2. \tag{7.8}$$

We verify this procedure by using the extracted beam parameters to calculate the Rabi frequencies of the same transitions. These are found to agree well, as shown in Figure 7.2. The extracted electric field[14] is lower than predicted from independent measurements of the beam waist and power, by a factor of ~ 0.6. This is believed to be due to slight vertical beam misalignment, optical aberrations, or having measured the beam waist at a plane that doesn't exactly coincide with the ion's position.

The four parameters $\{E, \vartheta_k, \gamma, \psi\}$ then allow us to calculate the sixteen elements of the full light shift matrix $\Delta^T_{T'}$.

### 7.2.2 Transition frequency and Rabi frequency calibration

The transition frequency and Rabi frequency on each transition in the polyqubit are calibrated individually. For convenience, the two states that participate in the transition

[14]This procedure measures the electric field amplitude of the sideband resonant with the transition. The total beam intensity can nonetheless be inferred because the modulation depth is known, as it is set to maximise the power in each sideband.

will be referred to as a "qubit" in this section. For both of these procedures, we employ a Robust Phase Estimation (RPE) routine, which allows us to achieve Heisenberg uncertainty scaling in the number of shots required for the calibration [223].

#### 7.2.2.1 RPE protocol

Suppose that we have some process that induces a rotation $R(\Omega t)$ about some axis – such as a Rabi oscillation, or state precession in a Ramsey experiment. We wish to measure the rotation rate, $\Omega$, and we have access to some way of measuring the angle $\theta = \Omega t$ by which the qubit has rotated from its initial state – in the case of a Ramsey experiment, by standard Ramsey fringe measurements. We assume that this measurement has an uncertainty $\sigma_\theta$, independent of $\theta$ or $t$. Then, naively, $\Omega$ could be measured with very low uncertainty if we let the rotation angle accumulate for a long time $T$, such that the uncertainty in omega will be $\sigma_\Omega = \frac{\sigma_\theta}{T}$. Unfortunately, such a measurement would be ambiguous, since we can only measure $\theta$ modulo $2\pi$.

The RPE protocol allows us to eliminate this ambiguity in an optimal number of steps. We start by measuring the angle $\theta_0 = \Omega t_0$ after a small time $t_0$, such that we can be certain[15] $\theta_0 < 2\pi$. Then, $\theta_1 = \Omega t_1$ is measured, with a delay $t_1 = 2^1 t_0$. Since $\theta_0$ has already been measured, we know whether $\theta_1$ wrapped around $2\pi$ or not. This procedure is repeated with durations $t_k = 2^k t_0$, such that at every point we know exactly how many times the phase has wrapped around $2\pi$, enabling an unwrapped measurement of $\theta$ with long times $T$. Then, the rate $\Omega$ can be extracted with low error as above.

The assumption that the uncertainty $\sigma_\theta$is independent of $\theta$ eventually breaks down for very large $\theta$. This sets the maximum duration in the estimation sequence.

#### 7.2.2.2 Calibrating the transition frequency

We wish to measure the laser frequency that drives a particular transition on resonance. This frequency is different to the transition's idle frequency, since the transition frequency is modified by the beam's LS. However, we will first explain how to measure the bare frequency, and then account for the LS.

[15] This requires an initial estimate of $\Omega$ that is not too far off the true value. In practice, the bounds on this are generous: frequency miscalibrations of up to ~ 10 kHz can be accurately corrected in most cases.

The bare frequency measurement is identical to the RPE sequence above. The rotation $R(\Omega t)$ is induced by the idle Hamiltonian $H_I = -\hbar\frac{\tilde{\delta}}{2}\sigma_z$ where $\tilde{\delta}$ is the detuning between the laser and the idle transition. Each RPE step thus involves a Ramsey experiment of duration $2^k t_0$ for some short duration $t_0$. The measurement of the phase $\theta_k$ accrued at each step is done by repeating the Ramsey sequence with the closing angles set to $[0, \pi/2, \pi, 3\pi/2]$, allowing the phase and amplitude of the Ramsey fringe to be fully determined. The duration $t_0 2^{k_{Max}}$ of the final Ramsey experiment is chosen to be just below the transition's coherence time.

There are many ways to account for the LS in this measurement, which all are equivalent to subtracting $\Delta_T^T$ from the measured detuning – this could be done, if desired. We choose to directly compensate for the LS in the Ramsey experiments by updating the phase of the closing rotation using the phase update from Section 5.2.1.5. This acts like a term $\hbar\frac{\Delta_T^T}{2}\sigma_z$, so that the measurement directly outputs $\tilde{\delta} - \Delta_T^T = \delta$, which is the detuning from resonance.

Both of the above methods have the consequence of coupling the LS and resonance frequency calibrations. Avoiding this would require a direct measurement of the driven transition frequency. This could be done by performing Rabi spectroscopy, but this was not possible to do with as much precision as the RPE sequence allows. A method based on driving the transition about the $\pm x$ axes sequentially was used in Reference [8]. However, this required the ability to implement pulse sequences with virtually no delay, which cannot be done in our system.

#### 7.2.2.3 Calibrating $t_\pi$ and $t_{\pi/2}$

For this calibration, we are interested in finding the pulse duration that induces a rotation $\theta$, rather than measuring the rate of rotation directly. We begin with an estimate $\tilde{t}_\theta$ of this time, which is the base time $t_0$ in the RPE sequence. Then, the $k^{\text{th}}$ step in the sequence is done by repeating this pulse $2^k$ times, rather than performing a single pulse of duration $2^k t_0$. This makes the rate of phase accumulation consistent even if there are intensity variations due to AOM turn-on dynamics.

The measurement of the rotation angle $\theta_k$ at each step is done by performing an additional rotation[16] by an angle $\theta_M \in [0, \frac{\pi}{2}, \pi, \frac{3\pi}{2}]$ before measuring in the $z$ basis. These are equivalent to population measurements about the $[+z, -y, -z, +y]$ axes, from which the qubit's angle in the $y-z$ plane can be extracted.

Once the unwrapped rotation angle at the final step is measured, $\tilde{\theta}_{Max}$, we obtain the rotation angle induced by each pulse, $\tilde{\theta} = \frac{\tilde{\theta}_{Max}}{2^k{}_{Max}}$. The correct pulse duration is obtained by scaling the initial time appropriately, $t_\theta = \tilde{t}_\theta \frac{\theta}{\tilde{\theta}}$

### 7.2.3 Driving tone phases

As discussed in Section 3.4.2, the ability to drive population around a loop makes the system evolution depend non-trivially on the phase of all driving tones. Specifically, the dynamics are sensitive to the (signed) sum $\Theta$ of the drive phases, relative to some well-defined reference time - invariably the start of an experimental shot. Since all DDS drives can be phase-locked to each other (Section 6.4.2.3), this phase can be controlled arbitrarily, up to constant phase offsets. These offsets likely arise due to a frequency dependence in the RF multiplication and amplification chain's phase response.

These phase offsets are measured by performing the experiment described in Section 3.4.2. We set up a superposition between a pair of states connected by a single transition, but by driving the population around the other three transitions in the manifold – this is around "the other side" of a loop. These pulses are driven with the phase of all DDS chips set to zero (with respect to the phase at the start of the shot), which, in the absence of phase offsets or detunings, would mean all the TSRs are $x$-rotations. We then scan the phase of the final rotation, which can undo the superposition with the correct phase. From Equation (3.27), the phase that maximises the population in $|0\rangle$ is the sum of the constant phase offsets. Thus, we account for this by offsetting the DDS phase for one of the transitions (arbitrarily chosen to be $|00\rangle \leftrightarrow |01\rangle$) by this amount.

This measurement is slightly sensitive to transition frequency miscalibrations. This is because the pulses are not instantaneous, so the phase $\Theta$ may change in a manner

[16] The final measurement rotations use previously calibrated pulse durations, which may add an offset to each estimate of $\theta_k$. However, because the RPE protocol uses the difference in phases measured at different steps, this does not affect the final calibration, to first order.

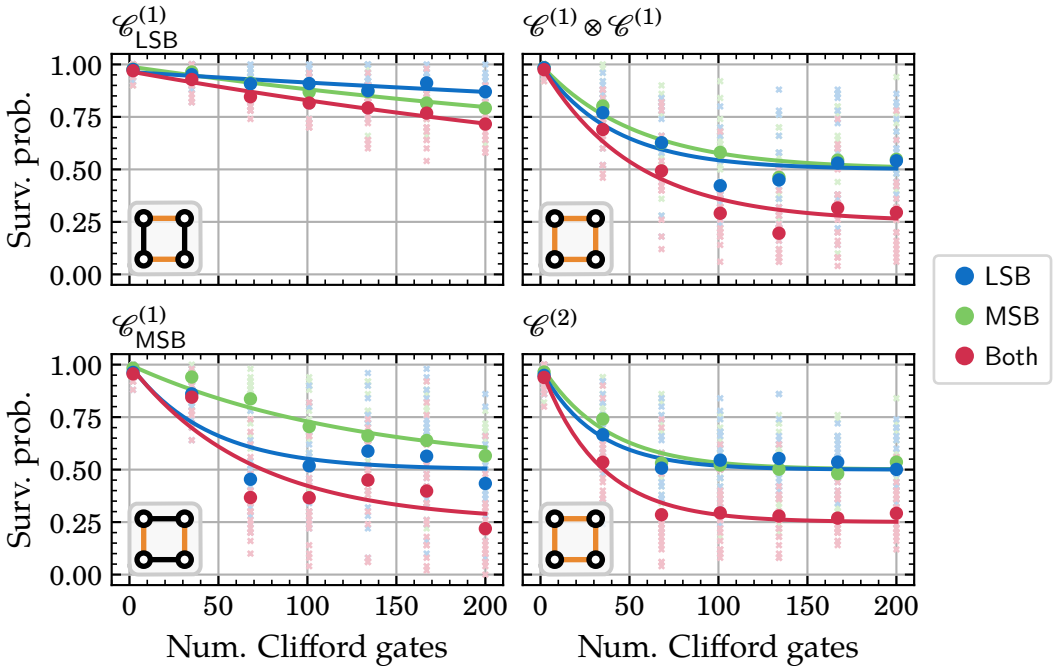



**Figure 7.3:** Results for all four RBM experiments. Average survival probabilities for the LSB, MSB and both qubits together are shown as blue, green and red circles. Light-coloured crosses show the survival probability in individual sequences and solid lines are fits to Equation (7.1). Inlays show which transitions in the encoding participate in the experiment (orange lines). In all cases, the polyqubit is initialised to a superposition of all four states, which is undone at the end of the sequence.

dependent on these miscalibrations. The impact on the calibration is small, since the duration of each experiment is $\approx 100$ μs.

## 7.3 RBM results

The results of the RBM experiments described in Section 7.1.1 are now presented. Three different sets of experiments were carried out, in which sequences of single-qubit Clifford gates are driven on just one qubit, which we refer to as $\mathscr{C}^{(1)}_{\mathrm{LSB}}$-RBM ($\mathscr{C}^{(1)}_{\mathrm{MSB}}$-RBM) when the target qubit is the LSB (MSB) qubit; sequences of single-qubit Cliffords are driven on both qubits in an interleaved fashion, $\mathscr{C}^{(1)} \otimes \mathscr{C}^{(1)}$-RBM; and sequences of two-qubit Clifford gates are driven, $\mathscr{C}^{(2)}$-RBM. These allow us to verify that we can address just one qubit in the ion, while leaving its neighbour idle, as well as being able to address both independently or together. The results of these experiments are shown in Figure 7.3. The extracted errors are given in Table 7.1.

| RBM Experiment | Qubit | Error per Clifford ($\times 10^{-3}$) | Error per $\pi/2$ pulse ($\times 10^{-3}$) | Pulses per Clifford | Mean $t_{\pi/2}$ ($\mu$s) |
|---|---|---|---|---|---|
| $\mathscr{C}^{(1)}_{\mathsf{LSB}}$ | LSB | 0.6(1) | 0.29(7) | 2 | 5.8 |
| | MSB | 1.2(1) | 0.62(5) | | |
| | Both | 1.6(1) | 0.8(6) | | |
| $\mathscr{C}^{(1)}_{\mathsf{MSB}}$ | LSB | 11(5) | 6(2) | 2 | 56.1 |
| | MSB | 3.9(5) | 1.9(3) | | |
| | Both | 11(3) | 5(1) | | |
| $\mathscr{C}^{(1)} \otimes \mathscr{C}^{(1)}$ | LSB | 12(4) | 3.0(9) | 4 | 31.0 |
| | MSB | 9(2) | 2.3(4) | | |
| | Both | 14(2) | 3.6(6) | | |
| $\mathscr{C}^{(2)}$ | LSB | 16(3) | 1.9(3) | 8.6 | 31.0 |
| | MSB | 13(2) | 1.6(2) | | |
| | Both | 23(3) | 2.6(3) | | |

**Table 7.1:** Errors for the experiments of Figure 7.3. The **Qubit** column indicates whether the error is calculated from the survival of just the LSB or MSB qubit, or both together. The mean $t_{\pi/2}$ is the average $t_{\pi/2}$ time of all transitions used to drive gates in each experiment.

The initial polyqubit state affects which states are populated during the $\mathscr{C}^{(1)}_{\mathsf{LSB}}$- and $\mathscr{C}^{(1)}_{\mathsf{MSB}}$-RBM experiments. This is because, as discussed in Section 4.1, single-qubit gates on the LSB (MSB) qubit are implemented by driving the two transitions corresponding to the horizontal (vertical) edges of the connectivity graph (see insets in Figure 7.3). Thus, there is no way to transfer population from the pair of states connected by one of these edges to the other pair. Because of this, if the population were initialised to a computational basis state such as $|00\rangle$, only two states would ever be populated. The experiment would thus resemble monoqubit RBM – with the addition of off-resonant light between the gate pulses – and we would not be sensitive to any effects which arise from populating the full computational manifold. This could lead to an unfair estimate of the gate errors.

To maximise the sensitivity to these effects, we perform all RBM sequences starting from an even superposition state $|\psi\rangle = 1/2(|00\rangle + |01\rangle + |10\rangle + |11\rangle)$. To do so, each RBM sequence is prepended and appended with $R_y^{\mathrm{MSB}}(\pi/2) \otimes R_y^{\mathrm{LSB}}(\pi/2)$ and $R_{-y}^{\mathrm{MSB}}(\pi/2) \otimes R_{-y}^{\mathrm{LSB}}(\pi/2)$ gates.

Furthermore, because gate errors and SPAM errors can be distinguished in RBM, we do not perform the heralded leakage detection protocol from Section 4.4.1.

Finally, it was found that the LS matrix $\Delta^{T}_{T'}$ obtained from the beam polarisation and intensity measured in Section 7.2.1.2 did not minimise the errors per Clifford. Instead, we

| Atomic transition | Logical polyqubit transition | Error per Clifford ($\times 10^{-4}$) | Error per $\pi/2$ pulse ($\times 10^{-4}$) | Target qubit |
|---|---|---|---|---|
| $\|S_{1/2},2,0\rangle \leftrightarrow \|D_{5/2},2,0\rangle$ | $\|00\rangle \leftrightarrow \|01\rangle$ | 7(3) | 3(2) | LSB |
| $\|S_{1/2},1,0\rangle \leftrightarrow \|D_{5/2},1,0\rangle$ | $\|11\rangle \leftrightarrow \|10\rangle$ | 4(3) | 2(1) | |
| $\|S_{1/2},2,0\rangle \leftrightarrow \|D_{5/2},1,0\rangle$ | $\|00\rangle \leftrightarrow \|10\rangle$ | 3(2) | 1.5(8) | MSB |
| $\|S_{1/2},1,0\rangle \leftrightarrow \|D_{5/2},2,0\rangle$ | $\|11\rangle \leftrightarrow \|01\rangle$ | 3(1) | 1.4(6) | |

**Table 7.2:** Error per Clifford on monoqubit RBM. A different Clifford gate decomposition was used for these experiments than the polyqubit experiments, so, on average, 2.17 $\pi/2$ pulses are used per Clifford gate.

iterated over these parameters until the error in $\mathscr{C}^{(1)}_{\mathsf{LSB}}$-RBM experiments was minimised; the resulting LS matrix was used for all RBM experiments. We discuss one possible reason for this in Section 7.3.1.4

#### 7.3.0.1 Monoqubit RBM

RBM experiments were also performed on each polyqubit transition individually, what we refer to as *monoqubit* RBM experiments. Previous works on qudit processors [25] report errors on a $d$-level system equal to the sum of the monoqubit RBM errors on each transition.

The errors in our system are given in Table 7.2. It was found that the detuning and $\pi/2$-times obtained from the calibrations in Section 7.2.2 did not coincide with the ones that minimised the error per Clifford on each transition. The results are given with these optimised values. For reasons that are not fully clear, such disparities in the detuning and $\pi/2$-time were less severe in polyqubit RBM, so in those experiments, the calibration values were used. It is possible that any such miscalibration may have been partially compensated for when correcting the light shift matrix in polyqubit RBM.

### 7.3.1 Sources of error

We can make some observations from the errors in Tables 7.1 and 7.2:

1. The error per $\pi/2$-pulse in the polyqubit RBM experiments is an order of magnitude, or more, larger than the sum of the error in each constituent pulse, as obtained from monoqubit RBM experiments. The exception to this rule is $\mathscr{C}^{(1)}_{\mathsf{LSB}}$-RBM. This is at odds with previous works.

2. The error per single $\pi/2$-pulse is much lower in the $\mathscr{C}^{(1)}_{\mathsf{LSB}}$-RBM experiment than in the rest, where it is approximately constant.

3. The error per $\pi/2$-pulse in $\mathscr{C}^{(1)}_{\mathsf{MSB}}$-RBM is much larger than in $\mathscr{C}^{(1)}_{\mathsf{LSB}}$-RBM, despite them both addressing just one qubit.

4. In (polyqubit) single-qubit RBM experiments, the error per Clifford on the spectator qubit is larger than the error on the target qubit. For $\mathscr{C}^{(1)}_{\mathsf{LSB}}$-RBM, the error on the MSB qubit is $\sim 2$ times larger; for $\mathscr{C}^{(1)}_{\mathsf{MSB}}$-RBM, the error on the LSB qubit is $\sim 3$ times larger.

As an extension to Observation 2, we point out that the error in $\mathscr{C}^{(2)}$-RBM experiments is slightly below that in $\mathscr{C}^{(1)}\otimes\mathscr{C}^{(1)}$-RBM. The gate sets used in both experiments differ only in the inclusion of the two-qubit CZ gate in $\mathscr{C}^{(2)}$, which is implemented virtually and is thus not included in the number of laser pulses per Clifford gate. As such, observing such similar errors per pulse in both experiments suggests that this gate adds no error. While this is expected, since the gate is implemented virtually, it is noteworthy to experimentally observe this in a two-qubit gate, which is a unique feature of polyqubits.

Nevertheless, Observation 1 implies that the error per pulse as measured in monoqubit RBM experiments does not account for the errors in polyqubit RBM experiments. In order to explain this discrepancy, we estimate the magnitude of the errors from the sources described in Section 5.2using measured experimental parameters.

#### 7.3.1.1 Rotation angle miscalibration

Observations 2 and 3 could be explained by a $t_{\pi/2}$ miscalibration on one of the transitions that is not involved in $\mathscr{C}^{(1)}_{\mathsf{LSB}}$-RBM. Such miscalibrations are difficult to diagnose post facto. Furthermore, as discussed in Section 5.2.3, these errors are quadratic in the rotation angle, so a substantially worse miscalibration in these transitions would have had to occur despite all of them being calibrated in the same way. Additionally, errors are uniform across all monoqubit RBM experiments, suggesting that any miscalibration is likely to be uniform across transitions – though the $\pi/2$ times in these experiments were calibrated to minimise the error per gate.

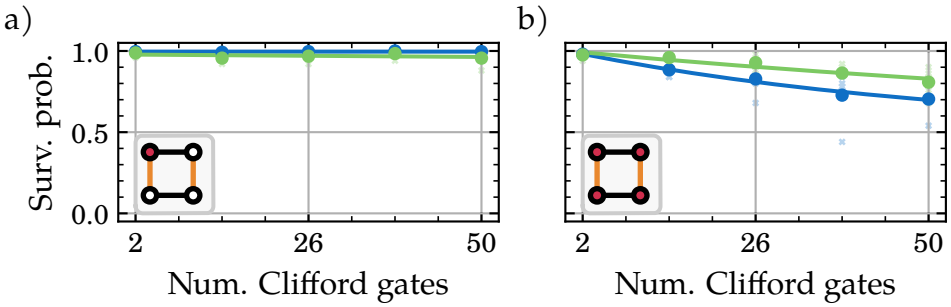



**Figure 7.4:** The same $\mathscr{C}^{(1)}_{\mathsf{MSB}}$-RBM experiment performed on a polyqubit initialised to a) the $|00\rangle$ state and b) an even superposition of all states. The insets show these states as red filled circles, as well as the transitions used (orange lines). The traces are coloured as per Figure 7.3. The error per Clifford gate on the LSB and MSB qubits are a) $\varepsilon_{\mathsf{LSB}} = 0(9) \times 10^{-5}$, $\varepsilon_{\mathsf{MSB}} = 3(5) \times 10^{-5}$ b) $\varepsilon_{\mathsf{LSB}} = 9.1(7) \times 10^{-3}$, $\varepsilon_{\mathsf{MSB}} = 4.2(8) \times 10^{-3}$.

Furthermore, the same $\mathscr{C}^{(1)}_{\mathsf{MSB}}$-RBM sequence was performed with the polyqubit initialised to an even superposition and to $|00\rangle$ (Figure 7.4). The error in the former case is orders of magnitude larger than in the latter[17]. While an error in the transition that does not involve $|00\rangle$ is not ruled out by this measurement, it appears more plausible that the disparity is a direct consequence of populating all states instead of just two, rather than a transition-specific error.

#### 7.3.1.2 Off-resonant excitation and spontaneous decay errors

Since the full heralded SPAM protocol of Section 4.4.1 was not used, we are sensitive both to population errors within the computational manifold as well as leakage outside it. However, the latter is bounded by the error on monoqubit RBM, since that is also sensitive to these errors. Thus, leakage outside the manifold cannot explain the observed disparity, although as calculated in Section 6.2.4, off-resonant excitation to spectator states would induce errors at the $10^{-4}$ level. This might be a leading contribution to the monoqubit RBM and $\mathscr{C}^{(1)}_{\mathsf{LSB}}$-RBM error.

We instead calculate the contribution due to scattering and decay to other states in the manifold. Using the expressions for errors due to state decay and elastic and inelastic scatter calculated in Section 5.2 (using the 1762 nm laser parameters), we find the errors

[17] The sequence lengths in Figure 7.4 were too short to properly estimate the low errors reported when starting from $|00\rangle$. Nonetheless, it is clear that this leads to much lower error than starting from a superposition.

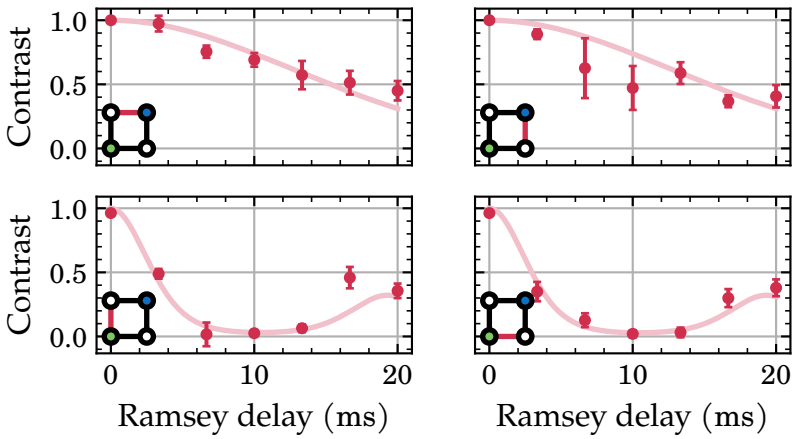



**Figure 7.5:** Ramsey contrast decay for each transition in the encoding. The transition is indicated by highlighting the corresponding edge in the connectivity graph drawn on each plot. The $D_{5/2}$ level states are coloured in the insets, with the high- and low-sensitivity states ($|D_{5/2},1,0\rangle$, $|D_{5/2},2,0\rangle$) in green and blue, respectively. The light-coloured traces are simulations with laser frequency noise of RMS $\sqrt{\langle \delta f_{1762^2} \rangle} = 17.8(10)$ Hzand magnetic field spurs at 50 Hz and 100 Hz, with RMS $\sqrt{\delta B_{50}} = 0.22(2)$ mGand $\sqrt{\delta B_{100}} = 0.1(2)$ mG.

due to these sources are dominated by state decay, and at a level of $\sim 10^{-7}$. These, as well as the intra-encoding off-resonant excitation rates from Section 6.2.4, are negligible.

#### 7.3.1.3 Sources of phase noise

Of the sources of phase noise considered in Section 5.2.2, we only consider fluctuations in the magnetic field and laser frequency. LS noise is neglected, since it would require large intensity fluctuations in the beam, which would also induce Rabi frequency fluctuations, whose consequences we don't observe. We can estimate the power spectral density (PSD) of both noise processes from Ramsey coherence measurements on each transition, as shown in Figure 7.5. For convenience, we will again refer to the pair of states in the transition as a "qubit" for this section. The error per Clifford can then be extracted from simulations of RBM sequences under this noise.

The Ramsey contrast decays at different rates for each transition, since they have different magnetic field sensitivities. The two transitions which include the $|D_{5/2},1,0\rangle$ state, (the bottom-left state in the connectivity graph), which is the only state in the polyqubit with a moderate magnetic field sensitivity, show a fast decay in contrast and a small revival at 20 ms. This suggests that there is a large spur in magnetic field fluctuations $\delta B(t)$ at

50 Hz and its multiples due to the AC line signal[18]. The remaining two transitions that involve $|D_{5/2},2,0\rangle$ (top-right state in the connectivity graph) have a very small magnetic field sensitivity, but still exhibit only a gradual drop in contrast. We identify this with quasi-static laser frequency noise $\delta f_{1762}(t)$.

The laser frequency noise variance $\langle\delta f_{1762}^2\rangle$is extracted considering only the transitions to $|D_{5/2},2,0\rangle$. Equation (5.21) can be used to extract the state fidelity $\mathscr{F}_s$ of the qubit state $|+\rangle$ after evolving under static noise, which is related to the Ramsey contrast by $C = 2\mathscr{F}_s - 1$. Thus, the contrast decays as $e^{-(t/\tau)^2}$ for a time constant $\frac{1}{\tau^2} = \frac{4\pi^2\langle\delta f_{1762}^2\rangle}{2}$ in agreement with [147]. Gaussian fits to both decays yield estimates of $\sqrt{\langle\delta f_{1762}^2\rangle}$ that differ by $\sim 1$ Hz; their mean is 17.8(10) Hz.

To extract the RMS amplitude of the magnetic field spurs, the `filter_functions` Python software package [193] (see Section 5.1.3.1) was used to calculate the contrast decays under a PSD containing the spurs and the laser frequency fluctuations together, considered as independent noise sources. The spurs were modelled using Lorentzian line shapes (5.12) with a FWHM of 1 Hz. For numerical stability, the laser frequency noise (whose RMS was found above) was assumed to have an exponentially decaying autocorrelation, with a correlation time $\tau_c = 100$ ms far exceeding the duration of an experimental shot even in the longest RBM sequence. The contrast decays using the magnetic field sensitivity of the $|S_{1/2},1,0\rangle \leftrightarrow |D_{5/2},1,0\rangle$ transition could then be calculated as a function of the spurs' RMS values. It was found that components at 50 Hz and 100 Hz were sufficient to yield a good fit, which gave fit values $\sqrt{\langle\delta B_{50}^2\rangle} = 0.22(2)$ mG and $\sqrt{\langle\delta B_{100}^2\rangle} = 0.1(2)$ mG. Simulations with the full spectrum also agree with the $|S_{1/2},2,0\rangle \leftrightarrow |D_{5/2},1,0\rangle$ contrast decay.

A full simulation of the polyqubit RBM experiments was then carried out using the full noise spectra and assuming no other sources of error. Equation (5.15) was used, assuming no detunings and that all LS and multi-photon resonance effects have been coherently corrected, thus eliminating them. The Rabi frequencies used were those of Figure 7.2. A total of 30 different sequences were generated for each sequence length. The initial state of the polyqubit in all cases was a superposition of states, as per experiment.

[18]The Ramsey experiments here, as well as all experiments in this thesis, were performed without line triggering.

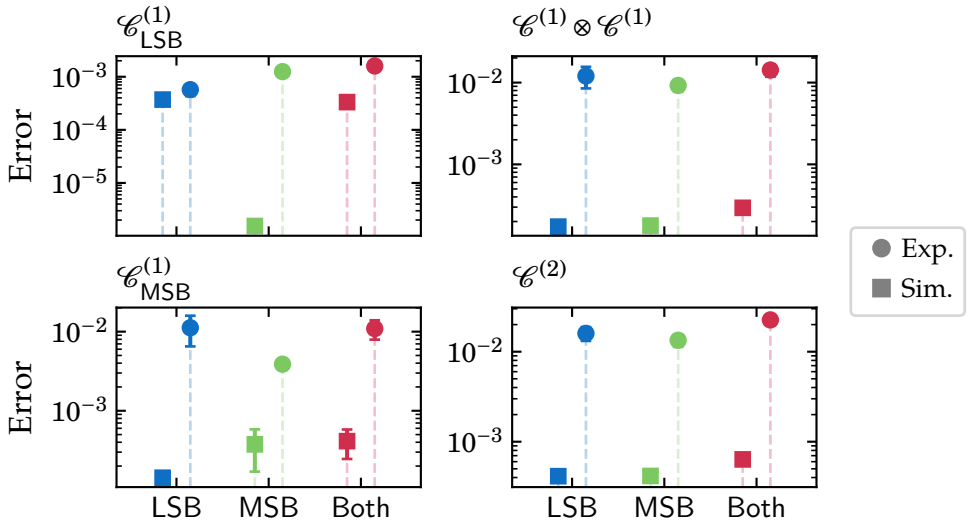



**Figure 7.6:** Simulated errors per Clifford gate (squares) assuming the PSD spectra described in the text, compared to the measured ones (circles). These are shown for each RBM experiment, as labelled in each pane.

The simulated errors per Clifford are given in Figure 7.6, alongside the measured ones. In almost every case, the simulated error was at least an order of magnitude smaller than the measured one, even though in many cases the sequence durations far exceed the 20 ms line signal periodicity. This is because the individual $\pi/2$ pulses are much shorter than the magnetic field fluctuations and thus effectively dynamically decouple the polyqubit from it, as well as from the laser frequency noise [191]. This is also expected, since the noise would affect monoqubit RBM sequences involving $|D_{5/2}, 1, 0\rangle$ similarly – although those experiments are much shorter.

#### 7.3.1.4 Breaking the multi-photon resonance condition

As discussed in Sections 5.2.1 and 3.4, a polyqubit with a cyclic connectivity graph can be affected by errors whose magnitude is time-dependent. A TSR applied at time $\tau$ is surrounded by $R_z^{\nu,\mu}(\pm\bar{\omega}_l\tau)$, where $\bar{\omega}_l = \frac{1}{d}\sum_T s^{(T)}|\omega_l^{(T)}|$ is the mean signed laser frequency. For long sequences, these errors may have a large impact even for small $\bar{\omega}_l$. Indeed, at times $\tau = \frac{\pi}{\bar{\omega}_l}$, the exact inverse of the intended TSRs will be implemented! Furthermore, virtual rotations will be unaffected by this, resulting in a net operation that is completely different to what is expected in a way that strongly depends on the sequence. For the longest sequences of duration $\sim 20$ ms or longer, this only requires $\bar{\omega}_l \approx 2\pi \times 25$ rad s$^{-1}$.

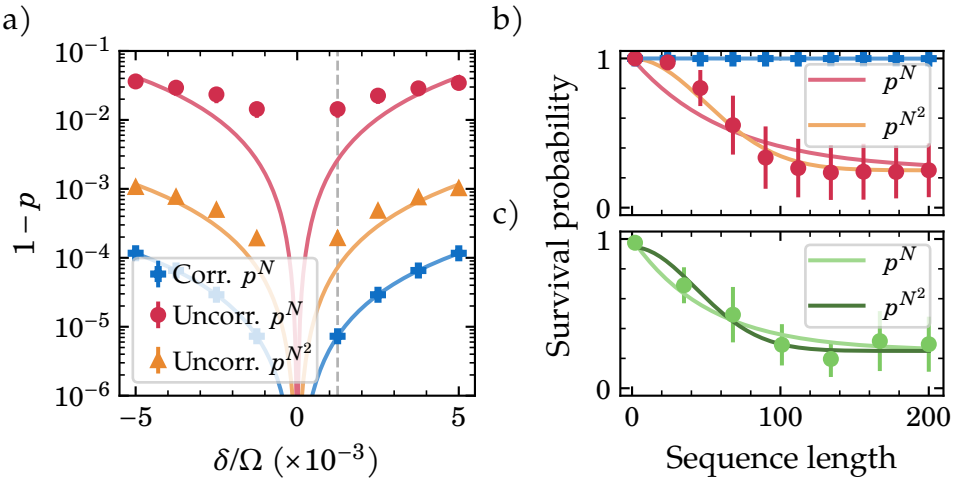



**Figure 7.7:** a) Simulations of $\mathscr{C}^{(1)} \otimes \mathscr{C}^{(1)}$-RBM on an idealised system with all Rabi frequencies set to $\Omega = 1$ rad s$^{-1}$ and no LS. The same RBM experiment, with 100 random sequences for each of 10 sequence lengths, is run with a detuning $\delta$ added to a *single* transition, so $\bar{\omega}_l = \frac{\delta}{4}$. The red circles show the decay parameter $p$ extracted from fitting the resulting survival probabilities to an exponential (Equation (7.1)) which for Markovian errors is proportional to the average fidelity. However, since the errors are non-Markovian, the survival probability does not decay exponentially; the orange chevrons are the decay parameters from a fit to $P(N) = Ap^{N^2} + \frac{1}{4}$. The errors can be coherently corrected (see Section 5.2.1), in which case the decays are exponential; the fitted $p$ are shown as blue crosses. The solid lines are parabolic fits to $p$ as a function of $\delta$, which is the usual dependence for coherent, Markovian errors. Only the $p$ parameters for the corrected case follow this dependence. b) The survivals for the detuning marked by a dashed gray line in a). The uncorrected survivals (red circles) follow a Gaussian decay $p^{N^2}$ (orange line) more closely than an exponential (red line). If the errors are coherently corrected (blue crosses) the error becomes negligible. c) The experimentally measured decays of both qubits for the $\mathscr{C}^{(1)} \otimes \mathscr{C}^{(1)}$-RBM experiment, reproduced from Figure 7.3. A fit to a Gaussian and exponential decay is shown in dark and light solid lines, respectively.

We may also expect these effects to be small at short times, so the survival probability may decay faster at longer times and no longer be exponential, as per (7.1).

To highlight this, we simulate[19] an idealised polyqubit system in Figure 7.7, with a detuning $\delta$ on a single transition so that $\bar{\omega}_l = \frac{\delta}{4}$. The non-Markovian nature of these errors can be seen from the fact that the RBM decays are Gaussian rather than exponential, following a decay $P(N) = Ap^{N^2} + \frac{1}{4}$ instead of Equation (7.1). Thus, we do not convert the decay parameter $p$ to an average error, and report its value directly; for exponential decay, the error is $\varepsilon = \frac{4}{5}(1-p)$. It can be seen that even for small $\bar{\omega}_l \approx \Omega \times 10^{-3}$, the error when considering an exponential decay would be very large ($>\sim 10^{-2}$). However, as discussed in Section 5.2.1, these errors can be coherently corrected. When doing so,

[19]The simulations evolved the state by calculating the operator Equation (5.15) at each gate; simulations with a fully time-dependent Hamiltonian gave identical results.

the effective errors are reduced by over two orders of magnitude. They also increase quadratically with the detuning as expected for coherent Markovian errors, unlike in the uncorrected case. This method was not known at the time of experiments, and thus could not be implemented.

We can thus search for signatures of non-Markovianity in the RBM data. The experimental statistics taken, particularly at shorter sequence lengths, were not sufficient to convincingly distinguish between the two types of decay (see Figure 7.7). Furthermore, in $\mathscr{C}^{(1)}_{\mathsf{LSB}}$-RBM, the decay is clearly linear, although since these sequences are much shorter than the rest due to the transitions having short $t_\pi$, the effect would be less pronounced. Another feature of non-Markovianity is a large variance in the survival probability at different sequence lengths [218]. We can see that this is indeed the case in many of the results in Figure 7.3. This may suggest non-Markovianity, although a thorough statistical analysis was not carried out.

We can also use our knowledge of the DDS frequencies that were used to drive the EOM (which were the same for all experiments in Figure 7.3) to infer the value of $\bar{\omega}_l$, which was $2\pi \times 27.3$ rad s$^{-1}$. From the LS matrix of 7.1, being perfectly on resonance with the transitions would imply that $\bar{\omega}_l = -2\pi \times 36.2$ rad s$^{-1}$. This may explain why the parameters used to calculate the LS corrections were not those extracted from 7.2, but were instead optimised to minimise the error per Clifford. Indeed, as argued in 5.2.1.5, the phase corrections used to cancel the LS phases likely also cancel the errors from breaking the multi-photon resonance condition when the transitions are driven on resonance. Thus, modifying the correction phases (by changing the LS matrix used to generate them) may mitigate any *additional* contributions to $\bar{\omega}_l$ from detuning miscalibrations.

Simulations of the RBM sequences taking the $\bar{\omega}_l$ and the LS matrix into account were carried out[20]. We simulated correcting only the LS through the phase of TSRs, as was done in experiments; correcting only the LS by applying the inverse of (3.26); and correcting both the LS and $\bar{\omega}_l$ by applying the correct inverse matrices in (5.15). Figure 7.8 compares the experimental results to these simulations. To reproduce the experimental $\bar{\omega}_l$, the detuning on each transition had the same magnitude (with appropriate signs). This

[20]The modified LS matrix was only used to implement the LS error compensation; the actual light shifts induced onto the polyqubit were calculated using the parameters from Figure 7.2

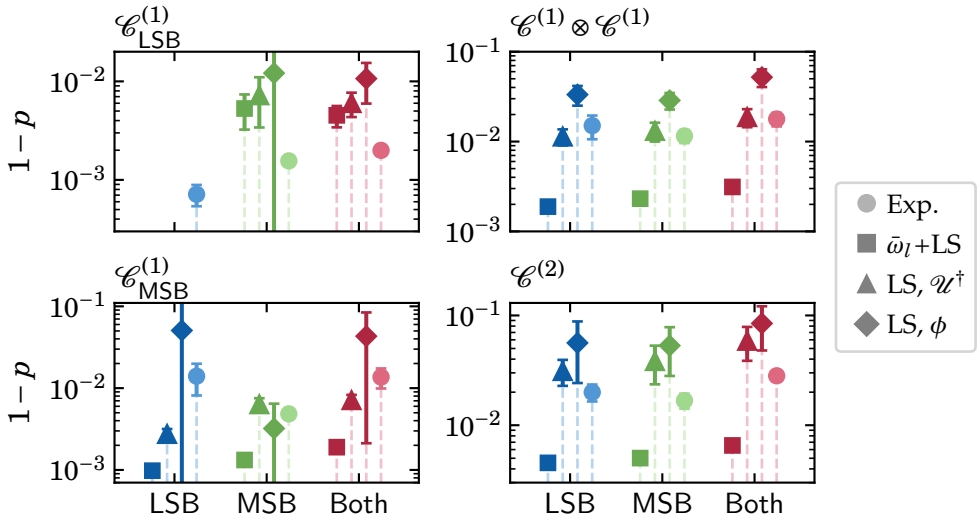



**Figure 7.8:** Simulated decay parameters using the experimental $\bar{\omega}_l$ and LS. Large $1-p$ indicates larger errors. For fair comparison, all fits were made to an exponential decay (7.1), which leads to large error bars in certain cases. Different levels of coherent correction were simulated, including correcting for the LS by updating the phase $\phi$ of TSRs (diamonds), which was done in the experiment; applying the inverse of the LS unitary (3.26)(chevrons); and applying the inverse of both the LS and $\bar{\omega}_l$ unitaries from (3.31)(squares). The experimentally measured values are also shown (light-coloured circles).

may not have been how the detunings were distributed in the experiment, though this was not found to have a large impact in simulations.

It can be seen that the simulated decay using the LS calibration procedure used in the experiment would yield an effective error significantly above the measured one. No conclusive explanation for this was found. We speculate that the presence of other small, incoherent errors may serve to wash out the coherent nature of these errors, thereby reducing their magnitude – although this was not simulated. In any case, breaking the multi-photon resonance condition by experimentally relevant amounts is clearly capable of producing errors of the magnitude observed. Furthermore, the simulations show a large drop in effective error when both the LS and multi-photon resonance effects are compensated, suggesting that these effects can be mitigated.

## 7.4 Quantum Process Tomography

We now present the implementation of the QPT experiments described in Section 7.1.2. This was done for all gates in the intra-ion universal gate set[21] $\{\mathtt{H}\otimes\mathbb{1}, \mathbb{1}\otimes\mathtt{H}, \mathtt{T}\otimes\mathbb{1}, \mathbb{1}\otimes\mathtt{T}, \mathtt{CZ}\}$, plus the identity process[22].

Given that a large contribution to the RBM infidelity may be due to non-Markovian errors (Section 7.3.1.4), it is valid to question whether extracting a quantum process for each gate is meaningful. Those errors were particularly relevant in RBM because the experimental sequences were long compared to $\frac{2\pi}{\tilde{\omega}_l}$. Indeed, Figure 7.7 shows that the (simulated) survival probability in the presence of these errors follows a Gaussian decay, suggesting that the first few gates in the sequences are mostly unaffected by these errors. These could be meaningfully described by a quantum process which we expect to be the same as if the non-Markovian errors were coherently corrected. QPT sequences are only a handful of gates long, placing them firmly within this regime. Nonetheless, it is clear that, if the non-Markovian errors are *not* corrected, the quantum processes are not applicable to each implementation of the gate in a long sequence.

### 7.4.1 Experimental procedure and data processing

The sequences that comprise a full QPT experiment are all identical: the state $|00\rangle$ is prepared, followed by the state preparation fiducial gate, the gate under test, and the measurement fiducial gate. Finally, the polyqubit is measured in the $Z$ basis. To do tomography on the identity process, as well as gates implemented virtually, the measurement fiducials were applied immediately after the preparation fiducials – with appropriate phases where relevant.

One disadvantage of QPT when compared to RBM is that it is sensitive to SPAM errors. As such, we make use of the leakage detection protocol from Section 4.4. A leakage occurred in ~ 2% of shots, the vast majority of which were errors in state preparation. These shots were rejected in post, out of the 400 shots taken for each circuit.

[21] Since an S gate can be constructed from two T gates, only the latter was characterised.
[22] We also point out that the tomography on the T gates was done months after the rest of the gate set.

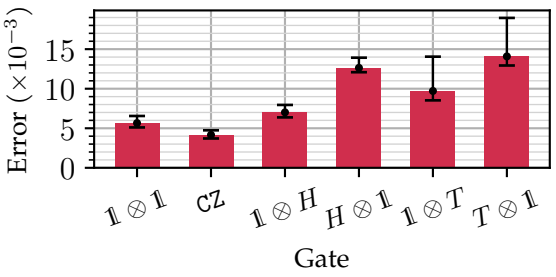



**Figure 7.9:** Average error of all gates in the gate set. Errorbars correspond to the 5$^{\text{th}}$ and 95$^{\text{th}}$ percentiles of the fidelities extracted from 100 bootstrap simulations.

The $\chi$ matrix (Equation (7.2)) for each gate process was then calculated using only the shots accepted. In order to estimate uncertainties, 100 rounds of bootstrapping simulations were performed [224]. To do so, we calculate the state that would be produced by perfect SPAM fiducials, with the measured quantum process between them. This state defines a multinomial distribution for the probability of observing each measurement outcome. A single round of bootstrapping involves generating an experimental dataset by sampling from these distributions. The number of samples was the number of accepted shots per point after leakage detection. The $\chi$ matrix for each simulated dataset was then calculated.

### 7.4.2 Results

The $\chi$ matrices and error matrices $\mathcal{E}_\chi$ for all gates characterised are given in Figures 7.11 - 7.16. The average error in each gate is also summarised in Figure 7.9.

A noteworthy observation is that there is little difference between the fidelity of diagonal gates (`CZ`, `T` gates and the identity process) compared to the `H` gates. This is unexpected, since the former are implemented virtually, while the latter require two $\pi/2$ pulses. Furthermore, the error in these gates is significantly larger than the average error per Clifford in the single-qubit RBM experiments (Table 7.1). This is likely attributable in part to errors in the SPAM fiducials, which affect the final $\chi$ matrix. These gates add a total of 6 $\pi/2$ pulses on average to each QPT, so a naïve estimate assuming an error per pulse comparable to that measured in RBM, $\sim 2\times10^{-3}$, yields $\sim 1.2\times10^{-2}$ additional error per QPT sequence. Such an analysis is inconsistent with the statement that the gate errors in short sequences are lower than in long ones (see Section 7.4), although it does overestimate the observed QPT errors in many cases (Figure 7.9). Thus,

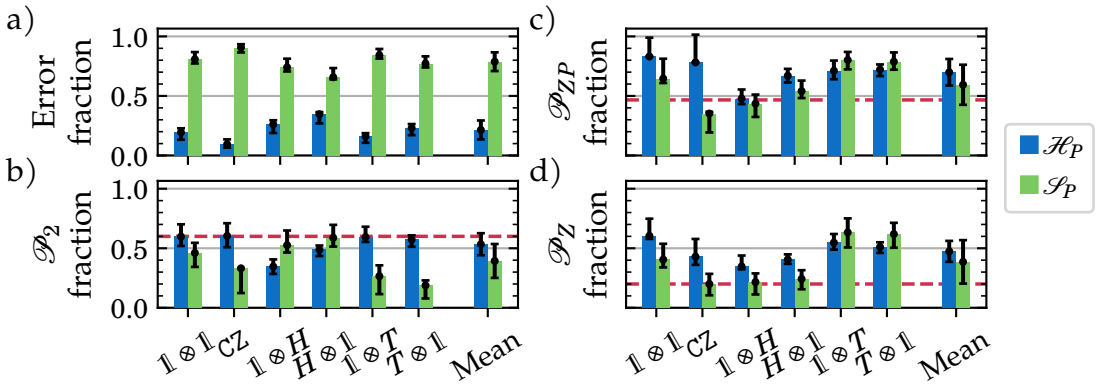



**Figure 7.10:** Blue (green) bars correspond to $\mathscr{H}_P$ ($\mathscr{S}_P$) generators. a) Errors due to $\mathscr{H}_P$ and $\mathscr{S}_P$ generators as a fraction of the total trace error for each gate. b) Total magnitude of two-qubit Pauli generator coefficients in $\mathscr{H}_P$ and $\mathscr{S}_P$, as a fraction of the sum of magnitudes of all coefficients in each. The red dashed line shows the fraction for an unbiased spread of coefficients about the Pauli matrices (3/5). c) and d) are like b), but for the fraction of coefficients corresponding to Pauli matrices that include $Z$, and matrices that *only* include $Z$ or the identity, respectively. The unbiased fractions would be 7/15 and 1/5. Quantities are plotted for each gate, with errorbars showing the bootstrapped $5^{\text{th}}$ and $95^{\text{th}}$ percentiles. The mean over all gates is also shown, whose errorbars are one standard deviation.

it is not unlikely that this plays a role in the added error, particularly since the gates under characterisation are the same as the fiducial gates. This would mean that the error matrices do not faithfully represent the true quantum process, particularly for the diagonal gates whose expected error is much lower than for the SPAM fiducials. Nevertheless, it may still be possible to make meaningful statements about the errors as a whole, instead of analysing each gate in isolation.

We also extract the Hamiltonian and Stochastic error generators from the extracted experimental error matrices. These are plotted alongside the $\chi$ and $\mathscr{E}$ matrices in Figures 7.11 - 7.16. We use them in an attempt to answer three questions. How much of the error processes is attributable to coherent and stochastic errors? What proportion of the errors are single-qubit as opposed to two-qubit? And do these error processes have a bias towards errors that affect the phase of the polyqubit ($Z$-type errors)?

To answer the first question, we calculate the errors $\epsilon_{\mathscr{H}}$ and $\epsilon_{\mathscr{S}}$ due to the processes generated by the Hamiltonian and Stochastic generators independently[23], $\mathscr{E}_{\mathscr{H}} = e^{\sum_P h_P \mathscr{H}_P}$ and $\mathscr{E}_{\mathscr{S}} = e^{\sum_P s_P \mathscr{S}_P}$. These generators generally do not commute, so such independent

[23]For clarity, the $\rho$ dependence in the generators is dropped throughout this section.

analysis is only valid in the limit of small total errors $\epsilon$. This is the case here: we find $\frac{|\epsilon-(\epsilon_{\mathscr{H}}+\epsilon_{\mathscr{S}})|}{\epsilon} < 0.01$ for all gates.

The ratios $\frac{\epsilon_{\mathscr{H}}}{\epsilon}$ and $\frac{\epsilon_{\mathscr{S}}}{\epsilon}$ are shown in Figure 7.10a. It can be seen that the proportion of Pauli Stochastic errors far exceeds that of Hamiltonian errors[24]. This is surprising if breaking the multi-photon resonance condition is the leading cause of the errors, since this is a coherent process. However, the error would depend on the exact time at which the gate under test is applied, which will depend on the measurement fiducials. This may emulate the effect of applying random small unitaries, which is identical to a stochastic error.

Next, Figure 7.10b shows the total fraction of coefficients that generate two-qubit errors. This is defined as $\frac{\sum_{P\in\mathscr{P}_2} a_P}{\sum_{P\in\mathscr{P}} a_P}$ where $a = h, s$; $\mathscr{P}$ is set of all 2-qubit Pauli matrices (excluding the identity); $\mathscr{P}_2$ is the set of all Pauli matrices such that $P = P_i \otimes P_j$ for $P_i, P_j \neq \mathbb{1}$. It can be seen that in all cases, the fraction of two-qubit coefficients is slightly below what it would be if the errors were unbiased (uniformly spread over all Pauli matrices). Surprisingly, this implies that the errors are biased towards single-qubit errors despite native operations being two-qubit (Section 4.1), although the proportion of two-qubit errors is certainly not negligible.

Finally, Figure 7.10c shows the total fraction of coefficients that generate errors involving $\sigma_z$. This is defined analogously to the fraction of two-qubit Pauli matrices. In nearly all cases, the measured fractions exceed the unbiased bound. Note that this metric includes matrices of the form $P_i \otimes \sigma_z \in \mathscr{P}_{ZP}$, where $P_i \neq \sigma_z$. Figure 7.10d shows the fraction of errors considering matrices $P \in \mathscr{P}_Z$ that *only* contain $\sigma_z$ or the identity (excluding $\mathbb{1} \otimes \mathbb{1}$). In all cases (except for stochastic errors in the CZ gate) the measured fraction exceeds this bound. This clearly displays the prevalence of $Z$ errors – although this would also be expected in monoqubits.

## 7.5 Summary

Intra-ion polyqubit gates have been characterised experimentally using RBM and QPT. RBM experiments that addressed just one qubit in the ion, and that addressed both

[24]This appears at odds with the fact that the $h_p$ coefficients in Figures 7.11 - 7.16 are two orders of magnitude larger than the $s_p$ coefficients. This is because the error associated with Stochastic Pauli errors is linear in $s_p$, whereas for Hamiltonian errors it is quadratic in $h_p$ [171].

of them independently or together, were carried out. Most of these experiments show errors per laser pulse that are about 3 – 10 times higher than monoqubit RBM. Notably, two-qubit RBM had comparable errors per laser pulse to independent single qubit RBM, confirming that the virtually applied CZ gate adds negligible error. Numerical simulations were used to calculate the expected contributions from various sources to the measured error to explain the disparity between polyqubit and monoqubit results. Drive tone detunings that did not fulfil the multi-photon resonance condition $\bar{\omega}_l = 0$ were found to be the most likely explanation. The errors induced by this are non-Markovian, but they can in theory be corrected in software through virtual rotations; this conclusion is also supported by simulations.

The $\chi$ matrices for all gates in a universal intra-ion gate set were extracted using QPT. These show higher error than the RBM measurements, which is likely due to errors in the SPAM fiducial gates. Analysis of the extracted errors suggests they are evenly spread across single- and two-qubit errors, and, for gates implemented virtually, are mostly concentrated about Pauli $Z$ errors.

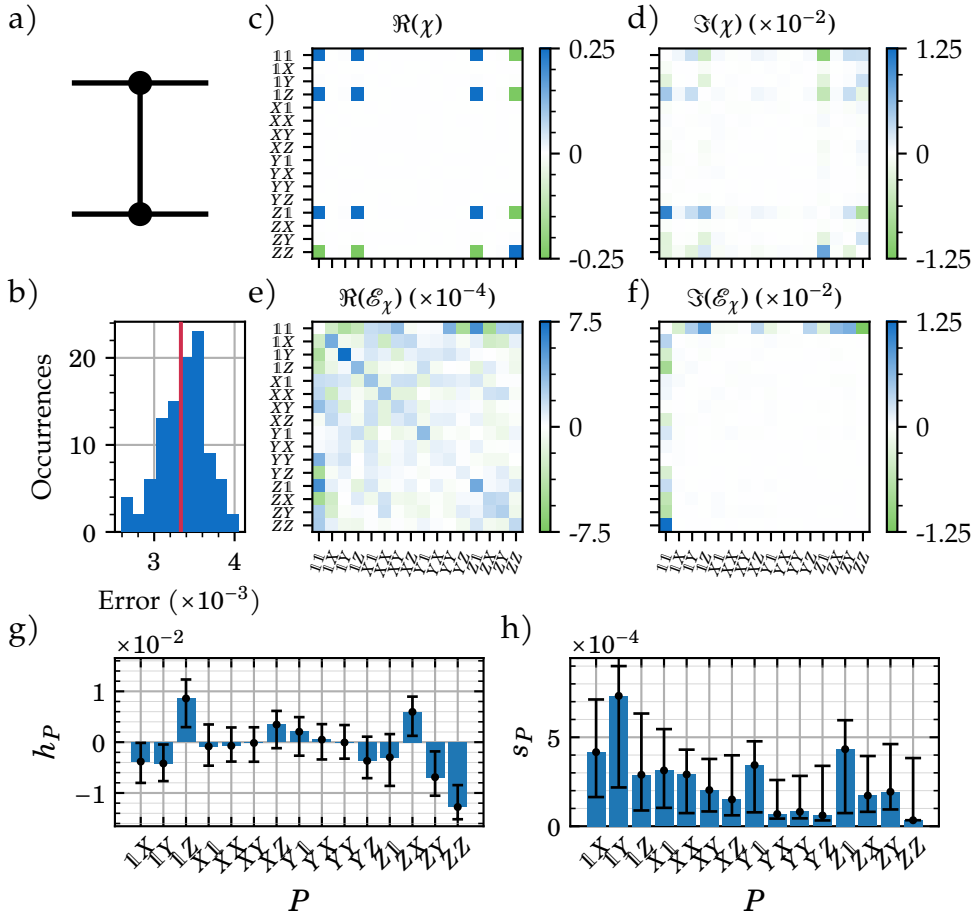



**Figure 7.11:** QPT data for the CZ gate. a) Circuit diagram. b) Error of the measured process matrix (red vertical line) and of the 100 bootstrapping simulations (blue histogram). c), d) Real and imaginary parts of the measured $\chi$ matrix. e) f) Real and imaginary parts of the measured error matrix $\mathcal{E}_\chi$. The entry $\Re(\mathcal{E}_{\chi,00})$ at the top left of e), which is related to the fidelity (Section 7.1.2.1), has been set to zero to allow the other entries to be visible. g), h) show, respectively, the Hamiltonian ($h_p$) and Stochastic ($s_p$) error generator coefficients extracted from the measured error matrix $\mathcal{E}_\chi$. Errorbars show the $5^{\text{th}}$ and $95^{\text{th}}$ percentile of the quantity in the bootstrapped data. In very rare cases, the measured data lay outside these bounds, in which case the length of the corresponding error bar was set to 0. The Hamiltonian and Stochastic error generators are used to analyse the nature of the errors (Figure 7.10).

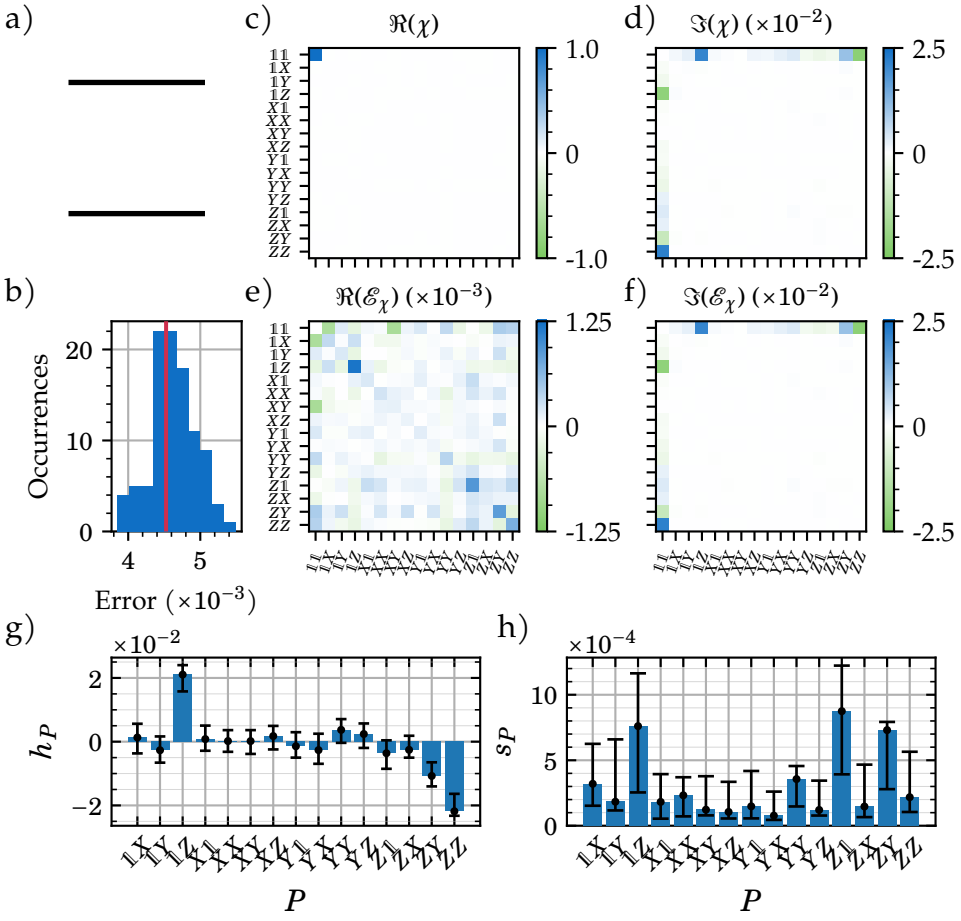



**Figure 7.12:** QPT data for the identity gate. Subfigures are as per Figure 7.11.

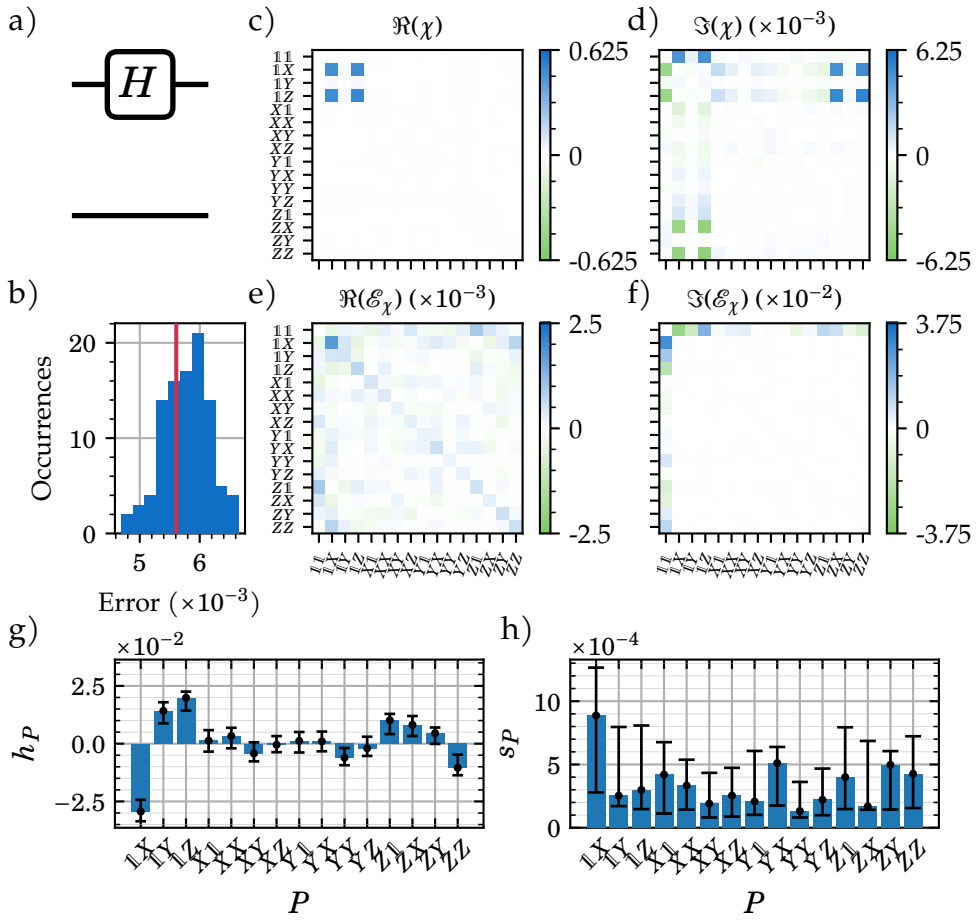



**Figure 7.13:** QPT data for a Hadamard gate on the LSB qubit. Subfigures are as per Figure 7.11.

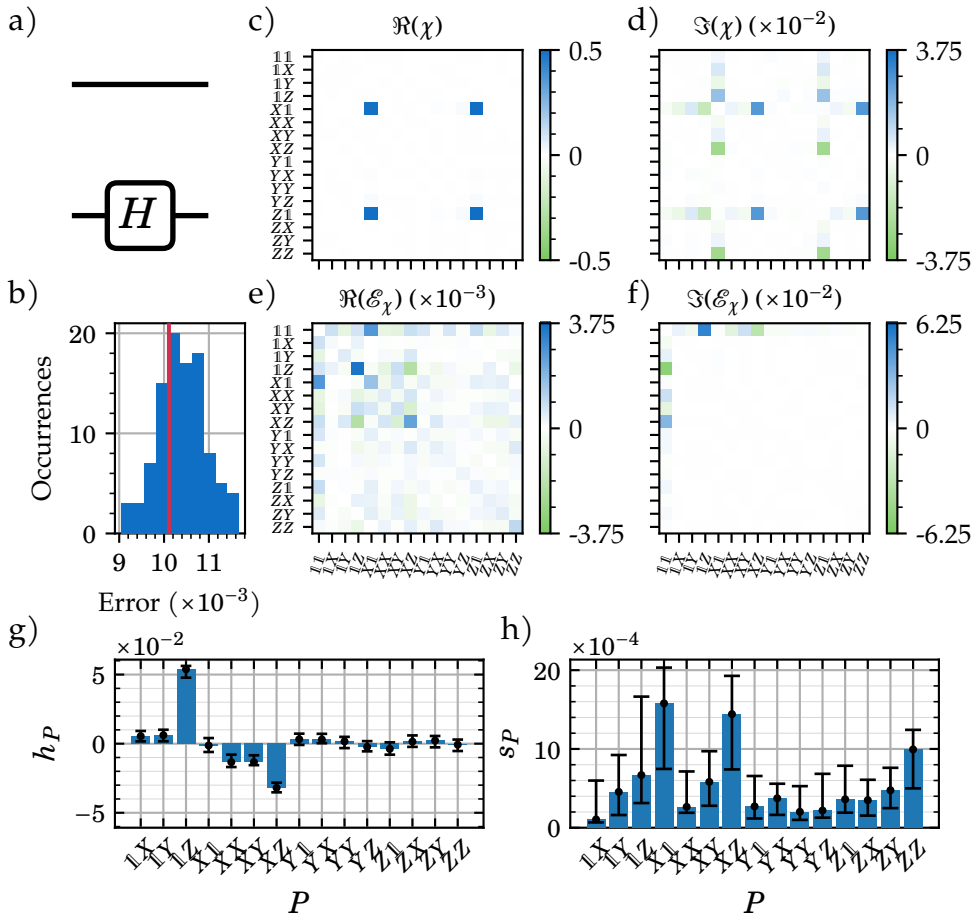



**Figure 7.14:** QPT data for a Hadamard gate on the MSB qubit. Subfigures are as per Figure 7.11.

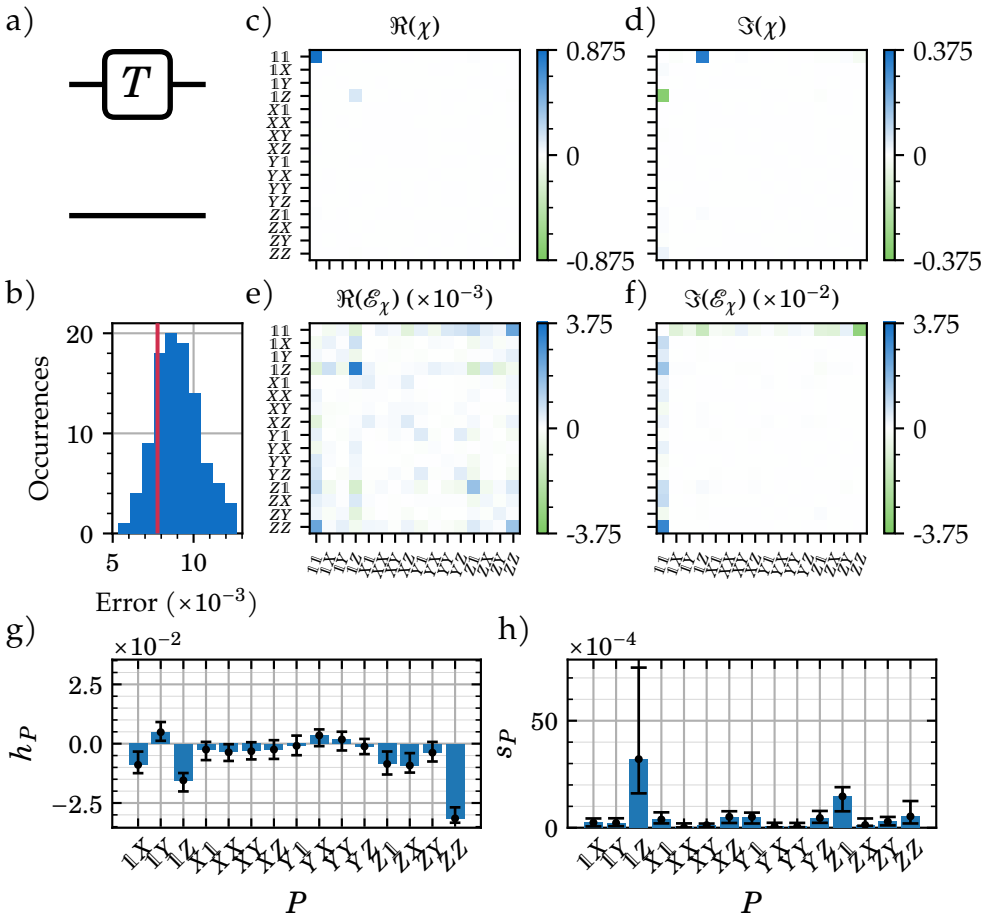



**Figure 7.15:** QPT data for a T gate on the LSB qubit. Subfigures are as per Figure 7.11.

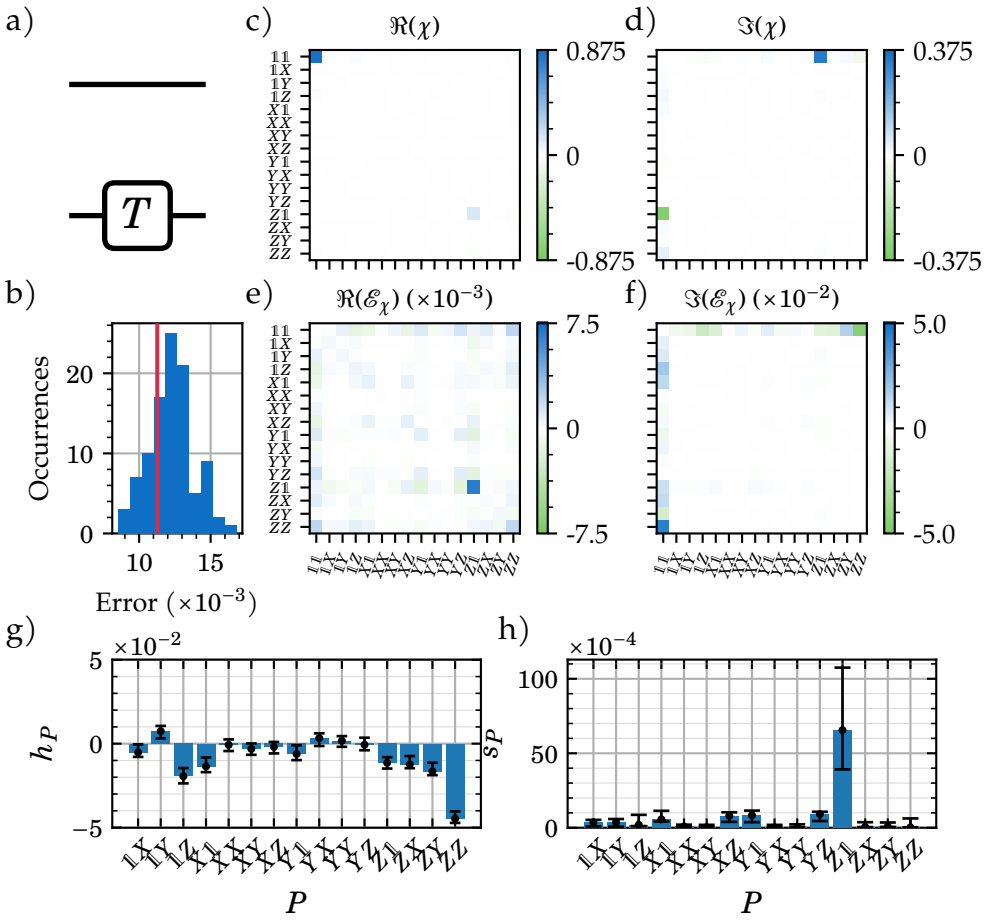



**Figure 7.16:** QPT data for a T gate on the MSB qubit. Subfigures are as per Figure 7.11.

*Can we stop the Greggs slander?*

— Oliver Hale, in defense of a bastion of British cuisine.

# 8

# Experimentally implementing inter-ion gates

This chapter describes the implementation of the two-ion Sleepy Gates from Chapter 4, which use a light-shift mechanism. $ZZ$ gates between the LSB/MSB qubits in both ions are applied without affecting the spectators, as well as $ZZZZ$ rotations involving all four qubits. As discussed in Chapter 4, $ZZZ$ and the remaining two-ion $ZZ$ gates could also be applied with almost identical methods. However, this requires individual addressing of the 1762 nm laser, which is not possible with the current setup.

The realisation of these gates leans heavily on the implementation of monoqubit LS gates across an optical transition in our experiment, laid out in reference [123]. The theoretical proposal for such monoqubit gates was laid out in reference [145], with a previous demonstration to ours presented in [204]. Finally, we point out that a light-shift two-qudit gate has also been demonstrated in reference [153].

The chapter begins by explaining the circuits used to implement and characterise the gate, followed by a discussion of which motional mode to use. The procedure for setting the polarisation of the 532 nm beams is then discussed. Measurements of single-ion spin-dependent forces on the four-state polyqubit subspace are then presented. Following this, the routines used to calibrate the gate are discussed. The chapter concludes by presenting parity and population measurements on two- and four-qubit GHZ states, and a discussion of expected errors.

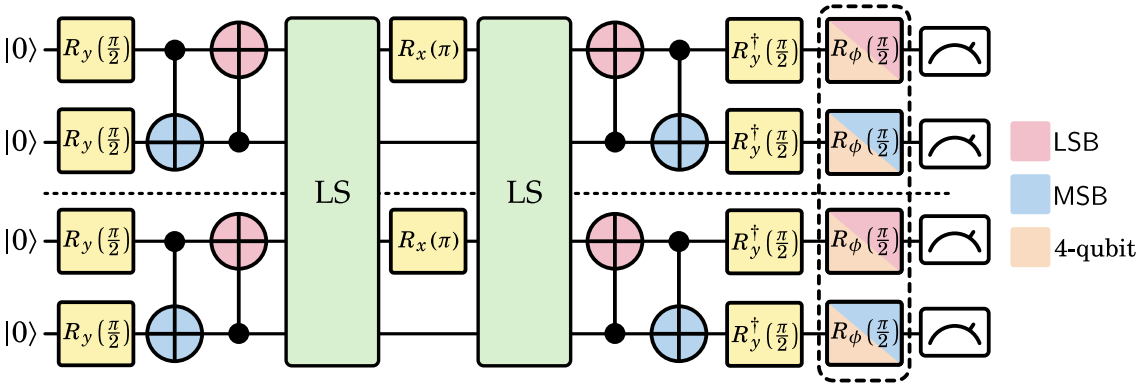



**Figure 8.1:** Circuit for preparing and measuring GHZ states. Each green LS pulse drives an $R_{zzzz}(\frac{\pi}{4})$ rotation. The CNOT gates are used to reduce this to $ZZ$ gates on the LSB (red) or MSB (blue) qubits, and are not used for $ZZZZ$ gates. Single-qubit gates used in every circuit – the *starting* and *closing* $y$-rotations, and the *echo* $x$-rotations – are shown in yellow. After the closing rotations, a GHZ state of either two or four qubits is prepared. The state would then be immediately measured to perform a population measurement. To perform a parity measurement, single-qubit *analysis* rotations (shown with a dashed square around them) are applied, whose phase is scanned. The gates are only applied on the qubits that participate in the GHZ state; blue, red and orange indicate gates used to measure MSB, LSB and four-qubit GHZ states. In the experiments of later in this section, the duration of the LS pulses was 80 µs. Using the transition Rabi frequencies from Table 6.2, the total duration of the circuits is 427 – 603 µs depending on which exact circuit is executed. This is dominated by the pulses on the MSB qubit.

## 8.1 Gate circuits

The circuits used later in this chapter are discussed here and are shown in Figure 8.1.

### 8.1.1 Partial tomography

The objective of these experiments is to demonstrate that the proposed light shift mechanism successfully implements two- and four-qubit gates. The gold standard for doing so would be to perform full tomography of the gate processes, as was done in Chapter 7 for intra-ion gates. This would yield full information of the quantum process that is implemented. However, doing so is infeasible, for two reasons: the number of experiments required for four qubit tomography is $\sim 2^{4\times4} \approx 64000$, which is prohibitive[1]; and implementing all preparation and measurement fiducials requires individually addressed single-ion gates, which cannot be done with the global 1762 nm beam.

Instead of this, the non-local nature of a gate can be demonstrated by generating a non-separable state from a separable one, as mentioned in Section 5.3. The most common

[1] Assuming the duration of a shot is ~ 10 ms (this is much longer than the duration of the circuits in Figure 8.1 due to the lengthy SPAM and cooling routines), performing QPT with 400 shots per experiment as was done in the intra-ion tomography (Section 7.4) would take approximately three full days.

choice for the non-separable state is an $n$-qubit GHZ state $|\mathrm{GHZ}_n\rangle = \frac{1}{\sqrt{2}}(|0\rangle^{\otimes n} + |1\rangle^{\otimes n})$. Then, the fidelity of the prepared state $\rho$ to the target one $\mathscr{F} = \langle \mathrm{GHZ}_n | \rho | \mathrm{GHZ}_n \rangle$ [174] can be used as a proxy for the true gate fidelity.

We can estimate this fidelity using full state tomography or, more commonly, partial state tomography [109, 140, 179, 180]. This procedure uses the sparseness of the density matrix of an $n$-qubit GHZ state, which has only four non-zero elements located at the corners of the matrix. This greatly simplifies the fidelity:

$$\mathscr{F} = \frac{1}{2}(\rho_{\mathbf{0},\mathbf{0}} + \rho_{\mathbf{1},\mathbf{1}}) + \frac{1}{2}(e^{i\phi_0}\rho_{\mathbf{0},\mathbf{1}} + e^{-i\phi_0}\rho_{\mathbf{1},\mathbf{0}}) = C + P \tag{8.1}$$

where $\mathbf{0} \triangleq 00...0$, $\mathbf{1} \triangleq 11...1$ and we allow for a phase offset $\phi_0$ between the $|\mathbf{0}\rangle$ and $|\mathbf{1}\rangle$ states. The *population* $P = (\rho_{\mathbf{0},\mathbf{0}} + \rho_{\mathbf{1},\mathbf{1}})/2$ is the probability of finding the target qubits in either state $|\mathbf{0}\rangle$ or $|\mathbf{1}\rangle$ directly after the GHZ state is prepared. To find the parity contrast $C = (e^{i\phi_0}\rho_{\mathbf{0},\mathbf{1}} + e^{-i\phi_0}\rho_{\mathbf{1},\mathbf{0}})/2$, a $R_\phi(\pi/2)^{\otimes n}$ rotation is applied to the GHZ qubits before reading them out. The expectation value $\langle \sigma_z^{\otimes n} \rangle$ (the parity) oscillates sinusoidally in $\phi$, so the contrast $C$ can be found by repeating the experiment at different values of[2] $\phi$ and fitting the measured parities to $\frac{C}{2}\cos(n(\phi - \phi_0))$. We refer to the final $R_\phi(\pi/2)^{\otimes n}$ rotations as *analysis pulses*.

### 8.1.2 Generating and measuring GHZ states

Because of the choice of atomic encoding (Section 6.2.4.1), the LS interaction should apply a $ZZZZ$ rotation[3]. As described in Chapter 4, this gate can be converted to inter-ion $ZZ$ and $ZZZ$ gates by applying intra-ion `CNOT` gates before and after the LS pulses. However, since these gates are driven by the global 1762 nm beam, only the $ZZ$ gates between the two LSB qubits, and between the MSB qubits, can be implemented; anything else requires applying different `CNOT` gates on each ion.

These gates are diagonal in the computational basis, so their action on a computational basis state is trivial. Instead, the resulting unitary is made to act along the $X$ basis[4] by applying $R_y^{\otimes n}(\pi/2)$ and $R_y^{\otimes n}(-\pi/2)$ gates before and after the LS unitary, respectively, which are referred to as the *opening* and *closing* pulses. The resulting $XX$ and $XXXX$ gates can directly generate GHZ states from an initial $|00{:}00\rangle$ state using the correct gate angle.

[2] A minimum of $n-1$ such experiments with different $\phi$ are required [180].
[3] If the atomic states are disentangled from the motion.
[4] We will still refer to the LS gates as $Z$ gates in the remainder of the chapter.

Curiously, even if the atomic and motional state remain entangled after the LS pulse, the population measured after the closing pulses is not spread out across all computational states[5], despite the state after the opening pulses being an even superposition. Indeed, as can be seen in Figure 8.2 and shown in Appendix D.2, only four states are ever populated. These are the two states that are in an even superposition in the GHZ state (e.g. $|00{:}00\rangle$ and $|11{:}11\rangle$) and the two *crossed* states formed by swapping the states of one ion (e.g. $|00{:}11\rangle$ and $|11{:}00\rangle$). All other states should not be populated, so they are referred to as *spectators*. In the case of $ZZ$ gates, these states exactly match those in which the spectator qubits are excited.

The full gate circuit for each gate, including the CNOT gates, and the opening, closing and analysis single-qubit gates, is shown in Figure 8.1. Because the intra-ion gates target the same qubit(s) in each ion, all TSRs can be executed in parallel with the global 1762 nm laser. The sequence is also designed such that qubits that are not the target of the gate should undergo no evolution and thus should remain in $|0\rangle$.

### 8.1.3 Echo sequences

While it is possible in theory to generate a GHZ state by pulsing the 532 nm beams only once, the beams generate unwanted interactions on the motional and atomic states that make this challenging in practice. Thus, routines that coherently cancel these interactions via generalised echo sequences are used.

#### 8.1.3.1 Echoing the atomic state

The two-ion gates are mediated by the two-beam light shifts induced by the pair of 532 nm beams. However, since each beam is high-intensity, large single-beam light shifts, which impart unwanted single-ion phase shifts, are inevitable. The light shifts have been engineered – via the choice of states and the beam polarisations (Section 8.3) – such that a differential LS is only experienced by pairs of states in different levels. The computational states are encoded such that $|00\rangle$ and $|11\rangle$ are in the $S_{1/2}$ level, so the single-beam LS unitaries look like $\text{diag}\left\{e^{-i\frac{\phi}{2}}, e^{i\frac{\phi}{2}}, e^{i\frac{\phi}{2}}, e^{-i\frac{\phi}{2}}\right\}$. This is an unwanted intra-ion $ZZ$ gate.

[5] More precisely, this is only the case for the Sleepy Gates, for which the two-beam LS on states in the same level is the same. For arbitrary LS gates, this is not the case.

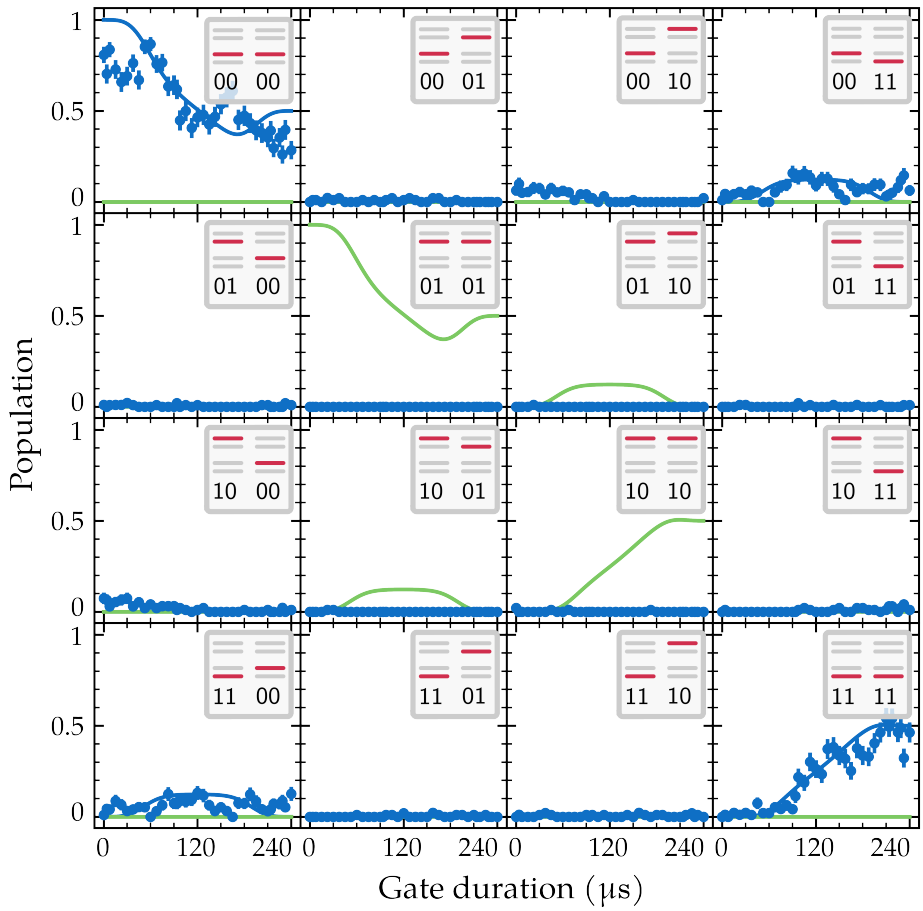



**Figure 8.2:** Time scan of a $ZZZZ$ gate. Each panel shows the population in a two-ion state; the computational states, and the atomic states used to encode them, are shown in the insets. Measured (blue circles) and simulated (blue lines) populations are shown for ions initialised to $|00{:}00\rangle$, as well as simulated populations for ions initialised to $|01{:}01\rangle$ (green lines). Notice that population is constrained to only four states, the two that form the GHZ state ($|00{:}00\rangle$ and $|11{:}11\rangle$ for the blue trace) and the crossed states ($|00{:}11\rangle$ and $|11{:}00\rangle$). There is a small amount of leaked population at small times. This is because phases induced during the gate are compensated by modifying the phase of single-ion gates, though this compensation is only correct at the gate duration (see Section 8.5.3).

In theory, these rotations could be corrected using virtual gates, if we had accurate knowledge of the accumulated phase $\phi$. However, the single-beam shifts are ~ 200 kHz, so since the gate duration is ~ 160 μs, the acquired phase is ~ 30 turns. Small fractional changes in the light shift frequency (due to, for example, slow beam pointing drifts) will thus result in large uncompensated phases. Additionally, individual addressing is required to correct for differential phases between the ions.

Instead, we can embed the light-shift SDF pulse in a spin-echo routine. The SDF is spread over two halves, and the ground and metastable states – which observe opposite

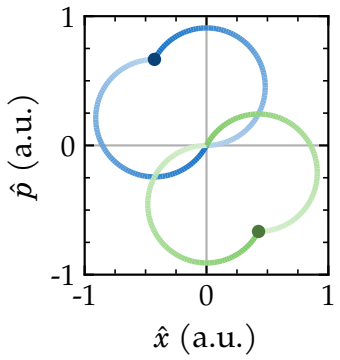



**Figure 8.3:** Sketch of the motional trajectories for an ideal echo sequence for states $|s{:}d\rangle$ ($|d{:}s\rangle$) in blue (green), where $|s/d\rangle$ is a single-ion state in the $S_{1/2}/D_{5/2}$ level. The SDFs on each state are equal in magnitude and opposite in phase, so they travel in opposite directions. The states follow the trajectories of increasing darkness. The SDF phase flips occur at the marked points; the subsequent displacement will always cancel the previous one. Notice that the same trajectories would be traversed if, instead of flipping the SDF phase by $\pi$, the atomic states were flipped and the phase reset to 0. This is the principle behind combining the motional and atomic echoes.

differential light shifts – are swapped between them. Thus, as long as each half induces the same single-beam light shifts, the phases accumulated in both will cancel.

Computationally, flipping the $S_{1/2}$ and $D_{5/2}$ states can be done via an $R_x(\pi)$ rotation on either the LSB or MSB qubit[6]. We choose the LSB, as the transitions involved have much shorter $\pi$ times.

If the light shifts between states in the same level were not equal – due to imperfections in the beam polarisation, or a different choice of atomic states – interactions that are not cancelled by this echo will be present. For example, any single-ion phase that results in a $Z$ rotation on the MSB qubit will clearly not be echoed by flipping the LSB qubit[7]. Furthermore, these interactions will generally not be single-ion, as described in Section 5.3.4. An extension to the echo sequence from this section that can cancel all diagonal rotations exists, which is similar to [141]. Because the states show the correct LS structure and the polarisation is well-aligned in our case, this is not needed.

#### 8.1.3.2 Echoing the motional state

As discussed in Section 5.3.1, one of the most important sources of error in two-ion gates is residual entanglement between the atomic and motional states at the end of the gate

[6]The atomic echo adds a phase of $n\pi$ and thus shifts the contrast fringe by the same amount. This is unobservable with an even number of qubits.

[7]This will be relevant in Section 8.5.3.

operation - often termed "loop closure" errors. This could occur due to a miscalibration in the gate time $\tau$ or detuning $\delta$, or fluctuations in the mode frequency that arise from electrical noise in the trap. Such errors can also be suppressed via generalised spin-echo sequences. These involve splitting a single SDF into a sequence of shorter SDFs which accumulate the same total geometric phase. The motional trajectories traversed in these pulses can be engineered to cancel with each other, eliminating motional entanglement. Furthermore, this scheme can be integrated with the atomic echo sequences, since those already split up the LS pulse.

The key idea is shown in Figure 8.3, which shows the motional trajectory $\alpha_{\mu\nu}$ due to the force on the $|\nu:\mu\rangle$ state. Ideally, this executes a circular path which returns to the origin, but due to some control imperfection such as a detuning error, the state stops before reaching the origin, leaving us with some residual displacement $\Delta\alpha_{\mu\nu}$. If a trajectory that was identical, but rotated by 180°, were subsequently traversed, the state would always return to the origin regardless of where it ended up after the first loop. This is the motional equivalent of a spin-echo. As described in Section 3.6, the orientation of the second loop with respect to the first can be set by shifting the phase of the SDF – the phase of the travelling optical lattice that drives the LS force. Thus, the phase of the second pulse should be shifted by $\pi$ from the first. However, the force and the motion are detuned by the gate detuning $\delta$, so they acquire an additional phase difference $\delta\tau_l$ over the single loop duration $\tau_l$. Thus, the phase of the force at the second loop must be shifted by $\pi - \delta\tau_l$.

This "motional echo" guarantees that, if the two loops are the same up to their orientation, the motion will always return to the origin. This will fully eliminate residual entanglement due to a constant gate time or detuning miscalibration. Any imbalance in the loops will still result in some residual entanglement, but it will generally be smaller than without the echo. Furthermore, this procedure can be generalised to correct such higher-order errors using exponentially increasing series of pulses [8, 148]. Since the phase on each pulse is determined by a Walsh function, this technique is often referred to as Walsh modulation. The two-loop gate is equivalent to a Walsh-1 sequence.

We must also ensure that the total geometric phase acquired in each loop is half of the geometric phase required for the gate. This is often done by keeping the laser power the

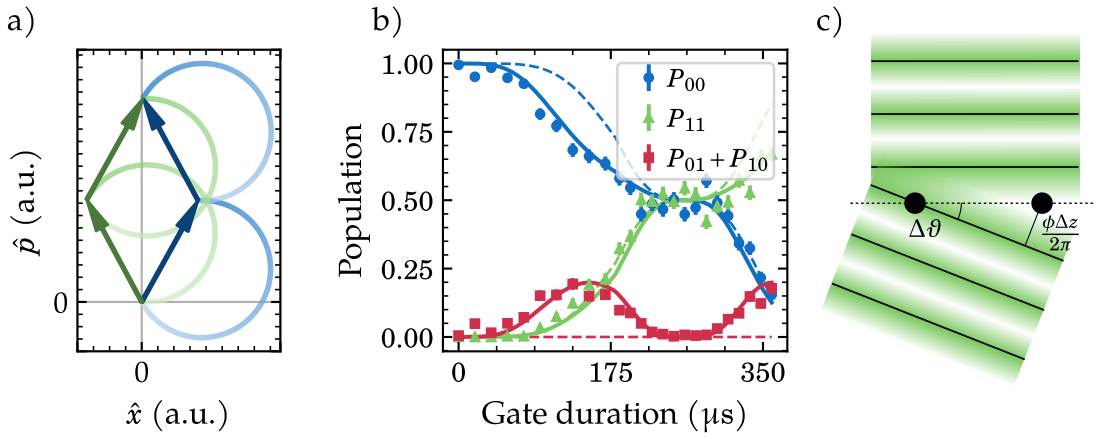



**Figure 8.4:** a) Sketch of the motional trajectories of states $|s{:}d\rangle$, $|d{:}s\rangle$ when there is a phase difference between the SDF on each ion. The loops traversed by each atomic state have different direction. The motional states reach the same point, so there is no motional entanglement, but via different routes, which results in additional single-ion geometric phases. b) Time scan of a monoqubit two-loop gate with the motional echo. Blue circles, green triangles and red squares show populations in $|0{:}0\rangle$, $|1{:}1\rangle$ and the sum of populations in $|0{:}1\rangle$ and $|1{:}0\rangle$, respectively. Solid lines are a fit to the theoretical curves due to an SDF phase difference between the ions. The fitted phase difference is $\phi = 2\pi \times 0.174(7)$ rad, which could arise from one beam being $\Delta\vartheta = 0.89(3)°$ away from being perfectly perpendicular to the chain. Dashed lines show the curves with no SDF phase difference; the $|0{:}0\rangle$ and $|1{:}1\rangle$ states are not excited. c) Sketch showing a beam geometry that could result in the SDF on each ion being out of phase by $\phi$ due to one beam being misaligned by $\Delta\vartheta$. Black solid lines show the wavefronts of each beam.

same as for a single-loop gate, but increasing the detuning[8] by $\sqrt{2}$. The total gate time needed to traverse both loops then also increases by $\sqrt{2}$ with respect to a single-loop gate.

#### 8.1.3.3 Combining the atomic and motional echoes

When combining the motional and atomic echoes, we must account for how the $R_x^{\mathrm{LSB}}(\pi)$ gates between the LS pulses affect the motional trajectory, since the atomic state that "drives" the motion will change between the two loops. If the SDF on these states is not the same phase or amplitude – which can occur due to beam misalignment, see Figure 8.4 c) – one may expect that the dynamics may be affected non-trivially.

A full discussion of these dynamics is given in Appendix D.1, with the key points summarised here. Suppose the echo $R_x^{\mathrm{LSB}}(\pi)$ gates flip the states $|s{:}d\rangle \leftrightarrow |d{:}s\rangle$, where $|s\rangle$ ($|d\rangle$) is a state in the $S_{1/2}$ ($D_{5/2}$) level. If there were no phase imbalances, the two states would traverse loops of the same radii, but opposite direction[9]. Thus, after the

[8] Which is proportional to the loop radius.

[9] This change in direction is due to us using a rocking mode, so the forces on $|s{:}d\rangle$ and $|d{:}s\rangle$ have the opposite phase.

echo pulse and with a suitable phase update, the two-loop trajectories look like Figure 8.3. In contrast, an SDF phase or amplitude mismatch between the states would modify the trajectories as per Figure 8.4 a): both states take different routes to the final motional state. It is shown in Appendix D.1 that all states reach the same point in phase space, so residual motional entanglement is still eliminated. However, the non-commutativity of displacement operators leads to additional single-ion geometric phases being acquired, which are different on each ion[10].

It is shown in Appendix D.1 that, as long as each individual loop closes, this only leads to a small reduction in the tolerance to detuning errors. However, the dynamics at arbitrary times are modified, in a way that allows us to measure the SDF phase differences and thus infer a potential misalignment between the ion chain and the optical field, as shown in Figure 8.4 c). Such a misalignment can have other deleterious effects, such as a (potentially arbitrary) reduction in the Rabi frequency of the target gate (see Section 8.6.1.5). Once the misalignment angle is known, it can be corrected by rotating the ion chain. Unfortunately, this scheme was found only during the preparation of this manuscript, but the measurement was still used in the error estimates of Section 8.6.1.

Figure 8.3 b) shows a time scan of a monoqubit $ZZ$ gate equivalent to a Sleepy Gate[11]. By fitting the data to the theoretical trajectories, the SDF phase difference between the ions can be found. A misalignment of $0.89(3)^\circ$ on either beam would be sufficient to cause this.

## 8.2 Choosing the mode

The Sleepy Gates mediate a two-ion interaction by coupling the atomic states to a single motional mode[12]. There are six possible modes to choose from: a CoM mode and a rocking mode for each of the three principal trap axes – the axial and radial LF/HF (low/high frequency) directions. However, since the gate is driven by the 532 nm beams, whose difference $\mathbf{k}$-vector has no projection onto the axial direction, only the radial modes can be coupled to. The radial mode which minimises the expected gate error should thus be chosen.

[10] Thus, they can't be corrected without individual addressing

[11] The experimental data is taken from [123] with permission.

[12] While it is possible to mediate the gate via more than one mode, ensuring that the atomic and motional states disentangle becomes complex.

| **Mode** | **Frequency** (MHz) | **Heating rate** ($s^{-1}$) | **Coherence time** (ms) |
|---|---|---|---|
| LF CoM | 1.60 | 110(2) | 4.6(4)<br>5.3(4) |
| LF Rocking | 1.51 | 0.00(4) | 1.9(1)<br>78(6) |
| HF CoM | 1.86 | 151(3) | 4.6(4)<br>6.2(4) |
| HF Rocking | 1.79 | 0.10(3) | 2.4(1)<br>71(4) |

**Table 8.1:** Properties of the four radial modes. Two values are given for the coherence time of each mode, which were measured without (top) and with (bottom) a spin-echo in the Ramsey sequence.

The sources of error that depend on the choice of mode are the heating and motional dephasing rates for each mode, as well as the spectral separation to hot spectator modes. A detailed study of these effects in our setup was carried out in a previous thesis [123] and, for brevity, is only briefly outlined here. A summary of the relevant properties of the four modes is given in Table 8.1.

The heating rate of each mode was found by measuring the mode's thermal occupation via sideband thermometry [225] after ground-state cooling, with a variable delay between the cooling and thermometry routines. A constant heating rate $\dot{\bar{n}}$ was fitted to $\bar{n}(t) = \dot{\bar{n}}t$.

It can be observed that the heating rate of the two CoM modes is orders of magnitude larger than for the rocking modes. This is not unexpected: the main contributor to the heating rate is coupling to noisy electric fields $\mathbf{E}(\mathbf{r}, t)$. The mode participation vector for the rocking mode $\xi = \frac{1}{\sqrt{2}}(1, -1)$ implies that only electric fields that have significant spatial structure over the separation between the ions ($\sim 6\ \mu$m) will excite this mode. In contrast, the CoM mode can be excited by fields that are spatially uniform over the ion separation. This provides a natural filter that shields the rocking modes from external noise sources.

The coherence times were found by measuring the contrast decay in Ramsey experiments on a motional superposition $|v\rangle_a \otimes \frac{1}{\sqrt{2}}(|0\rangle_m + |1\rangle_m)$, where the subscripts $a, m$ indicate atomic and motional states, respectively. Coherence times with and without a spin-echo in this experiment are given. In both cases, an exponential fit to the contrast

$C(t) = C_0 e^{-t/\tau_c}$ was used to extract the coherence time $\tau_c$[13].

The coherence time of the rocking modes without a spin-echo is slightly shorter than that for the CoM modes, while they are extended by a factor of ~ 10 with a spin-echo. This suggests that the dephasing is dominated by noise that is slow on the timescale of an experimental shot. The echo sequence of Section 8.1.3.2 is designed to yield partial tolerance to such slow noise, so the spin-echo coherence time (which is longer for the rocking modes) is the more experimentally relevant one.

It is thus clear that one of the rocking modes should be chosen for the gate. The primary difference between the two is the spectral separation to nearby modes, which is particularly important in our case due to the overall low mode frequencies. Maximal spectral separation is reached by driving the SDF red-detuned from the LF rocking mode. Thus, we choose this mode for the gate[14]. To further minimise excitation of the LF CoM mode, we modulate the power in the counter-propagating beam so that the rising and falling edges of the pulse have an approximately $\sin^2$ envelope. This effectively acts as a narrow-band frequency filter in motional space, since the dynamics are more adiabatic [140, 196]. In addition, this almost entirely removes the deleterious effect of two-beam, single-ion light shifts [140], which depend on the absolute SDF phase (see Equation (3.64)).

Choosing the LF rocking mode for the gate exposes it to errors from Kerr cross-coupling to the axial breathing and the HF rocking mode[120]. However, the coupling constant $\chi$ strongly depends on the magnitude of the axial frequency. This is particularly low in our trap, which leads to a small $\chi \sim 1\,\mathrm{Hz\,q^{-1}}$ and negligible expected errors of $O(10^{-5})$ for a cold gate mode ($\bar{n} \sim 0.1$) and Doppler-cooled spectator mode ($\bar{n} \sim 10$). These errors are negligible compared to other sources.

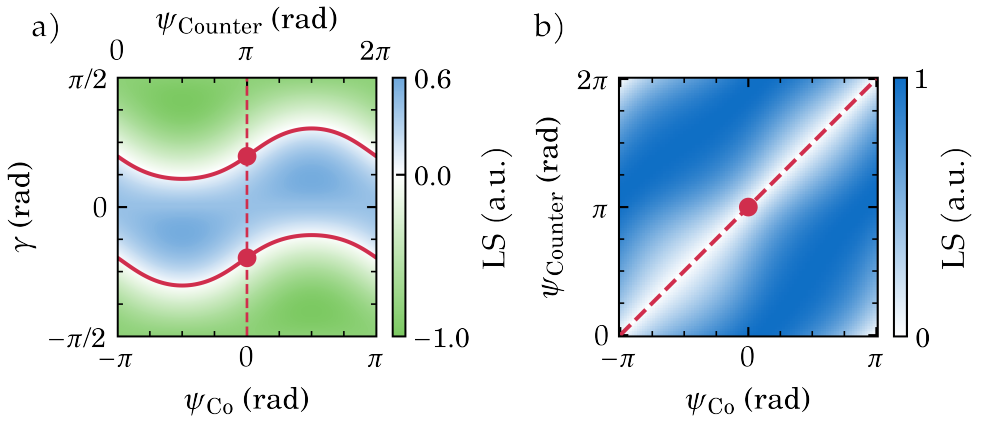



**Figure 8.5:** a) Simulated single-beam LS on the $|D_{5/2},2,0\rangle \leftrightarrow |D_{5/2},1,0\rangle$ transition due to the 532 nm beams. The angles $\gamma$ and $\psi$ set the relative amplitude and phase of the in-plane and out-of-plane polarisation components (see Section 3.5.2). The $\psi$ angle for the co- and counter-propagating beams have separate axes, so that at each point in the graph, the polarisation vector of both beams is equal, as discussed in Section 6.2.4.1. The polarisation angles $\psi_{\text{Co,Counter}}$ in this case are not the same, because the beams point in opposite directions. Contours of vanishing light shift are shown in red, with the points with linear polarisation ($\psi_{\text{Co}} = 0$, $\psi_{\text{Counter}} = \pi$) marked. The target polarisation has $\gamma \approx \pm 35.3°$. b) Simulated two-beam LS magnitude when both beams induce no single-beam LS, but have generally different polarisations (the polarisations lie on the red contour, so they can be parametrised by just one angle, $\psi$). Unless the beams have the same polarisation vector (points along the red dashed line), the two-beam LS on the transition does not vanish, even though the single-beam LSs do. The target polarisation is shown as a red circle.

## 8.3 Setting the beam polarisation

Here, we describe the procedure for setting the polarisation of the 532 nm beams that makes the LS pulse induce a pure $ZZZZ$ rotation. At this polarisation, the relative two-beam LS between the polyqubit states in the $D_{5/2}$ level ($|D_{5/2},2,0\rangle$ and $|D_{5/2},1,0\rangle$) is nulled (Section 6.2.4.1). Naïvely, one may try to do this by independently nulling each beam's single-beam LS. However, this only nulls the two-beam shift if the beams have the same polarisation vector (see Figure 8.5). Instead, the polarisation of the co-propagating beam is first set to null the single-beam light shift; the counter-propagating beam's polarisation is then matched, giving the desired arrangement.

The LS from either beam is measured using the Ramsey experiment shown in Figure 8.6 b). The co-propagating beam polarisation is modified until no excitation is observed.

[13]The constant $C_0$ was floated instead of being set to 1, since full contrast was not observed in these Ramsey experiments even with no Ramsey delay. The reason for this is unclear.

[14]Similar spectral isolation could be achieved using the HF mode by rotating the principal axes of the potential to make the LF radial direction perpendicular to the beams' $\Delta\mathbf{k}$. While this has been implemented in our experiment, it was not sufficiently well characterised for use in the gate experiments.

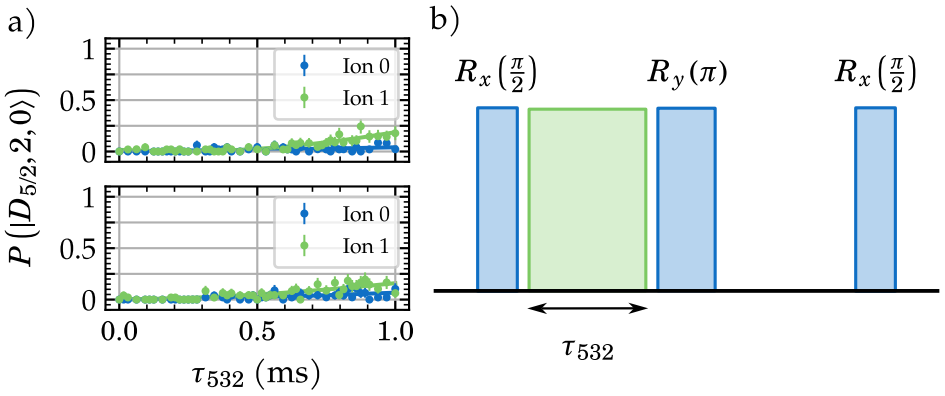



**Figure 8.6:** a) Single-beam light shifts on a superposition of the $\{|D_{5/2},1,0\rangle, |D_{5/2},2,0\rangle\}$ states for the co-propagating (top) and counter-propagating beam (bottom). The populations for each ion in the trap are shown in blue and green. Sinusoidal fits are shown, whose frequency is ~ 90 Hz, though this excitation is most likely due to dephasing from magnetic field noise (see text). The Ramsey circuit is shown in b) where blue squares denote a sequence of quadrupole pulses that implement the indicated rotation on the two-state subspace. This is embedded in a spin-echo to cancel any phases due to frequency miscalibrations in the 1762 nm tone.

A single HWP downstream of a PBS (through which the beam passes in transmission) is used to ensure the polarisation is linear. The PBS is placed as close as possible to the trap, to avoid any birefringence in the downstream optics making the polarisation elliptical. Thus, the final polarisation is one of those marked in Figure 8.6 a). This same PBS is used to set the polarisation of the counter-propagating beam, which travels unimpeded through the trap. Waveplates on the counter-propagating side of the trap are used to minimise the reflection on this PBS. This makes the two beams have the same polarisation vector at the ions[15].

Figure 8.6 shows the measured single-beam LS on a chain of two ions after the polarisation from each beam has been set. The increase in population at[16] $\tau_{532} \sim 1$ ms is consistent with a decoherence time of ~ 10 ms due to magnetic field noise[17]. At the powers used in this experiment[18], the single-beam light shifts on the $|S_{1/2},2,0\rangle \leftrightarrow |D_{5/2},2,0\rangle$ transition are of order 100 kHz, at least three orders of magnitude larger than those on the measured transition. In principle, this measurement does not rule out that the two

[15]This works because the co-propagating beam is forced to have linear polarisation; otherwise, the helicity of the counter-propagating polarisation set up by this procedure would have the wrong sign.

[16]This corresponds to a total Ramsey duration of 2 ms.

[17]This is significantly longer than the coherence time extracted from Figure 7.5 since there the experiments did not use a spin-echo.

[18]50 mW and 100 mW for the co- and counter-propagating beams, respectively, comparable to those used in two-ion gates.

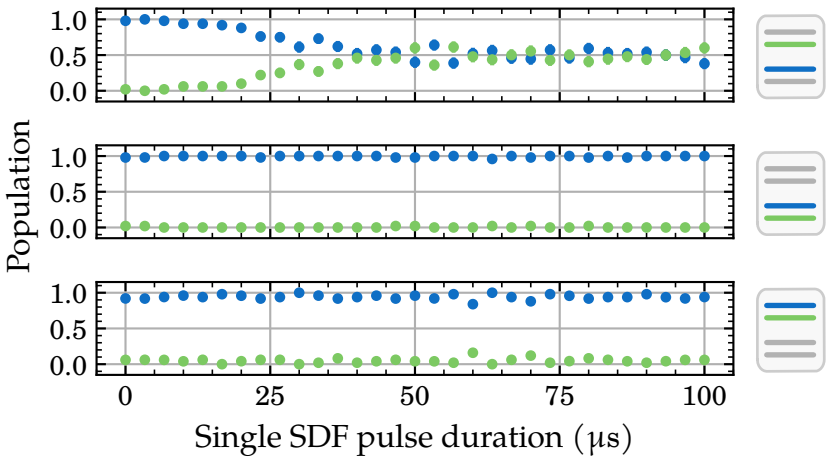



**Figure 8.7:** State-dependent forces on a superposition of two states across the $S_{1/2}$ and $D_{5/2}$ levels (top), and with both in the $S_{1/2}$ (middle) and $D_{5/2}$ (bottom) levels. The diagrams highlight the two states in the superposition for each experiment, as per Figure 6.4. If the SDF entangles the atomic and motional states, the superposition cannot be returned to a single atomic state. This is observed when the superposition is across the two levels, but not when it is contained to the $S_{1/2}$ or $D_{5/2}$ level.

beams still have different polarisation, leading to potentially significant two-beam light shifts. Nonetheless, this can be verified by measuring the strength of the SDF on the metastable transition relative to an optical transition. This is done in the next section.

## 8.4 State-Dependent Forces on a Single Polyqubit

Before driving SDFs on a two-ion chain to implement LS gates, it is useful to assess the quality of the SDFs on a simpler system comprising just one ion. The experiments used for this all follow the same pattern, which is almost identical to the full gate circuit of Figure 8.1. A superposition of all (or some) polyqubit states is set up, followed by an SDF, after which the superposition is undone. If the SDF successfully entangles the atomic and motional states, the reduced state of just the atomic states will be a mixed state. To avoid echoing the motion, which would always eliminate the entanglement, we do not modify the optical phase of the second LS pulse. Thus, the population only returns to a single state if both loops return to the origin, or if the SDF is on resonance with the mode frequency[19].

[19] If the force is on resonance with the motion, the optical phase at the start of the second pulse is the same as in the first one, since there is no phase acquisition between the motion and the beat note. Thus, the first and second pulse impart the same mode displacement on all atomic states in each of the $S_{1/2}$ and $D_{5/2}$ levels. Hence, since the population in the ground and metastable levels is exchanged for each pulse, the net displacement is the same for all states.

First, experiments were carried out on a superposition of two atomic states, in which the duration of the SDF pulses was scanned. If the light induces a differential two-beam LS between the two atomic states, they periodically become entangled and disentangled with the motion. The superposition can then only be undone when there is no motional entanglement, which occurs when the duration of each SDF pulse is equal to an integer multiple of the loop duration[20] ($200\ \mu s$). However, if the light induces the same LS on each state, there is never any motional coupling and the superposition can always be undone. Figure 8.7 shows such experiments for pulse durations up to 100 $\mu s$, at which point the motional entanglement should be maximal. This is done with superpositions of polyqubit states across the two levels ($|S_{1/2},2,0\rangle$, $|D_{5/2},2,0\rangle$), within the $S_{1/2}$ level ($|S_{1/2},2,0\rangle$, $|S_{1/2},1,0\rangle$) and within the $D_{5/2}$ level ($|D_{5/2},2,0\rangle$, $|D_{5/2},1,0\rangle$). It can be seen that the atomic superposition can always be undone when the states are in the same level, but not when they are across the levels. This suggests that the atomic and motional states only couple in the latter case[21], implying that the polarisation is correctly set.

A similar experiment using a superposition of all four polyqubit states is shown in Figure 8.8. Here, the duration of each LS pulse in the two-loop sequence was fixed at 100 $\mu s$ with a 30 $\mu s$ ramp[22] and the detuning between the beat-note and the mode frequency was scanned. When the SDF is resonant with the mode and when the individual loops close, the population returns to the state the polyqubit was in before the superposition was set up ($|00\rangle$). Otherwise, the population is evenly split between the two ground-level states; it never populates the metastable-level states[23]. This again is a consequence of correctly nulling the differential two-beam LS between states in the same level.

## 8.5 Gate implementation

Here, the procedures used to tune up and calibrate the gate are presented.

[20] The SDF detuning was chosen to be 5 kHz for these experiments.

[21] It could be that there is a small motional coupling to superpositions within each level which cannot be distinguished over the experimental shot noise. If one wished to quantify the ratio between the motional coupling for superpositions across and within each level, the experiment could be repeated with more laser power until the small motional excitations became visible.

[22] This long ramp duration was used in the experiments in [123] and thus was re-used for this experiment. The loop closure detunings occur at unexpected points because of this. However, the two-ion gates in the later section used a shorter ramp time.

[23] This effect is the same as the one observed in Figure 8.2 for a full two-ion gate

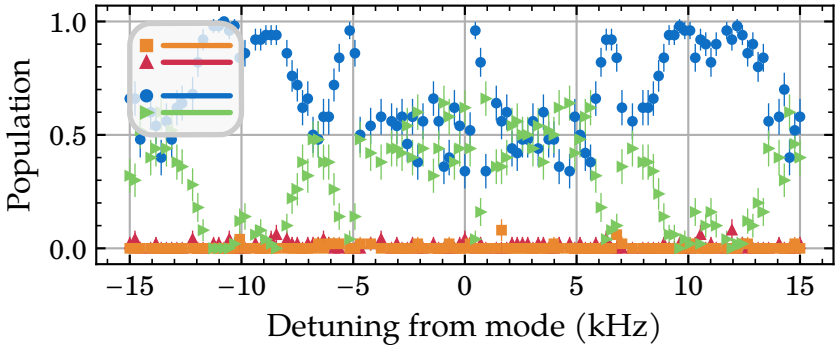



**Figure 8.8:** Two-loop SDF experiment on a superposition of all computational states, with no phase correction in the second loop. The inset shows the computational state identified by each colour and marker. Despite the SDF acting on a superposition of all states, only the two $S_{1/2}$ level states are ever populated, as per Figure 8.2. Detunings at which motional loops close (where population returns to the blue state ($|00\rangle$)) are clearly observed. The mode frequency was miscalibrated by ~ 700 Hz, which shifts the central loop-closure point off-centre. The 532 nm intensity was 10 – 100 times lower than in the gate experiments.

### 8.5.1 Beam alignment

The intensity of the three beams[24] involved in the gate operation (the co- and counter-propagating 532 nm beams and the 1762 nm beam, which are all perpendicular to the trap axis) should be the same at the location of each ion. Otherwise, more 532 nm power would be needed for the same SDF magnitude, and different intra-ion gates would be applied on each ion.

This is done first for the 1762 by moving the ions[25] until the Rabi frequency on the $|S_{1/2},2,0\rangle \leftrightarrow |D_{5/2},2,0\rangle$ transition in each ion is matched. Then, we steer each 532 nm beam using motorised mirrors until the LS induced on the $|S_{1/2},2,0\rangle \leftrightarrow |D_{5/2},2,0\rangle$ is the same in each ion. We use a Ramsey-type experiment embedded in an RPE sequence as per Section 7.2.2 to measure this shift [84, 207]. Furthermore, the 532 nm beams are also aligned along the direction perpendicular to the chain axis by maximising their LS on the ions. The quadrupole Rabi frequencies and light-shift frequencies on each ion are matched to ~ 1%.

In addition, the total beam power required to achieve a given SDF magnitude is minimised when the intensities of both beams are matched [123]. Since the co- and counter-propagating beams have very different radii (~ 16 µm and ~ 43 µm respectively),

[24] The metastable 532 nm beam is also aligned to maximise sideband cooling efficiency using the same method as the co- and counter-propagating beam (done by hand, since there are no motorised mirrors in its path). However, good alignment of this beam is far less critical.

[25] There are no motorised mirrors in this beam path.

this requires them to have different powers. The ratio of powers that makes the beams have equal intensity is found by measuring their single-ion LS frequency[26] at different powers and fitting a straight line. The ratio of the gradients is the desired ratio.

In the gate experiments, the power in the counter-propagating beam was 3.0 times larger than in the co-propagating one. However, for reasons that are not presently clear, the beam intensities at the ions estimated using their measured radii do not match with this ratio of powers. Instead, the power in the counter-propagating beam should be approximately $\frac{43^2}{16^2} \approx 7$ times larger than in the co-propagating one[27]. This could be due to systematic errors in power or beam radius measurements. Thus, it could be that the optimal intensities were not used.

### 8.5.2 Calibrating gate parameters

Three quantities need to be calibrated to correctly drive the gate: the mode frequency[28]; the detuning at which phase space loops are closed for the chosen loop duration; and the laser power at which the target geometric phase is acquired. Clearly, the gate mode and detuning are properties of the motional state, not the atomic one, and the two-beam light-shifts are designed to be equal on all states in each of the $S_{1/2}$ and $D_{5/2}$ levels. Thus, these calibrations can be performed by using only a pair of states across the two levels instead of the full polyqubit manifold[29]. The $|S_{1/2},2,0\rangle$ and $|D_{5/2},2,0\rangle$ are chosen, and labelled $|0\rangle$ and $|1\rangle$ for convenience. The procedure is then identical to the standard procedure for calibrating a two-ion monoqubit gate.

#### 8.5.2.1 Mode frequency

The mode frequency is measured using SDFs. As described in Section 8.4, when performing the two-loop gate sequence *without* modifying the phase of the second SDF, the

[26] Since the polarisations of both beams are matched, the LS induced by each beam is proportional to the intensity, with the same proportionality constant.

[27] The ion separation $\approx 6$ μm is small compared to the beam radii, so taking this into account only slightly changes the expected ratio.

[28] This is needed to calculate the correct phase shift to apply to the SDF on the second pulse of the motional echo.

[29] It is of course possible to carry out these calibrations using the full polyqubit manifold. If the circuit for the $ZZZZ$ gate is done, only the $|00/11\rangle$ states will ever be populated (Figure 8.2) so the procedure is the same as for calibrating with only two states per ion through the mapping $|0/1\rangle \rightarrow |00/11\rangle$. However, the full polyqubit is more sensitive to stray phases than a monoqubit (see Figure 8.9), so it is more convenient to use two states.

atomic and motional states only disentangle if the SDF is on resonance with the motion. At these points, the population in the crossed states ($|0{:}1\rangle$ and $|1{:}0\rangle$) is minimised. The target feature is the two-ion analogue of the central feature in Figure 8.7. Since the detuning between the beams is far from any atomic transition, no extraneous light shifts are introduced, leading to an accurate measurement of the mode frequency.

Driving the SDF on resonance creates a large coherent state, which is sensitive to sources of dephasing that would wash out the resonance feature. Thus, the laser power is significantly reduced compared to that used in the gate experiments.

#### 8.5.2.2 Gate detuning

The echo sequences of Section 8.1.3.2 should disentangle the atomic and motional states irrespective of the SDF detuning. Nevertheless, as described in Section 8.1.3.3, a slight misalignment between the chain and the lasers leads to unwanted single-qubit phases unless the detuning is set to close the motional loop at each pulse. Furthermore, knowledge of this detuning is necessary to calculate the correct phase update in the echo. While the loop duration $\tau_l$ fixes this detuning by $\delta_g = \pm 2\pi/\tau_l$, for robustness, we also determine this detuning experimentally. As mentioned in Section 8.2, the detuning is chosen to be negative to maximise the separation to other motional modes.

The procedure is identical to that used for finding the mode frequency: the (mono-qubit) two-loop gate sequence is performed with the chosen $\tau_l$, while scanning the SDF detuning about $-2\pi/\tau_l$. If the phase of the second SDF pulse is not updated, the crossed population at the end of the gate sequence is only nulled at the correct detuning. This procedure is done at approximately the gate power, since the motional displacement induced is small enough to not lead to motional decoherence[30].

#### 8.5.2.3 Laser power

After fixing the gate time and detuning, the geometric phase must be set to that which generates a GHZ state, which is controlled through the laser power. The power in

[30] And fortunately so, otherwise this would occur during the gate!

the co-propagating beam is scanned - with the counter-propagating power being accordingly set using the power ratio found in Section 8.5.1 - until the populations in the $|0{:}0\rangle$ and $|1{:}1\rangle$ cross at $\frac{1}{2}$.

### 8.5.3 Calibrating gate phases

The final calibration step involves measuring any stray intra-ion phases acquired during the gate, so that they can be compensated for using virtual diagonal gates. These are measured using all polyqubit states.

The primary source of such phases are the large single-ion light shifts induced by the 532 nm beams, which should appear like a $ZZ$ rotation. These should be cancelled with the echo sequence from Section 8.1.3.1. However, as discussed in Reference [123], we observe a slight imbalance between the power in each LS pulse, which makes the cancellation imperfect. Furthermore, stray $Z$ rotations on the MSB and LSB qubit (which we write as $Z\mathbb{1}$ and $\mathbb{1}Z$ rotations) that are small relative to the main $ZZ$ shift result in non-negligible phases, since the beams are very intense at the ions. The $Z\mathbb{1}$ rotations would not be cancelled by the echo, since they act on the LSB qubit only.

The diagonal gate induced by the 532 nm pulses ($D$ in Figure 8.9) must be measured in order to cancel it. This is done using the same circuit as for driving a $ZZZZ$ gate, but with the SDF frequency set to ~ 1.1 MHz to be far off-resonant from any motional mode and any ground-state transition. Then, in analogy to a simple Ramsey experiment, the phase of the closing pulses is scanned. The resulting traces can be fitted to a simulation of the circuit in Figure 8.9 b). This yields the phase acquired by each state, as well as any phase shift on the TSRs due to frequency errors in the quadrupole tones[31]. Then, the inverse gates are applied using virtual gates.

The uncorrected and corrected traces are shown in Figure 8.9 for two ions in the same chain, from which we draw two observations. Firstly, it was not possible to simultaneously correct the phases on both ions. This may be due to mismatches in the 1762 nm frequencies

[31] In monoqubits, phase errors on the driving laser have the same effect as a diagonal gate before the pulse. However, since the closing gates are implemented by a sequence of TSRs, this is not the case in the multi-level system, since the phases on different TSRs need not commute. This results in the $ZZ$ gate between the two single-qubit rotations in Figure 8.9 b).

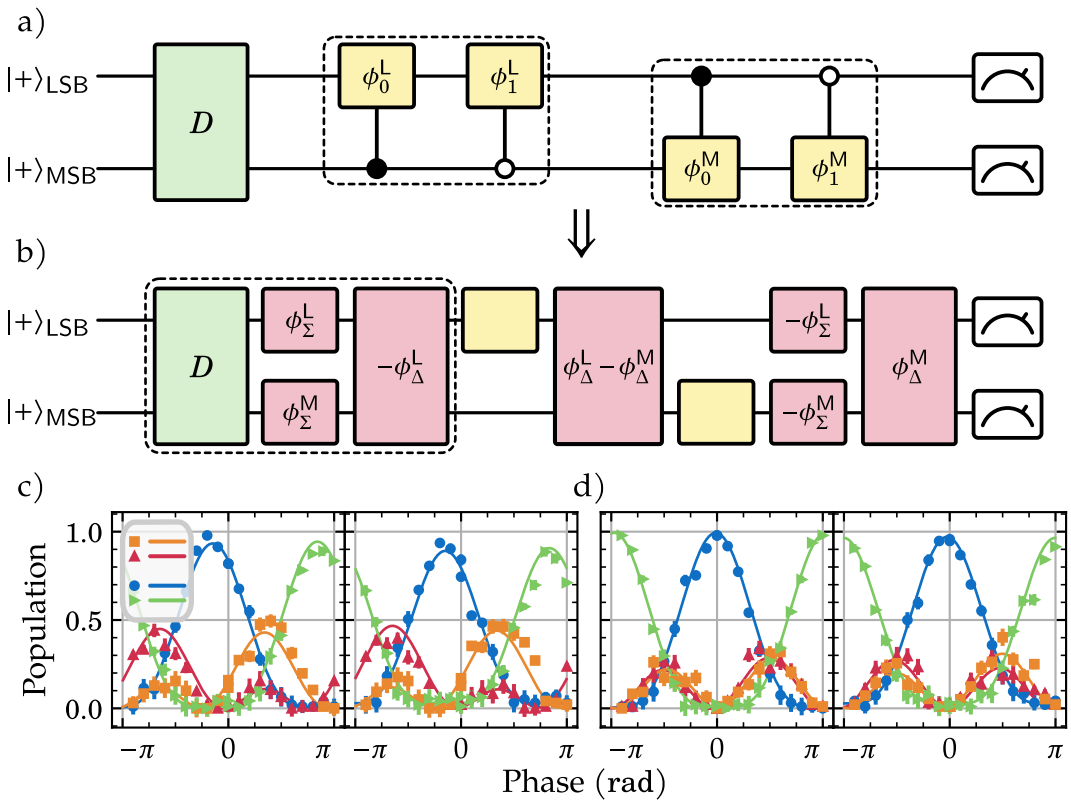



**Figure 8.9:** a) Detail of the four TSRs that implement the closing $R_y^\dagger\left(\frac{\pi}{2}\right)^{\otimes 2}$ gates on a single ion. A diagonal unitary $D$ (in green) may be acquired over the SDF pulse, and the TSRs (in yellow), which drive controlled rotations on the LSB (L) and MSB (M) qubits, may have phase offsets $\phi_{0/1}^{L/M}$ due to frequency errors. b) The imperfect TSRs can be rewritten as perfect TSRs (which are reduced to pure single-qubit gates) and $Z$ and $ZZ$ gates (in red), whose rotation angles are given by $\phi_{\Sigma,\Delta}^i = \left(\phi_0^i \pm \phi_1^i\right)/2$. The set of gates before the rotation on the LSB qubit can be grouped and corrected together. The last three diagonal gates have no impact on the dynamics. c) Scan of the phase of the closing (yellow) gates with a far detuned SDF, for two ions. When the phase is 0, the gates are $R_y^\dagger\left(\frac{\pi}{2}\right)$, as per Figure 8.1. The populations are shifted off-centre primarily due to a stray $Z\mathbb{1}$ component in $D$ or the single-qubit rotation; all other rotations are much smaller. These are corrected in d) using virtual rotations before each pair of TSRs.

at the two ions arising from magnetic field inhomogeneities, or a difference in the single-beam LS induced by the 532 nm beams. Secondly, the $Z\mathbb{1}$ rotation angle ($\sim 2\pi \times 0.13$ rad) is considerably larger than the $\mathbb{1}Z$ or $ZZ$ rotation angle. This is partly expected, since $Z\mathbb{1}$ rotations are not cancelled by the echo. Nonetheless, the $\{|00\rangle, |01\rangle\}$ states would need to be shifted by $\sim 650$ Hz relative to the $\{|10\rangle, |11\rangle\}$ states to account for this phase acquisition over the 200 μs gate duration. This cannot be explained by the small light shifts measured in Section 8.3[32].

[32]This is also unlikely to be due to frequency errors in the quadrupole tones, since this would almost certainly result in a non-zero $ZZ$ rotation between the gates; the value extracted from the fits is negligible.

Once corrected, all rotation angles are smaller than $2\pi \times 0.05$ rad[33], though they could not be fully eliminated. Furthermore, differences in the measured phases of both ions remain. Since these phases commute with the LS gate, we can easily calculate their contribution to the infidelity to be $\sim 42 \times 10^{-3}$. As discussed later, this is a large contribution to the GHZ infidelity in these experiments.

We also point out that this method has interesting behaviour if dephasing is present, which was unknown at the time of the experiments. Indeed, the effect that a small $ZZ$ rotation before the closing gates has on the populations is *indistinguishable* from the effect of a weak dephasing term proportional to $ZZ$[34]. This is counter to the intuition from monoqubits, where dephasing reduces the Ramsey fringe contrast while a unitary error (an uncorrected phase) changes the fringe phase; thus, both are always distinguishable. The only effect of this is that it may appear that the $ZZ$ rotation angle cannot be completely removed, though in minimising it, the unitary error will have been compensated.

Finally, the intra-ion `CNOT` gates are implemented by a single TSR, whose phase must also be corrected. Instead of applying the same virtual diagonal gate before the TSR, it is easy to scan the phase angle to minimise the population in the crossed states. We find that the resulting phase shift agrees with the one that would be applied with the virtual gates above.

## 8.6 Results

Figure 8.10 shows population $P$ and parity contrast $C$ measurements on two-qubit GHZ states over the MSB and LSB qubits in each ion, and a GHZ state over all four qubits. The parity scans were taken with 300 shots per point, and the contrast extracted by fitting a sinusoid of the correct periodicity, floating the phase; the population measurement was taken with 1000 shots. The extracted fidelities and the gate parameters used across all gates are summarised in Tables 8.2 and 8.3, respectively.

It was found that updating the phase of the second SDF pulse to perform the motional echo from Section 8.1.3.2 resulted in higher crossed population than when the phase

[33]The only rotation with this angle is the $ZZ$ rotation before the TSRs, which, as explained, may be due to decoherence.

[34]Contrastingly, small single-qubit rotations *are* distinguishable from $Z\mathbb{1}$ or $\mathbb{1}Z$ noise.

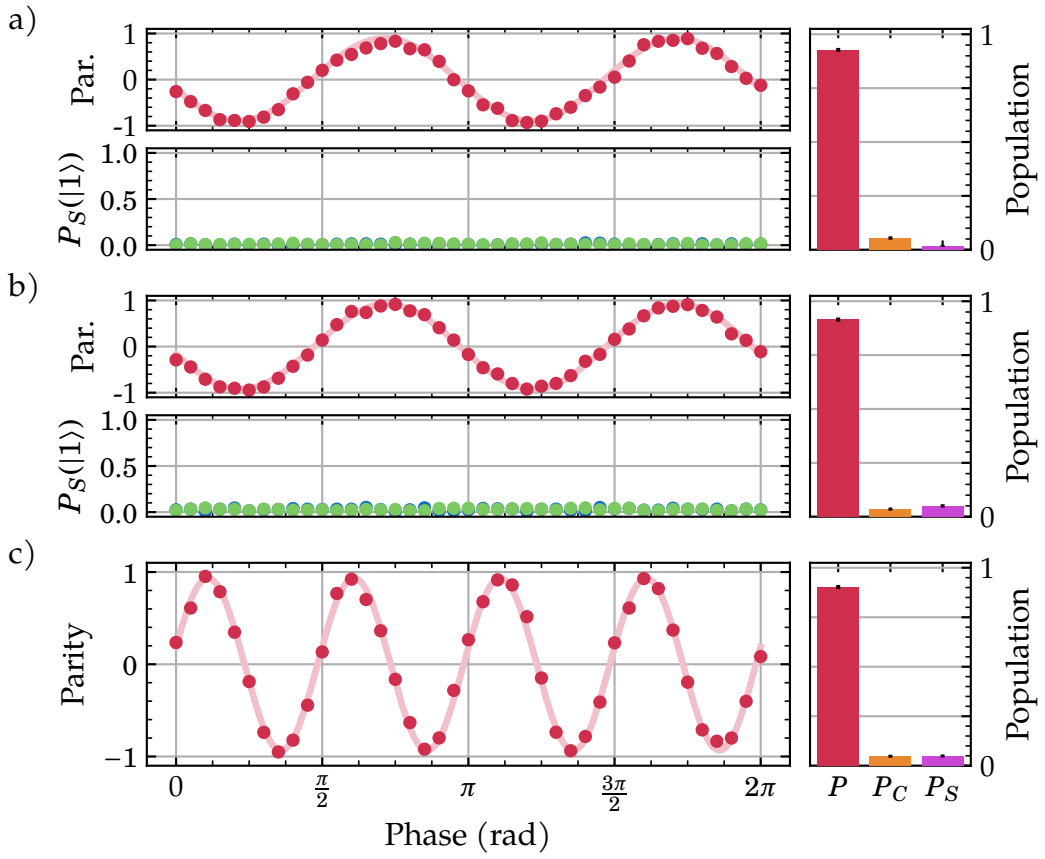



**Figure 8.10:** Fidelity measurements for $ZZ$ gates on a) the MSB and b) the LSB qubits, and c) for $ZZZZ$ gates (errorbars are smaller than the markers). The rightmost plots show population measurements. $P$ (red) is the total population in the target GHZ states; $P_C$ (orange) is the population in the "crossed" GHZ states (e.g. for a 4-qubit GHZ state, this would be the total population in $|00{:}11\rangle$ and $|11{:}00\rangle$); and $P_S$ (purple) is the population in all remaining "spectator" states. For the two-qubit gates, $P_S$ is the excited population of the spectator qubit. The leftmost plots show parity contrast measurements. For the two-qubit gates, the probability of exciting the spectator qubit in the MSB (LSB) ion is shown in blue (green) below the contrast scan (red).

| Gate | Fidelity | $C$ | $P$ | $P_C$ | $P_S$ |
|---|---|---|---|---|---|
| $R_{zz}^{\mathrm{MSB}}$ | 0.912(7) | 0.90(1) | 0.928(9) | 0.054(8) | 0.018(5) |
| $R_{zz}^{\mathrm{LSB}}$ | 0.919(6) | 0.923(8) | 0.915(10) | 0.035(6) | 0.050(8) |
| $R_{zzzz}$ | 0.918(7) | 0.933(8) | 0.90(1) | 0.048(7) | 0.049(8) |

**Table 8.2:** GHZ fidelity, parity contrast $C$ and $P$, $P_C$ and $P_S$ as defined in Figure 8.10.

| Parameter | Value |
|---|---|
| Gate duration | $2 \times 80$ μs |
| Gate detuning | $\approx -12.5$ kHz |
| Co-propagating power | $\approx 38$ mW |
| Counter-propagating power | $\approx 115$ mW |
| Ramp duration | 3 μs |

**Table 8.3:** Common parameters used for all gates.

was not updated. Thus, all gates here were performed *without* the phase update, so the motional echo from Section 8.3 was not implemented. It is not clear why this is the case, particularly since this was not observed when running experiments on previous days.

Table 8.2 highlights a key benefit of polyqubit systems: all gates have almost identical errors, independent of the number of qubits addressed. While this is entirely expected – all gates are identical up to single-ion gates – it is in stark contrast with monoqubit systems, which display a drop in GHZ fidelity with higher numbers of qubits [109].

Nevertheless, the observed errors are large. In particular, they are almost an order of magnitude larger than those observed in monoqubit experiments on the $|S_{1/2}, 2, 0\rangle \leftrightarrow |D_{5/2}, 2, 0\rangle$ ($|00\rangle \leftrightarrow |01\rangle$) transition. Reference [123] (also Figure 8.4) reports a fidelity of 0.990(7), which matches the fidelity measured on the same day as the polyqubit data – 0.99(4). However, the analysis carried out in Chapter 5 suggests that monoqubit and polyqubit gates should have almost identical fidelities. Thus, a detailed exploration of these sources of error using experimentally measured parameters is now presented, to attempt to explain this disparity.

### 8.6.1 Sources of error

In what follows, all calculations and simulations assume that the errorscan be added independently[35], so when estimating a particular source of error, the gate is assumed to be otherwise perfect. This is a good assumption when the individual sources of error are

[35]This can be justified by considering the full error process for the gate as the composition of errors from many sources of small error, so that $\mathcal{E} \approx (\mathcal{E}^{(0)} \circ ... \circ \mathcal{E}^{(n-1)})$. It can be shown that, to first order, the error matrix of the composition of two such error processes is $\mathcal{E}_\chi \approx \mathcal{E}_\chi^{(1)} + \mathcal{E}_\chi^{(2)} - \chi_{\mathbb{1}}$, where $\chi_{\mathbb{1}}$ is the $\chi$ matrix for the identity process (defined with $U^\dagger$ applied before or after the erroneous process), whose only non-zero entry is $\chi_{\mathbb{1},00} = 1$ [172]. By inserting this into Equation (5.4), it is found that the error from the two processes adds up linearly. This first-order approximation breaks down when the errors are coherent and act in the same basis, as discussed in Section 5.1.2, or when errors are large.

small which, in many cases, they are. Furthermore, since all gates exhibit very similar errors, we only analyse the error for the four-qubit gate.

#### 8.6.1.1 Motional dephasing

We consider errors due to fluctuations in the motional mode frequency during or between shots, which are characterised by the Ramsey coherence times of Table 8.1. As discussed there, the frequency fluctuations have a strong quasi-static component. Nevertheless, the contrast in the spin-echo experiment decays exponentially, suggesting a white noise plateau on top of this. To calculate the expected errors, we crudely treat the two spectral components separately and use the results of Section 5.3.3.

The quasi-static contribution is dealt with by assuming that the mode frequency is constant over a shot, but varies shot-to-shot according to a Gaussian distribution. This results in a shot-to-shot detuning miscalibration $\Delta_\delta$ with an RMS $\sqrt{\langle\Delta_\delta^2\rangle}$ that can be estimated from the Ramsey coherence time $\tau$ without a spin echo[36] using $\frac{1}{\tau^2} = \frac{\langle\Delta_\delta^2\rangle}{2}$ [147]. The RMS is found to be $\sqrt{\langle\Delta_\delta^2\rangle} = 2\pi \times 116(3)\,\mathrm{rad\,s^{-1}}$. Then, using Equation (5.52), we find an error of $1.14 \times 10^{-3}$.

The error due to the white noise spectrum is found by numerically solving the master equation with the gate Hamiltonian (3.66) and Lindblad operators given by Equation (5.49). Using the spin-echo coherence time (78 ms), the erroris found to be $1.34 \times 10^{-3}$.

Thus, the total error due to motional dephasing is $2.48 \times 10^{-3}$.

A master equation simulation could also be carried out to calculate the errors due to motional heating. However, no measurable heating of the LF rocking mode is observed, so this error is negligible.

#### 8.6.1.2 Atomic dephasing

We now turn to dephasing of the atomic state in each ion. Since the gate Hamiltonian is diagonal in the computational basis, it commutes with dephasing noise. Thus, in the interaction frame with respect to the gate Hamiltonian, the state evolution is identical

[36] This statement requires justification, since the observed contrast decay is exponential rather than Gaussian, thereby implying a white noise spectrum. However, if the spectrum were purely white, the effect of a spin-echo would not be as drastic as is observed, since it only eliminates low-frequency noise. We consider this sufficient to identify the primary contributor to the short coherence time without the echo as slow noise, in which case these approximations are valid.

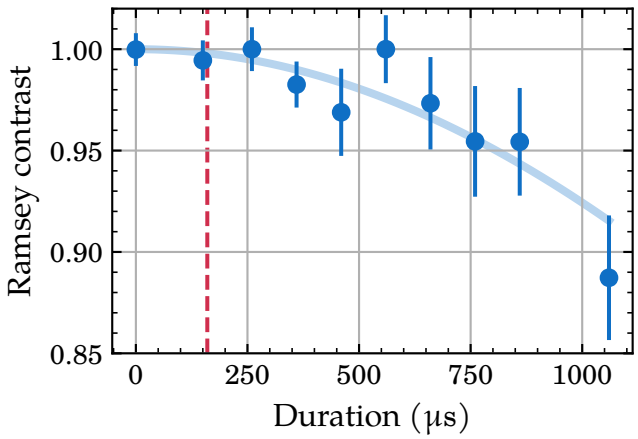



**Figure 8.11:** Contrast for a Ramsey sequence identical to that in Figure 8.6, but on a superposition of $\{|S_{1/2},2,0\rangle, |D_{5/2},2,0\rangle\}$. A Gaussian fit to the decay is shown in light blue. The duration of the gates in Figure 8.10 is marked with a dashed red line.

to that of an idle polyqubit subject to dephasing noise. Then, we can calculate the drop in fidelity once the form of the error (the sensitivities $\Xi_\nu$) is known.

In Section 7.3.1, the coherence time of a single polyqubit was found to be limited by magnetic field noise $\delta B$ and frequency noise on the 1762 nm laser $\delta f_{1762}$. However, intensity noise in the 532 nm beams contribute another source of dephasing by inducing fluctuating light shifts $\delta\Delta_{532}$. The echo sequence from Section 8.1.3.1 mitigates this noise, but doesn't fully cancel it.

To characterise it, we again treat the gate circuit as a Ramsey experiment with an echo, using a monoqubit. Figure 8.11 shows the resulting Ramsey contrast decay on the $|S_{1/2},2,0\rangle \leftrightarrow |D_{5/2},2,0\rangle$ transition, with the 532 nm beatnote far detuned from the motion. We expect that the noise spurs from Section 7.3.1.3 have no effect on this transition, since it is magnetically insensitive, and that the quasi-static laser frequency noise would be cancelled by the echo. However, we observe a Gaussian drop in Ramsey contrast, with a coherence time of 3.6(4) ms. This suggests that there are significant single-ion LS fluctuations, arising from intensity noise in the 532 nm beams.

Because the polarisations have been set up to null the LS between states in the same manifold, the effect of this noise on the full polyqubit manifold would behave the same way as for a single qubit. Thus, the drop in fidelity on both systems would be the same. By relating the state fidelity $F = \frac{C+1}{2}$ to the Ramsey contrast $C$ [217], we can extrapolate

what the drop in fidelity would be over the two SDF pulses, whose total duration is 160 μs from the measured coherence time. The error from this is $0.98 \times 10^{-3}$ per ion, which should be doubled for the full system.

We can also calculate the drop in fidelity from magnetic field noise on the polyqubit, which will couple to the $|D_{5/2}, 1, 0\rangle \leftrightarrow |D_{5/2}, 2, 0\rangle$ transition. This is done using a filter function formalism using the noise spectrum with the spurs calculated in Section 7.3.1.3. The error from this at the gate duration for both ions together is $0.52 \times 10^{-3}$. The error due to laser phase noise is negligible, since it is static.

#### 8.6.1.3 Single ion operations

The gate circuit contains many single-ion operations, which were found in the previous chapter to have significant errors. Indeed, the circuit in Figure 8.1 contains two sets of parallel $R_y(\pi/2)$ rotations per ion and one $R_x(\pi)$ rotation on the LSB qubit in each ion, requiring a total of 12 single-tone $\pi/2$ pulses. Table 7.1 contains the error per $\pi/2$ pulse extracted from parallel single-qubit RBM and from RBM on just the LSB qubit. In both cases, we use the error found by considering the joint survival of both qubits. Adding the contributions from each gate, and assuming that they have the same error on each ion, we obtain an error from single-ion operations of $\varepsilon_{SI} = 63(10) \times 10^{-3}$. The analysis pulses would further increase this by $29(5) \times 10^{-3}$.

This error is likely a significant overestimate, since as argued in Section 7.3.1.4, the majority of the error in the RBM experiments is mostly due to breaking the multi-photon resonance excitation. However, the phase correction of Section 8.5.3 would at least partially compensate these, despite not knowing about these errors at the time of the experiment. Furthermore, the duration of the inter-ion experiments is much shorter than the RBM experiments. Thus, it is possible that the error per $\pi/2$ pulse is best represented by that observed in monoqubit RBM (Table 7.2). This would result in an error of $5(1) \times 10^{-3}$.

However, a more thorough analysis would be needed to determine exactly how well the phase compensation corrects for multi-photon resonance errors, since it was not possible to remove the stray phases. It is possible that the contribution of the multi-photon resonance errors is included in the error added by the phases. Nonetheless, the

true contribution will lie somewhere between the error measured with polyqubit and monoqubit RBM, so we quote both errors.

#### 8.6.1.4 Scattering

To find the errors due to elastic and inelastic scattering from the 532 nm beams, we numerically integrate the master equation with the Lindblad operators from Equation 5.39 and the gate Hamiltonian. Each beam contributes its own set of Lindblad operators. Using the measured beam intensities and the gate duration from Table

8.3, an error of $\varepsilon_{\mathrm{Scat}} = 0.04 \times 10^{-3}$ is obtained.

#### 8.6.1.5 Beam pointing and polarisation

If there are differential two-beam light shifts between the two $D_{5/2}$ states, the unitary implemented by the gate circuit will no longer be a pure $R_{zzzz}$ rotation. In general, additional terms that cannot be removed through single-ion interactions will be present, causing an uncorrectable[37] unitary error.

Such differential light shifts arise if the polarisation vector of at least one of the beams is mis-set. In Section 8.3, a negligible single-ion differential light shift on the $D_{5/2}$ states was observed. However, as discussed there, this does not imply that the two-beam light shift is nulled, since there are many polarisations that produce no single-beam light shift. While measures were taken to make the polarisation vectors equal, which *does* null two-beam light shifts, and the measurements from Section 8.4 support this, it is instructive to estimate how large the error *could* be.

These errors can be found by calculating the two-ion, two-beam light shifts at each polarisation[38]. The resulting unitary will be a product of $ZZ$, $ZZZ$ and $ZZZZ$ rotations, whose effective Rabi frequencies depend on the two-beam LSs. This unitary is then normalised by choosing the effective "gate time" that makes the $R_{zzzz}$ rotation angle equal to $\pi/2$, as required to generate a GHZ state[39]. In addition, the rotation angles of intra-ion gates are set to zero, since these can be compensated with virtual rotations.

[37] Without additional two-ion gates.
[38] See Section 3.6.2.
[39] For this we use the decomposition into generalised $Z$ rotations from Section 4.2.3.

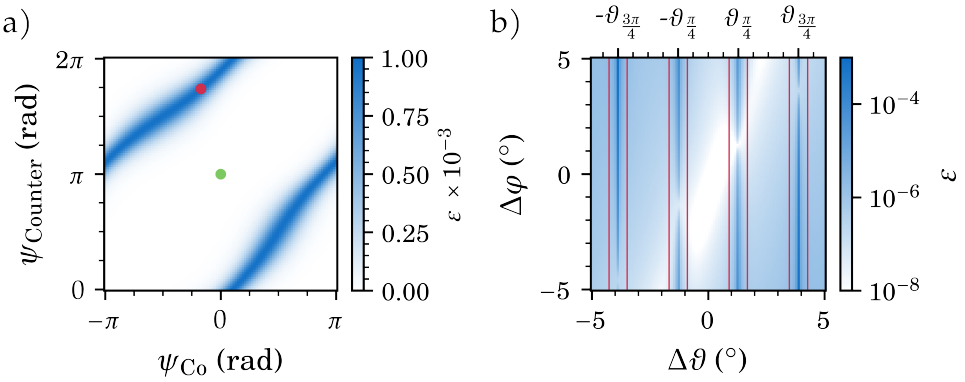



**Figure 8.12:** a) Simulated error as a function of the polarisation of each beam, assuming that the single-beam light shifts are nulled. The polarisation of the co-propagating beam is forced to lie on the bottom red contour in Figure 8.5, and the counter-propagating beam on the equivalent contour, which is shifted in $\psi$ by $\pi$. Points along these contours are parametrised by $\psi$. The green dot marks where both beams have the target polarisation. The largest error of $0.97 \times 10^{-3}$ occurs at the red dot. b) Errors due to counter-propagating beam misalignment in the plane containing the beam and the axial direction ($\Delta\vartheta$) and perpendicular to it ($\Delta\varphi$) when the polarisation is that of the green dot. Lines at which the $ZZZZ$ component vanishes occur at angles for which the optical path difference between the two ions is an odd multiple of $\pi/4$. Angles that lead to the SDF phase difference from Figure 8.4 are shown in red.

The final unitary is then applied to the $|{+}{+}{:}{+}{+}\rangle$ state and the fidelity of the resulting state to a 4-qubit GHZ state is found.

Figure 8.12 a) shows this gate error for all combinations of co- and counter-propagating beam polarisations which induce no single-beam light shift on the $D_{5/2}$ states. The point corresponding to both beams having the same (linear) polarisation is at the centre of the graph, where the error vanishes. Regions of large error can be observed, which correspond to polarisations at which the $ZZZZ$ Rabi frequency is small, while the Rabi frequency of other rotations is non-zero. Thus, when normalising the unitary, the angle of these stray rotations becomes non-negligible[40]. The largest error in the plot is $0.97 \times 10^{-3}$.

Even if the polarisation vectors of the two beams are set perfectly, the rank-1 polarisation tensor components depend on the beam directions, so unitary errors can also arise from misalignment. This dependence is very small even for significant beam pointing angles. However, as discussed in Section 8.1.3.3, the beam directions also determine the local SDF phase observed by each ion, which affects the Rabi frequency of the $ZZZZ$

[40]There in fact exist polarisations for which the $ZZZZ$ Rabi frequency vanishes, while other two-ion rotations do not! At these polarisations, it would be impossible to generate a 4-qubit GHZ state from a separable state and, in their vicinity, the effective gate error would be unbounded. However, these polarisations lead to significant single-ion light shifts between $D_{5/2}$ level states, and thus are easy to avoid.

| **Error source** | **Calculated error** $(\times 10^{-3})$ |
|---|---|
| Motional dephasing | 2.48 |
| Polarisation and beam pointing | 0.00 |
| Scattering | 0.04 |
| Magnetic field noise | 0.52 |
| Light shift noise | 1.96 |
| Single ion operations | 5 – 63 |
| Uncompensated stray phases | 42 |
| **Total** | 52 – 110 |

**Table 8.4:** Summary of errors. As discussed in Section 8.6.1.3, the error in the single ion operations is difficult to estimate. This uncertainty dominates over that of other errors, so we do not quote uncertainties.

rotation. Indeed, as shown in Appendix D.1, the $ZZZZ$ Rabi frequency vanishes if the forces on the two ions are in quadrature, even with the ideal two-beam light shifts. Thus, *any* stray rotation that arises from the small change in polarisation due to beam pointing errors can in principle become dominant!

The simulated errors due to misalignment of the counter-propagating beam in the plane containing the beam and the quantisation axis (along $\vartheta$) and perpendicular to it (along $\varphi$) are plotted in Figure 8.12 b), assuming perfect co-propagating beam pointing. We also mark the misalignment angles that would lead to the difference in SDF phase at the two ions found in Section 8.1.3.3, assuming the chain is perpendicular to the co-propagating beam. Since the optical phase is sufficiently far from $\pi/2$, the error is almost identical to that observed with perfect beam pointing ($\sim 10^{-7}$). Furthermore, there is almost no dependence on $\Delta\varphi$, which is fortunate since this misalignment would be much harder to detect.

Since we expect the method from Section 8.3 to result in near-ideal polarisations, unitary errors due to incorrect polarisation are deemed negligible.

#### 8.6.1.6 Summary

Table 8.4 provides a summary of the error sources analysed. The measured gate errors are $0.08 - 0.09$, which are not too far off the most pessimistic assessment of the single-ion error contributions. Furthermore, the sum of errors other than those from single-ion operations is $4.5 \times 10^{-3}$, which is not too far from the monoqubit errors. This is consistent

with the discussion in Section 5.3, which concluded that errors that affect the two-ion gate mechanism have almost identical impact on polyqubits as on monoqubits[41].

Nonetheless, the large contribution from the uncompensated stray phases and the ambiguity over how the errors from breaking the multi-photon resonance affect these experiments, makes the total expected error inconclusive. This is particularly the case since these sources contribute the largest infidelity. Improving the fidelity of intra-ion gates and correcting the multi-photon resonance errors with the method from Section 5.2.1 would make the analysis more robust. Additionally, the scheme used to measure and cancel the stray phases could be redesigned. Using an RPE-based method to extract the measured phases instead of directly fitting traces may be more accurate. The mismatch in the phase of the two ions could also be corrected, by either using LSs from individually addressed beams or reducing the inhomogeneities in the magnetic field and the beam intensities at the ions. Finally, the sources of uncompensated LS in the SDF pulses, such as the imbalance between the optical power in both pulses, must be mitigated. The echo scheme can also be modified to cancel $Z\mathbb{1}$ rotations as well as $ZZ$ and $\mathbb{1}Z$ ones.

One possible additional source of error, which would be difficult to quantify, would stem from issues with the 532 nm laser. Approximately one month after the experiments presented here, the laser unit was sent for repair due to damage to the second-harmonic-generation crystal. This damage stemmed from sustained use over years and, since it remained mostly unused between these experiments and the repair, it was certainly present while taking the data presented here. Similar damage to an identical unit was believed to be the cause of large two-qubit gate errors in Reference [207]. Furthermore, large variations in parity contrast between almost consecutive days were observed despite using the same calibration routine, which may be related (see Figure 8.13). However, it is unclear why this would affect polyqubit gates more than monoqubit gates; they also did not exhibit such large variations in parity contrast. More detailed investigation, with better single-ion gate fidelity, would be required to fairly compare polyqubit and monoqubit gate errors.

[41] The expected error from single-ion monoqubit operations is $\sim 2.4 \times 10^{-3}$, which would be a small fraction of the measured monoqubit error.

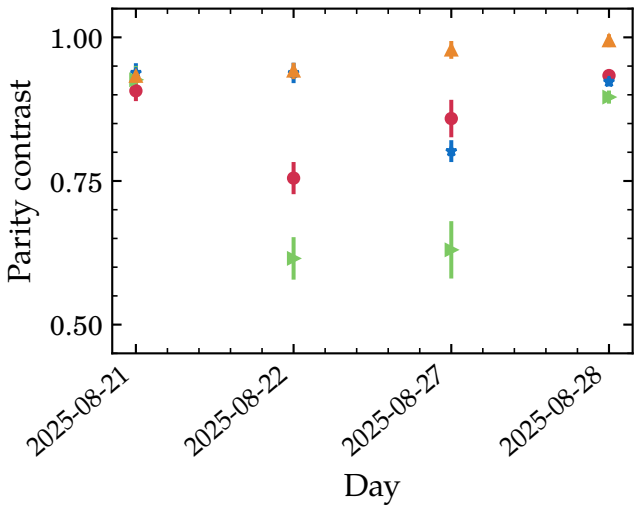



**Figure 8.13:** Parity contrast measured for the different gates over various (non-consecutive) days. Red circles denote $ZZZZ$ gates; green horizontal triangles $ZZ$ gates on the MSB qubits; blue stars $ZZ$ gates on the LSB qubits; and orange vertical triangles monoqubit $ZZ$ gates.

## 8.7 Conclusion

This chapter has demonstrated the inter-ion Sleepy Gates scheme proposed in Chapter 4. These were used to prepare Bell states of just the LSB or MSB with only minimal ($\leq 5\%$) excitation of spectator qubits. A four-qubit GHZ state was also prepared with the same mechanism, and almost identical error. Not only does this extend the single-ion gates of Chapter 7 to a full universal gate set, but it also clearly displays the large expressivity and ability to natively implement exotic gates that is inherent to polyqubit platforms.

Nevertheless, the gate fidelity is low when compared to state-of-the-art qudit gates [25, 153], multi-qubit gates in monoqubit systems [37, 109] and, most importantly, monoqubit gates in our own system. The latter finding contradicts the predictions of comparable polyqubit and monoqubit errors discussed in Chapter 5. However, this disparity is primarily due to uncompensated stray phases and intra-ion gate errors, which are not fundamental to the scheme and may mask a much higher-fidelity inter-ion gate. Improving both these aspects is within experimental reach and would allow for a clearer and fairer assessment of the inter-ion gate performance.

The error budget of Table 8.4 is otherwise promising, since errors fundamental to the gate mechanism – polarisation and scattering errors – are negligible in comparison

to other sources of technical errors. Even pessimistic conclusions from the light-shift measurements of Section 8.3 would result in an error lower than that due to all technical sources, except fluctuations in the 1762 nm beam frequency. Furthermore, such errors would be unitary, and could be addressed with composite pulse schemes. Indeed, an extension of the echo sequence of Section 8.1.3.1 that can eliminate all stray rotations except for $ZZZZ$ ones (from which any other pure rotation can be synthesised) can be found. Thus, fundamental polarisation errors (which may be relevant if different states, or a different ion species, were to be employed) can always be eliminated, at the cost of an increase in gate complexity. Furthermore, these echo sequences can also be natively combined with higher-order motional echoes with no extra complexity [148], thereby further reducing the impact of technical errors on the motion.

Indeed, the sum of these technical errors *does* match the infidelity in monoqubit gates, suggesting that these errors do behave equivalently. These errors can all be addressed by technical improvements to the experiment, such as improving the 532 nm power stability; enclosing the system in a $\mu$-metal shield[42]; reducing electronic noise in the trap voltages, to extend our motional coherence; and extending the coherence time of the 1762 nm laser. Work towards most of these is already underway. Additionally, the trap's complex electrode structure could be taken advantage of to engineer the trapping potential which would optimise the gate. For example, the SDF phase difference between the ions could be eliminated by tilting the axis of the chain towards or away from the 532 nm beam axes. This would remove issues when combining the motional and atomic echo protocols and reduce the necessary laser power. As well as this, the radial principal axes of motion could be rotated to maximise the projection of the gate mode and null the projection of all others, further reducing the necessary power.

Overall, the work in this chapter is a promising first step towards fully exploiting the advantages of the novel architecture presented by polyqubits.

[42]This is in fact already installed! But, due to various technical reasons, it was left open for all the work presented in this thesis.

*It's the lift.*

— Chris Ballance, after months of searching for the source of frequency jumps. Whether or not it was the lift is left to the reader's discretion.

# 9 Conclusion

The main contributions of this thesis have been twofold. The first is theoretical, with the proposal of a novel scheme for native inter-ion polyqubit gates. In addition, a detailed analysis of errors in multi-level ion systems, applicable to qudits as well as polyqubits, was carried out, which identified errors that the author has not seen discussed in the literature. The second was the experimental implementation of intra-ion and inter-ion gates, which together form the building blocks of a universal gate set[1]. While existing universal qudit processors would also be capable of demonstrating similar gate sets [25, 32, 33], to the author's knowledge, this constitutes the first implementation that optimises two-body gates for a polyqubit architecture across any platform.

More broadly, this work has extended the capabilities of our experimental apparatus, which has previously only been used as a monoqubit system, to those of a full multi-level processor. While its present fidelities are below the state-of-the-art [27, 39], clear strategies for improving these have been laid out.

## 9.1 Outlook

This work leaves open intriguing avenues for future exploration. Many of these are currently being worked towards by the other members of the ABaQuS experiment,

[1] Individual ion addressing would have made this a truly universal gate set. This is currently being worked towards.

Sophie Decoppet and William Cutler; the author is excitedly looking forward to the outcomes of their investigation.

Furthermore, an aspect of the system that has not been discussed in depth is the plethora of gate-driving mechanisms accessible to it. As well as the 1762 nm laser, the main workhorse for the intra-ion gates in Chapter 7, two-photon Raman processes with the 532 nm beams and microwaves have been previously used to implement high-fidelity single-qubit gates in the system [123, 207]. Inter-ion Mølmer-Sørensen gates have also been applied using the 532 nm beams [207] in addition to the LS gates used here, and Cirac-Zoller gates can in principle also be implemented. This flexibility compares very favourably with other existing systems [25–28, 150]. These capabilities, alongside the large Hilbert space afforded by $^{137}Ba^{+}$, and current efforts towards implementing individual addressing, will hopefully make this system into a flexible and general qudit processor.

### 9.1.1 Breaking the multi-photon resonance condition

The analysis of Chapter 7 suggested that the main error contribution likely arose from small laser detunings, which broke the multi-photon resonance condition. These errors are non-Markovian, making their analysis in the context of a quantum circuit challenging. Nonetheless, any multi-level system whose connectivity graph contains at least one cycle is sensitive to these effects. If connectivity graphs more complex than the simple linear and star topologies of current systems [25, 26, 35] are to be explored, a deeper understanding of these effects will be needed.

Thus, a more thorough theoretical investigation, which also explores the effect on graphs with more than one loop, would be widely useful. Direct experimental observations could then follow, such as performing RBM with enough statistics to reveal non-Markovian signatures. Furthermore, the coherent correction protocol of Section 5.2.1 could be implemented in order to replicate Figure 7.7 experimentally.

### 9.1.2 Improving error characterisation

The error analyses of both the intra- and inter-ion gates could not conclusively match the observed error to calculations from independent sources. If the errors from breaking the multi-photon resonance condition were removed using the proposed mechanism,

the remaining intra-ion gate errors would become easier to study. Gate Set Tomography could also be carried out to robustly extract the error processes for each gate, which in the absence of non-Markovianity would be more widely applicable.

In the inter-ion gate experiments, the largest source of error was stray single-ion phases. Eliminating their contribution would allow for the fidelity of the raw inter-ion gates to be assessed fairly. Various avenues can be explored towards this goal. Redesigning the phase measurement and compensation scheme could allow them to be cancelled directly. Improving the intra-ion gate error and correcting the multi-photon resonance errors would reduce their contribution to these phases. Finally, better control of the 532 nm intensity in the SDF pulses and improvements to the echo circuits would also mitigate these effects.

### 9.1.3 Expressive inter-ion gates

The Sleepy Gate mechanism demonstrated in Chapter 8 makes use of a particular LS structure (Figure 4.5). However, as discussed in Chapter 4, other light shift structures can efficiently implement more exotic gates. An LS structure for a four-qubit CCCZ gate was also given, which could be easily implemented once suitable atomic states are found[2].

In addition, previous studies of how MS gates can be applied to polyqubits have focused on implementing two-qubit gates[3] [47, 50, 51]. These, as well as Cirac-Zoller gates, are natively multi-qubit in a polyqubit architecture. These gates are expensive to implement with the minimal universal gate set we have demonstrated and appear in various algorithms [154]. Thus, a theoretical study of the set of computational polyqubit gates made available by these mechanisms could be widely useful. This would maximise the expressivity of systems capable of applying all of LS, MS and Cirac-Zoller gates, such as ours, making the most of the gate connectivity afforded by multi-level systems [25, 39, 153].

### 9.1.4 Increasing the system size

As mentioned, the work in this thesis does not fully meet the requirements for a universal gate set, since intra-ion operations could not be individually addressed between ions.

[2] If states with exactly the correct LS structure cannot be found, techniques similar to those proposed in [141] could likely be used to remove unwanted interactions.

[3] Some multi-qubit gates have been proposed, as discussed in Chapter 4.

While the diffraction limit makes focusing 1762 nm light tightly enough to achieve low crosstalk challenging, doing so with the 532 nm beams, which is technically much simpler, enables individually addressed single-ion LS. These, in combination with a global 1762 nm beam, can be used to implement arbitrary addressed intra-ion operations [207], as well as addressed inter-ion gates. An individual addressing system using laser-written waveguides has previously been implemented in our system [84] and an addressing system using acousto-optic deflectors is currently being installed by William Cutler.

Additionally, up to four qubits could be stored in a single $^{137}Ba^{+}$ ion [26]. However, the inter-ion Sleepy Gates heavily rely on the ability to choose states with particular atomic properties. It is unlikely that there are enough states with these properties to apply them to a 4-polyqubit, but it seems feasible that enough states with sufficiently similar properties could be found to manipulate a 3-polyqubit with these techniques. Otherwise, decompositions such as those proposed in [141] could be employed to filter out unwanted interactions. Intra-ion gates with multiple states also become more sensitive to decoherence, particularly due to magnetic field fluctuations [26]. A $\mu$-metal shield is installed in the system, but was unused for this work (with minimal impact on the results); this will be invaluable if any investigations into higher-dimensional systems are carried out.

### 9.1.5 Partitioned intra-ion gates

The Sleepy Gate protocol makes use of a Hamiltonian that is partitioned – it is a tensor product of single-qubit operators. This enables efficient and direct inter-ion multi-qubit gates, thus reducing the expected errors in comparison to other gate decompositions.

In contrast, intra-ion gates were still constructed from sequences of TSRs, which are not partitioned. However, it is possible to generate a partitioned intra-ion Hamiltonian by simultaneously driving all transitions in a loop – referred to as a Closed-Contour Interaction (CCI) [128, 129, 131]. Such interactions are particularly interesting, since unlike single-tone interactions, the driving phases change the *eigenvalues* as well as the eigenvectors of the Hamiltonian. It can be shown that if the Rabi frequencies of all transitions are made equal, the resulting Hamiltonian partitions across the two qubits in

a 2-polyqubit. Whether one qubit or the other is addressed, or whether the interaction is one- or two-qubit, is controlled entirely through the driving phases. This has the additional advantage of simplifying the effect of intra-ion LS, since the intensity and frequency of the beams – the only parameters that determine the LS – remain constant throughout intra-ion gates in a circuit. Theoretical and experimental work towards this is currently being carried out by Sophie Decoppet, with contributions from Oliver Hale.

# Appendices

# A

# Fidelity Expressions and Proofs

## A.1 Exponentials of null operators

In many points in this thesis, we must take the exponential $e^{iO}$ of an operator $O$ that is only non-zero within a subspace, and zero everywhere else. This can cause some confusion, particularly when using Dirac notation, because it is not readily apparent that $e^{iO}$ is in fact non-zero in the subspaces where $O$ vanishes. This is particularly true when using Dirac notation: it is tempting to deduce $\exp(i\theta |0\rangle\langle 0|) = \mathrm{diag}\{e^{i\theta}, 0, ...\}$, which is not full rank. This confusion is dispelled by noting that the exponential of a matrix is defined by the power series

$$e^X = \sum_{m=0}^{\infty} \frac{X^m}{m!} \tag{A.1}$$

with crucially $X^0 \triangleq \mathbb{1}$ by definition [159]. Thus, it is clear that, in the nullspaces of $O$, $e^{iO}$ is the identity. Relating to the previous example, $\exp(i\theta |0\rangle\langle 0|) = \mathrm{diag}\{e^{i\theta}, 1, ...\}$.

## A.2 Small rotations of involutory operators

We present some expressions for errors due to small unitary rotations on a $d$-level system of the form

$$R_O(\theta) \triangleq \exp\left[-i\frac{\theta}{2}O\right] \tag{A.2}$$

where $O$ is an involutory Hermitian operator within a subspace of dimension $\tilde{d}$ such that $O^2 = \mathbb{1}_{\tilde{d}}$. In that case, the rotations have the form

$$R_O(\theta) = \cos(\theta/2)\mathbb{1}_{\tilde{d}} - i\sin(\theta/2)O + \tilde{\mathbb{1}}_{\tilde{d}} \tag{A.3}$$

where we define $\tilde{\mathbb{1}}_{\tilde{d}} \triangleq \mathbb{1} - \mathbb{1}_{\tilde{d}}$. Then, a rotation error is the application of a unitary $R_O(\theta_{Err}) = R_O(\theta_{Id})R_O(\delta\theta)$, where $R_O(\theta_{Id})$ is the target rotation.

We are interested in finding two fidelity metrics for this, which are used in intra- and inter-ion gates. These are the average gate fidelity, and the state fidelity after application of the unitary, $\left|\langle\psi|R_O^\dagger(\theta_{Id})R_O(\theta_{Err})|\psi\rangle\right|^2$, where we choose the starting state $|\psi\rangle$ to be orthogonal to the eigenstates of $O$. The state fidelity is

$$\mathscr{F}_s = \left|\langle\psi|R_O(\delta\theta)|\psi\rangle\right|^2 = \cos^2(\delta\theta/2) \approx 1 - \delta\theta^2/4 \tag{A.4}$$

since, by assumption, $\langle O\rangle_{|\psi\rangle} = 0$. To find the average gate fidelity, we can see that the error process $\mathscr{E}(\rho) = R_O(\delta\theta)\rho R_O^\dagger(\delta\theta)$ has a single Kraus operator, $K = R_O(\delta\theta)$. We then find

$$\sum_i |\mathrm{Tr}(K_i)|^2 = (d + \tilde{d}[\cos(\delta\theta/2) - 1])^2 + \mathrm{Tr}(O)^2\sin^2(\delta\theta/2) \tag{A.5}$$

since $\mathrm{Tr}(\mathbb{1}_{\tilde{d}}) = \tilde{d}$, $\mathrm{Tr}(\tilde{\mathbb{1}}_{\tilde{d}}) = d - \tilde{d}$, and we used the fact that $\mathrm{Tr}(O) \in \mathbb{R}$ since $O$ is Hermitian. We now use Equation 5.3 to obtain the average gate fidelity to second order in $\delta\theta$

$$\bar{\mathscr{F}} = 1 - \frac{\delta\theta^2}{4}\frac{d\tilde{d} + \mathrm{Tr}(O)^2}{d(d+1)}. \tag{A.6}$$

From this, an over- or under-rotation error in a TSR, for which $\mathrm{Tr}(O) = 0$ and $\tilde{d} = 2$, leads to an average fidelity

$$\bar{\mathscr{F}}_{\mathrm{TSR}} = 1 - \frac{\delta\theta^2}{2(d+1)}. \tag{A.7}$$

## A.3 State fidelity of small diagonal unitaries

We derive the average state fidelity of small, random diagonal unitaries as a function of Hilbert space dimension $d$. The state $|\psi\rangle$ chosen is an even superposition, as usual.

We define these matrices as $U = \mathrm{diag}\{e^{i\phi_0}, e^{i\phi_1}, ...\}$ where the $d$ phases $\{\phi_i\}$ are random variables independently sampled from a zero-mean normal distribution of standard

deviation $\sigma_\phi$, which is small. The fidelity is given by

$$\begin{aligned}\mathscr{F}_s &= |\langle\psi|U|\psi\rangle|^2 \\ &= \frac{1}{d^2}\left|\sum_{j=0}^{d-1} e^{i\phi_j}\right|^2 \\ &= \frac{1}{d^2}\left(\sum_{j=0,k=0}^{d-1}\cos(\phi_j-\phi_k)\right).\end{aligned} \tag{A.8}$$

Taking a small angle approximation, we reach

$$\mathscr{F}_s = \frac{1}{d^2}\left(d^2 - \sum_{j=0}^{d-1}\sum_{k\neq j}\phi_j^2+\phi_k^2-2\phi_j\phi_k\right). \tag{A.9}$$

Now, we take an average over the random phases. Since all the variables are sampled from zero-mean normal distributions with the same variance, we have $\langle\phi_j\phi_k\rangle = 0$, $\langle\phi_j^2\rangle = \sigma_\phi^2$. Thus, we find

$$\langle\mathscr{F}_s\rangle = 1 - \frac{d(d-1)}{d^2}\sigma_\phi^2. \tag{A.10}$$

# B

# Sequence of TSRs in the atomic frame

## B.1 Derivation of a sequence of TSR pulses

Here, we re-derive the expression for the unitary of a TSR in a circuit with no dependence on the absolute time at which the pulse is executed (3.24) using the atomic interaction picture. The frame change Hamiltonian that reaches this frame is the bare atomic Hamiltonian $H_0 = \hbar \sum_{T=0}^{d-1} \omega_T |T\rangle\langle T|$. Then, using Equation (3.19) for the lab-frame pulse Hamiltonians, the full Hamiltonian during the $n^{\text{th}}$ pulse in the atomic frame is

$$H_{n,A} = \frac{\hbar\Omega^{(T_n)}}{2}\left(e^{-i(\tilde{\delta}^{(T_n)}_{T_n} t - \phi_n^{(T_n)})}|T_n+1\rangle\langle T_n| + h.c.\right) + \hbar\sum_{T=0}^{d-1}\left(\sum_{T'=0}^{T-1}\Delta^{T'}_{T_n}\right)|T\rangle\langle T| \tag{B.1}$$

where $\tilde{\delta}^{(T)}_{T'} = \omega_l^{(T)} - (\omega_{T+1} - \omega_T) = \delta^{(T)}_{T'} + \Delta^{T}_{T'}$ and we have used Equation (3.20) (without the $\Delta^{|0\rangle}_{T_n}$ term) to write the LS matrix.

The time dependence in this Hamiltonian makes directly finding the propagator non-trivial. Instead, we can "hop" into an interaction picture that removes the time dependence for the duration of the pulse, as was done in Section 3.4.3. This is done with the frame change Hamiltonian $H_F = -\hbar/2\,\tilde{\delta}^{(T_n)}_{T_n}\sigma_z^{(T_n)}$, so we obtain the Hamiltonian

$$\tilde{H}_{n,A} = \frac{\hbar}{2}\left(\Omega^{(T_n)}\sigma^{(T_n)}_{\phi_n^{(T_n)}} + \delta^{(T_n)}\sigma_z^{(T_n)}\right) + \hbar\left(\sum_{T=0}^{d-1}\left(\sum_{T'=0}^{T-1}\Delta^{T_n}_{T_n}\right)|T\rangle\langle T| + \frac{\Delta^{T_n}_{T_n}}{2}\sigma_z^{(T_n)}\right). \tag{B.2}$$

This is identical to the Hamiltonian in the drive frame (3.22) without the dependence on $\delta^{(T)}_{T_n}$ in the second term. Again, the operators in each set of brackets commute with each other.

Taking into account the frame change unitaries (Equation (3.3)), the full propagator for the pulse (including an inter-pulse delay $\tau_n^{(Int)}$ during which the atomic frame Hamiltonian vanishes, thereby adding nothing to the unitary) is thus[1]

$$\tilde{U}_n = R_z^{(T_n)}\left(-\tilde{\delta}_{T_n}^{(T_n)} t_{n,i}\right) R_z^{(T_n)}\left(-\delta^{(T_n)}\tau_n\right) \tilde{\mathscr{U}}_n^{(LS)} R^{(T_n)}\left(\theta_n, \phi_n^{(T_n)}, \nu^{(T_n)}\right) R_z^{(T_n)}\left(\tilde{\delta}_{T_n}^{(T_n)} t_{n,i}\right) \tag{B.3}$$

with

$$\tilde{\mathscr{U}}_n^{(LS)} = \exp\left[-i\tau_n \sum_{T=0}^{d-1}\left(\sum_{T'=0}^{T-1} \Delta_{T_n}^{T'}\right)|T\rangle\langle T|\right]. \tag{B.4}$$

The unitary for a full circuit is $C = \prod_n \tilde{U}_n$.

Now, we show how to remove the dependence on the absolute start time $t_{n,i}$ by spreading the first and last $z$ rotations in (B.3) over surrounding pulses. First, we introduce the following two matrices:

$$\mathfrak{R}_z^{(T)}(\phi) \triangleq \mathrm{diag}\{\underbrace{1,\ldots,1}_{T}, \underbrace{e^{+i\phi},\ldots,e^{+i\phi}}_{d-T}\}, \tag{B.5}$$

$$\tilde{\mathfrak{R}}_z^{(T)}(\phi) \triangleq \mathrm{diag}\{\underbrace{e^{+i\phi/2},\ldots,e^{+i\phi/2}}_{T-1}, 1, 1, \underbrace{e^{-i\phi/2},\ldots,e^{-i\phi/2}}_{d-T-1}\}. \tag{B.6}$$

The signs are picked so that

$$R_z^{(T)}(\phi) = \mathfrak{R}_z^{(T)}(\phi)\,\tilde{\mathfrak{R}}_z^{(T)}(\phi) \tag{B.7}$$

times an irrelevant global phase. It can be seen that $\tilde{\mathfrak{R}}_z^{(T)}$ commutes with a TSR on the $T^{\text{th}}$ transition and, if the connectivity graph is linear, $\mathfrak{R}_z^{(T)}$ commutes with TSRs on all other transitions.

We can thus expand the first and last $z$-rotations in (B.3) using (B.7). The $\tilde{\mathfrak{R}}_z^{(T_n)}$ terms commute through the TSR and cancel. The $\mathfrak{R}_z^{(T_n)}$ term after the TSR commutes through all TSRs after this one that drive transitions other than $T_n$, until reaching the next TSR that drives this transition. They thus produce terms of the form[2] $\mathfrak{R}_z^{(T_n)}\left(\tilde{\delta}_{T_n}^{(T_n)}(t_{\tilde{n},i} - t_{n,i})\right)$,

[1] The $R_z^{(T_n)}\left(-\delta^{(T_n)}\tau_n\right)$ term comes from the $\hbar/2\,\Delta_{T_n}^{T_n}\sigma_z^{(T_n)}$ term in (B.2) times part of the frame change unitary $R_z^{(T_n)}\left(-\tilde{\delta}_{T_n}^{(T_n)}(t_{n,i}+\tau_n)\right)$.

[2] The $\mathfrak{R}_z^{(T_n)}$ after the last TSR that drives $T_n$ cannot be multiplied with a further term that cancels its time dependence, since this would arise from a later TSR. However, this just means that there will be a diagonal gate $D_F = \prod_{T=0}^{d-1}\mathfrak{R}_z^{(T)}\left(-\delta^{(T)} t_{N_T,f}\right)$ at the end of the circuit, where $N_T$ is the index of the last pulse on transition $T$. Because we measure in the computational basis, this diagonal unitary has no observable effect. A similar thing occurs at the *first* pulses on each transition, which produce an irrelevant diagonal matrix at the very start of the circuit.

where the $\tilde{n}^{\text{th}}$ pulse is the next pulse on transition $T_n$ after the $n^{\text{th}}$ one. These terms can be placed anywhere between the $n^{\text{th}}$ and $\tilde{n}^{\text{th}}$ TSR, since they commute with the middle TSRs. We thus split them up such that a term $\mathfrak{R}_z^{(T_m)}\left(\tilde{\delta}_{T_n}^{(T_n)}(\tau_m + \tau_m^{(Int)})\right)$ is added to the $m^{\text{th}}$ TSR, leaving a similar term on the $n^{\text{th}}$ TSR. This can be interpreted by observing that these unitaries add phase differences between the states below $|T_n\rangle$ and those above $|T_n+1\rangle$ while the drive for the $T_n^{\text{th}}$ transition is off: this is the phase accumulation that arises from the detuning between the laser and the transition frequency.

Taking into account all pulses, the unitary for the full circuit can be expressed as[3] $C = \prod_n U_n$ with

$$U_n = R_z^{(T_n)}\left(-\delta^{(T_n)}\tau_n\right)\tilde{\mathscr{U}}_n^{(LS)} \times \left(\prod_{T=0}^{d-1}\mathfrak{R}_z^{(T_n)}\left(\tilde{\delta}_T^{(T)}(\tau_n + \tau_n^{(Int)})\right)\right)R^{(T_n)}\left(\theta_n, \phi_n^{(T_n)}, \nu^{(T_n)}\right). \tag{B.8}$$

Rearranging the diagonal operators, we reach Equation (3.24).

This construction does not work if the connectivity graph is cyclical, because the $\mathfrak{R}_z^{(T)}$ operators now *do not* commute with TSRs on all transitions other than $T$. In particular, they don't commute with TSRs on the $|d-1\rangle \leftrightarrow |0\rangle$ transition. Thus, we cannot pass through these unitaries through the necessary TSRs that allow the time dependence to reduce to a dependence on time differences instead. However, the decomposition (B.7) for $R_z^{(T)}$ rotations is not unique, and this argument does not prove that there exists some other decomposition which *could* allow for time dependences to cancel. Nonetheless, attempts by the author using alternative decompositions were not successful, leading him to conjecture that this is not possible.

## B.2 Deriving the LS correction through the TSR phase

Here, we derive the phase correction technique of Equation (5.17).

For this, we can write $\mathscr{U}_n^{(LS)}$ (Equation (3.26)) as

$$\mathscr{U}_n^{(LS)} = \prod_{T=0}^{d-1}\mathfrak{R}_z^{(T)}\left((\tau_n + \tau_n^{(Int)})\Delta_T^T - \tau_n\Delta_{T_n}^T\right). \tag{B.9}$$

Thus, considering all pulses in the circuit, we can group together all the $\mathfrak{R}_z^{(T_n)}$ unitaries between pulse $n$ and the previous pulse that drives transition $T_n$, pulse $\tilde{n}$. Then the

[3] Up to the diagonal matrices at the start and end from the previous footnote.

circuit can be rewritten as the product of the pulse unitaries

$$U'_n = \mathscr{U}_n^{(\delta)} R^{(T_n)}\left(\theta_n, \phi_n^{(T_n)}, \nu^{(T_n)}\right) \mathfrak{R}_z^{(T_n)}\left(\sum_{m=\tilde{n}}^{n-1} (\tau_m + \tau_m^{(Int)}) \Delta_{T_n}^{T_n} - \tau_m \Delta_{T_m}^{T_n}\right). \tag{B.10}$$

Now, we make use of the identity $R_\phi^{(T)}(\theta)\mathfrak{R}_z^{(T)}\left(\Delta\phi\right) = \mathfrak{R}_z^{(T)}\left(\Delta\phi\right) R_{\phi-\Delta\phi}^{(T)}(\theta)$, similar to (3.13). This allows us to pass the matrices through the TSRs until they are at the end of the circuit. This transforms the phase of the TSRs according to

$$\phi_n^{(T_n)} \to \phi_n^{(T_n)} - \phi_n^{(LS)} \quad , \quad \phi^{(LS)} = (t_{n,i} - \mathscr{T}_n^{(T_n)}) \Delta_{T_n}^{T_n} - \sum_{T \neq T_n} \mathscr{T}_n^{(T)} \Delta_T^{T_n} \tag{B.11}$$

where $\mathscr{T}_n^{(T)}$ is the total time for which the $T^{\text{th}}$ transition has been driven before the $n^{\text{th}}$ pulse. Thus, in order to undo this effect, we can drive the same circuit with the phases $\phi_n^{(T_n)} \to \phi_n^{(T_n)} + \tilde{\phi}_n^{(LS)}$, where $\tilde{\phi}_n^{(LS)}$ has the same form as $\phi_n^{(LS)}$ but with measured estimate of the LS matrix $\tilde{\Delta}_{T'}^{T}$.

# C
# Bit-string identities

In this Appendix, we derive useful expressions for sums of the form

$$\sum_{\mathbf{b}\in\mathbf{B}} (-1)^{\mathbf{b}\cdot\mathbf{c}} \tag{C.1}$$

where $\mathbf{c}$ is some $n$-bit string, $\mathbf{B}$ is some set of $n$-bit strings and $\mathbf{b}\cdot\mathbf{c} = \bigoplus_i b_i c_i$.

## C.1 Sum over all bit-strings

Let $\mathbf{B}_n$ be the set of all $n$-bit strings. We can clearly see that, if $\mathbf{c} = (0,0,0,...) = \mathbf{0}$,

$$\sum_{\mathbf{b}\in\mathbf{B}_n} (-1)^{\mathbf{b}\cdot\mathbf{0}} = \sum_{\mathbf{b}\in\mathbf{B}} (-1)^0 = 2^n. \tag{C.2}$$

However, in any other case, the sum is 0. This is because $\mathbf{c}$ will contain at least one bit, say $c_i$, which is equal to 1, so $\mathbf{b}\cdot\mathbf{c} = \tilde{\mathbf{b}}\cdot\tilde{\mathbf{c}} \oplus b_j$, where $\tilde{\mathbf{i}}$ is the $(n-1)$-bit string composed of all bits in $\mathbf{i}$ other than $i_j$. Clearly, the set $B_n$ is then split into two equal sets, with $b_j = 0, 1$, and where the remaining bit-strings $\tilde{\mathbf{b}}$ span $\mathbf{B}_{n-1}$. Thus, for $\mathbf{c} \neq \mathbf{0}$, we can write

$$\sum_{\mathbf{b}\in\mathbf{B}_n} (-1)^{\mathbf{b}\cdot\mathbf{c}} = \sum_{\tilde{\mathbf{b}}\in\mathbf{B}_{n-1}} \left((-1)^{\tilde{\mathbf{b}}\cdot\tilde{\mathbf{c}}\oplus 0} + (-1)^{\tilde{\mathbf{b}}\cdot\tilde{\mathbf{c}}\oplus 1}\right) = \sum_{\tilde{\mathbf{b}}\in\mathbf{B}_{n-1}} \left((-1)^{\tilde{\mathbf{b}}\cdot\tilde{\mathbf{c}}} - (-1)^{\tilde{\mathbf{b}}\cdot\tilde{\mathbf{c}}}\right) = 0. \tag{C.3}$$

Thus, $\sum_{\mathbf{b}\in\mathbf{B}_n} (-1)^{\mathbf{b}\cdot\mathbf{c}} = 2^n \delta_{\mathbf{c},\mathbf{0}}$.

## C.2 Sum over bit-strings of definite parity

We now consider sums of the form

$$\sum_{\mathbf{b}\in\mathbf{B}_n^p} (-1)^{\mathbf{b}\cdot\mathbf{c}} \tag{C.4}$$

where $\mathbf{B}_n^p$ are all $n$-bit strings of the same parity $p = 0, 1$, which is the number of 1s in the bit-string, modulo 2. We can clearly see that, since there are $2^{(n-1)}$ such bit-strings,

$$\sum_{\mathbf{b}\in\mathbf{B}_n^p} (-1)^{\mathbf{b}\cdot\mathbf{0}} = 2^{(n-1)}, \tag{C.5}$$

$$\sum_{\mathbf{b}\in\mathbf{B}_n^p} (-1)^{\mathbf{b}\cdot\mathbf{1}} = (-1)^p 2^{(n-1)}. \tag{C.6}$$

where $\mathbf{1} = (1, 1, ...)$.

Now, if $\mathbf{c} \neq \mathbf{0}, \mathbf{1}$, we know that there is at least one bit $c_j = 0$. We can thus see that, for a bit-string $\mathbf{b}$ of any parity $p$, $\mathbf{b}\cdot\mathbf{c} = \tilde{\mathbf{b}}\cdot\tilde{\mathbf{c}}$ independent of $p$. The bit-strings $\tilde{\mathbf{b}}$ span the full $B_{n-1}$, since for any $(n-1)$-bit string $\tilde{\mathbf{b}}$, an $n$-bit string $\mathbf{b}$ of either parity can be constructed by suitably choosing $b_j = 0, 1$. Thus, we can write for $\mathbf{c} \neq \mathbf{0}, \mathbf{1}$

$$\sum_{\mathbf{b}\in\mathbf{B}_n^p} (-1)^{\mathbf{b}\cdot\mathbf{c}} = \sum_{\tilde{\mathbf{b}}\in\mathbf{B}_{n-1}} (-1)^{\tilde{\mathbf{b}}\cdot\tilde{\mathbf{c}}} = 0 \tag{C.7}$$

using the result from the previous section and the fact that, since $\mathbf{c} \neq \mathbf{0}$, $\tilde{\mathbf{c}} \neq \mathbf{0}$. Thus,

$$\sum_{\mathbf{b}\in\mathbf{B}_n^p} (-1)^{\mathbf{b}\cdot\mathbf{c}} = 2^{n-1}(\delta_{\mathbf{c},\mathbf{0}} + (-1)^p \delta_{\mathbf{c},\mathbf{1}}). \tag{C.8}$$

# D

# Sleepy gate identities

## D.1 Sleepy Gate with imbalanced SDF phase and amplitude

Consider a Sleepy Gate between two ions, such that the states in both of them are split into two equal halves denoted by $\uparrow, \downarrow$ depending on the two-beam LS they observe. These are $\Delta_{\uparrow(\downarrow)} = \Delta_\Sigma \pm \Delta_\Delta$, where $\Delta_\Sigma$, $\Delta_\Delta$ are common-mode and differential components of the light shifts. Suppose that the intensity and phase of the optical lattice at the position of the two ions are $(1 \pm \beta)$ and $e^{\mp i\phi/2}$ respectively. Then, the SDF on any pair of states is one of the following (assuming we couple to a radial mode), independently of the dimension $d$:

$$\Omega_{\downarrow\downarrow} = \sqrt{2}(\Delta_\Sigma - \Delta_\Delta)\left(\beta\cos\left(\frac{\phi}{2}\right) - i\sin\left(\frac{\phi}{2}\right)\right) \tag{D.1}$$

$$\Omega_{\uparrow\uparrow} = \sqrt{2}(\Delta_\Sigma + \Delta_\Delta)\left(\beta\cos\left(\frac{\phi}{2}\right) - i\sin\left(\frac{\phi}{2}\right)\right) \tag{D.2}$$

$$\Omega_{\downarrow\uparrow} = \sqrt{2}\left(\cos\left(\frac{\phi}{2}\right)[\beta\Delta_\Sigma - \Delta_\Delta] - i\sin\left(\frac{\phi}{2}\right)[\Delta_\Sigma - \beta\Delta_\Delta]\right) \tag{D.3}$$

$$\Omega_{\uparrow\downarrow} = \sqrt{2}\left(\cos\left(\frac{\phi}{2}\right)[\beta\Delta_\Sigma + \Delta_\Delta] - i\sin\left(\frac{\phi}{2}\right)[\Delta_\Sigma + \beta\Delta_\Delta]\right) \tag{D.4}$$

It is clear that, in general, these light shifts will be different. However, if we naïvely carry out the echo as per Section 8.1.3.2, it turns out that, despite the final displacements on all states being non-zero, they are all equal. Indeed, this is because the states that observe the SDF $\Omega_{ij}$ in the first loop will have a net displacement $\alpha_{ij}$ in this loop, but since the SDF phase is reset for the second loop, when they flip and feel the SDF $\Omega_{ji}$, they will

undergo a second displacement $\alpha_{ij}$. The total displacement is thus

$$\begin{aligned}\alpha_{ij}+\alpha_{ji} &= \frac{2\sqrt{2}\eta}{\delta}e^{i\delta t/2}\sin\frac{\delta t}{2}\Delta_\Sigma\left(\beta\cos(\phi/2)-i\sin(\phi/2)\right)\\ &\triangleq \alpha_F\end{aligned} \tag{D.5}$$

for any $i,j$.

However, because of the non-commutativity of displacement operators (3.59), different states will acquire different phases upon reaching this state, depending on the trajectory. Indeed, a state that initially observes an SDF $\Omega_{ij}$ will acquire an additional geometric phase $\Im\left(\alpha_{ji}\alpha_{ij}^*\right)$. These differ by a sign for state arrangements $ij$ and $ji$, but are different in magnitude for $ij$ and $ii$. We call $\xi=\Im\left(\alpha_{\uparrow\uparrow}\alpha_{\downarrow\downarrow}^*\right)$ and $\chi=\Im\left(\alpha_{\uparrow\downarrow}\alpha_{\downarrow\uparrow}^*\right)$.

We must also consider the regular geometric phases from (3.70), $\Phi_{ij}$, which are by design the same for all states that start in these levels. Furthermore, they depend quadratically on the SDF of each state. Thus, unlike the displacements, initial state arrangements $\{ii,jj\}$ and $\{ij,ji\}$ acquire the same geometric phase, without a sign flip. Then, the final state at the end of the gate is of the form

$$\begin{aligned}|\psi\rangle = \frac{1}{d}\Bigg[&e^{i(\Phi_{\downarrow\downarrow}+\Phi_{\uparrow\uparrow})}\left(e^{i\xi}\sum_{\nu_\downarrow,\mu_\downarrow}|\nu_\downarrow:\mu_\downarrow\rangle+e^{-i\xi}\sum_{\nu_\uparrow,\mu_\uparrow}|\nu_\uparrow:\mu_\uparrow\rangle\right)\\ &+e^{i(\Phi_{\downarrow\uparrow}+\Phi_{\uparrow\downarrow})}\left(e^{i\chi}\sum_{\nu_\downarrow,\mu_\uparrow}|\nu_\downarrow:\mu_\uparrow\rangle+e^{-i\chi}\sum_{\nu_\uparrow,\mu_\downarrow}|\nu_\uparrow:\mu_\downarrow\rangle\right)\Bigg]\otimes|\alpha_F\rangle\end{aligned} \tag{D.6}$$

Since the atomic and motional states disentangle, we ignore the latter.

The difference in geometric phase acquired between sets of states with different parity is

$$\Phi_\Delta=(\Phi_{\downarrow\uparrow}+\Phi_{\uparrow\downarrow})-(\Phi_{\downarrow\downarrow}+\Phi_{\uparrow\uparrow})=\frac{\eta^2}{\delta^2}|\Delta_\Delta|^2\cos^2(\phi)(1-\beta^2)(\delta t-\sin\delta t) \tag{D.7}$$

and the fidelity of the target state after the second SDF pulse, which is

$$|\psi_{Id}\rangle=\frac{1}{d}\left[\sum_{\nu_i,\mu_i}|\nu_i:\mu_i\rangle+i\sum_{\nu_i,\mu_{\bar{i}}}|\nu_i:\mu_{\bar{i}}\rangle\right] \tag{D.8}$$

where $\bar{i}$ means the opposite arrow direction to $i$. Then, the fidelity of (D.6) to $|\psi_{Id}\rangle$ is

$$F=\frac{1}{4}\left(\cos^2\chi+\cos^2\xi+2\sin\Phi_\Delta\right) \tag{D.9}$$

expanding this about the ideal loop duration, $\delta t=2\pi$ shows that the errors are suppressed to second order, instead of fourth order in a regular two-loop gate.

We can also calculate the population in the $|0{:}1\rangle$, $|1{:}0\rangle$ state in the monoqubit experiment of figure 8.4 by applying the $R_y$ rotations at the end of the gate. We find that if $\xi = 0$, as it is if the two-beam LS $\Delta_\Delta$, $\Delta_\Sigma$ are real, the population in these states is

$$P(|0{:}1\rangle) = P(|1{:}0\rangle) = \frac{\sin^2\chi}{4} \tag{D.10}$$

## D.2 General expression for the Sleepy Gates unitary

Consider a Sleepy Gate LS structure, with the states arranged over two levels $\uparrow, \downarrow$ such that all single-ion states of even (odd) parity are in the $\uparrow$ ($\downarrow$) level, for both ions. This would generate a rotation that affects all qubits in the polyqubits (the equivalent of the $ZZZZ$ rotations in 2-polyqubits). Then, the two-ion states $|\mathbf{a}:\mathbf{b}\rangle$ can pick up one of four geometric phases $\Phi_{i,j}$ and motional displacements $\alpha_{i,j}$ depending on whether $|\mathbf{a}(\mathbf{b})\rangle$ are in level $i(j) \in \{\uparrow, \downarrow\}$. Thus, the full unitary is

$$\begin{aligned} U = &\sum_{\substack{\mathbf{a}\in\mathbf{B}_n^e \\ \mathbf{b}\in\mathbf{B}_n^e}} D(\alpha_{\uparrow\uparrow}) \otimes e^{i\Phi_{\uparrow\uparrow}} |\mathbf{a}:\mathbf{b}\rangle\langle\mathbf{a}:\mathbf{b}| + \sum_{\substack{\mathbf{a}\in\mathbf{B}_n^o \\ \mathbf{b}\in\mathbf{B}_n^o}} D(\alpha_{\downarrow\downarrow}) \otimes e^{i\Phi_{\downarrow\downarrow}} |\mathbf{a}:\mathbf{b}\rangle\langle\mathbf{a}:\mathbf{b}| \\ &+ \sum_{\substack{\mathbf{a}\in\mathbf{B}_n^e \\ \mathbf{b}\in\mathbf{B}_n^o}} D(\alpha_{\uparrow\downarrow}) \otimes e^{i\Phi_{\uparrow\downarrow}} |\mathbf{a}:\mathbf{b}\rangle\langle\mathbf{a}:\mathbf{b}| + \sum_{\substack{\mathbf{a}\in\mathbf{B}_n^o \\ \mathbf{b}\in\mathbf{B}_n^e}} D(\alpha_{\downarrow\uparrow}) \otimes e^{i\Phi_{\downarrow\uparrow}} |\mathbf{a}:\mathbf{b}\rangle\langle\mathbf{a}:\mathbf{b}| \end{aligned} \tag{D.11}$$

where $\mathbf{B}_n^{e(o)}$ is the set of even (odd) $n$-bit strings. Now, using $|\mathbf{c}\rangle\langle\mathbf{c}| = 1/2^n \sum_{\mathbf{b}\in\mathbf{B}_n} (-1)^{\mathbf{c}\cdot\mathbf{b}} \Sigma_z^{\otimes\mathbf{b}}$, we can express the sums over the projectors $|\mathbf{a}:\mathbf{b}\rangle\langle\mathbf{a}:\mathbf{b}|$ of parity $p_\mathbf{a}$, $p_\mathbf{b}$ as

$$\begin{aligned} \sum_{\substack{\mathbf{a}\in\mathbf{B}_n^{p_\mathbf{a}} \\ \mathbf{b}\in\mathbf{B}_n^{p_\mathbf{b}}}} |\mathbf{a}:\mathbf{b}\rangle\langle\mathbf{a}:\mathbf{b}| &= \frac{1}{2^{2n}} \sum_{\substack{\mathbf{c}\in\mathbf{B}_n \\ \mathbf{d}\in\mathbf{B}_n}} \left( \sum_{\mathbf{a}\in\mathbf{B}_n^{p_\mathbf{a}}} (-1)^{\mathbf{a}\cdot\mathbf{c}} \right) \left( \sum_{\mathbf{b}\in\mathbf{B}_n^{p_\mathbf{b}}} (-1)^{\mathbf{b}\cdot\mathbf{d}} \right) \Sigma_z^{\otimes(\mathbf{c},\mathbf{d})} \\ &= \frac{1}{4} \sum_{\substack{\mathbf{c}\in\mathbf{B}_n \\ \mathbf{d}\in\mathbf{B}_n}} \big( \delta_{(\mathbf{c},\mathbf{d}),(\mathbf{0},\mathbf{0})} + (-1)^{p_\mathbf{a}} \delta_{(\mathbf{c},\mathbf{d}),(\mathbf{1},\mathbf{0})} \\ &\qquad + (-1)^{p_\mathbf{b}} \delta_{(\mathbf{c},\mathbf{d}),(\mathbf{0},\mathbf{1})} + (-1)^{p_\mathbf{a}+p_\mathbf{b}} \delta_{(\mathbf{c},\mathbf{d}),(\mathbf{1},\mathbf{1})} \big) \Sigma_z^{\otimes(\mathbf{c},\mathbf{d})} \end{aligned} \tag{D.12}$$

where $(\mathbf{i},\mathbf{j})$ is the concatenation of $\mathbf{i}, \mathbf{j}$, $\mathbf{0}$ and $\mathbf{1}$ are the bit-strings composed of all 0s or 1s and the $\Sigma_z^{\otimes\mathbf{b}}$ are generalised Pauli operators. In the last line, we have used the bit-string identity (C.8).

Substituting this into the above, we find

$$\begin{aligned} U = \frac{1}{4}\Big[ & D(\alpha_{\uparrow\uparrow}) \otimes e^{i\Phi_{\uparrow\uparrow}} \left(\Sigma_z^{\otimes(\mathbf{0},\mathbf{0})} + \Sigma_z^{\otimes(\mathbf{0},\mathbf{1})} + \Sigma_z^{\otimes(\mathbf{1},\mathbf{0})} + \Sigma_z^{\otimes(\mathbf{1},\mathbf{1})}\right) \\ & + D(\alpha_{\downarrow\downarrow}) \otimes e^{i\Phi_{\downarrow\downarrow}} \left(\Sigma_z^{\otimes(\mathbf{0},\mathbf{0})} - \Sigma_z^{\otimes(\mathbf{0},\mathbf{1})} - \Sigma_z^{\otimes(\mathbf{1},\mathbf{0})} + \Sigma_z^{\otimes(\mathbf{1},\mathbf{1})}\right) \\ & + D(\alpha_{\uparrow\downarrow}) \otimes e^{i\Phi_{\uparrow\downarrow}} \left(\Sigma_z^{\otimes(\mathbf{0},\mathbf{0})} - \Sigma_z^{\otimes(\mathbf{0},\mathbf{1})} + \Sigma_z^{\otimes(\mathbf{1},\mathbf{0})} - \Sigma_z^{\otimes(\mathbf{1},\mathbf{1})}\right) \\ & + D(\alpha_{\downarrow\uparrow}) \otimes e^{i\Phi_{\downarrow\uparrow}} \left(\Sigma_z^{\otimes(\mathbf{0},\mathbf{0})} + \Sigma_z^{\otimes(\mathbf{0},\mathbf{1})} - \Sigma_z^{\otimes(\mathbf{1},\mathbf{0})} - \Sigma_z^{\otimes(\mathbf{1},\mathbf{1})}\right)\Big]. \end{aligned} \tag{D.13}$$

We can now consider converting the $\Sigma_z^{\otimes\mathbf{b}}$ operators into $\Sigma_x^{\otimes\mathbf{b}}$ ones by surrounding the gate with the opening and closing gates of Section 8.1. When this is applied to a computational basis state, only four states can ever populated even if the loops have not closed, which are the result of multiplying the initial state by $\Sigma_x^{\otimes(\mathbf{0},\mathbf{0})}$, $\Sigma_x^{\otimes(\mathbf{1},\mathbf{0})}$, $\Sigma_x^{\otimes(\mathbf{0},\mathbf{1})}$ and $\Sigma_x^{\otimes(\mathbf{1},\mathbf{1})}$. This is observed in Figure 8.2.

As a concrete example, if the two ions are equally illuminated and the phase of the SDF at either is the same (so $\Phi_{\uparrow\downarrow} = \Phi_{\downarrow\uparrow} = \Phi$) and we use a rocking mode (so $\Phi_{\uparrow\uparrow} = \Phi_{\downarrow\downarrow} = 0$) then, when the loops close,

$$U = e^{i\frac{\Phi}{2}} \left(\cos\frac{\Phi}{2}\Sigma^{(\mathbf{0},\mathbf{0})} - i\sin\frac{\Phi}{2}\Sigma^{(\mathbf{1},\mathbf{1})}\right) = R_z^{\otimes(\mathbf{1},\mathbf{1})}(\Phi) \tag{D.14}$$

as required.

# E

# LS Gate decompositions

Here we give the expressions for the two-beam LS in the presence of the polarisation errors described in Section 5.3.4. The reader is referred there for a definition of the terms. These were obtained using the `sympy` Python package [226].

| **Operator** $\Sigma_z^{\otimes \mathbf{b}}$ | $\Omega_{\mathbf{b}}/C$ |
|---|---|
| $\mathbb{1}\mathbb{1} \otimes \mathbb{1}\mathbb{1}$ | $-\Delta_\Delta^2 - \frac{\delta_D^2}{2} - \frac{\delta_S^2}{2}$ |
| $\mathbb{1}\mathbb{1} \otimes \mathbb{1}Z$ | $\frac{\Delta_\Delta(\delta_D+\delta_S)}{2}$ |
| $\mathbb{1}\mathbb{1} \otimes Z\mathbb{1}$ | $\frac{\Delta_\Delta(-\delta_D+\delta_S)}{2}$ |
| $\mathbb{1}\mathbb{1} \otimes ZZ$ | $\frac{\delta_D^2}{4} - \frac{\delta_S^2}{4}$ |
| $\mathbb{1}Z \otimes \mathbb{1}\mathbb{1}$ | $\frac{\Delta_\Delta(\delta_D+\delta_S)}{2}$ |
| $\mathbb{1}Z \otimes \mathbb{1}Z$ | $\frac{\delta_D^2}{4} - \frac{\delta_D\delta_S}{2} + \frac{\delta_S^2}{4}$ |
| $\mathbb{1}Z \otimes Z\mathbb{1}$ | $-\frac{\delta_D^2}{4} + \frac{\delta_S^2}{4}$ |
| $\mathbb{1}Z \otimes ZZ$ | $\frac{\Delta_\Delta(\delta_D-\delta_S)}{2}$ |
| $Z\mathbb{1} \otimes \mathbb{1}\mathbb{1}$ | $\frac{\Delta_\Delta(-\delta_D+\delta_S)}{2}$ |
| $Z\mathbb{1} \otimes \mathbb{1}Z$ | $-\frac{\delta_D^2}{4} + \frac{\delta_S^2}{4}$ |
| $Z\mathbb{1} \otimes Z\mathbb{1}$ | $\frac{\delta_D^2}{4} + \frac{\delta_D\delta_S}{2} + \frac{\delta_S^2}{4}$ |
| $Z\mathbb{1} \otimes ZZ$ | $\frac{\Delta_\Delta(-\delta_D-\delta_S)}{2}$ |
| $ZZ \otimes \mathbb{1}\mathbb{1}$ | $\frac{\delta_D^2}{4} - \frac{\delta_S^2}{4}$ |
| $ZZ \otimes \mathbb{1}Z$ | $\frac{\Delta_\Delta(\delta_D-\delta_S)}{2}$ |
| $ZZ \otimes Z\mathbb{1}$ | $\frac{\Delta_\Delta(-\delta_D-\delta_S)}{2}$ |
| $ZZ \otimes ZZ$ | $\Delta_\Delta^2$ |

**Table E.1:** Rotation rates for calculating the generalised $Z$ rotation angles in the presence of incorrect two-beam LS. The constant $C \triangleq \frac{\pi}{2\Omega_{ZZZZ}\tau_g}$ contains all contributions that are independent of the LSs on each state when the gate parameters are set to make $\Omega_{ZZZZ}\tau_g = \frac{\pi}{2}$.

# References


[1] D. W. Davies. *The Bombe a Remarkable Logic Machine*. In: *Cryptologia* 23.2 (Apr. 1999), pp. 108–138.

[2] R. P. Feynman. *Simulating physics with computers*. en. In: *International Journal of Theoretical Physics* 21.6 (June 1982), pp. 467–488.

[3] S. Haroche and J.-M. Raymond. *Exploring the quantum*. Oxford ; New York: Oxford University Press, 2006.

[4] W. K. Wootters and W. H. Zurek. *A single quantum cannot be cloned*. en. In: *Nature* 299.5886 (Oct. 1982), pp. 802–803.

[5] D. Gottesman. *Surviving as a Quantum Computer in a Classical World*. May 2024.

[6] P. W. Shor. *Scheme for reducing decoherence in quantum computer memory*. In: *Physical Review A* 52.4 (Oct. 1995), R2493–R2496.

[7] A. M. Steane. *Error Correcting Codes in Quantum Theory*. In: *Physical Review Letters* 77.5 (July 1996), pp. 793–797.

[8] M. C. Smith et al. *Single-Qubit Gates with Errors at the ${10}^{\ensuremath{-}7}$ Level*. In: *Physical Review Letters* 134.23 (June 2025). Publisher: American Physical Society, p. 230601.

[9] A. C. Hughes et al. *Trapped-ion two-qubit gates with >99.99% fidelity without ground-state cooling*. arXiv:2510.17286 [quant-ph] version: 1. Oct. 2025.

[10] A. Ransford et al. *Helios: A 98-qubit trapped-ion quantum computer*. arXiv:2511.05465 [quant-ph]. Nov. 2025.

[11] D. Bluvstein et al. *Logical quantum processor based on reconfigurable atom arrays*. en. In: *Nature* 626.7997 (Feb. 2024). Publisher: Nature Publishing Group, pp. 58–65.

[12] R. Acharya et al. *Quantum error correction below the surface code threshold*. en. In: *Nature* 638.8052 (Feb. 2025). Publisher: Nature Publishing Group, pp. 920–926.

[13] D. Bluvstein et al. *A fault-tolerant neutral-atom architecture for universal quantum computation*. en. In: *Nature* 649.8095 (Jan. 2026), pp. 39–46.

[14] E. Granet et al. *Superconducting pairing correlations on a trapped-ion quantum computer*. arXiv:2511.02125 [quant-ph]. Feb. 2026.

[15] M. Cain et al. *Shor's algorithm is possible with as few as 10,000 reconfigurable atomic qubits*. arXiv:2603.28627 [quant-ph]. Mar. 2026.

[16] Y. Igarashi. *Computing : a historical and technical perspective.* eng. 1st edition. Place of publication not identified: CRC Press, 2017.

[17] R. Blume-Kohout, C. M. Caves, and I. H. Deutsch. *Climbing Mount Scalable: Physical Resource Requirements for a Scalable Quantum Computer*. en. In: *Foundations of Physics* 32.11 (Nov. 2002), pp. 1641–1670.

[18] A. S. Sotirova et al. *High-fidelity heralded quantum state preparation and measurement*. en. arXiv:2409.05805 [physics, physics:quant-ph]. Sept. 2024.

[19] H.-L. Huang et al. *Superconducting quantum computing: a review*. en. In: *Science China Information Sciences* 63.8 (July 2020), p. 180501.

[20] K. Wintersperger et al. *Neutral atom quantum computing hardware: performance and end-user perspective*. en. In: *EPJ Quantum Technology* 10.1 (Dec. 2023), p. 32.

[21] H. Zhu et al. *Recent progress towards large-scale integrated photonic quantum computation*. en. In: *npj Nanophotonics* 3.1 (Mar. 2026), p. 20.

[22] F. A. Zwanenburg et al. *Silicon quantum electronics*. In: *Reviews of Modern Physics* 85.3 (July 2013), pp. 961–1019.

[23] C. Zhang et al. *Universal logical operations in a silicon quantum processor*. en. In: *Nature Nanotechnology* (Mar. 2026), pp. 1–7.

[24] R. Katsumi et al. *Recent progress in hybrid diamond photonics for quantum information processing and sensing*. en. In: *Communications Engineering* 4.1 (May 2025), p. 85.

[25] M. Ringbauer et al. *A universal qudit quantum processor with trapped ions*. en. In: *Nature Physics* 18.9 (Sept. 2022), pp. 1053–1057.

[26] P. J. Low et al. *Quantum logic operations and algorithms in a single 25-level atomic qudit*. July 21, 2025. arXiv: 2507.15799[quant-ph].

[27] X. Shi et al. *Efficient Implementation of a Quantum Algorithm with a Trapped Ion Qudit*. June 11, 2025. arXiv: 2506.09371[quant-ph].

[28] K. DeBry et al. *Error correction of a logical qubit encoded in a single atomic ion*. en. arXiv:2503.13908 [quant-ph]. Mar. 2025.

[29] I. V. Zalivako et al. *Towards a Multiqudit Quantum Processor Based on a 171Yb+ Ion String: Realizing Basic Quantum Algorithms*. en. In: *Quantum Reports* 7.2 (June 2025), p. 19.

[30] B. L. Brock et al. *Quantum error correction of qudits beyond break-even*. en. In: *Nature* 641.8063 (May 2025), pp. 612–618.

[31] S. Cao et al. *Emulating two qubits with a four-level transmon qudit for variational quantum algorithms*. en. In: *Quantum Science and Technology* 9.3 (Apr. 2024), p. 035003.

[32] N. Goss et al. *Extending the computational reach of a superconducting qutrit processor*. en. In: *npj Quantum Information* 10.1 (Oct. 2024), p. 101.

[33] Y. Chi et al. *A programmable qudit-based quantum processor*. en. In: *Nature Communications* 13.1 (Mar. 2022). Publisher: Nature Publishing Group, p. 1166.

[34] M. Erhard et al. *Experimental Greenberger–Horne–Zeilinger entanglement beyond qubits*. en. In: *Nature Photonics* 12.12 (Dec. 2018), pp. 759–764.

[35] X. Yu et al. *Schrödinger cat states of a nuclear spin qudit in silicon*. en. In: *Nature Physics* 21.3 (Mar. 2025). Publisher: Nature Publishing Group, pp. 362–367.

[36] P. Imany et al. *High-dimensional optical quantum logic in large operational spaces*. en. In: *npj Quantum Information* 5.1 (July 2019), p. 59.

[37] S. A. Moses et al. *A Race-Track Trapped-Ion Quantum Processor*. In: *Physical Review X* 13.4 (Dec. 2023). Publisher: American Physical Society, p. 041052.

[38] G. Li, Y. Ding, and Y. Xie. *Tackling the Qubit Mapping Problem for NISQ-Era Quantum Devices*. en. In: *Proceedings of the Twenty-Fourth International Conference on Architectural Support for Programming Languages and Operating Systems*. Providence RI USA: ACM, Apr. 2019, pp. 1001–1014.

[39] M. Meth et al. *Simulating two-dimensional lattice gauge theories on a qudit quantum computer*. en. In: *Nature Physics* (Mar. 2025). Publisher: Nature Publishing Group, pp. 1–7.

[40] D. Rattacaso et al. *Quantum algorithms for equational reasoning*. en. arXiv:2508.21122 [quant-ph]. Aug. 2025.

[41] S. Upadhyay et al. *A Shuttle-Efficient Qubit Mapper for Trapped-Ion Quantum Computers*. en. arXiv:2204.03695 [quant-ph]. Apr. 2022.

[42] D. Maslov. *Basic circuit compilation techniques for an ion-trap quantum machine*. en. In: *New Journal of Physics* 19.2 (Feb. 2017), p. 023035.

[43] F. J. R. Ruiz et al. *Quantum circuit optimization with AlphaTensor*. en. In: *Nature Machine Intelligence* 7.3 (Mar. 2025), pp. 374–385.

[44] K. Mato et al. *Compilation of Entangling Gates for High-Dimensional Quantum Systems*. en. In: *Proceedings of the 28th Asia and South Pacific Design Automation Conference*. Tokyo Japan: ACM, Jan. 2023, pp. 202–208.

[45] A. S. Nikolaeva, E. O. Kiktenko, and A. K. Fedorov. *Efficient realization of quantum algorithms with qudits*. en. In: *EPJ Quantum Technology* 11.1 (Dec. 2024). Publisher: SpringerOpen, pp. 1–25.

[46] M. A. Nielsen and I. L. Chuang. *Quantum Computation and Quantum Information: 10th Anniversary Edition*. Cambridge University Press, 2010.

[47] W. C. Campbell and E. R. Hudson. *Polyqubit quantum processing*. en. arXiv:2210.15484 [physics, physics:quant-ph]. Oct. 2022.

[48] S. Shivam et al. *Utility of virtual qubits in trapped-ion quantum computers*. en. arXiv:2406.19332 [physics, physics:quant-ph]. June 2024.

[49] A. R. Kessel and N. M. Yakovleva. *Implementation schemes in NMR of quantum processors and the Deutsch-Jozsa algorithm by using virtual spin representation*. en. In: *Physical Review A* 66.6 (Dec. 2002), p. 062322.

[50] A. S. Nikolaeva, E. O. Kiktenko, and A. K. Fedorov. *Universal quantum computing with qubits embedded in trapped-ion qudits*. In: *Physical Review A* 109.2 (Feb. 2024). Publisher: American Physical Society, p. 022615.

[51] E. O. Kiktenko, A. S. Nikolaeva, and A. K. Fedorov. *Colloquium : Qudits for decomposing multiqubit gates and realizing quantum algorithms*. en. In: *Reviews of Modern Physics* 97.2 (June 2025), p. 021003.

[52] J. Bian et al. *Implementation of a scalable universal two-qubit quantum processor with electron and nuclear spins in a trapped ion*. en. arXiv:2407.01196 [quant-ph]. July 2024.

[53] P. Zanardi. *Virtual Quantum Subsystems*. en. In: *Physical Review Letters* 87.7 (July 2001), p. 077901.

[54] P. Zanardi, D. A. Lidar, and S. Lloyd. *Quantum Tensor Product Structures are Observable Induced*. In: *Physical Review Letters* 92.6 (Feb. 2004). Publisher: American Physical Society, p. 060402.

[55] A. Barenco et al. *Elementary gates for quantum computation*. en. In: *Physical Review A* 52.5 (Nov. 1995), pp. 3457–3467.

[56] D. Gottesman. *The Heisenberg Representation of Quantum Computers*. en. arXiv:quant-ph/9807006. July 1998.

[57] J. S. Bell. *On the Einstein Podolsky Rosen paradox*. In: *Physics Physique Fizika* 1.3 (Nov. 1964). Publisher: American Physical Society, pp. 195–200.

[58] M. S. Guimaraes, I. Roditi, and S. P. Sorella. *Introduction to Bell's inequality in Quantum Mechanics*. en. In: *Universe* 10.10 (Oct. 2024). arXiv:2409.07597 [quant-ph], p. 396.

[59] A. Aspect, J. Dalibard, and G. Roger. *Experimental Test of Bell's Inequalities Using Time-Varying Analyzers*. In: *Physical Review Letters* 49.25 (Dec. 1982). Publisher: American Physical Society, pp. 1804–1807.

[60] S. J. Freedman and J. F. Clauser. *Experimental Test of Local Hidden-Variable Theories*. In: *Physical Review Letters* 28.14 (Apr. 1972). Publisher: American Physical Society, pp. 938–941.

[61] B. P. Lanyon et al. *Experimental Violation of Multipartite Bell Inequalities with Trapped Ions*. en. In: *Physical Review Letters* 112.10 (Mar. 2014), p. 100403.

[62] A. Einstein, B. Podolsky, and N. Rosen. *Can Quantum-Mechanical Description of Physical Reality Be Considered Complete?* In: *Physical Review* 47.10 (May 1935). Publisher: American Physical Society, pp. 777–780.

[63] V. Krutyanskiy et al. *Light-matter entanglement over 50 km of optical fibre*. en. In: *npj Quantum Information* 5.1 (Aug. 2019). Publisher: Nature Publishing Group, p. 72.

[64] C. H. Bennett and G. Brassard. *Quantum cryptography: Public key distribution and coin tossing*. In: *Theoretical Computer Science*. Theoretical Aspects of Quantum Cryptography – celebrating 30 years of BB84 560 (Dec. 2014), pp. 7–11.

[65] D. P. Nadlinger et al. *Experimental quantum key distribution certified by Bell's theorem*. en. In: *Nature* 607.7920 (July 2022). Publisher: Nature Publishing Group, pp. 682–686.

[66] D. Main et al. *Distributed quantum computing across an optical network link*. en. In: *Nature* 638.8050 (Feb. 2025). Publisher: Nature Publishing Group, pp. 383–388.

[67] P. Drmota et al. *Verifiable Blind Quantum Computing with Trapped Ions and Single Photons*. In: *Physical Review Letters* 132.15 (Apr. 2024). Publisher: American Physical Society, p. 150604.

[68] S. Debnath et al. *Demonstration of a small programmable quantum computer with atomic qubits*. en. In: *Nature* 536.7614 (Aug. 2016). Publisher: Nature Publishing Group, pp. 63–66.

[69] G. Crooks. *Quantum Gates*. Mar. 2024.

[70] C. Godfrin et al. *Operating Quantum States in Single Magnetic Molecules: Implementation of Grover's Quantum Algorithm*. en. In: *Physical Review Letters* 119.18 (Nov. 2017), p. 187702.

[71] J. Lindon et al. *Complete Unitary Qutrit Control in Ultracold Atoms*. In: *Physical Review Applied* 19.3 (Mar. 2023). Publisher: American Physical Society, p. 034089.

[72] H. Ahmed et al. *Coherent Control Over the High-Dimensional Space of the Nuclear Spin of Alkaline-Earth Atoms*. en. In: *PRX Quantum* 6.2 (June 2025), p. 020352.

[73] S. R. Hedemann. *Hyperspherical Parameterization of Unitary Matrices*. en. arXiv:1303.5904 [quant-ph]. Mar. 2013.

[74] G. Brennen, D. O'Leary, and S. Bullock. *Criteria for exact qudit universality*. en. In: *Physical Review A* 71.5 (May 2005), p. 052318.

[75] P. J. Low et al. *Practical trapped-ion protocols for universal qudit-based quantum computing*. en. In: *Physical Review Research* 2.3 (July 2020), p. 033128.

[76] Y. Wang et al. *Qudits and High-Dimensional Quantum Computing*. en. In: *Frontiers in Physics* 8 (Nov. 2020), p. 589504.

[77] J.-L. Brylinski and R. Brylinski. *Universal quantum gates*. en. arXiv:quant-ph/0108062. Aug. 2001.

[78] G. Brennen, S. Bullock, and D. O'Leary. *Efficient circuits for exact-universal computation with qudits*. en. In: *Quantum Information and Computation* 6.4&5 (July 2006), pp. 436–454.

[79] M. S. Blok et al. *Quantum Information Scrambling on a Superconducting Qutrit Processor*. In: *Physical Review X* 11.2 (Apr. 2021). Publisher: American Physical Society, p. 021010.

[80] N. Goss et al. *High-fidelity qutrit entangling gates for superconducting circuits*. en. In: *Nature Communications* 13.1 (Dec. 2022). Publisher: Nature Publishing Group, p. 7481.

[81] P. P. Popov et al. *Variational quantum simulation of $U(1)$ lattice gauge theories with qudit systems*. en. In: *Physical Review Research* 6.1 (Feb. 2024), p. 013202.

[82] P. H. Leung and K. R. Brown. *Entangling an arbitrary pair of qubits in a long ion crystal*. en. In: *Physical Review A* 98.3 (Sept. 2018), p. 032318.

[83] V. M. Schäfer et al. *Fast quantum logic gates with trapped-ion qubits*. en. In: *Nature* 555.7694 (Mar. 2018). Publisher: Nature Publishing Group, pp. 75–78.

[84] A. S. Sotirova et al. *Low cross-talk optical addressing of trapped-ion qubits using a novel integrated photonic chip*. en. In: *Light: Science & Applications* 13.1 (Aug. 2024). Publisher: Nature Publishing Group, p. 199.

[85] K. Mølmer and A. Sørensen. *Multiparticle Entanglement of Hot Trapped Ions*. In: *Physical Review Letters* 82.9 (Mar. 1999). Publisher: American Physical Society, pp. 1835–1838.

[86] D. Leibfried et al. *Experimental demonstration of a robust, high-fidelity geometric two ion-qubit phase gate*. en. In: *Nature* 422.6930 (Mar. 2003). Publisher: Nature Publishing Group, pp. 412–415.

[87] J. I. Cirac and P. Zoller. *Quantum Computations with Cold Trapped Ions*. en. In: *Physical Review Letters* 74.20 (May 1995), pp. 4091–4094.

[88] K. Gili, M. Sveistrys, and C. Ballance. *Introducing nonlinear activations into quantum generative models*. In: *Physical Review A* 107.1 (Jan. 2023), p. 012406.

[89] A. Bocharov, M. Roetteler, and K. M. Svore. *Efficient Synthesis of Universal Repeat-Until-Success Quantum Circuits*. In: *Physical Review Letters* 114.8 (Feb. 2015), p. 080502.

[90] Y. Hong et al. *Long-range-enhanced surface codes*. In: *Physical Review A* 110.2 (Aug. 2024). Publisher: American Physical Society, p. 022607.

[91] D. Bruß and C. Macchiavello. *Optimal Eavesdropping in Cryptography with Three-Dimensional Quantum States*. en. In: *Physical Review Letters* 88.12 (Mar. 2002), p. 127901.

[92] H. Bechmann-Pasquinucci and W. Tittel. *Quantum cryptography using larger alphabets*. en. In: *Physical Review A* 61.6 (May 2000), p. 062308.

[93] N. J. Cerf et al. *Security of Quantum Key Distribution Using d -Level Systems*. en. In: *Physical Review Letters* 88.12 (Mar. 2002), p. 127902.

[94] D. Collins et al. *Bell Inequalities for Arbitrarily High-Dimensional Systems*. en. In: *Physical Review Letters* 88.4 (Jan. 2002), p. 040404.

[95] T. Kraft et al. *Characterizing Genuine Multilevel Entanglement*. en. In: *Physical Review Letters* 120.6 (Feb. 2018), p. 060502.

[96] B. P. Lanyon et al. *Simplifying quantum logic using higher-dimensional Hilbert spaces*. en. In: *Nature Physics* 5.2 (Feb. 2009). Publisher: Nature Publishing Group, pp. 134–140.

[97] A. Saha et al. *Asymptotically improved circuit for a d -ary Grover's algorithm with advanced decomposition of the n -qudit Toffoli gate*. en. In: *Physical Review A* 105.6 (June 2022), p. 062453.

[98] A. S. Nikolaeva, E. O. Kiktenko, and A. K. Fedorov. *Decomposing the generalized Toffoli gate with qutrits*. In: *Physical Review A* 105.3 (Mar. 2022). Publisher: American Physical Society, p. 032621.

[99] A. S. Nikolaeva et al. *Scalable Improvement of the Generalized Toffoli Gate Realization Using Trapped-Ion-Based Qutrits*. In: *Physical Review Letters* 135.6 (Aug. 2025). Publisher: American Physical Society, p. 060601.

[100] C. Fang et al. *Realization of Scalable Cirac-Zoller Multi-Qubit Gates*. en. arXiv:2301.07564 [quant-ph]. Jan. 2023.

[101] D. González-Cuadra et al. *Hardware Efficient Quantum Simulation of Non-Abelian Gauge Theories with Qudits on Rydberg Platforms*. In: *Physical Review Letters* 129.16 (Oct. 2022). Publisher: American Physical Society, p. 160501.

[102] R. J. MacDonell et al. *Analog quantum simulation of chemical dynamics*. en. In: *Chemical Science* 12.28 (2021), pp. 9794–9805.

[103] K. Mato, S. Hillmich, and R. Wille. *Compression of Qubit Circuits: Mapping to Mixed-Dimensional Quantum Systems*. In: *2023 IEEE International Conference on Quantum Software (QSW)*. July 2023, pp. 155–161.

[104] A. Wu et al. *AutoComm: A Framework for Enabling Efficient Communication in Distributed Quantum Programs*. In: *2022 55th IEEE/ACM International Symposium on Microarchitecture (MICRO)*. Oct. 2022, pp. 1027–1041.

[105] D. Ferrari et al. *Compiler Design for Distributed Quantum Computing*. In: *IEEE Transactions on Quantum Engineering* 2 (2021), pp. 1–20.

[106] R. Zhou et al. *Optimizing Compilation for Distributed Quantum Computing via Clustering and Annealing*. en. arXiv:2508.15267 [quant-ph]. Aug. 2025.

[107] Y. Mao, Y. Liu, and Y. Yang. *Qubit Allocation for Distributed Quantum Computing*. In: *IEEE INFOCOM 2023 - IEEE Conference on Computer Communications*. ISSN: 2641-9874. May 2023, pp. 1–10.

[108] A. Wu, Y. Ding, and A. Li. *QuComm: Optimizing Collective Communication for Distributed Quantum Computing*. In: *2023 56th IEEE/ACM International Symposium on Microarchitecture (MICRO)*. Oct. 2023, pp. 479–493.

[109] T. Monz et al. *14-Qubit Entanglement: Creation and Coherence*. en. In: *Physical Review Letters* 106.13 (Mar. 2011), p. 130506.

[110] J. J. . Bollinger et al. *Optimal frequency measurements with maximally correlated states*. en. In: *Physical Review A* 54.6 (Dec. 1996), R4649–R4652.

[111] N. Goldman and J. Dalibard. *Periodically Driven Quantum Systems: Effective Hamiltonians and Engineered Gauge Fields*. In: *Physical Review X* 4.3 (Aug. 2014), p. 031027.

[112] D. Wineland et al. *Experimental issues in coherent quantum-state manipulation of trapped atomic ions*. en. In: *Journal of Research of the National Institute of Standards and Technology* 103.3 (May 1998), p. 259.

[113] D. Leibfried et al. *Quantum dynamics of single trapped ions*. en. In: *Reviews of Modern Physics* 75.1 (Mar. 2003), pp. 281–324.

[114] M. Knoop. *Trapped Charged Particles: A Graduate Textbook with Problems and Solutions*. In: ed. by M. Knoop, N. Madsen, and R. Thompson. World Scientific, 2016. Chap. Radiofrequency Traps.

[115] H. G. Dehmelt. *Radiofrequency Spectroscopy of Stored Ions I: Storage**. In: *Advances in Atomic and Molecular Physics*. Ed. by D. R. Bates and I. Estermann. Vol. 3. Academic Press, Jan. 1968, pp. 53–72.

[116] D. J. Berkeland et al. *Minimization of ion micromotion in a Paul trap*. en. In: *Journal of Applied Physics* 83.10 (May 1998), pp. 5025–5033.

[117] M. Weber. *High-Fidelity, Near-Field Microwave Gates in a Cryogenic Surface Trap*. PhD thesis. University of Oxford, 2022.

[118] D. James. *Quantum dynamics of cold trapped ions with application to quantum computation*. en. In: *Applied Physics B* 66.2 (Feb. 1998), pp. 181–190.

[119] D. F. V. James and J. Jerke. *Effective Hamiltonian Theory and Its Applications in Quantum Information*. In: *Canadian Journal of Physics* 85.6 (June 2007). arXiv:0706.1090 [quant-ph], pp. 625–632.

[120] X. R. Nie, C. F. Roos, and D. F. V. James. *Theory of cross phase modulation for the vibrational modes of trapped ions*. In: *Physics Letters A* 373.4 (Jan. 2009), pp. 422–425.

[121] L. N. Egan. *Scaling Quantum Computers with Long Chains of Trapped Ions*. en. PhD thesis. 2021, p. 239.

[122] C. J. Foot. *Atomic physics*. en. Oxford master series in physics 7. Atomic, Optical, and laser physics. OCLC: ocm57478010. Oxford ; New York: Oxford University Press, 2005.

[123] J. D. Leppard. *Quantum Computing Fundamentals with Mixed Qubit Types in 137Ba+*. en. PhD thesis. University of Oxford, 2025.

[124] D. P. Nadlinger. *Device-Independent Key Distribution between Trapped-Ion Quantum Network Nodes*. en. PhD thesis. University of Oxford, 2022.

[125] D. C. McKay et al. *Efficient Z gates for quantum computing*. en. In: *Physical Review A* 96.2 (Aug. 2017), p. 022330.

[126] F. Bloch and A. Siegert. *Magnetic Resonance for Nonrotating Fields*. en. In: *Physical Review* 57.6 (Mar. 1940), pp. 522–527.

[127] W. C. Campbell. *Angular Geometry of Atomic Multipole Transitions*. en. arXiv:2510.07451 [quant-ph]. Oct. 2025.

[128] D. V. Kosachiov, B. G. Matisov, and Y. V. Rozhdestvensky. *Coherent phenomena in multilevel systems with closed interaction contour*. en. In: *Journal of Physics B: Atomic, Molecular and Optical Physics* 25.11 (June 1992), p. 2473.

[129] S. Buckle et al. *Atomic Interferometers*. In: *Optica Acta: International Journal of Optics* 33.9 (Sept. 1986), pp. 1129–1140.

[130] D. A. Cardimona, M. P. Sharma, and M. A. Ortega. *Effect of three-level atomic state coherence on collapse and revival dynamics*. en. In: *Journal of Physics B: Atomic, Molecular and Optical Physics* 22.24 (Dec. 1989), pp. 4029–4039.

[131] A. Barfuss et al. *Phase-controlled coherent dynamics of a single spin under closed-contour interaction*. en. In: *Nature Physics* 14.11 (Nov. 2018). Publisher: Nature Publishing Group, pp. 1087–1091.

[132] B. E. King. *Angular Momentum Coupling and Rabi Frequencies for Simple Atomic Transitions*. arXiv:0804.4528 [physics]. Apr. 2008.

[133] G. A. Araneda Machuca. *Experiments with single photons emitted by single ions*. PhD. Universitat Innsbruck, 2019.

[134] J. D. Jackson. *Classical electrodynamics*. en. 3. ed., [Nachdr.] Hoboken, NY: Wiley, 2009.

[135] D. M. Brink and G. R. Satchler. *Angular momentum*. eng. 2nd ed. Oxford library of the physical sciences. Oxford: Clarendon Press, 1968.

[136] C. Zhang et al. *Submicrosecond entangling gate between trapped ions via Rydberg interaction*. en. In: *Nature* 580.7803 (Apr. 2020). Publisher: Nature Publishing Group, pp. 345–349.

[137] A. Sorensen and K. Molmer. *Entanglement and quantum computation with ions in thermal motion*. In: *Physical Review A* 62.2 (July 2000). arXiv: quant-ph/0002024, p. 022311.

[138] G. J. Milburn. *Simulating nonlinear spin models in an ion trap*. en. arXiv:quant-ph/9908037. Aug. 1999.

[139] A. Sørensen and K. Mølmer. *Quantum Computation with Ions in Thermal Motion*. In: *Physical Review Letters* 82.9 (Mar. 1999). Publisher: American Physical Society, pp. 1971–1974.

[140] C. J. Ballance. *High-Fidelity Quantum Logic in Ca+*. en. Springer Theses. Cham: Springer International Publishing, 2017.

[141] P. Kamenskikh et al. *Analysis of the action of conventional trapped-ion entangling gates in qudit space*. en. arXiv:2602.21886 [quant-ph]. Feb. 2026.

[142] P. Carruthers and M. M. Nieto. *Coherent States and the Forced Quantum Oscillator*. en. In: *American Journal of Physics* 33.7 (July 1965), pp. 537–544.

[143] S. Blanes et al. *The Magnus expansion and some of its applications*. en. In: *Physics Reports* 470.5-6 (Jan. 2009). arXiv:0810.5488 [math-ph], pp. 151–238.

[144] O. Băzăvan. *Easy as XYZ: Exploring non-commuting coherent interactions in trapped ions*. en. PhD thesis. University of Oxford, 2024.

[145] B. C. Sawyer and K. R. Brown. *Wavelength-insensitive, multispecies entangling gate for group-2 atomic ions*. en. In: *Physical Review A* 103.2 (Feb. 2021), p. 022427.

[146] P. Drmota. *Blind Quantum Computing with Trapped Ions and Single Photons*. en. PhD thesis. University of Oxford, 2023.

[147] A. C. Hughes. *Benchmarking Memory and Logic Gates for Trapped-Ion Quantum Computing*. PhD thesis.

[148] D. Hayes et al. *Coherent Error Suppression in Multiqubit Entangling Gates*. en. In: *Physical Review Letters* 109.2 (July 2012), p. 020503.

[149] D. P. DiVincenzo. *The Physical Implementation of Quantum Computation*. en. In: *Fortschritte der Physik* 48.9-11 (2000), pp. 771–783.

[150] M. A. Aksenov et al. *Realizing quantum gates with optically addressable $^{171}\mathrm{Yb}^{+}$ ion qudits*. In: *Physical Review A* 107.5 (May 2023). Publisher: American Physical Society, p. 052612.

[151] Z. Jia et al. *An architecture for two-qubit encoding in neutral ytterbium-171 atoms*. en. In: *npj Quantum Information* 10.1 (Nov. 2024). Publisher: Nature Publishing Group, p. 106.

[152] D. M. Abrams et al. *Implementation of XY entangling gates with a single calibrated pulse*. en. In: *Nature Electronics* 3.12 (Dec. 2020). Publisher: Nature Publishing Group, pp. 744–750.

[153] P. Hrmo et al. *Native qudit entanglement in a trapped ion quantum processor*. en. In: *Nature Communications* 14.1 (Apr. 2023). Publisher: Nature Publishing Group, p. 2242.

[154] A. M. Childs and N. Wiebe. *Hamiltonian simulation using linear combinations of unitary operations*. en. In: *Quantum Information and Computation* 12.11&12 (Nov. 2012), pp. 901–924.

[155] M. W. Sze et al. *Hamiltonian dynamics simulation using linear combination of unitaries on an ion trap quantum computer*. en. In: *Quantum Science and Technology* (2025).

[156] C. Monroe. *Primer on Mølmer-Sørensen Gates in Trapped Ions*. en. 2020.

[157] C. Wang et al. *Experimental Realization of Direct Entangling Gates between Dual-Type Qubits*. In: *Physical Review Letters* 134.1 (Jan. 2025), p. 010601.

[158] D. Leibfried et al. *Creation of a six-atom 'Schrödinger cat' state*. en. In: *Nature* 438.7068 (Dec. 2005). Publisher: Nature Publishing Group, pp. 639–642.

[159] B. C. Hall. *Lie Groups, Lie Algebras, and Representations: An Elementary Introduction*. en. Vol. 222. Graduate Texts in Mathematics. Cham: Springer International Publishing, 2015.

[160] J. E. Christensen et al. *High-fidelity manipulation of a qubit enabled by a manufactured nucleus*. en. In: *npj Quantum Information* 6.1 (Dec. 2020), p. 35.

[161] F. A. An et al. *High Fidelity State Preparation and Measurement of Ion Hyperfine Qubits with I > 1 2*. en. In: *Physical Review Letters* 129.13 (Sept. 2022), p. 130501.

[162] D. Hume, T. Rosenband, and D. Wineland. *High-Fidelity Adaptive Qubit Detection through Repetitive Quantum Nondemolition Measurements*. en. In: *Physical Review Letters* 99.12 (Sept. 2007), p. 120502.

[163] Z.-Y. Chen et al. *Non-invasive mid-circuit measurement and reset on atomic qubits*. en. arXiv:2504.12538 [quant-ph]. Apr. 2025.

[164] Y. Wu et al. *Erasure conversion for fault-tolerant quantum computing in alkaline earth Rydberg atom arrays*. en. In: *Nature Communications* 13.1 (Aug. 2022), p. 4657.

[165] A. Kubica et al. *Erasure Qubits: Overcoming the ${T}_{1}$ Limit in Superconducting Circuits*. In: *Physical Review X* 13.4 (Nov. 2023). Publisher: American Physical Society, p. 041022.

[166] B. M. Varbanov et al. *Leakage detection for a transmon-based surface code*. en. In: *npj Quantum Information* 6.1 (Dec. 2020). Publisher: Nature Publishing Group, p. 102.

[167] M. Kang, W. C. Campbell, and K. R. Brown. *Quantum Error Correction with Metastable States of Trapped Ions Using Erasure Conversion*. en. In: *PRX Quantum* 4.2 (June 2023), p. 020358.

[168] T. P. Harty. *High-Fidelity Microwave-Driven Quantum Logic in Intermediate-Field 43Ca+*. PhD thesis. University of Oxford, 2013.

[169] D. Greenbaum. *Introduction to Quantum Gate Set Tomography*. arXiv:1509.02921 [quant-ph]. Sept. 2015.

[170] C. J. Wood, J. D. Biamonte, and D. G. Cory. *Tensor networks and graphical calculus for open quantum systems*. en. In: *Quantum Information and Computation* 15.9&10 (July 2015), pp. 759–811.

[171] R. Blume-Kohout et al. *A Taxonomy of Small Markovian Errors*. en. In: *PRX Quantum* 3.2 (May 2022), p. 020335.

[172] A. N. Korotkov. *Error matrices in quantum process tomography*. en. arXiv:1309.6405 [quant-ph]. Nov. 2013.

[173] D. Aharonov, A. Kitaev, and N. Nisan. *Quantum Circuits with Mixed States*. arXiv:quant-ph/9806029. June 1998.

[174] R. Jozsa. *Fidelity for Mixed Quantum States*. In: *Journal of Modern Optics* 41.12 (Dec. 1994), pp. 2315–2323.

[175] M. A. Nielsen. *A simple formula for the average gate fidelity of a quantum dynamical operation*. In: *Physics Letters A* 303.4 (Oct. 2002), pp. 249–252.

[176] A. Hashim et al. *A Practical Introduction to Benchmarking and Characterization of Quantum Computers*. en. In: *PRX Quantum* 6.3 (Aug. 2025). arXiv:2408.12064 [quant-ph], p. 030202.

[177] A. A. Mele. *Introduction to Haar Measure Tools in Quantum Information: A Beginner's Tutorial*. en. In: *Quantum* 8 (May 2024). arXiv:2307.08956 [quant-ph], p. 1340.

[178] M. A. Nielsen. *Conditions for a Class of Entanglement Transformations*. en. In: *Physical Review Letters* 83.2 (July 1999), pp. 436–439.

[179] C. A. Sackett et al. *Experimental entanglement of four particles*. en. In: *Nature* 404.6775 (Mar. 2000). Publisher: Nature Publishing Group, pp. 256–259.

[180] O. Gühne et al. *Toolbox for entanglement detection and fidelity estimation*. en. In: *Physical Review A* 76.3 (Sept. 2007). arXiv:0706.2432 [quant-ph], p. 030305.

[181] N. Johnston and D. W. Kribs. *Quantum gate fidelity in terms of Choi matrices*. en. In: *Journal of Physics A: Mathematical and Theoretical* 44.49 (Nov. 2011), p. 495303.

[182] H.-P. Breuer et al. *Colloquium: Non-Markovian dynamics in open quantum systems*. In: *Reviews of Modern Physics* 88.2 (Apr. 2016), p. 021002.

[183] F. A. Pollock et al. *Non-Markovian quantum processes: Complete framework and efficient characterization*. In: *Physical Review A* 97.1 (Jan. 2018), p. 012127.

[184] G. A. L. White et al. *Unifying Non-Markovian Characterization with an Efficient and Self-Consistent Framework*. In: *Physical Review X* 15.2 (May 2025), p. 021047.

[185] A. K. Rajagopal, A. R. Usha Devi, and R. W. Rendell. *Kraus representation of quantum evolution and fidelity as manifestations of Markovian and non-Markovian forms*. In: *Physical Review A* 82.4 (Oct. 2010), p. 042107.

[186] C. W. Gardiner. *Handbook of stochastic methods : for physics, chemistry and the natural sciences*. eng. 3rd ed. Springer series in synergetics (Unnumbered). Berlin: Springer-Verlag, 2004.

[187] D. Manzano. *A short introduction to the Lindblad Master Equation*. en. In: *AIP Advances* 10.2 (Feb. 2020). arXiv:1906.04478 [quant-ph], p. 025106.

[188] C. Chatfield. *The analysis of time series : an introduction*. eng. 6th ed. Texts in Statistical Science. Boca Raton, Fla: Chapman & Hall/CRC, 2004.

[189] G. Lindblad. *On the generators of quantum dynamical semigroups*. en. In: *Communications in Mathematical Physics* 48.2 (June 1976), pp. 119–130.

[190] T. Monz. *Quantum information processing beyond ten ion-qubits*. en. PhD thesis. Innsbruck: Universitat Innsbruck, 2011.

[191] P. Cerfontaine, T. Hangleiter, and H. Bluhm. *Filter Functions for Quantum Processes under Correlated Noise*. en. In: *Physical Review Letters* 127.17 (Oct. 2021), p. 170403.

[192] T. Hangleiter, P. Cerfontaine, and H. Bluhm. *Filter-function formalism and software package to compute quantum processes of gate sequences for classical non-Markovian noise*. en. In: *Physical Review Research* 3.4 (Oct. 2021), p. 043047.

[193] T. Hangleiter, P. Cerfontaine, and H. Bluhm. *filter_functions: A package for efficient numerical calculation of generalized filter functions to describe the effect of noise on quantum gate operations*. 2021.

[194] T. H. Einwohner, J. Wong, and J. C. Garrison. *Analytical solutions for laser excitation of multilevel systems in the rotating-wave approximation*. en. In: *Physical Review A* 14.4 (Oct. 1976), pp. 1452–1456.

[195] R. Schutjens et al. *Single qubit gates in frequency-crowded transmon systems*. en. In: *Physical Review A* 88.5 (Nov. 2013). arXiv:1306.2279 [quant-ph], p. 052330.

[196] C. Bauer et al. *Gaussian pulses*. In: *Journal of Magnetic Resonance (1969)* 58.3 (July 1984), pp. 442–457.

[197] J. J. McClelland and M. H. Kelley. *Detailed look at aspects of optical pumping in sodium*. en. In: *Physical Review A* 31.6 (June 1985), pp. 3704–3710.

[198] H. A. Janacek. *Optical Bloch equations for simulating trapped-ion qubits*. en. PhD thesis. University of Oxford, 2015.

[199] H. Uys et al. *Decoherence due to Elastic Rayleigh Scattering*. In: *Physical Review Letters* 105.20 (Nov. 2010), p. 200401.

[200] M. B. Plenio and S. Virmani. *An introduction to entanglement measures*. en. arXiv:quant-ph/0504163. June 2006.

[201] J. Watrous. *The Theory of Quantum Information*. en. 1st ed. Cambridge University Press, Apr. 2018.

[202] S. C. Burd. *Squeezing and amplification of trapped-ion motion*. en. PhD. University of Colorado Boulder, 2020.

[203] S. M. Barnett and P. M. Radmore. *Methods in Theoretical Quantum Optics*. Oxford University Press, Nov. 2002.

[204] C. R. Clark et al. *High-Fidelity Bell-State Preparation with $^{40}{\mathrm{Ca}}^{+}$ Optical Qubits*. In: *Physical Review Letters* 127.13 (Sept. 2021), p. 130505.

[205] M. Brownnutt et al. *Ion-trap measurements of electric-field noise near surfaces*. en. In: *Reviews of Modern Physics* 87.4 (Dec. 2015), pp. 1419–1482.

[206] Q. A. Turchette et al. *Decoherence and decay of motional quantum states of a trapped atom coupled to engineered reservoirs*. en. In: *Physical Review A* 62.5 (Oct. 2000), p. 053807.

[207] A. S. Sotirova. *Trapped Ion Quantum Information Processing Using Multiple Qubit Encodings*. University of Oxford, 2024.

[208] T. R. Tan et al. *Suppressing Inhomogeneous Broadening in a Lutetium Multi-ion Optical Clock*. In: *Physical Review Letters* 123.6 (Aug. 2019), p. 063201.

[209] Z. Zhang et al. *Branching fractions for ${P}_{3/2}$ decays in ${\mathrm{Ba}}^{+}$*. In: *Physical Review A* 101.6 (June 2020), p. 062515.

[210] D. R. Lide et al. *CRC Handbook of Chemistry and Physics*. Vol. 85. CRC Press, 2005.

[211] F. Kondev et al. *The NUBASE2020 evaluation of nuclear physics properties* *. In: *Chinese Physics C* 45.3 (Mar. 1, 2021), p. 030001.

[212] C. Huang et al. *Electromagnetically Induced Transparency Cooling of High-Nuclear-Spin Ions*. en. In: *Physical Review Letters* 133.11 (Sept. 2024), p. 113204.

[213] K. J. Arnold et al. *Measurements of the branching ratios for $6{P}_{1/2}$ decays in $^{138}\mathrm{Ba}^{+}$*. In: *Physical Review A* 100.3 (Sept. 2019), p. 032503.

[214] H. Haken and H. C. Wolf. *Atomic and Quantum Physics*. Springer-Verlag, 1987.

[215] C. H. Baldwin et al. *High-fidelity light-shift gate for clock-state qubits*. In: *Physical Review A* 103.1 (Jan. 2021), p. 012603.

[216] G. Breit and I. I. Rabi. *Measurement of Nuclear Spin*. en. In: *Physical Review* 38.11 (Dec. 1931), pp. 2082–2083.

[217] A. C. Hughes et al. *Benchmarking a High-Fidelity Mixed-Species Entangling Gate*. en. In: *Physical Review Letters* 125.8 (Aug. 2020), p. 080504.

[218] E. Magesan, J. M. Gambetta, and J. Emerson. *Scalable and Robust Randomized Benchmarking of Quantum Processes*. en. In: *Physical Review Letters* 106.18 (May 2011), p. 180504.

[219] J. F. Poyatos, J. I. Cirac, and P. Zoller. *Complete Characterization of a Quantum Process: The Two-Bit Quantum Gate*. In: *Physical Review Letters* 78.2 (Jan. 1997), pp. 390–393.

[220] R. T. Thew et al. *Qudit quantum-state tomography*. en. In: *Physical Review A* 66.1 (July 2002), p. 012303.

[221] J. Řeháček et al. *Diluted maximum-likelihood algorithm for quantum tomography*. In: *Physical Review A* 75.4 (Apr. 2007), p. 042108.

[222] E. Nielsen et al. *Gate Set Tomography*. en. In: *Quantum* 5 (Oct. 2021). arXiv:2009.07301 [quant-ph], p. 557.

[223] S. Kimmel, G. H. Low, and T. J. Yoder. *Robust calibration of a universal single-qubit gate set via robust phase estimation*. en. In: *Physical Review A* 92.6 (Dec. 2015), p. 062315.

[224] R. Srinivas et al. *High-fidelity laser-free universal control of trapped ion qubits*. en. In: *Nature* 597.7875 (Sept. 2021), pp. 209–213.

[225] D. M. Meekhof et al. *Generation of Nonclassical Motional States of a Trapped Atom*. In: *Physical Review Letters* 76.11 (Mar. 1996), pp. 1796–1799.

[226] A. Meurer et al. *SymPy: symbolic computing in Python*. In: *PeerJ Computer Science* 3 (Jan. 2017), e103.